

**AFRL-ML-WP-TR-1999-4178**

**MECHANICAL BEHAVIOR OF  
ADVANCED AEROSPACE  
MATERIALS**

**N.E. ASHBAUGH  
D.J. BUCHANAN  
A.L. HUTSON  
R. JOHN  
K. LI  
W.J. PORTER  
D.A. STUBBS**

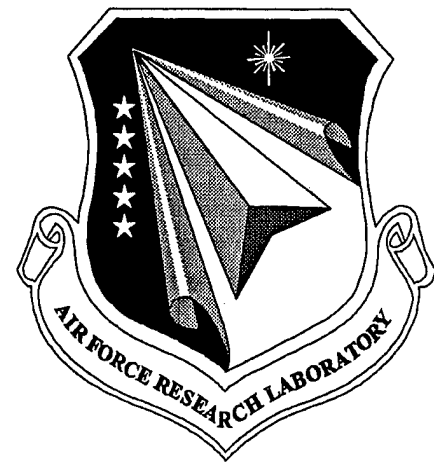
**UNIVERSITY OF DAYTON RESEARCH INSTITUTE  
STRUCTURAL INTEGRITY DIVISION  
300 COLLEGE PARK  
DAYTON, OHIO 45469-0128**

**SEPTEMBER 1999**

**FINAL REPORT FOR 05/25/1994 – 05/24/1998**

**APPROVED FOR PUBLIC RELEASE; DISTRIBUTION UNLIMITED**

**MATERIALS AND MANUFACTURING DIRECTORATE  
AIR FORCE RESEARCH LABORATORY  
AIR FORCE MATERIEL COMMAND  
WRIGHT-PATTERSON AIR FORCE BASE OH 45433-7750**



**DTIC QUALITY INSPECTED 4**

**20000809 043**

## NOTICE

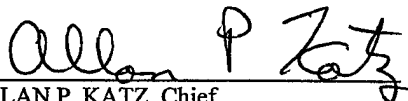
USING GOVERNMENT DRAWINGS, SPECIFICATIONS, OR OTHER DATA INCLUDED IN THIS DOCUMENT FOR ANY PURPOSE OTHER THAN GOVERNMENT PROCUREMENT DOES NOT IN ANY WAY OBLIGATE THE US GOVERNMENT. THE FACT THAT THE GOVERNMENT FORMULATED OR SUPPLIED THE DRAWINGS, SPECIFICATIONS, OR OTHER DATA DOES NOT LICENSE THE HOLDER OR ANY OTHER PERSON OR CORPORATION; OR CONVEY ANY RIGHTS OR PERMISSION TO MANUFACTURE, USE, OR SELL ANY PATENTED INVENTION THAT MAY RELATE TO THEM.

THIS REPORT IS RELEASABLE TO THE NATIONAL TECHNICAL INFORMATION SERVICE (NTIS). AT NTIS, IT WILL BE AVAILABLE TO THE GENERAL PUBLIC, INCLUDING FOREIGN NATIONS.

THIS TECHNICAL REPORT HAS BEEN REVIEWED AND IS APPROVED FOR PUBLICATION.



JAY R. JIRA, Project Engineer  
Ceramics Development & Materials  
Behavior Branch  
Metals, Ceramics & NDE Division



ALLAN P. KATZ, Chief  
Ceramics Development & Materials  
Behavior Branch  
Metals, Ceramics & NDE Division



GERALD J. PETRAK, Asst. Chief  
Metals, Ceramics, and Nondestructive  
Evaluation Division  
Materials and Manufacturing Directorate

Do not return copies of this report unless contractual obligations or notice on a specific document requires its return.

REPORT DOCUMENTATION PAGE			Form Approved OMB No. 0704-0188	
Public reporting burden for this collection of information is estimated to average 1 hour per response, including the time for reviewing instructions, searching existing data sources, gathering and maintaining the data needed, and completing and reviewing the collection of information. Send comments regarding this burden estimate or any other aspect of this collection of information, including suggestions for reducing this burden, to Washington Headquarters Services, Directorate for Information Operations and Reports, 1215 Jefferson Davis Highway, Suite 1204, Arlington, VA 22202-4302, and to the Office of Management and Budget, Paperwork Reduction Project (0704-0188), Washington, DC 20503.				
1. AGENCY USE ONLY (Leave blank)		2. REPORT DATE Sept. 1999		3. REPORT TYPE AND DATES COVERED Final Report for period 25 May 1994 - 24 May 1998
4. TITLE AND SUBTITLE Mechanical Behavior of Advanced Aerospace Materials			5. FUNDING NUMBERS C - F33615-94-C-5200 PE - 62102F PR - 2302 TA - B1 WU - 06	
6. AUTHOR(S) N.E. ASHBAUGH, D.J. BUCHANAN, A.L. HUTSON, R. JOHN, K. LI, W.J. PORTER, AND D.A. STUBBS				
7. PERFORMING ORGANIZATION NAME(S) AND ADDRESS(ES) UNIVERSITY OF DAYTON RESEARCH INSTITUTE STRUCTURAL INTEGRITY DIVISION 300 COLLEGE PARK DAYTON, OHIO 45469-0128			8. PERFORMING ORGANIZATION REPORT NUMBER  UDR-TR-1999-00074	
9. SPONSORING/MONITORING AGENCY NAME(S) AND ADDRESS(ES) Materials and Manufacturing Directorate Air Force Research Laboratory Air Force Materiel Command Wright-Patterson AFB, OH 45433-7734 POC: Jay Jira, AFRL/MLLN, (937) 255-1358			10. SPONSORING/MONITORING AGENCY REPORT NUMBER  AFRL-ML-WP-TR-1999-4178	
11. SUPPLEMENTARY NOTES				
12a. DISTRIBUTION AVAILABILITY STATEMENT Approved for public release, distribution unlimited			12b. DISTRIBUTION CODE	
13. ABSTRACT (Maximum 200 words) This report summarizes investigations involving the characterization of second tier mechanical properties of current and advanced aerospace materials and the development of damage tolerant design approaches and durability analyses for the applications of these materials. Specifically, studies of gamma-titanium aluminides have dealt with the identification and origins of defects that are associated with processing procedures and with the role of defects and grain orientation on fatigue crack initiation. Growth of both through-the-thickness and surface bridged cracks in unidirectional metal matrix composites was studied over ranges of stress ratios and temperatures. The shear lag model that was developed to predict through-the-thickness crack growth was modified to successfully predict the effect of stress ratio and temperature on the surface crack growth. Damage evolution, associated with fiber breakage, and deformation models were developed for sustained loading of unidirectional metal matrix composites and extended to fatigue conditions. Studies of ceramic composite systems were conducted to understand the mechanics and mechanisms of damage initiation and crack growth in smooth sided and notched specimens under monotonic and fatigue loads. The influences of high cycle fatigue, fretting fatigue, and fatigue-load interactions on damage tolerance and mixed-mode crack growth of current monolithic structural alloys have been investigated for an enhanced understanding of improved life prediction methodologies. In support of the preceding investigations, the following experimental tools and methodologies were investigated and/or developed - a) surface wave amplitudes for correlation with the formation and the opening and closing of ceramic matrix cracks during load/unload cycles, b) broadband sensors for detection of surface waves and rod waves to locate fiber breaks in metal matrix composites, c) step stress test method for evaluation of fatigue lives greater than $10^6$ cycles, d) an infrared system for crack detection, e) a stable LVDT based extensometer for long time and small-strain resolution, and e) electromagnetic shaker system with improved loading and response capabilities and magnetostrictive system for high frequency loading.				
14. SUBJECT TERMS Titanium aluminides, gamma, orthorhombic, titanium matrix composites, SiC fibers, ceramic matrix composites, nickel-base superalloys, turbine blade materials, high cycle fatigue, fatigue crack growth, elevated temperatures, creep, thermal fatigue, thermomechanical fatigue, fretting fatigue, load interactions, mixed-mode, stress intensity factors, finite element analysis, nondestructive evaluation			15. NUMBER OF PAGES 238	
			16. PRICE CODE	
17. SECURITY CLASSIFICATION OF REPORT  Unclassified	18. SECURITY CLASSIFICATION OF THIS PAGE  Unclassified	19. SECURITY CLASSIFICATION OF ABSTRACT  Unclassified	20. LIMITATION OF ABSTRACT  SAR	

## **TABLE OF CONTENTS**

---

	<b>PAGE</b>
<b>1.0 EXECUTIVE SUMMARY .....</b>	<b>1</b>
1.1 $\gamma$ TiAl-BASE ALUMINIDES .....	1
1.2 Ti-MATRIX AND Ti-ALUMINIDE COMPOSITES .....	1
1.3 CERAMIC MATRIX COMPOSITES .....	3
1.4 INITIATION AND GROWTH OF FATIGUE CRACKS IN AEROSPACE MATERIALS .....	4
1.5 DEVELOPMENT OF EXPERIMENTAL PROCEDURES, METHODOLOGIES AND LABORATORY ENHANCEMENTS .....	5
<b>2.0 INTRODUCTION .....</b>	<b>7</b>
2.1 BACKGROUND .....	7
2.2 PROGRAM OBJECTIVES .....	7
2.3 REPORT ORGANIZATION .....	7
<b>3.0 DAMAGE TOLERANCE STUDIES OF <math>\gamma</math> TiAl-BASE TITANIUM ALUMINIDE     ALLOYS .....</b>	<b>9</b>
3.1 OBSERVED DEFECTS, FLAWS, AND OTHER INHOMOGENEITIES IN DESIGNATED ALLOYS .....	9
3.2 DEVELOPMENT OF HEAT TREATMENT FOR 3-95 .....	9
3.3 HIGH CYCLE FATIGUE INITIATION IN LAMELLAR KD-CBS (Ti-46Al-2Cr-2.7Nb-0.2W-0.15Si-0.1B-0.2C) .....	10
3.4 THE EFFECTS OF PROLONGED HIGH TEMPERATURE AIR EXPOSURE ON MONOTONIC AND CYCLIC PROPERTIES OF A GAMMA TITANIUM ALUMINIDE ALLOY .....	10
3.5 OPTIMIZATION OF ELECTROPOLISHING .....	10
3.6 FATIGUE INITIATION SITES FOR 3-95 .....	11
<b>4.0 DAMAGE ACCUMULATION AND FAILURE OF Ti-MATRIX AND     Ti-ALUMINIDE-MATRIX COMPOSITES .....</b>	<b>12</b>
4.1 FATIGUE AND FCG BEHAVIOR .....	12
4.1.1 Unnotched Fatigue and Fatigue Crack Growth Behavior of Trimarc-1™/Ti-6Al-2Sn-4Zr-2Mo .....	12



4.1.2	Effect of Stress Ratio on Surface-Crack Growth in a Continuously Reinforced Metal Matrix Composite .....	12
4.1.3	Fatigue Crack Growth Behavior of SCS-ULTRA™/Ti-22Al-26Nb .....	13
4.1.4	Bridging Stress Distributions During Fatigue Crack Growth in [0] Metal Matrix Composites .....	14
4.1.5	The Effect of Temperature on Fiber/Matrix Interface Sliding in SCS-6/TIMETAL®21S [C1] <sup>1</sup> .....	14
4.1.6	Prediction of Transverse Fatigue Behavior of Unidirectionally Reinforced Metal Matrix Composite [C2] .....	15
4.2	TENSILE AND CREEP BEHAVIOR .....	15
4.2.1	Creep Behavior of Ti-22Al-26Nb and SCS-ULTRA™/ Ti-22Al-26Nb .....	15
4.2.2	Modeling the Deformation and Failure of a Unidirectional Metal Matrix Composite Under Sustained Load .....	16
4.2.3	Influence of Carbon on Tensile Behavior of Ti-22Al-26Nb .....	16
4.2.4	Influence of Viscoplasticity on Residual Stress and Strength of a Titanium Matrix Composite After Thermomechanical Fatigue [C3] .....	17
4.3	CHARACTERIZATION AND HEAT TREATMENT DEVELOPMENT OF ORTHORHOMBIC SYSTEMS .....	17
4.3.1	Microstructure and Properties of Tape Cast Ti-22Al-23Nb and Ti-25Al-17Nb-1Mo .....	17
4.3.2	Heat Treatment Development for SCS-ULTRA™/Ti-22Al-26Nb .....	18
4.4	CHARACTERIZATION OF CONSTITUENTS .....	19
4.4.1	Constitutive Model of Neat Ti-6Al-4V .....	19
4.4.2	FCG of Neat Ti-22Al-26Nb .....	19
5.0	DAMAGE ACCUMULATION AND FAILURE OF CERAMIC MATRIX COMPOSITES (CMC) .....	21
5.1	FRACTURE BEHAVIOR OF AN OXIDE/OXIDE CERAMIC MATRIX COMPOSITE [C4] .....	21
5.2	FRACTURE BEHAVIOR OF SEVERAL WOVEN OXIDE/OXIDE CMCs .....	21
5.3	CHARACTERIZATION OF NOTCHED BEHAVIOR OF WOVEN OXIDE/OXIDE CERAMIC MATRIX COMPOSITES .....	22
5.4	TEMPERATURE EFFECTS ON DAMAGE EVOLUTION IN CERAMIC MATRIX COMPOSITES .....	22
5.5	DEVELOPMENT AND EVALUATION OF A TEST TECHNIQUE TO MEASURE TRANSTHICKNESS TENSILE STRENGTH OF CERAMIC-MATRIX COMPOSITES .....	24

<sup>1</sup> Notation in square brackets refer to manuscripts in Compendium.

5.6	INFLUENCE OF HEAT TREATMENT TIMES ON THE UNIAXIAL TENSILE, TRANS-THICKNESS TENSILE, AND COMPRESSION BEHAVIOR OF NEXTEL 312™/493 BLACKGLAST™ (BN).....	25
6.0	<b>INITIATION AND GROWTH OF FATIGUE CRACKS IN AEROSPACE MATERIALS.....</b>	<b>26</b>
6.1	HIGH CYCLE FATIGUE OF TITANIUM ALLOYS .....	26
6.1.1	A Rapid Method for Generation of a Haigh Diagram for High Cycle Fatigue [C5] .....	26
6.1.2	Fretting Fatigue of Ti-6Al-4V Under Flat on Flat Contact [C6].....	26
6.1.3	S-N Behavior at 1800 Hz of Ti-6Al-4V .....	27
6.2	FATIGUE CRACK GROWTH.....	28
6.2.1	Stress-Level-Dependent Stress Ratio Effect on Fatigue Crack Growth [C7].....	28
6.2.2	Near-Threshold Crack Growth Behavior of a Single Crystal Ni-Base Superalloy Subjected to Mixed Mode Loading [C8] .....	28
6.2.3	The Role of Threshold Fatigue Crack Growth in Life Prediction of the Alloy Ti-6Al-2Sn-4Zr-6Mo Under High Cycle Fatigue Spectra [C9] .....	29
6.2.4	The Role of Threshold Fatigue Crack Growth in Life Prediction for Two Titanium Alloys Under High Cycle Fatigue Spectra [C10] .....	29
6.2.5	Fractographic Study of Load Sequence Induced Mixed-Mode Fatigue Crack Growth in an Al-Cu Alloy [C11].....	30
6.2.6	Fatigue Crack Growth Rate Characteristics of Laser Shock Peened Titanium [C12].....	30
7.0	<b>DEVELOPMENT OF EXPERIMENTAL PROCEDURES, METHODOLOGIES AND LABORATORY ENHANCEMENTS .....</b>	<b>31</b>
7.1	INFRARED CRACK DETECTION SYSTEM .....	31
7.2	NONDESTRUCTIVE EVALUATION TECHNIQUES FOR DETECTING SURFACE DEFECTS IN $\gamma$ TITANIUM ALUMINIDES [C13].....	31
7.3	FEASIBILITY OF EDDY CURRENT IMAGING TECHNIQUE TO DETECT TMF-INITIATED SURFACE CRACKS IN MMC .....	32
7.4	DEVELOPMENT OF BROADBAND ACOUSTIC EMISSION FOR DETECTING FIBER CRACKING IN MMCs DURING CREEP TESTING .....	33
7.5	DEVELOPMENT OF A DRY-COUPPLANT ULTRASONIC SCANNING SYSTEM FOR <i>IN SITU</i> DETECTION OF DAMAGE IN CMC .....	34
7.6	EXTENSOMETER USE IN ELEVATED TEMPERATURE TESTING .....	34
7.7	LEFM SOLUTION FOR A CENTRALLY NOTCHED DISK .....	36

7.8	DESIGN, FABRICATION AND OPERATION OF NEW SHAKER BASED HCF TEST SYSTEMS.....	36
7.8.1	Design and Fabrication.....	36
7.8.2	Operation .....	37
7.8.3	Laser Measurement Enhancement of HCF Test System 1 .....	37
7.9	DATA ARCHIVE AND KEYSERVER® STATUS .....	38
8.0	REFERENCES .....	39
	Appendix A: COMPENDIUM OF MANUSCRIPTS .....	41
	Appendix B: LIST OF SYMBOLS, ABBREVIATIONS, AND ACRONYMS .....	231
	BIBLIOGRAPHY .....	233

## ***LIST OF FIGURES***

---

5.4.1	Observed cracking pattern in $[0/90]_{3S}$ SiC/BMAS at 21 and 900°C during tension loading.....	24
6.1.1	S-N curve for Ti-6Al-4V at 1800 Hz and $R=0.8$ .....	27

## ***LIST OF TABLES***

---

6.1.1	Test Matrix for Haigh Diagram Evaluation .....	28
-------	--	----

## **FOREWORD**

The work described in this report was performed at the Ceramics Development & Materials Behavior Branch, Metals, Ceramics & Nondestructive Evaluation Division, Materials and Manufacturing Directorate, Air Force Research Laboratory (AFRL/MLLN) under Contract No. F33615-94-C-5200, "Mechanical Behavior of Advanced Aerospace Materials." The contract is administered under the direction of AFRL by Mr. Jay R. Jira. The program is being conducted by the Structural Integrity Division, University of Dayton Research Institute, Dayton, Ohio with Dr. Noel E. Ashbaugh and Mr. Robert J. Andrews acting as the Principal Investigator and Program Manager, respectively. This report is a final report on the progress of the 4-year contract effort.

In the last year of the contract, the investigations were developed and directed by Drs., Robert Brockman, Reji John, Andrew Rosenberger, and Brian Worth and Messrs. Dennis Buchanan, Richard Goodman, George Hartman, Joseph Kroupa, David Maxwell, W. John Porter, and David Stubbs and Mrs. Alisha Hutson and graduate students Ms. Victoria Kramb and Messrs. Roger Gural and Stetson Planck. Mrs. Jacqui Hawkins was responsible for coordinating the input and typing of this document. This final report covers the work performed during the period of 25 May 1994 to 24 May 1998.

## **SECTION 1**

### **EXECUTIVE SUMMARY**

---

#### **1.1 $\gamma$ -TIAL-BASE ALUMINIDES**

Gamma titanium aluminides continue to receive widespread interest as candidate materials for demanding aerospace applications. The implementation of gamma into turbine engines currently under development has been hindered by a general lack of design methodology for low toughness, limited ductility materials such as gamma. The focus of our research has been geared towards the development of a damage tolerant design methodology for gamma titanium aluminides. This design philosophy will be suitable for application to future limited ductility, low toughness intermetallic materials. To achieve this goal, a test program designed to emphasize critical needs for life prediction model development was organized and undertaken.

Understanding fatigue crack initiation and growth under a variety of loading situations and environmental conditions, similar to those seen in service, was paramount in our program. The role played by different microstructural conditions was also an important factor in the testing. Highlights from our work during this period include: 1) while processing defects play an important role in fatigue initiation, grain orientation is an even more important factor with initiation often occurring at poorly oriented grains instead of at known defects; 2) long duration, elevated temperature exposure of gamma leads to the formation of oxides that are detrimental to fatigue performance, however, when the oxides are removed, original base metal mechanical properties are observed; and 3) materials manufactured for alloy development programs often are not processed as carefully as material used in industry, i.e., the number and types of defects seen in development material would be significantly reduced if manufactured using standard industrial practice for rotor grade materials.

#### **1.2 TI-MATRIX AND Ti-ALUMINIDE COMPOSITES**

Metal matrix composites have great potential for application in gas turbine engines due to their high specific-strength-to-weight ratio and elevated temperature capabilities. Over the past four years IHPTET, TMCTECC, and F-22 Advanced Tactical Fighter programs have targeted advanced titanium matrix composites (TMC) for specific applications such as blings, blades and actuator rods, respectively. The MMC Life Prediction Cooperative (PRDA-IV) is developing a comprehensive state-of-the-art code to predict the life of these TMC components. During this reporting period, substantial

efforts were directed towards supporting the IHPTET, TMCTECC, PRDA-IV and F-22 Advanced Tactical Fighter programs.

Extensive testing of unidirectionally reinforced Trimarc-1/Ti-6Al-2Sn-4Zr-2Mo, SCS-6/Ti-6Al-4V and SCS-ULTRA™/Ti-22Al-26Nb was conducted to evaluate the damage tolerance under simulated service loading conditions. During fabrication, some degree of fiber swimming and touching can be expected in the TMC. A statistical analysis on the fatigue tests of Trimarc-1/Ti-6-2-4-2 showed that the number of occurrences of touching fibers did not exhibit a significant correlation with the number of cycles to failure. The primary mode of damage during fatigue loading is the growth of cracks. Although most of the available fatigue crack growth (FCG) data are from through-crack specimens, surface cracks occur more frequently during service. Hence, surface crack growth in SCS-6/Ti-6-4 was studied at various stress ratios and temperatures. The shear lag model, which was developed to predict through-crack growth, was modified to successfully predict the effect of stress ratio and temperature on the surface crack growth in SCS-6/Ti-6Al-4V. The knowledge of the *in situ* fiber strength is required to predict the onset of fiber failure. Analysis of crack growth and crack opening displacements in SCS-ULTRA™/Ti-22Al-26Nb showed that the *in situ* fiber strength was significantly lower than the reported mean strength. In addition, bridging fiber stress distributions were deduced from crack opening displacements measured during crack growth. The bridging stress profile was consistent with the new shear lag models with nonzero bridging stress at the crack tip. These bridging models utilize the fiber/matrix frictional shear stress ( $\tau$ ) to determine the bridging stresses. Hence, the influence of temperature on  $\tau$  was determined using crack opening displacements. A frictional law, in which  $\tau$  was proportional to the radial residual stress, was found to predict the effective  $\tau$  for a bridged crack at temperatures  $\leq 400^\circ\text{C}$ . The [0] TMC are susceptible to transverse loading. Hence, a net-section-based model was developed to predict the fatigue behavior of [0] TMC subjected to transverse loading.

Extensive testing was conducted to characterize the creep and tensile behavior of neat Ti-22Al-26Nb and SCS-ULTRA™/Ti-22Al-26Nb. A new model based on the statistical variation of the fiber strength was developed to predict the deformation and failure of unidirectionally reinforced TMC subjected to sustained loading. Since most of the fibers used in TMC systems contain carbon coatings, the influence of carbon on the tensile behavior of neat Ti-22Al-23Nb was also investigated. Using modified Bodner-Partom constitutive equations for the matrix, the influence of viscoplasticity on the



residual stress and strength of a TMC after thermomechanical fatigue loading was predicted. In addition, due to the increased creep resistance of orthorhombic titanium matrices, a large effort was devoted to developing advanced orthorhombic matrices through alloy additions and heat treatments.

Life prediction of the TMC components requires the characterization of the individual constituents. Tensile, creep and FCG experiments were conducted to generate the baseline data for the neat matrices. A new constitutive model using a combination of the power-law and a hyperbolic sine function was developed to better represent the primary and secondary creep response of the neat matrix.

### **1.3 CERAMIC MATRIX COMPOSITES**

Ceramic matrix composites (CMC) are targeted for high temperature aerospace applications such as advanced turbine burners, divergent flaps and seals, and combustors. Due to the inherent resistance to environmental effects such as oxidation, CMC systems with oxide fibers and oxide matrices are being considered for these applications, which include stress concentration sites, such as cooling holes and attachment points. Hence, a program was initiated to understand the mechanics and mechanisms of damage initiation and growth from notches in two Oxide/Oxide CMC systems, namely Nextel610/AS and Nextel720/AS.

The fracture toughness of Nextel610/AS decreased by 50% when the temperature increased from 23 to 950°C, in contrast to the 15% decrease in unnotched strength. Ultrasonic C-scans and fractographic studies showed that the decrease in notched strength was associated with surface matrix crack growth and damage restricted to the notch plane. Nextel720/AS made by different manufacturers exhibited similar deformation response and strength when corrected for the differences in volume fraction of the fibers. The notched strength of Nextel720/AS and Nextel610/AS was proportional to the corresponding fiber strength. During room tests, local displacements and strains around circular and sharp notches were measured. The longitudinal strain was nearly linear up to the peak stress, while the off-axis strain was nonlinear even at low stresses. Predictions obtained using finite element analysis, based on homogeneous nonlinear orthotropic material properties, correlated well with the displacement and strain response.

A unique integrated NDE/Mechanical testing system was developed to aid development of damage-based life prediction models. Surface replicates and *in situ*

high-magnification photography were used to establish the relationship between the formation of cracks and the changes in the ultrasonic wave signals. The changes in the transmitted surface wave signal were correlated with the formation, and opening and closing of matrix cracks during load/unload cycles at 23 and 900°C. Some of these CMC components are typically held in place using special attachments, which were molded *in situ*. Hence, a unique test system using button (round and square) specimens was developed to determine the transthickness tensile strength of several CMC systems. Some of the CMC properties could be sensitive to the exposure to intermediate temperatures during service. Hence, the effect of exposure of Nextel312(BN)/Blackglas to 600°C on the tensile, transthickness tensile and compression behavior was studied. Increase in exposure times resulted in 45% increase in tensile strength. However, the increase in tensile strength was associated with 60 and 80% decrease in compressive and transthickness tensile strength, respectively.

#### **1.4 INITIATION AND GROWTH OF FATIGUE CRACKS IN AEROSPACE MATERIALS**

Initiation and growth of fatigue cracks are the primary factors in the assessment of life and damage tolerance of components. The influence of high cycle fatigue (HCF) is one of the most important problems affecting the readiness of the Air Force fleet. To understand this problem and to develop life prediction models, tests must be conducted in the laboratory for lives greater than  $10^6$  cycles.

A step stress test method has been developed, and shown to be an effective method to evaluate fatigue lives greater than  $10^6$  cycles. The step stress method was applied to Ti-6Al-4V at stress ratio (R) values from -1 to 0.90 for  $10^7$  cycles. The lives were confirmed by conventional S-N methods for R=0.1, 0.5, and 0.8. In addition, lives for Ti-6Al-4V at R=0.8 were being determined for  $10^9$  cycles at 1800 Hz. Fretting fatigue has been studied using a flat-on-flat contact with blended contact radii to simulate turbine blade attachment. Resulting lives at  $10^7$  cycles have indicated that stresses must be increased for increasing R or for decreasing contact radius.

Fractographic measurements of fatigue-crack-growth rates in an Al alloy for cracks as small as 0.03 mm revealed R effects even when crack closure was absent. A model of these rates must use both stress intensity range and a second independent parameter, such as R, to reflect the influence of the loading conditions. The importance of the threshold regime in life prediction methodology for crack growth was

demonstrated for two Ti alloys under load spectra where lives greater than  $10^7$  cycles were expected.

In cases of persistent mixed-mode loading in single crystal Ni-base superalloy, self-similar crack growth was achieved with relative ease. With the addition of a mode II or shear stress intensity factor, the crack growth rate was more than an order of magnitude higher than without the mode II component. On the other hand, the initiation of mixed-mode growth in an Al alloy by load interaction between high-amplitude, low-R and low-amplitude, high-R load cycles created retardation in growth rates.

The influence of residual stress was investigated for laser shock peened (LSP) Ti-6Al-4V. Differences in fatigue growth rates between LSP processed material and unprocessed material at small positive values of R were explained by use of an effective stress intensity range. Only the portion of loading above the crack opening load was effective in growing the crack.

#### **1.5 DEVELOPMENT OF EXPERIMENTAL PROCEDURES, METHODOLOGIES AND LABORATORY ENHANCEMENTS**

Maintaining excellence in material behavior research requires that the staff have the best possible tools and procedures for monitoring damage and specimen response to the imposed test conditions. For nondestructive evaluation (NDE), the hardware for an infrared crack detection system has been checked out and utility software has been written for early detection of cracks. A "dry couplant" methodology showed promise in the detection of planar defects in ceramic matrix composites. An investigation of three NDE techniques, eddy current imaging, ultrasonic surface wave imaging, and fluorescent dye penetrant, indicated that all three could provide viable tools to detect surface flaws as small as 0.20 by 0.13 mm in  $\gamma$ -titanium aluminide. In another study, eddy current imaging detected cracks as small as 0.25 mm in metal matrix composites under thermomechanical fatigue conditions. Broadband acoustic emission has been used to successfully detect and locate fiber breakage events in metal matrix composites under creep loading.

An LVDT based extensometer has been developed to measure small strain deformation. Variability in strain by as much as  $\pm 500$  microstrain that has been attributable to changes in lab air humidity has occurred with expensive off-the-shelf high temperature extensometers. The new extensometer has been relatively insensitive to lab air variations and provided good long term electrical stability.

Stress intensity factor solutions for modes I and II for center-cracked disk geometry that were available in the literature have been extended to longer crack length-to-diameter ratios. This effort supported the mixed-mode crack growth investigation of single crystal Ni-base superalloy.

The in-house test capability for the HCF test program has been augmented by the design and construction of two electromagnetic shaker systems with improved loading and response capabilities as compared to earlier systems.

## **SECTION 2**

### **INTRODUCTION**

---

#### **2.1 BACKGROUND**

Lighter-weight higher-strength damage-tolerant materials must be used to achieve the Air Force goals for future aircraft and engines. The durability and damage tolerance analysis requirements defined in the Aircraft Structural Integrity Program (ASIP) and the Engine Structural Integrity Program (ENSIP) standards provide guidelines for damage tolerance of Air Force vehicles. Engine performance goals have been set forth in the Integrated High Performance Turbine Engine Technology (IHPTET) program. A new program has been initiated to improve the design methodology being applied to engine components that are subjected to high cycle fatigue. To apply the advanced materials effectively, a thorough understanding of the material behavior must be obtained and a methodology for life prediction of these materials must be developed.

#### **2.2 PROGRAM OBJECTIVES**

The objectives of this program are to (a) obtain experimental data on the material behavior of current and advanced aerospace materials, (b) develop state-of-the-art techniques for determining mechanical properties of materials under simulated engine service conditions, (c) develop the methodology for a damage tolerant design approach and durability analysis for application of these materials, (d) analyze experimental results and governing microstructure mechanisms, and (e) transition the findings to the scientific and design communities.

#### **2.3 REPORT ORGANIZATION**

This final report presents the research conducted on the material behavior and modeling of advanced aerospace materials under contract within the Ceramics Development and Materials Behavior Branch (MLLN) of the Metals, Ceramics & Nondestructive Evaluation Division of the Materials and Manufacturing Directorate at Wright-Patterson Air Force Base. This effort was conducted over a 4 year period from 25 May 1994 to 24 May 1998. Progress during the first 3 years of the contract has been reported in three interim annual reports [Ashbaugh, 1996; Ashbaugh, *et al.*, 1997; Ashbaugh, *et al.*, 1999]. The investigations that have been completed and were in progress during the final year of the contract will be discussed in this report.

Copies of the manuscripts describing completed efforts are provided in the compendium for the convenience of readers who wish to have more detailed information of the investigations readily available. Extended discussions of the work-in-progress are presented to provide as much information as possible about the current investigations. For completeness, the publications that have resulted from the research in the first 3 years of the contract are listed in the bibliography.

In Sections 3, 4, 5, and 6, the material properties and damage assessment for  $\gamma$ -titanium aluminides, TMC, CMC, and engine blade materials, respectively, are discussed. The development of experimental procedures and test techniques, methodologies, and laboratory enhancements is presented in Section 7.

### **SECTION 3**

#### **DAMAGE TOLERANCE STUDIES OF $\gamma$ TIAL-BASE TITANIUM ALUMINIDE ALLOYS**

##### **3.1 OBSERVED DEFECTS, FLAWS AND OTHER INHOMOGENEITIES IN DESIGNATED ALLOYS**

To ensure reliability in aircraft gas turbine engines and to satisfy specific structural requirements, damage tolerance must be demonstrated with respect to intrinsic or service-generated defects. The overall objective of the present research was to detect, quantify and determine the nature of intrinsic defects in wrought  $\gamma$  titanium aluminides and to develop an understanding of their detrimental effects on fatigue behavior. The materials studied were 3-95 (Ti-48Al-2Cr-2Nb-1Mo-0.2B) and several K5 derivative materials (KD-CB, KD-CBS and KD-HTCBS). The roles of microstructure, particularly lamellar colony size and orientation, in determining fatigue behavior were studied. X-ray, ultrasonic inspection, SEM, EDS and Auger electron microscopy were employed to accomplish the goal.

Most of the defects are believed to have originated from melting and casting processes, and these defects survived through the subsequent forging and/or heat treatment processes. Serious compositional segregation, residual cast dendrite microstructure, porosity and oxides were observed in these alloys. In many instances of fractographic observation of fatigued specimens, the defects observed did not result in initiation; rather, fatigue failure originated in grains situated in a weak orientation. The results of this work help to develop a mechanistic understanding of the fatigue behavior of gamma alloys and offer suggestions for improving the fatigue capacity of this class of materials.

##### **3.2 DEVELOPMENT OF HEAT TREATMENT FOR 3-95**

In collaboration with researchers from MLLM, efforts were undertaken to develop a heat treatment for the 3-95 alloy to produce a microstructure similar to that used by Pratt & Whitney (P&W) in demonstrator components. Various solution treatment temperatures and cooling rates were employed in developing an appropriate heat treatment. This effort resulted in a heat treatment that closely matched the P&W microstructure. Having a nearly identical microstructure allowed for the results of our 3-95 research programs to be directly applicable to ongoing development programs outside of ML.

### **3.3 HIGH CYCLE FATIGUE INITIATION IN LAMELLAR KD-CBS (Ti-46Al-2Cr-2.7Nb-0.2W-0.15Si-0.1B-0.2C)**

The objectives of this program were threefold, to: 1) assess the fatigue performance of KD-CBS, 2) determine the mechanisms leading to initiation and 3) better define life prediction and life management techniques for gamma alloys.

The primary reason for fatigue initiation was found to be lamellar separation in large grains oriented perpendicular to the loading direction. This mode of failure is common in fully lamellar  $\gamma$  alloys. Fatigue initiation was also found to occur in lamellar/near-gamma interface regions in areas where microstructural inhomogeneities or defects existed. Careful analysis of the KD-CBS alloy found a wide disparity in grain size probably due to inadequate boron distribution in the cast ingot. These defects are symptomatic of improper or insufficient processing of the wrought material used in this project.

### **3.4 THE EFFECTS OF PROLONGED HIGH TEMPERATURE AIR EXPOSURE ON MONOTONIC AND CYCLIC PROPERTIES OF A GAMMA TITANIUM ALUMINIDE ALLOY**

It is known that TiAl suffers from poor ductility and toughness at temperatures below the ductile to brittle transition temperature and may suffer a further reduction in tensile ductility following high temperature exposure in air. Currently, however, there is not a clear understanding of the effect of high temperature exposure on the fatigue performance of this class of alloys. Experiments were performed to determine the degree of degradation of the monotonic and cyclic properties due to prolonged high temperature exposure of the 3-95 alloy. Tensile and fatigue tests at RT, 540 and 760°C were conducted following 50 and 500-hour exposures at 760°C. The properties of the embrittled layer that formed during exposure were characterized using hardness testing and scanning electron microscopy. It is proposed that fracture of this layer leads to lower ductility and shortens the time to crack initiation and that its removal restores the virgin properties. Examination of the failed specimens using SEM was used to identify the relationship between the embrittled surface and mechanical performance of the bulk material.

### **3.5 OPTIMIZATION OF ELECTROPOLISHING**

It is believed that the fatigue behavior of the TiAl is sensitive to the surface roughness and residual stresses induced by machining. However, removal of the machined surface material using a common electropolishing technique employing



perchloric acid plus methanol often resulted in surface pitting which served as fatigue crack initiation sites. The surface imperfections were attributed to long polishing times and subsequent uneven rates of material removal based on local microstructural chemistry differences. An electropolishing technique using a solution of sulfuric acid and methanol was adopted and modified to produce high quality specimens. Some of the information concerning this technique was obtained from Rockwell Science Center personnel. The new method was found to be much more efficient, working up to 20 times faster than the original (i.e., perchloric) approach. This polishing procedure has also been successfully applied to most other titanium-based alloys such as Ti-6-4, Ti-6-2-4-6 and Ti-6-2-4-2, as well as various  $\gamma$  alloys.

### **3.6 FATIGUE INITIATION SITES FOR 3-95**

A considerable amount of work was performed attempting to identify fatigue crack initiation sites in the 3-95 material. For the nearly lamellar structure found in 3-95, the cleavage character of the equiaxed gamma phase indicates the presence of the initiation regions at relatively low magnification. However pinpointing the exact location of the initiation site was found to be very difficult. On the other hand, when tests were conducted at 540 and 760°C, thumbnail- or circular-shaped initiation sites were clearly visible due to the presence of oxides that formed after initiation. The oxides were of varying thickness depending on the duration of exposure of the crack surface at temperature. Not only was it possible to study the microstructural characteristics of the initiation site, but the ability to measure the critical crack size before significant crack propagation occurred was also made possible.

## SECTION 4

### **DAMAGE ACCUMULATION AND FAILURE OF TI-MATRIX AND TI-ALUMINIDE MATRIX COMPOSITES**

---

#### **4.1 FATIGUE AND FCG BEHAVIOR**

##### **4.1.1 Unnotched Fatigue and Fatigue Crack Growth Behavior of Trimarc-1™/Ti-6Al-2Sn-4Zr-2Mo**

The influence of temperature, stress ratio and fiber touching on the fatigue behavior of [0]<sub>10</sub> Trimarc-1™/Ti-6Al-2Sn-4Zr-2Mo has been examined through a large cooperative effort between government and industry to develop a cost effective manufacturing program for the implementation of TMC actuators into engine and airframe systems. All tests were conducted at temperatures of 23°C, 163°C and 371°C. Tension, fatigue crack growth and low-cycle fatigue tests were conducted and compared to other TMC systems such as SCS-6/Ti-15-3 and SCS-6/Ti-6-4 in monotonic tension and fatigue crack growth. The results of these comparisons showed that fiber volume fraction and fiber strength could significantly effect the performance of the composite. Isothermal fatigue tests were conducted at several stress ratios to show that increased tensile mean stresses reduce the number of cycles to failure for a given stress amplitude. A statistical analysis on the fatigue tests of specimens with fibers orientated in the longitudinal and transverse direction to the applied loading showed that the number of occurrences of touching fibers does not exhibit a significant correlation with the number of cycles to failure.

##### **4.1.2 Effect of Stress Ratio on Surface-Crack Growth in a Continuously Reinforced Metal Matrix Composite**

A simplified methodology was developed to predict surface crack growth from semi-elliptical unbridged flaws in a continuously reinforced metal matrix composite. Exact calculation of the bridging stress intensity factor range for a surface crack,  $\Delta K_{b,PS(T)}$  requires the use and/or development of two-dimensional weight functions and a time consuming iteration procedure. Hence, as a first approximation,  $\Delta K_{b,PS(T)}$  was calculated using the  $\Delta K_b$  for a corresponding center-crack geometry as,

$$\Delta K_{b,PS(T)} = \Delta K_{b,M(T)} \frac{F_{PS(T)}}{F_{M(T)}} \quad (1)$$

where  $\Delta K_{b,M(T)}$  = bridging stress intensity factor range for a center-through crack,  $F_{PS(T)}$  = normalized stress intensity factor for a surface crack under tension, and  $F_{M(T)}$  = normalized stress intensity factor for a center through-crack under tension. The fiber/matrix interfacial shear stress,  $\tau$ , deduced from center through-crack data, was used to predict the crack growth response of the semi-elliptical surface crack at three stress ratios ( $R$ ). The aspect ratio of the surface crack during crack growth was assumed to be the same as the initial aspect ratio consistent with fracture surface observations. The predictions obtained at  $R=0.1$ ,  $0.5$  and  $0.7$  at room temperature correlated satisfactorily with the data. An expression similar to that of Eqn. (1) was also used to predict the bridged crack opening displacement range during surface crack growth and these predictions correlated well with the data. The results from this study confirm that the  $\tau$  deduced from through-crack specimens can be used to successfully predict the bridged semi-elliptical surface crack growth in thick TMC components.

#### 4.1.3 Fatigue Crack Growth Behavior of SCS-ULTRA™/Ti-22Al-26Nb

Extensive characterization of the fatigue crack growth behavior of unidirectionally reinforced SCS-ULTRA™/Ti-22Al-26Nb was conducted in support of a collaborative program between AFRL/ML and Allison Engine Company. Crack growth parallel and perpendicular to fibers was investigated at stress ratios ( $R$ ) of  $0.05$ ,  $0.5$  and  $0.8$ , and temperatures of  $23$ ,  $482$  and  $649^\circ\text{C}$ . In addition, the crack growth behavior of neat Ti-22Al-26Nb was also characterized as discussed in section 4.4.2.

In  $[0]_8$  SCS-ULTRA™/Ti-22Al-26Nb, fully bridged crack growth behavior was observed in all cases except at high maximum stress ( $\sigma_{\max}$ ) and low  $R$ . In some cases, multiple (distributed) cracks were also observed above and below the primary machined notch. At  $482^\circ\text{C}$ , partially bridged or unbridged crack growth was observed at  $\sigma_{\max} \geq 400$  MPa at all stress ratios. In contrast, at  $649^\circ\text{C}$ , we could not initiate crack growth from the machined notch at  $\sigma_{\max} \leq 550$  MPa. This increased damage tolerance at  $649^\circ\text{C}$  can be attributed to the increased ductility. The results from this study also show that (1) crack growth behavior of SCS-ULTRA™/Ti-22Al-26Nb is similar to that of SCS-6/Ti-22Al-23Nb and SCS-6/Ti-24Al-11Nb at room temperature, and (2) at  $649^\circ\text{C}$ , SCS-ULTRA™/Ti-22-26 exhibits significantly better performance compared to that of SCS-6/Ti-22Al-23Nb and SCS-6/Ti-24Al-11Nb. A shear lag model was used to successfully predict fully bridged and partially bridged crack growth at room temperature. The predictions of crack opening displacements also correlated well with the measurements. The analysis also

showed that the predicted fiber stresses at the onset of failure ( $\approx 3000$  MPa) were significantly lower than the reported mean strength ( $\approx 6500$  MPa). Tension testing of fibers extracted from untested and tested specimens is in progress to investigate the degradation of *in situ* fiber strength.

Crack growth parallel to fibers in SCS-ULTRA™/Ti-22Al-26Nb was associated with significant R effects and crack closure at 23 and 482°C. At 649°C, no R effect was observed. The closure corrected crack growth behavior of  $[90]_8$  was similar to that of neat matrix behavior contrary to that expected in a matrix with uniformly spaced holes. The increased crack growth resistance of the  $[90]_8$  composite could be attributed to (1) staggered distribution of fibers, (2) plane stress dominated growth in matrix ligament between fibers, and/or (3) stiffness contribution from fibers. Analysis is in progress to correlate the  $[90]_8$  crack growth behavior to that of the neat matrix.

#### **4.1.4 Bridging Stress Distributions During Fatigue Crack Growth in $[0]$ Metal Matrix Composites**

An optimization procedure was used to deduce the bridging stress from crack opening displacements measured during fatigue crack growth in a unidirectionally reinforced metal matrix composite (SCS-6/TIMETAL®21S). The results have indicated that the bridging stress was nonzero at the crack tip contrary to predictions from conventionally used shear lag models. The bridging stress at the crack tip was proportional to the applied farfield stress. This bridging law, deduced from experimental measurements, supports new shear lag models that include nonzero bridging stress at the crack tip.

#### **4.1.5 The Effect of Temperature on Fiber/Matrix Interface Sliding in SCS-6/TIMETAL®21S [C1]**

This paper discusses the determination of  $\tau$  as a function of temperature from COD measured *in situ* via a laser IDG technique during crack growth along long fully bridged cracks in SCS-6/TIMETAL®21S. A fatigue test was conducted on a center-cracked specimen made of unidirectional 4-ply SCS-6/TIMETAL®21S with a volume fraction of 0.355. The initial notch length was  $\approx 1.7$  mm; maximum stress achieved through constant amplitude loading was 300 MPa with a load ratio of 0.1 at 1 Hz. After a crack extension of  $\approx 4$  mm was achieved at 23°C, microhardness indents were placed along the crack wake. Load versus COD was measured at each indent for each temperature step: 21, 100, 200, 300, 400 and 500°C. The tau values obtained at 23°C

for the two shear lag models evaluated were  $\tau_{MCE} = 7.55$  MPa and  $\tau_{McC} = 2.80$  MPa. It was found that  $\tau$  decreased with increasing temperature. A friction law, in which  $\tau$  is proportional to the radial residual stress on the fibers, was found to successfully predict the temperature effect on the effective  $\tau$  for a bridged crack. The deduced  $\tau$  was underestimated for temperatures above 400°C, due to the onset of oxidation of the fiber coatings. The above analysis assumed that  $\sigma_r$  does not change due to mechanical cycling at room and elevated temperatures. Additional analysis is required to verify this assumption.

#### **4.1.6 Prediction of Transverse Fatigue Behavior of Unidirectionally Reinforced Metal Matrix Composites [C2]**

A net-section-based model was used to successfully predict the overall isothermal fatigue behavior of unidirectionally reinforced MMC subjected to transverse loading. The model correctly predicts the relatively flat transverse fatigue behavior (S-N) of the MMC including the ultimate strength during tension loading and the threshold stress. The threshold stress is close to the stress corresponding to the onset of debonding between the fiber the matrix during transverse tension loading. The near-flat transverse fatigue behavior (S-N) implies that a damage tolerance based approach may be inapplicable under transverse loading for some MMC systems.

### **4.2 TENSILE AND CREEP BEHAVIOR**

#### **4.2.1 Creep Behavior of Ti-22Al-26Nb and SCS-ULTRA™/Ti-22Al-26Nb**

Creep behavior of neat Ti-22Al-26Nb has been evaluated for stress and temperature ranges from 34.5 to 621 MPa (5.0 to 90 ksi) and from 482 to 760°C (900 to 1400°F), respectively. The  $[0]_8$  SCS-ULTRA™/Ti-22Al-26Nb composite was tested at 371, 538, and 649°C (700, 1000, and 1200°F) for stresses ranging from 1030 to 1520 MPa (150 to 220 ksi). The  $[90]_8$  SCS-ULTRA™/Ti-22Al-26Nb composite was tested at temperatures ranging from 482 to 760°C (900 to 1400°F) for stresses ranging from 13.8 to 172 MPa (2.00 to 25 ksi). For the  $[0]_8$  and  $[90]_8$  composites, the measured fiber volume ranged from 0.37 to 0.42.

Preliminary results indicated that the neat matrix has comparable creep response as orthorhombic Ti-22Al-23Nb. Based on limited data, the fiber-volume-corrected time and temperature creep performance of  $[0]_8$  SCS-ULTRA™/Ti-22Al-26Nb was slightly

better than SCS-ULTRA™/Ti-22Al-23Nb. Perhaps with enough data to evaluate scatter, the response of the two composites would be comparable.

#### **4.2.2 Modeling the Deformation and Failure of a Unidirectional Metal Matrix Composite Under Sustained Load**

A one-dimensional deformation and rupture model for a unidirectional continuously reinforced titanium matrix composite, SCS-6/Ti-6Al-4V, has been extended for application to fatigue-dwell loading. A refined constitutive model for the Ti-6Al-4V matrix has been shown to be more accurate than the Bodner-Partom model for predicting creep and relaxation behaviors. The deformation model also incorporates a two-parameter Weibull distribution to characterize the SCS-6 fiber strengths. The Weibull parameters,  $m$  and  $\sigma_0$ , were deduced for an entire panel from a single test specimen. The deformation, accumulation of fiber failures, and rupture life for other specimens in the panel were predicted with the deduced values of  $m$  and  $\sigma_0$ . Acoustic emission data were collected during the tests and provided the history of the damage accumulation to compare with the predicted fiber failures from the model. The predictions accurately captured the creep and relaxation behavior and predicted time to failure within a factor of two.

#### **4.2.3 Influence of Carbon on Tensile Behavior of Ti-22Al-23Nb**

Carbon has long been known as a potent alpha phase stabilizer in titanium and titanium aluminide alloys. Most of the fibers used for manufacturing TMC have carbon coatings to develop interfaces between the fiber and the matrix that allow for load shedding. The carbon, however, readily diffuses into the surrounding matrix material during composite manufacturing and creates areas of alpha- or alpha-2-rich regions around the fibers. Systematic studies to understand the effects on the mechanical properties of TMC due to carbon diffusion have not been undertaken. This study attempted to measure the mechanical properties of matrix material following the introduction of various amounts of carbon as might be seen in TMC. The information from tests such as these should allow for more accurate matrix properties to be fed into life prediction models currently under development.

The material used in this study was the orthorhombic alloy Ti-22Al-23Nb (Ti-22-23). Compositions containing 0, 1, 2 and 3 at% carbon were cast. Studies performed to determine the effect of the carbon additions indicate an expected upward shift of the beta transus with increasing carbon content. The material was then heat-treated using

common Ti-22-23 TMC solution treatment temperatures. The following results were obtained: the volume fraction of  $\alpha_2$  increased with 1% carbon addition but not with further carbon addition, 1% carbon appeared to increase the yield strength and the failure stress at room temperature and 650°C, room temperature ductility was observed to drop significantly even with 1% carbon additions, strength and ductility of 1% carbon material at 650°C was better than the 0% material, and room and elevated temperature modulus values were not significantly influenced by any level of carbon addition.

#### **4.2.4 Influence of Viscoplasticity on Residual Stress and Strength of a Titanium Matrix Composite After Thermomechanical Fatigue [C3]**

Modifications to the Bodner-Partom (B-P) constitutive equations provide improved flexibility in fitting a larger strain-rate range than previously available. Using the modified B-P equations, the importance of good matrix characterization becomes apparent for an SCS-6/Timetal®21S composite under thermomechanical and isothermal fatigue, as well as sustained loading. An interesting observation is that the residual stress after thermomechanical fatigue (TMF) can be significantly different than those found in the as-received composite. This phenomenon is caused by prestraining the fiber at high loads and temperatures during TMF. This phenomenon also provides an excellent opportunity to compare the predictive capabilities between the older and newer B-P models. When the maximum and minimum strains during TMF are obtained with the two models and compared to experimental measurements, the difference between the two models is minimal. However, inspection of the shifts in residual stress from the as-received condition shows significant difference between the older and newer B-P formulation. Lastly, pre-strained fibers caused by thermomechanical loading can cause a loss of room temperature tensile strength. To show this, a rudimentary fiber failure model is defined. This model is used to show that the loading type strongly influences residual strength. The loss of residual strength is significantly more sensitive to loading type, rather than the viscoplastic characterization.

### **4.3 CHARACTERIZATION AND HEAT TREATMENT DEVELOPMENT OF ORTHORHOMBIC SYSTEMS**

#### **4.3.1 Microstructure and Properties of Tape Cast Ti-22Al-23Nb and Ti-25Al-17Nb-1Mo**

The inherent high cost of continuous-fiber-reinforced TMC has been a significant barrier to widespread acceptance of these systems for aerospace application. Serious

problems have also been encountered in working large ingots of intermetallic, orthorhombic alloys down to foil for use in foil-fiber-foil composite manufacturing processes. To address both issues, powder metallurgy (P/M) processes for fabricating TMC were investigated. The two primary objectives of this work were to: 1) evaluate P/M tape casting as a method for manufacturing orthorhombic titanium matrix composites and 2) evaluate various orthorhombic alloys for use as matrices in tape cast OTMC systems.

Tensile and creep properties of 'neat' panels of Ti-22-23 and Ti-25-17-1 manufactured using tape cast and foil-based approaches were compared. The tensile properties of the tape cast material were similar to the foil-based material at room temperature and 650°C; however, the tape cast material was substantially less creep resistant than the foil-based material. The poor creep resistance was primarily due to the much finer grain size of the tape cast material, however, the phase morphology of the orthorhombic phase (blocky appearance in tapecast versus needle-like in foil-based), in particular, was also a contributing factor.

#### **4.3.2 Heat Treat Treatment Development for SCS-ULTRA™/Ti-22Al-26Nb**

Initial testing of the SCS-ULTRA™/ Ti-22Al-26Nb (US/Ti-22-26) material for Allison found it to exhibit low room temperature ductility and poor low cycle fatigue performance when tested in the longitudinal orientation. Fractographic and microstructural analysis of this material indicated the presence of significant alpha-2 phase in both the Textron- and Allison-processed material.

The alpha-2 phase is known for its limited ductility due to the inherent limited number of slip systems available. A study was executed with the goal of developing a heat treatment that minimized the amount of alpha-2 present. Solution treatment temperatures were kept below the  $\beta$ -transus temperature in an effort to avoid precipitous grain growth. To achieve this, the  $\beta$ -transus temperature for the US/Ti-22-26 composite was determined using the disappearing phase technique. The  $\beta$ -transus temperature for the composite was found to be 1080°C, so a solution temperature of 1074°C was selected. Test coupons from Allison were heat treated using the 1074°C solution temperature followed by the simulated bling-bond HIP cycle and two subsequent stress relief cycles, as is the practice for manufacturing components. The 1074°C solution temperature is considerably higher than the highest temperatures seen in either the



Textron (1018°C) or Allison (1010°C) processes. As expected, the alpha-2 content of the material heat treated at 1074°C was lower than that of the original material.

To determine the effects of the new heat treatment on mechanical properties, two room temperature tensile tests were performed. The results of the testing were mixed. While the average ductility and ultimate tensile strength were improved with the new heat treatment, the average yield stress results were lower. A limited supply of material and no additional transverse samples limited our ability to fully characterize the new heat treatment.

#### **4.4 CHARACTERIZATION OF CONSTITUENTS**

##### **4.4.1 Constitutive Model of Neat Ti-6Al-4V**

The effort on assessing the capabilities of a different model to characterize the primary and secondary creep behavior of neat Ti-6Al-4V than the Bodner-Partom unified constitutive model has been progressing. This model is a combination of a power law to simulate primary creep response and of a hyperbolic sine to simulate secondary creep. In the initial step of the assessment, the creep data at 427°C were used to determine the coefficients in the model. The model was used to predict the relaxation responses from various levels of applied strain.

Since the predictions were in good agreement with the relaxation data, the model was used to predict the cyclic fatigue response at 1 and 0.01 Hz and at 427°C under controlled strain limits. The fatigue predictions were in fairly good agreement with data even though one of the fatigue tests included an interruption and restart of the test. The development of the model was expanded to include creep data for temperatures from 260 to 538°C. Preliminary results have indicated that the predictions of relaxation from stepped strain controlled tests were accurate.

##### **4.4.2 FCG of neat Ti-22Al-26Nb**

The R effects on the crack growth behavior of neat Ti-22Al-26Nb was characterized at 23, 482 and 649°C. The single edge cracked geometry with clamped ends was used during this investigation. Compliance measurements were made to determine the closure effects. Crack closure based correction of the applied  $\Delta K$  collapsed data obtained at different R at 23 and 482°C. In contrast, effects of R, not accounted for by closure, were observed at 649°C at low  $\Delta K$ . The closure corrected threshold stress intensity factor range,  $\Delta K_{th,eff}$  decreased with increasing R at 649°C. At

high  $\Delta K$ , the lowest crack growth rate occurred at 482°C. These data were used to obtain trend lines, which were used in analyzing the crack growth behavior in SCS-ULTRA™/Ti-22Al-26Nb as discussed in section 4.1.3.

## **SECTION 5**

### **DAMAGE ACCUMULATION AND FAILURE OF CERAMIC MATRIX COMPOSITES (CMC)**

---

#### **5.1 FRACTURE BEHAVIOR OF AN OXIDE/OXIDE CERAMIC MATRIX COMPOSITE [C4]**

The fracture behavior of an oxide/oxide ceramic matrix composite, Nextel610/Aluminosilicate (Nextel610/AS), was investigated at 23 and 950°C using a single edge notched specimen geometry with clamped ends. Crack growth and damage progression was monitored during the tests using optical microscopy, ultrasonic C-scans, and crack mouth opening displacement. Nextel610/AS was found to be notch sensitive, with failure stresses below that predicted from unnotched tension data. The failure mode was nonbrittle with considerable nonlinear deformation prior to and after the peak load at 23 and 950°C. The stress intensity factor at the peak load decreased 50% when temperature was increased from 23 to 950°C. The reduction in notch strength with temperature was associated with a change in damage mode. At 23°C distributed matrix cracking resulted in stress redistribution around the notch and no evidence of damage on the specimen surface. In contrast at 950°C, C-scans indicated damage was confined to the notch plane and crack growth was characterized by surface matrix crack growth. The extent of ultrasonic attenuation ahead of the notch tip correlated with the extent of matrix cracking at 23°C, and crack length measured on the specimen surface at 950°C. The maximum length of exposed 0° fibers on the fracture surfaces was 4 mm and 1 mm at 23 and 950°C, respectively.

#### **5.2 FRACTURE BEHAVIOR OF SEVERAL WOVEN OXIDE/OXIDE CMCs**

The fracture behavior of two Nextel 720/Aluminosilicate (N720/AS) composites manufactured by General Electric (GE) and Composite Optics (CO) and one Nextel 610/Aluminosilicate (N610/AS) manufactured by 3M were investigated using the modified single edge notched geometry, MSE(T), at room temperature in lab air. Load versus crack mouth opening displacement (CMOD) data were acquired continuously throughout the testing. Results of the fracture tests indicate that all three systems exhibited notch sensitive behavior at room temperature. The fracture data showed a 22.5%, 32% and 19% decrease in the net section peak stress as compared to the unnotched tensile data for the GE, CO and 3M composites, respectively. Analysis of the fracture surfaces revealed that all materials exhibited distributed damage for the room

temperature fracture tests. Preliminary fracture tests at elevated temperature (1000°C) show a single dominant crack in the notch plane and no distributed damage.

### **5.3 CHARACTERIZATION OF NOTCHED BEHAVIOR OF WOVEN OXIDE/OXIDE CERAMIC MATRIX COMPOSITES**

The effect of sharp notches and open center holes on the tensile behavior of an oxide/oxide ceramic matrix composite, Nextel610/Aluminosilicate (Nextel610/AS), was investigated at room temperature. Crack growth and damage progression was monitored during the tests using optical microscopy, ultrasonic C-scans, local strain measurements, CMOD and hole end-point displacements ( $\delta$ ). Effect of notch length and specimen size on the failure strength was investigated. Failure stress for the edge notched geometry was well below that predicted by the unnotched tensile strength and correlated well with an average peak stress intensity factor of  $14.6 \text{ MPa}\sqrt{\text{m}}$ . The open center hole specimens failed at a maximum net section stress that was close to the unnotched tensile stress. The observed load versus displacement (CMOD or  $\delta$ ) response for both specimen geometries was highly nonlinear prior to and after the peak load. In contrast, local strain measurements close to the location of maximum stress concentration showed that longitudinal strains increased linearly up to the point of fiber breakage. The load versus displacement (CMOD or  $\delta$ ) and load versus strain responses were predicted satisfactorily using finite element analysis. The inelastic-plastic material behavior, used in the analysis, was based on the unnotched tensile response. Damage modes identified on polished sections were correlated with enhanced ultrasonic attenuation in the damage zone and observed deformation behavior.

### **5.4 TEMPERATURE EFFECTS ON DAMAGE EVOLUTION IN CERAMIC MATRIX COMPOSITES**

Under the AFOSR-AASERT program, a detailed study of damage initiation and progression in CMC at elevated temperatures was conducted [Gural, 1998]. This study also demonstrated the first successful application of the surface wave technique during elevated temperature testing of CMC and the correlation between the change in surface wave characteristics and damage mechanisms.

The characterization of damage initiation and progression in [0] and [0/90] CMC at room and elevated temperatures using an ultrasonic surface wave technique was investigated. An integrated NDE/mechanical test system was successfully used to characterize damage initiation and accumulation in [0] and [0/90] CMC systems. The *in*

*situ* surface wave technique was used at room and elevated temperatures (up to 900°C). Extensive surface replication and photography were used to correlate changes in the ultrasonic wave characteristics to damage mechanisms.

The sudden decrease in the peak to peak amplitude of the surface wave signal coincided with the onset of matrix cracking at room and elevated temperatures. The amplitude of the surface wave signal decreased with increasing crack density. Matrix cracking occurred first in the matrix rich regions where the fiber spacing was the widest. Figure 5.4.1 is a schematic of the experimentally observed matrix cracking in [0/90]<sub>3S</sub> SiC/BMAS during testing at room and elevated temperatures. Unlike the typically idealized sequence of damage progression, matrix cracking was observed to occur simultaneously in both ply orientations. As shown in Figure 5.4.1, testing at elevated temperatures delayed the onset of matrix cracking in the [0/90] material. A delay in the onset of matrix cracking was also observed in the [0] material. The overall number of matrix cracks was reduced during testing of both materials at elevated temperatures.

The surface wave technique was used to differentiate between the initiation and propagation of damage. The change in peak to peak amplitude was shown to be sensitive to the maximum stress levels during load/unload testing. Load/unload testing also revealed that a portion of the surface wave response might be attributed to the partial contact of fracture surfaces in the form of opening and closing fiber bridged cracks. The longitudinal wave technique did not demonstrate the same sensitivity to crack progression as the surface wave technique. Instead, the longitudinal wave appeared to be sensitive to changes in the overall stiffness of the material.

A shear lag model was used to infer the interfacial sliding stress,  $\tau$ , as a function of temperature for [0]<sub>16</sub> Nicalon/MAS-5 and [0/90]<sub>3S</sub> SiC/BMAS. The average  $\tau$  decreased with increasing temperature for both materials.

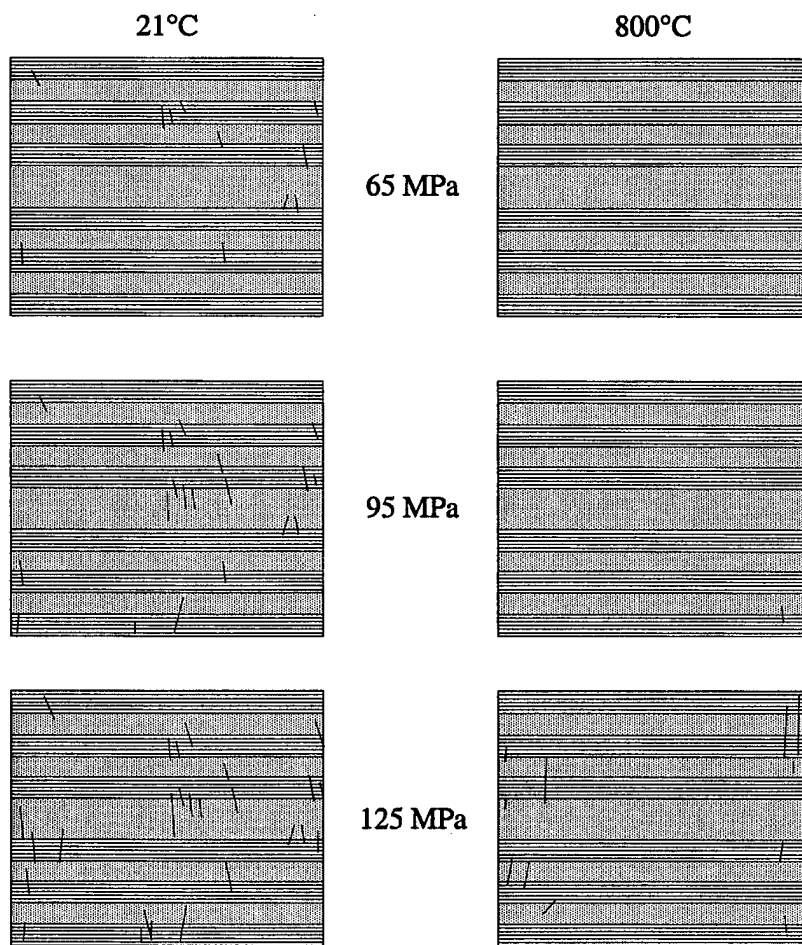


Figure 5.4.1. Observed cracking pattern in  $[0/90]_{3s}$  SiC/BMAS at 21 and 900°C during tension loading.

### 5.5 DEVELOPMENT AND EVALUATION OF A TEST TECHNIQUE TO MEASURE TRANSTHICKNESS TENSILE STRENGTH OF CERAMIC MATRIX COMPOSITES

The designs of the test fixture attachments need to account for low transthickness strength of CMC's to accurately characterize transthickness strength. A unique loading arrangement was designed and constructed to generate these important design data. This arrangement included the use of an adhesive to bond the test specimen to the test fixture, a precision alignment procedure to align the fixture in the test machine, and the development of a test procedure. The effects of specimen geometry were investigated using round and square specimens because of machine costs related to round button specimen design. The round button specimens were 25.4 mm in diameter by 6 mm thick, while the square specimens were 17 mm on a side and 6

mm thick. Test results accurately characterized the transthickness strength of the CMC and showed no statistically significant differences between the means or the variances of the two specimen geometries.

#### **5.6 INFLUENCE OF HEAT TREATMENT TIMES ON THE UNIAXIAL TENSILE, TRANS-THICKNESS TENSILE, AND COMPRESSION BEHAVIOR OF NEXTEL 312™/493 Blackglas™ (BN)**

The influence of three heat treatment times on the tensile, transthickness tensile, and compression behavior of Nextel 312™/493 Blackglas™ (BN) was investigated at room temperature. Heat treatment temperature of 600°C at times of 50, 100, and 500 hours were used to condition machined specimens. Testing was conducted on a servo-hydraulic testing machine in actuator ram displacement control, at a displacement rate of 0.05 mm per second.

Tensile results showed an increase in ultimate tensile strength of 45% with the increase in heat treatment time. However, compression ultimate strengths decreased by 60% with an increase in heat treatment times. Transthickness tensile strength also showed a decrease in ultimate tensile strength (80%) as heat treatment times increased. Detailed studies of the microstructure and fracture surfaces revealed that a loss in the matrix integrity with the increase in heat treatment times contributed to the observed behavior.

## **SECTION 6**

### **INITIATION AND GROWTH OF FATIGUE CRACKS IN AEROSPACE MATERIALS**

#### **6.1 HIGH CYCLE FATIGUE OF TITANIUM ALLOYS**

##### **6.1.1 A Rapid Method for Generation of a Haigh Diagram for High Cycle Fatigue [C5]**

A rapid test method was developed for generating data points for a Haigh diagram for Ti-6Al-4V at a constant life of  $10^7$  cycles at room temperature. It involves subjecting specimens to loading blocks of  $10^7$  fatigue cycles and progressively increasing the load until failure occurs. An equivalent stress is obtained for each test specimen for plotting on the Haigh diagram. The method was applied to tests conducted at stress ratios (ratio of minimum to maximum stress) from  $R=-1$  to  $R=0.9$ . The validity of the method was confirmed by comparing data with those obtained using the conventional S-N interpolation approach at values of  $R=0.1$ ,  $0.5$ , and  $0.8$ . The rapid testing technique was then extended to the generation of a Haigh diagram for the same material subjected to prior low cycle fatigue (LCF) for 10% of its LCF life. No degradation of the fatigue limit is observed from subsequent HCF testing using the rapid testing technique.

##### **6.1.2 Fretting Fatigue of Ti-6Al-4V Under Flat-on-Flat Contact [C6]**

A fretting fatigue test system was developed to simulate the fretting fatigue damage that occurs in turbine engine blade attachments. The test system employs a flat-on-flat contact with blending radii, which reproduces the nominal levels of normal and internal shear stresses present in dovetails. These stress states are achieved through the application of the normal loads required to grip a fatigue specimen coupled with the cyclic axial loads used to generate fatigue data. This geometry was used to evaluate the effects of normal contact stress, contact radius, contact length, and load ratio on fretting fatigue of Ti-6Al-4V against Ti-6Al-4V. Nominal pad lengths were 25.4 mm and 12.7 mm; static normal loads were 70 kN and 42 kN; and contact radii were 3.2 mm and 0.4 mm. Average specimen dimensions were 100 mm long X 10 mm wide X 2 mm thick. All tests were conducted using a step loading technique at 300 Hz in lab air at room temperature on an electro-dynamic shaker test system. Successful fretting tests have been conducted as evidenced by the characteristic fretting damage and failure locations observed in test specimens via SEM analysis. In addition, trends in data,



based on variation of different parameters, show that stresses required for constant lives of  $10^7$  cycles increased with increasing stress ratio, or decreasing contact radius.

### 6.1.3 S-N Behavior at 1800 Hz of Ti-6Al-4V

A study has begun to define the Haigh diagram in  $10^9$ -cycle regime for Ti-6Al-4V. The tests for this study will be conducted in a specially designed magnetostrictive driven system that operates at 1800 Hz. For the first part of the study, an S-N curve, Figure 6.1.1, has been compiled for  $R = 0.8$ . The next step involves completion of the test matrix shown in Table 6.1.1. These tests include conditions for results that have been obtained from other test machines at lower frequencies to allow quantification of the frequency effect. However, work has progressed slowly due to several factors including inability of the software to automatically step loads, intermittent overload problems, and inability of the test machine to reach the dynamic loads required for tests at lower stress ratios on the existing specimen design.

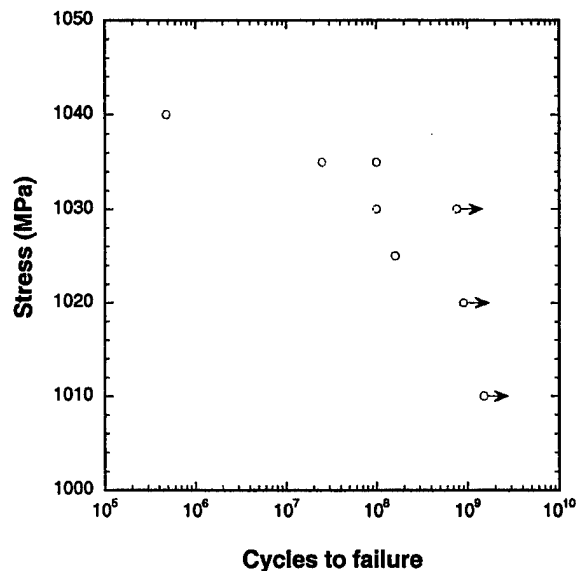


Figure 6.1.1.: S-N curve for Ti-6Al-4V at 1800 Hz and  $R = 0.8$ .

**Table 6.1.1. Test Matrix for Haigh Diagram Evaluation.**

# of tests	10,000,000 cycles; 1800 Hz	10,000,000 cycles; 400 Hz	100,000,000 cycles; 1800 Hz	1,000,000,000 cycles; 1800 Hz	1,000,000 cycles; 1800 Hz
R = 0.1	0	0	0	3	0
R = 0.3	0	0	0	3	0
R = 0.5	1	1	1	4	1
R = 0.6	1	1	0	2	1
R = 0.7	1	1	0	2	1
R = 0.8	1	1	1	4 (1 complete)	1
R = 0.9	1	1	0	2	1
	5 tests	5 tests		20 tests	5 tests

## 6.2 FATIGUE CRACK GROWTH

### 6.2.1 Stress-Level-Dependent Stress Ratio Effect on Fatigue Crack Growth [C7]

Fractographic measurements of fatigue crack growth rate for small cracks reveal stress-ratio effects even when fatigue crack closure is absent. These effects are restricted to low fatigue crack growth rates and become significant with increase in net stress levels. To characterize the effect, experiments and analyses were conducted on notched coupons of an Al alloy at stress levels producing inelastic conditions on initial loading. As a reference, fatigue crack growth rates were obtained for a long crack tested under fully elastic loading well below yield stress. The results indicate that for fatigue growth associated with low applied stress intensity range, minor changes in stress ratio can cause substantial variation in crack growth rate. A model is proposed for the small-crack fatigue growth rate as a function of applied stress intensity and stress ratio. The model is based on crack growth rates obtained under several stress levels with crack size as small as 0.03 mm.

### 6.2.2. Near-Threshold Crack Growth Behavior of a Single Crystal Ni-Base Superalloy Subjected to Mixed Mode Loading [C8]

Ni-base single crystal superalloys, which are used in applications such as gas turbine engine blades, are primarily loaded along the  $\langle 001 \rangle$  direction. Mode II (crystallographic shear) type cracking along the (111) plane is frequently the mode of growth in the early stages of fatigue failure of these components. Disks with a middle crack were used to characterize crystallographic shear crack growth from machined flaws oriented parallel to a (111) plane of a single crystal alloy. Automated crack growth experiments were conducted at constant stress ratio in the near threshold regime. Various combinations of mode I and mode II loading were achieved by orienting the machined flaw at different angles ( $\theta$ ) to the loading axis. Loading angle  $\theta=0^\circ$  (pure mode

I loading) resulted in crystallographic crack extension along alternating (111) slip systems producing a zigzag pattern. This orientation exhibited significant resistance to self-similar crack growth from the machined flaw. In contrast, self-similar crack growth was achieved with relative ease for loading angles,  $\theta \neq 0^\circ$  (mixed mode). In the mixed mode tests with  $K_I > 0$ , the crack growth rate was 10 to 50 times higher than that under mode I loading. Preliminary results indicated that crack growth was noncrystallographic at 593°C.

#### **6.2.3 The Role of Threshold Fatigue Crack Growth in Life Prediction of the Alloy Ti-6Al-2Sn-4Zr-6Mo Under High Cycle Fatigue Spectra [C9]**

Threshold fatigue crack growth rate data were obtained for titanium alloy Ti-6Al-2Sn-4Zr-6Mo at room temperature over a range of stress ratios ( $R = \sigma_{\min}/\sigma_{\max}$ ) from 0.1 to 0.9. The data from these tests were used to predict the crack propagation life analysis in a component that has an initial flaw. Using the crack propagation life and a known initial defect size, the remaining life of a component can be determined. The effect of various surface finishing methods on the residual stress field of a component was also investigated. The effect of residual stress fields on allowable crack size was discussed.

#### **6.2.4 The Role of Threshold Fatigue Crack Growth in Life Prediction for Two Titanium Alloys Under High Cycle Fatigue Spectra [C10]**

Life prediction under fatigue spectra that contain combinations of LCF and HCF must address a variety of potentially interactive damage events. These events include fatigue crack formation at slip bands and intrinsic material defects, surface fretting fatigue, and foreign object impacts. The present effort addresses a key aspect of the life prediction process – the role of the conventional crack growth rate threshold,  $\Delta K_{th}$ , based on data from large fatigue cracks.

The results of the life analyses indicate that, for Ti-6Al-2Sn-4Zr-6Mo at room temperature, a crack growth methodology is useful for life management under low cycle fatigue (lives  $\leq 10^4$  cycles). However, the typical crack propagation lifetimes available from this alloy under realistic loading conditions are insufficient to permit crack growth under high cycle fatigue, given the large number of cycles that may be expected under HCF (lives  $\geq 10^7$  cycles). Recognizing that crack formation due to a variety of potential mechanisms cannot be avoided, it appears that an effective damage tolerance life prediction system must focus on the conditions necessary for threshold crack growth. Moreover, because the crack growth analyses presented here were based on the behavior of large fatigue cracks, which exhibited a distinct  $\Delta K_{th}$ , the predicted crack

growth behavior probably represents a *best-case* scenario. For example, it is well known that, under certain conditions, small cracks may propagate faster than predicted by large-crack trends, which could render the analyses nonconservative.

#### **6.2.5 Fractographic Study of Load Sequence Induced Mixed-Mode Fatigue Crack Growth in an Al-Cu Alloy [C11]**

Fatigue crack growth behavior was studied on C(T) and SE(T) specimens from Al-Cu alloy 2014 using specially-designed load sequences. The experiments were organized to induce microscopic mixed-mode fatigue crack growth while at the same time reducing or eliminating fatigue crack closure. The mixed-mode growth was achieved by switching between high-amplitude, low-stress ratio and low-amplitude, high-stress ratio cycles. Retardation effects observed under these conditions are attributed to local crack branching and mixed-mode conditions induced by variable amplitude loading.

#### **6.2.6. Fatigue Crack Growth Rate Characteristics of Laser Shock Peened Titanium [C12]**

The fatigue crack growth rate (FCGR) characteristics of LSP Ti-6Al-4V were examined and compared to those of unprocessed material. The FCGR resistance of LSP processed material tested at low stress ratios ( $R$ ) was shown to be significantly greater than for unprocessed, baseline material. The increased damage tolerance would be attributed to the large residual compressive stresses generated by the LSP process. Differences in the growth rate behavior due to LSP would be accounted for by using the closure corrected effective stress intensity range,  $\Delta K_{\text{eff}}$ , which takes into account only the portion of loading above the crack opening load. The rationale of using  $\Delta K_{\text{eff}}$  is also demonstrated through fractographic investigations.

## **SECTION 7**

### **DEVELOPMENT OF EXPERIMENTAL PROCEDURES, METHODOLOGIES AND LABORATORY ENHANCEMENTS**

---

#### **7.1 INFRARED CRACK DETECTION SYSTEM**

Preliminary checkouts of the infrared camera hardware, image grabber board, and manufacturer's software have been completed. Communication between the camera and the image grabber board has been established. Utility software has been written which allows the images from the camera to be displayed on the computer with the use of a library of function calls provided by the manufacturer of the image grabber board.

A three stage mounting system was designed and built to enable the camera system to be integrated with the existing mechanical test frames. Each axis is equipped with a linear translation stage that allows precise position control of the camera head in three orthogonal directions. The mounting system will allow the operator to quickly move the camera to various regions of the specimen for interrogation.

#### **7.2 NONDESTRUCTIVE EVALUATION TECHNIQUES FOR DETECTING SURFACE DEFECTS IN $\gamma$ -TITANIUM ALUMINIDES [C13]**

The goal of this project was to evaluate the capability of existing NDE imaging methodologies and equipment for small crack detection in  $\gamma$ -titanium aluminide alloys.  $\gamma$ -Titanium aluminide alloys exhibit very short crack growth lives (compared to crack initiation) during mechanical fatigue. Detection of cracks just after initiation would help in the development of life prediction models by providing information about when crack growth begins. Specimens with simulated defects were tested using three NDE techniques. The three NDE techniques selected for evaluation were: eddy current imaging, ultrasonic surface wave imaging, and fluid dye penetrant inspection. These techniques were selected because each one detects surface cracks in a unique way. Eddy current imaging is sensitive to changes in the electric and magnetic properties of the material. Ultrasonic surface wave imaging uses propagating sound waves, and detects changes in the mechanical properties of the material. Fluid penetrant inspection uses fluorescent dyes that fill the cracks, allowing optical inspection. Since each method interacts with the defects differently, it was thought that one of the methods would have superior signal-to-noise ratios allowing detection of small cracks. It was hoped that evaluation of the three techniques and the differences in their sensitivities might lead to

an optimized inspection method for crack detection in  $\gamma$ -titanium aluminides. The results showed that the microstructure of the alloys creates significant noise in the inspection process, making detection of small defects difficult. However, inspection of specimens with small EDM notches on the surface showed that notches as small as 0.200 by 0.130 mm were detectable with ultrasonic surface wave imaging, eddy current imaging, and fluorescent dye penetrant imaging.

### **7.3 FEASIBILITY OF EDDY CURRENT IMAGING TECHNIQUE TO DETECT TMF-INITIATED SURFACE CRACKS IN MMC**

To help characterize damage in MMCs, NDE techniques were evaluated for capability to detect cracks less than 500 microns *in situ* during mechanical testing. Several existing NDE techniques were identified that could detect surface cracks this size, but not all of them were suited for *in situ* application in a mechanical testing environment. Ultrasonic and eddy current methods were considered but the coupling requirements of ultrasound, especially for ultrasonic scanning/imaging techniques, complicated *in situ* use. Eddy current imaging, a technique infrequently applied to MMCs, appeared to be viable for *in situ* use in the mechanical test systems.

Mechanical testing was conducted to produce surface-initiated matrix cracks in MMC specimens using OP TMF, and evaluate the suitability of eddy current scanning/imaging techniques for detecting matrix cracks. The MMC composite specimens were machined from a six-ply, unidirectional BP Sigma-1240 SiC/Titanium-6Al-2Sn-4Zr-2Mo panel with a fiber volume percentage of 24.5%. The specimens were subjected to 180 OP TMF using a horizontal mechanical testing frame operating under load control to produce matrix cracking.

The eddy current images were acquired by raster scanning a differential eddy current probe across the gage section of the MMC specimen. Typical scanning parameters were 0.1 to 0.2mm step sizes with scanning speeds of 20 mm/s. Eddy current images were usually acquired in less than 15 minutes. To assess the eddy current scanning techniques several other non *in situ* NDE techniques were used to measure damage in the tested specimens including ultrasonic imaging, fluid penetrants and optical SEM techniques.

The eddy current imaging technique detected surface cracks with high enough resolution to enable crack length measurements. Cracks as short as 250 microns were detected and imaged. The eddy current images compared well with ultrasonic surface

wave images and fluorescent penetrant inspection results. SEM analysis was used to provide additional verification of the size and location of cracks.

#### **7.4 DEVELOPMENT OF BROADBAND ACOUSTIC EMISSION FOR DETECTING FIBER CRACKING IN MMCs DURING CREEP TESTING**

To support the development of models predicting the deformation and failure of unidirectional MMCs under sustained loads, experimental evidence characterizing individual fiber breaks is needed. Acoustic emission (AE) NDE is an appropriate sensing technology for detecting fiber breaks in MMC specimens and has been used by many researchers for several years with limited success. However, UDRI researchers have found that sustained load tests on MMCs using traditional "resonance-type" AE systems often result in the "detection" of more fiber breaks than was practically possible. To provide more realistic MMC fiber break detection capability, UDRI has implemented AE systems, sensors, and signal processing techniques that have much more capability for discriminating between material generated events and immaterial noise.

UDRI has accomplished several tasks to improve AE fiber break discrimination. During the past year:

- 1) New broadband sensors have been specified and procured,
- 2) The Digital Wave AE system has been implemented into MMC tests,
- 3) The Digital Wave system was modified to expand the frequency bandwidth,
- 4) Wave guides were designed, built, and implemented so that the sensors could be placed on the specimen surface, rather than the grips, at temperatures as high as 500°C,
- 5) AE event location techniques have been refined so that events can be located in the specimen to within 1 mm, and
- 6) Signal processing techniques have been investigated so that extraneous noise is rejected and unwanted modes/echoes of acoustic energy can be removed from the AE signal.

One of the results of the improvements have been that the AE methodology is producing event locations that match well with fiber break locations obtained from destructive analysis of the specimens. Another result is that the number of AE events, that are thought to result from actual fiber breaks during a sustained load test on an MMC specimen, has decreased from (unrealistic) numbers such as several hundred to much more realistic values such as 15 to 40. Recent progress in the analysis of the

frequency content of the AE signals suggests that extraneous signals, probably generated as wave guide harmonics, can be removed from the AE signal thus increasing the accuracy of event location.

#### **7.5 DEVELOPMENT OF A DRY-COUPPLANT ULTRASONIC SCANNING SYSTEM FOR *IN SITU* DETECTION OF DAMAGE IN CMC**

A need developed for an NDE technique to detect planar-type cracking in CMCs resulting from mechanical testing. A significant complication was the requirement that the CMC specimens not get wet during testing, which ruled out the use of immersion ultrasound and liquid couplant based, contact, ultrasonic NDE. X-ray radiography was tried but, as anticipated, had poor sensitivity to the planar defects. Several specimens were evaluated using a thermal imaging technique but the spatial resolution was low and the technique was not fully calibrated making comparison of different images difficult. It was decided to adapt an existing ultrasonic sensor that required no liquid couplant, to the scanning and imaging of the CMC specimens.

The "dry couplant" sensor required that the sensor be compressed perpendicular to the specimen surface with sufficient force to provide transmission of ultrasonic energy into the specimen. A mechanical X-Y translation system was coupled with a solenoid-driven Z-axis to provide the appropriate movements of the transducer necessary to raster scan a specimen. An electronic system was designed and developed to coordinate solenoid actuation and trigger ultrasonic data acquisition.

Software to analyze and display the data was developed. Initial tests showed that the dry couplant C-scan system produced C-scans images with enough consistency to be used to detect planar defects in CMCs. Several CMCs thought to contain various levels of damage (based on load levels applied to the specimens) were C-scan with the dry-couplant system. Areas of low ultrasonic transmission were detected in the dry couplant C-scan images and their location correlated well subsequent immersion ultrasonic C-scan images.

#### **7.6 EXTENSOMETER USE IN ELEVATED TEMPERATURE TESTING**

Variations in the strain readings obtained using a commercially available strain gage-type high temperature extensometer during creep testing of unidirectional composite has been a continuing problem over the last few years. We conducted an investigation to determine the source of these strain variations.



At the low strain rates typical with many composite creep tests, the strain readings obtained can be affected by many environmental factors. Electrical interference from the test system itself can cause a high frequency noise band of up to  $\pm 150$  microstrain. Although electrical noise did not cause the gradual changes in strain seen in our creep tests, that noise is an indication of the limited range of these extensometers. To minimize the electrical noise in the strain signal, additional filters or shielding may be required.

Our investigation revealed that the major source of strain variations during our creep tests is the sensitivity of the extensometers to changes in relative humidity. During a series of tests at room temperature with the extensometer rods held in a fixed position, as the relative humidity changed the strain reading obtained from the extensometer also changed (up to  $\pm 1000$  microstrain). The tests were conducted on seven different test machines, using eight different extensometers. Also, note that in room air, the change in strain reading lags behind humidity changes 4 to 18 hours depending on the rate at which the humidity level changes. The cause of the variation in strain reading is unknown, but may be due to effects of moisture content on the strain gages mounted in the extensometer, or on the epoxy used to attach these strain gages. To minimize the effect of humidity on the strain readings, either the environment would have to be better controlled, or another type of strain reading device not affected by humidity changes would have to be used.

The effect of humidity changes on strain readings was further illustrated by the placement of an extensometer in a vacuum chamber. As the air was evacuated from the chamber, the strain reading decreased steadily despite the fact that the extensometer rods were held fixed. When room air was reintroduced into the chamber, the strain readings gradually returned to the pretest values.

The cause of the variation in strain reading is unknown, but may be due to effects of moisture content on the strain gages mounted in the extensometer, or on the epoxy used to attach these strain gages. To minimize the effect of humidity on the strain readings, either the environment would have to be better controlled, or another type of strain reading device not affected by humidity changes would have to be used.

As a follow-up to the previous tests, a comparison of some alternate strain measuring devices was made. Of these, a prototype LVDT (linear variable differential transformer) extensometer showed the most promise for use in our testing applications. The LVDT detects variations in an electric field as a copper rod moves inside the field to

measure displacement. Initial tests with the LVDT extensometer demonstrated that this device was unaffected by humidity changes and that the electrical noise level obtained was as low as that obtained using strain gage-type extensometers. Because the prototype test fixture used to mount the LVDT was made of aluminum, the strain readings varied slightly with changes in temperature. Further testing on the LVDT extensometer using a low CTE attachment fixture is currently in progress.

## **7.7 LEFM SOLUTION FOR A CENTRALLY NOTCHED DISK**

Mode I and mode II stress intensity factor ( $K_I$  and  $K_{II}$ ) are available in the open literature for the centrally notched disk geometry for crack length to width ratio ( $\alpha$ ) up to 0.6. In addition, convenient expressions are unavailable for  $K_I$  and  $K_{II}$  as function of  $\alpha$  and loading angles ( $\theta$ ). During our investigations (see section 6.2.2) on a Ni-base superalloy, mixed mode crack growth data was obtained for  $\alpha$  up to 0.8. Hence, an extensive finite element analysis was conducted using the finite element code ADINA™ to generate normalized  $K_I$  and  $K_{II}$  for the range  $0.1 \leq \alpha \leq 0.8$  and  $0 \leq \theta \leq 90^\circ$ . Limiting solutions were used to obtain the normalized  $K_I$  and  $K_{II}$  for  $\alpha = 0$ . Using the finite element results and the limiting solutions, we obtained expressions for  $K_I$  and  $K_{II}$  as function of  $\alpha$  and  $\theta$ . These solutions were used to analyze the mixed mode crack growth in a Ni-base superalloy as discussed in section 6.2.2.

## **7.8 DESIGN, FABRICATION AND OPERATION OF NEW SHAKER BASED HCF TEST SYSTEMS**

### **7.8.1 Design and Fabrication**

A new shaker based HCF test system was designed and two systems built – one system was delivered to MLS and the other to MLN. The system load design goal was for 10 kN dynamic load at 500 Hz with at least 10 kN mean load. The Unholtz-Dickie model S102 shaker was purchased for the dynamic load actuator; the pneumatic cylinder (for mean load) and test frame and were designed and fabricated in house.

The selected shaker, an Unholtz-Dickie model S102, was superior to other options in performance, quality and price. It was purchased with a power amplifier for about \$42,000, which is close to the cost of a shaker alone from MB Dynamics. The model S102 is rated for 4400 lb-force and for frequencies up to 3.5 kHz.

Unholtz-Dickie engineering was given details of the intended application of their shaker and they agreed to supply the shakers with some modifications. Unholtz built the

shakers per a UDRI drawing with special adapters for bolting the shaker to the pneumatic actuator, which insures simplified alignment of the shaker to the test frame. The shakers were supplied with extra armature bumper stop material to protect against slamming the armature against its stops by the mean load upon specimen failure. Their engineering also approved the intended up-side-down operation of the shaker.

Incorporating on recent design experience with the magnetostrictive test system, the frame was designed to be as resonance free through 500 Hz. Large diameter columns (4.5 inch) were used with short spaces between points of clamping. The shaker is inverted to simplify the use of a Wood's metal alignment device, which is situated below on a moveable crosshead.

### **7.8.2 Operation**

Preliminary system tests on sample specimens showed distortion free loading waveforms and no discernible load frame resonance through above 500 Hz. With a rigid dummy specimen, the system has proved capable of dynamic loads over 12 kN (peak-to-peak) at 500 Hz and over 6 kN at 700 Hz. The test system is being utilized for a study to determine the effects of foreign object damage on fatigue life of Ti-6Al-4V. Because the FOD specimens are more compliant, loads of only 5 kN were achievable at 500 Hz and it was decided to conduct the testing of these FOD specimens at 350 Hz.

### **7.8.3 Laser Measurement Enhancement of HCF Test System 1**

A LaserMike was fitted on the C10 HCF test system (HCF system #1) enabling the measurement of specimen strain without contact to the specimen surface. The C10 version of MATE software was modified to automatically read the output of the LaserMike via the RS232 port so that the laser readings may be logged as a function of load and time. The system has good stability and seems unaffected by the high vibration environment. The HF load is interrupted briefly to periodically acquire the LaserMike reading. A series of baseline creep tests were conducted on Ti-6Al-4V followed by fatigue tests at 400 Hz in which the elongation with load and time were measured to study creep-fatigue interaction.

Experiments comparing measurements taken between the grips with measurements taken between small "flags" attached to the specimen demonstrated a consistent relationship and established confidence in the between-the-grips measurements. A second LaserMike has been ordered for installation on another HCF test system.

## **7.9 DATA ARCHIVE AND KEYSERVER® STATUS**

The Data Archive is a central computer on which all test data generated by WUD 1 is stored and indexed. Its purpose is to prevent the loss of valuable test data and provide independent user access within WUD 1. The framework for the archive was established in 1995. Few fundamental changes have been implemented since it was established; however, some additions have been made to keep pace with current technology and user demands on the system. An external hard drive chassis and additional hard drive space have been added. The Windows NT® operating system was maintained to facilitate user access from both Macintosh and Windows based platforms. A large volume of test data was added to the archive, and administrative support was maintained.

The Keyserver® system, which was put in place in 1996, has also been maintained to provide hands-off control of commercial software licenses. This system controls the number of copies of a software package that can run at a given time by requiring the software to contact the Keyserver® over the network to see if a license, or key, is available. Pre-modified software for the Macintosh platform was updated as necessary, and detailed instructions for users to follow to install the software on their own computers were updated. The system that houses the Keyserver® was upgraded to a faster machine to keep pace with current computer technology.

## **SECTION 8**

### **REFERENCES**

---

Ashbaugh, N.E., Mechanical Behavior of Advanced Aerospace Materials, Interim Annual Report for Period 25 May 1994-24 May 1995, Materials Directorate, Wright Laboratory, Air Force Materiel Command, Wright-Patterson AFB, OH 45433-7734, 1996.

Ashbaugh, N.E., John, R., Porter, W.J., and Worth, B.D., Mechanical Behavior of Advanced Aerospace Materials, Interim Annual Report for Period 25 May 1995-24 May 1996, WL-TR-96-4087, Materials Directorate, Wright Laboratory, Air Force Materiel Command, Wright-Patterson AFB, OH 45433-7734, 1997.

Ashbaugh, N.E., John, R., Porter, W.J., Worth, B.D., Mechanical Behavior of Advanced Aerospace Materials Interim Technical Report for period 25 May 1996-24 May 1997, AFRL-ML-WP-TR-1999-4049, Wright Laboratories, Wright-Patterson Air Force Base, Ohio, 1999.

Gural, R., "*In Situ* Nondestructive Characterization Of Damage Progression In Ceramic Matrix Composites At Room And Elevated Temperatures," Masters thesis submitted to the Graduate Engineering & Research, School of Engineering, University of Dayton, December 1998.

**This page intentionally left blank.**

**Appendix A**  
**Compendium of Manuscripts**

## **LIST OF MANUSCRIPTS**

---

C1	The Effect of Temperature on Fiber/Matrix Interface Sliding in SCS-6/TIMETAL®21S, Alisha Hutson, Reji John and Jay Jira.....	47
C2	Prediction of Transverse Fatigue Behavior of Unidirectionally Reinforced Metal Matrix Composite, Reji John, Dennis Buchanan, and James Larsen.....	55
C3	Influence of Viscoplasticity on Residual Stress and Strength of a Titanium Matrix Composite After Thermomechanical Fatigue, J. Kroupa and M. Bartsch.....	63
C4	Fracture Behavior of an Oxide/Oxide Ceramic Matrix Composite, V. Kramb, R. John, and L. Zawada.....	79
C5	A Rapid Method for Generation of a Haigh Diagram for High Cycle Fatigue, David Maxwell and Ted Nicholas .....	101
C6	Fretting Fatigue of Ti-6Al-4V Under Flat on Flat Contact, Alisha Hutson and Theodore Nicholas .....	117
C7	Stress-Level-Dependent Stress Ratio Effect on Fatigue Crack Growth, R. Sunder, W. J. Porter, and N. Ashbaugh.....	125
C8	Near-Threshold Crack Growth Behavior of a Single Crystal Ni-Base Superalloy Subjected to Mixed Mode Loading, R. John, D. DeLuca, T. Nicholas, and W.J. Porter .....	135
C9	The Role of Threshold Fatigue Crack Growth in Life Prediction of the Alloy Ti-6Al-2Sn-4Zr-6Mo Under High Cycle Fatigue Spectra, J. Larsen, S. Russ, D. Maxwell, and Brian Worth.....	153
C10	The Role of Threshold Fatigue Crack Growth in Life Prediction for Two Titanium Alloys Under High Cycle Fatigue Spectra, J. Larsen, S. Russ, R. John, and D. Maxwell .....	161
C11	A Fractographic Study of Load Sequence Induced Mixed-Mode Fatigue Crack Growth in an Al-Cu Alloy, N. Ashbaugh, W.J. Porter, R. V. Prakash, and R. Sunder.....	171
C12	Fatigue Crack Growth Rate Characteristics of Laser Shock Peened Titanium, J. Ruschau, R. John, S. Thompson, and T. Nicholas .....	195
C13	Nondestructive Evaluation Techniques for Detecting Surface Defects in $\gamma$ Titanium Aluminides, Erdahl, D.S., Stubbs, D.A., and Rosenberger, A.H. ....	221



## Effect of Temperature on Fiber/Matrix Interface Sliding Stress in SCS-6/Timetal®21S

Alisha Hutson<sup>1</sup>, Reji John, and Jay Jira

Materials and Manufacturing Directorate, Air Force Research Laboratory (AFRL/MLLN)  
Wright Patterson Air Force Base, OH 45433-7817, USA.

<sup>1</sup>Advanced Materials Characterization Group, Structural Integrity Division  
University of Dayton Research Institute, Dayton, OH 45469-0128, USA.

### Introduction

Many potential applications exist for components manufactured using Titanium Matrix Composites (TMC) because of the high specific strength and stiffness the material exhibits at elevated temperature. Since the potential application environments may expose components to mechanical fatigue under conditions favorable for crack initiation and growth, many studies have focussed on TMC fatigue crack growth behavior (1-16). Results of these studies indicate that the fatigue crack growth behavior under certain conditions exhibits a decreasing crack growth rate, which is caused by fiber bridging in the wake of matrix cracks. Fiber bridging is produced by load transfer from the matrix to the fibers in the crack wake due to friction at the fiber/matrix interface. Since the fiber and matrix are not chemically bonded, mechanical load transfer results from residual compressive stresses created by coefficient of thermal expansion mismatch between the matrix and the fibers. Accordingly, the residual stresses will vary with temperature, implying that the frictional shear stresses will also vary with temperature.

Several methods have been employed to determine or deduce the fiber/matrix interfacial shear stress,  $\tau$ . Fiber push-out and pull-out techniques have been used to measure  $\tau$ , but efforts to apply these values to accurate fatigue crack growth prediction have failed (1,2,4,5,8). Other methods include determination of  $\tau$  as a fitting parameter based on correlation with parameters measured during fatigue crack growth tests. A common approach is to calibrate  $\tau$  using the crack length versus cycles data ( $a-N$ ) from a fully bridged crack growth test at a given applied stress (1,2,5,7,11,14,15). Subsequently, this value of  $\tau$  has been shown to have predictive capabilities for crack opening displacements (COD), slip lengths, and  $a-N$  at other stress levels and volume fractions. (1,2,7,11,13-15) This method requires accurate knowledge of the *in situ* crack growth behavior of the neat (fiberless) matrix. An alternate method is to use the displacements measured across a bridged crack to deduce  $\tau$ . Connell and Zok (12) prepared specimens with edge-to-edge through cracks from center-cracked specimens which were tested under fatigue. The load versus crack opening displacement response of these specimens was used to deduce  $\tau$  as a function of temperature (up to 300°C) in Sigma/Ti-6Al-4V (12). In this technique, COD was measured across large gage lengths, thus requiring the actual COD across the crack surface to be deduced from the measured displacement. Hence, the actual COD could be a small fraction of the total displacement. The procedure also assumed that  $\tau$  is constant along the entire crack length. These problems could be minimized by measuring the COD directly across the crack faces *in situ* during crack growth using the

laser interferometric displacement gage (IDG) system. This technique has been used extensively at the Air Force Research Laboratory to verify the applicability of fiber bridging models to describe crack growth in SCS-6/Ti-24Al-11Nb (2,5), SCS-6/TIMETAL®21S (2,17) and SCS-6/Ti-6Al-4V (13,14) and also by Ghonem et al. (15) in SM1240/TIMETAL®21S. John et al. (13) used this technique to determine the stress ratio effects on  $\tau$  and Zheng and Ghonem (15) to determine the temperature effects on  $\tau$ . Zheng and Ghonem's (15) measurements were based on short crack extensions ( $\approx 1.5$  mm). Application of fiber bridging models to components under service loading conditions requires  $\tau$  as a function of temperature over a wide range of crack lengths. Hence, this paper discusses the determination of  $\tau$  as a function of temperature from COD measured *in situ* during crack growth along long fully-bridged cracks in SCS-6/TIMETAL®21S. Two commonly used shear lag models (18,19) were evaluated during this study.

### Experimental Procedure

The material selected for this study was unidirectionally reinforced 4-ply SCS-6/TIMETAL®21S. SCS-6 is a silicon carbide fiber which is 142  $\mu\text{m}$  in diameter and consists of a carbon core, four layer beta phase SiC, and two layers of a carbon vapor deposited coating (3). TIMETAL®21S is a metastable beta phase titanium alloy, Ti-15Mo-2.6Al-3Nb-0.3Si. The composite material was fabricated using the foil-fiber-foil technique and the hot isostatic pressing process. The resulting material volume fraction was 0.355.

Testing was conducted on a center-cracked specimen, M(T) which was 152 mm long x 19 mm wide x 1 mm thick. The initial notch length,  $2a_0$ , was  $\approx 1.7$  mm. A schematic of the geometry is shown in Figure 1. Additional details can be found in Ref. (3). A tension-tension fatigue test was conducted under constant amplitude loading at a maximum stress = 300 MPa and with a

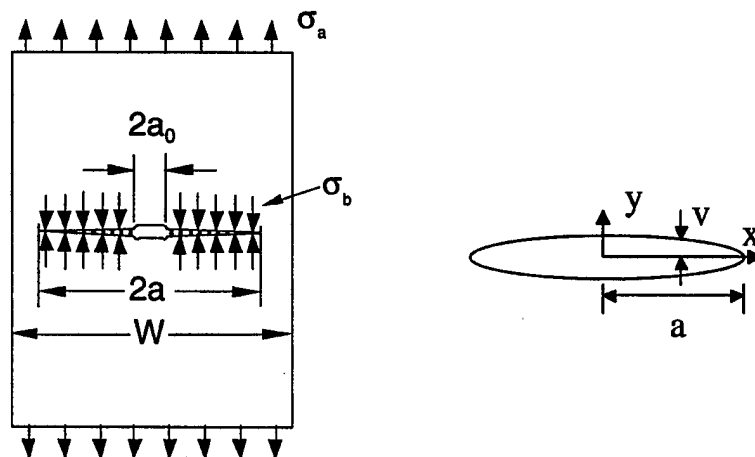


Figure 1. Schematic of test specimen geometry.

load ratio  $R =$  minimum load/maximum load = 0.1 at 1 Hz. The test was continued until an average crack extension of  $\approx 4$  mm was achieved. At the end of the test, the specimen was removed and microhardness indents were placed along the crack

wake, as shown in Figure 2. The indents appear at 750  $\mu\text{m}$  intervals along the crack wake, starting at 150  $\mu\text{m}$  from the notch root. The indents were  $\approx 25$   $\mu\text{m}$  x 25  $\mu\text{m}$ , and the center of the indents were located  $\approx 50$   $\mu\text{m}$  from the crack face. The laser IDG system, which has a measurement accuracy of  $\pm 5$  nm, was used to measure the load versus COD range response at each indent location. More details about the laser IDG system can be found in Ref. (20). The maximum stress = 300 MPa and  $R = 0.1$  was used for all COD range measurements.

The crack extension of  $\approx 4$  mm was achieved at 23°C. After the indents were placed, the specimen was reloaded in the test machine along with the induction coil. The induction heating system was used to heat the specimen to the desired temperatures 23, 100, 200, 300, 400 and 500°C. After a five minute soak time at each temperature, COD range measurements were obtained at each of the 10 indent locations along the crack length. After making measurements at the maximum temperature (500°C), the process was repeated during the cool down to room temperature. Representative data sets are shown in Figure 3.

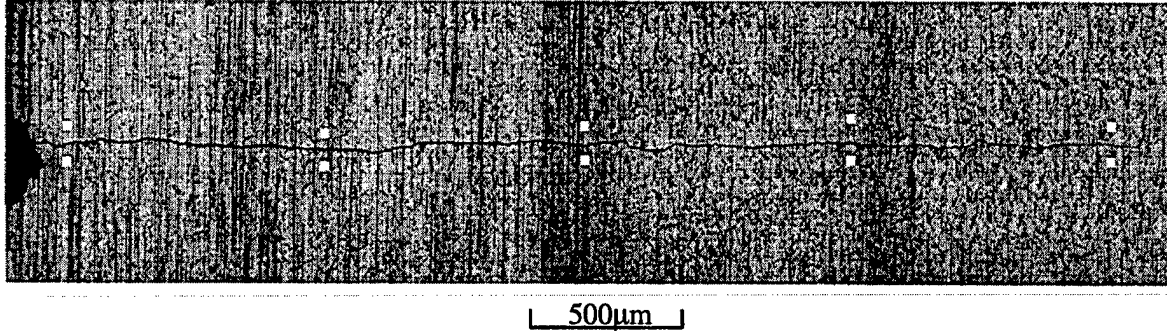


Figure 2. Crack extension from EDM notch. Solid white squares above and below notch indicate location of microhardness indents along the crack.

### **Procedure to Deduce Fiber/Matrix Interfacial Shear Stress**

An iterative program developed by John, Kaldon, and Ashbaugh (5) was used in this study to deduce  $\tau$  from the COD data. This method relates the half COD ( $v$  in figure 1) to the bridging stress ( $\sigma_b$ ) based on the shear lag models developed by Marshall, Cox, and Evans (MCE) (19) and McCartney (McC) (18). The half-crack-opening displacement range ( $\Delta v$ ) is given by

$$\Delta v(x) = \frac{1}{E_o} \int_x^a \left[ \int_0^a h(x, a) [\Delta \sigma_a(x) - \Delta \sigma_b(x)] dx \right] h(x, a) da \quad (1)$$

where  $E_o$  is the orthotropic modulus (6),  $h(x, a)$  is a weight function independent of load (21),  $\Delta \sigma_a$  is the applied stress range, and  $\Delta \sigma_b$  is the bridging stress range exerted across the crack by the bridging fibers. Note that  $\Delta \sigma_b = 0$  for  $x < a_o$ . The bridging law is given by

$$\Delta \sigma_b(x) = \beta \sqrt{\Delta v(x)} \quad (2)$$

where

$$\beta = \frac{8V_f^2 E_c^2 E_f \tau_{McC}}{(1 - V_f)^2 E_m^2 R_f}, \text{ or} \quad (3)$$

$$\beta = \frac{8V_f^2 E_f E_c \tau_{MCE}}{(1 - V_f) E_m R_f} \quad (4)$$

$V_f$  is the fiber volume fraction,  $E_c$  is the composite modulus,  $E_f$  is the fiber modulus,  $\tau$  is the shear stress at the fiber/matrix interface,  $E_m$  is the matrix modulus, and  $R_f$  is the fiber radius

(18,19). Note that  $\tau_{McC}$  and  $\tau_{MCE}$  correspond to  $\tau$  in the McCartney (McC) (18) and Marshall, Cox, and Evans (MCE) (19) bridging models, respectively. These equations were solved by iteration using a FORTRAN program that related COD measurements from the fatigue tests to the test conditions, and material and geometry specifications (5). An unbridged crack length of 0.1 mm adjacent to the crack mouth was assumed to allow for one cut or broken fiber at the notch root in each layer. Using this procedure, values for  $\tau$  were deduced at each temperature using MCE and McC shear lag models.

### **Results and Discussion**

Crack opening displacements were measured during the heat-up and cool-down to determine the effect of the thermal cycle. As shown by the representative data in Figure 3, the displacements increase with increasing temperature. The largest change in COD is produced at the notch root where the initial slip lengths, and the change in slip lengths due to elevated temperature are the greatest, as predicted by the MCE (19) and McC (18) shear lag models. COD values during cool-down remained slightly higher than the corresponding values obtained during heat-up (Figure 3). Fiber surface wear caused by the mechanical cycling required to obtain the COD measurements is probably the cause of the different COD values for increasing versus decreasing temperature.

A representative half-COD data set and the resulting half-COD prediction from the analysis are shown in Figure 4, and illustrate the accuracy of the procedure to deduce  $\tau$  from the COD profile. The prediction indicated by the solid line in Figure 4 correlates well with the experimental data over the entire crack length, including the region near the notch root. Connell and Zok made the assumption in Ref. (12) that  $\tau$  was constant over the entire crack length, an assumption confirmed by the accuracy of the predictions in this study using a constant  $\tau$ . The analysis does indicate a sharp drop in COD near the crack tip. This gradient was not supported by experimental data because a COD profile was not made close to the crack tip. However, the results of push-out tests conducted by Larsen, et. al. (22) and Kantzos, et. al. (23) support such behavior.

$\tau$  values deduced from half-COD ranges obtained at different temperatures are shown in Figures 5 and 6 for the Marshall, Cox and Evans, and McCartney bridging models, respectively. The difference in magnitude of  $\tau_{McC}$  and  $\tau_{MCE}$  is consistent with the difference between equations (3) and (4).  $\tau_{MCE}$  and  $\tau_{McC}$  at 23°C were 7.6 and 2.8 MPa, respectively. These 23°C values are consistent with the values reported in the literature (1-5,7,11,12,23). Figures 5 and 6 show that  $\tau$  decreases with increase in temperature. This trend is similar to the results reported by Connell and Zok (12) for Sigma/Ti-6Al-4V and Zheng and Ghonem (15) for SM1240/TIMETAL®21S. When the temperature increases from 23 to 500°C,  $\tau$  decreases by  $\approx$  50%. Similar significant decrease in  $\tau$  was also reported by Zheng and Ghonem (15). Figures 5 and 6 also show a slight difference between the  $\tau$  values obtained during the heat-up and that obtained during the cool-down, especially at 23°C. The lower value of  $\tau$  during the cool-down is consistent with the higher  $\Delta v$  shown in Fig. 3. The difference between  $\tau$  during heat-up and cool-down cycles could be attributed to the irreversible frictional wear at the fiber/matrix surface during mechanical cycling throughout the temperature excursion.

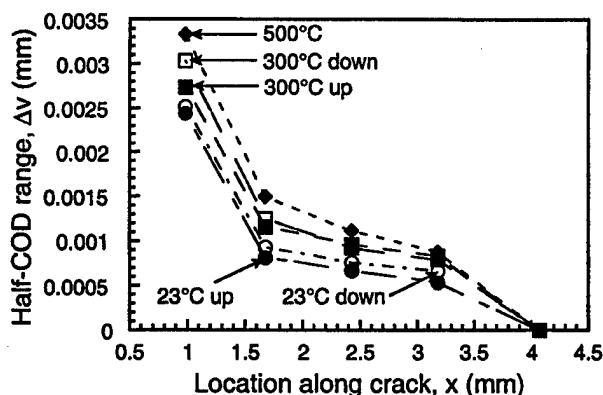


Figure 3. Half-COD profile measured at different temperatures on one crack length.

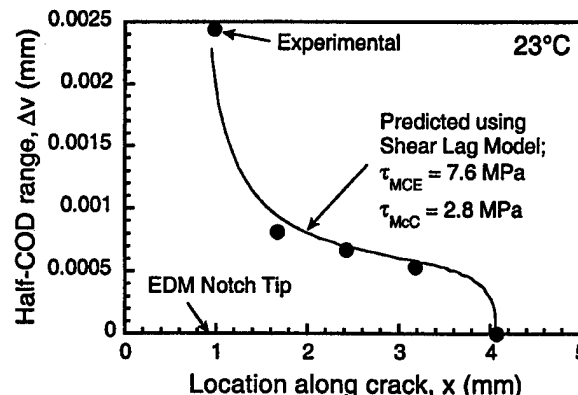


Figure 4. Comparison of measured half-COD profile with that predicted using the MCE and McC shear lag models.

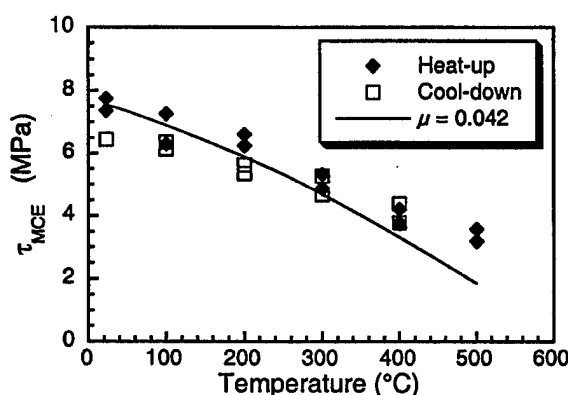


Figure 5. Effect of temperature on deduced  $\tau_{MCE}$ . Symbols = data, Lines = predictions

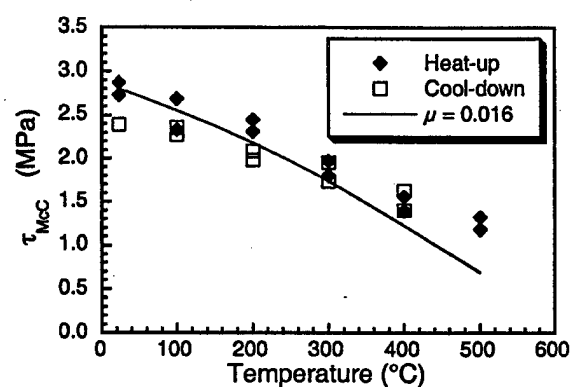


Figure 6. Effect of temperature on deduced  $\tau_{McC}$ . Symbols = data, Lines = predictions

As discussed earlier, the interfacial shear stress at the fiber/matrix surface occurs primarily due to the residual compressive radial stresses exerted on the fiber by the matrix. These residual stresses are generated during the fabrication process due to mismatch between the coefficient of thermal expansion of the fiber and the matrix. A thermoviscoplastic code based on the concentric cylinder model (24,25) was used to calculate the radial residual stresses for [0]<sub>4</sub> SCS-6/TIMETAL®21S for various temperatures as shown in Figure 7. As the temperature increases from 23°C to 500°C, the radial stress,  $\sigma_r$  decreases in magnitude from  $\approx -180$  to  $\approx -45$  MPa. This decrease in clamping stress on the fiber is consistent with the decrease in deduced  $\tau$  as shown in Figures 5 and 6. Hence, the use of frictional law to relate  $\tau$  and  $\sigma_r$  was investigated as given below.

$$\tau = -\mu \sigma_r \quad (5)$$

where  $\mu$  = coefficient of friction. The fiber/matrix interfacial sliding occurs between the multiple carbon coatings on the SCS-6 fiber. Hence,  $\mu$  represents the coefficient of sliding friction between the carbon layers. A similar relationship between  $\tau$  and  $\sigma_r$  was also proposed by Larsen et al. (3). Predictions using equation (5) are shown as solid lines in Figures 5 and 6 for  $\mu=0.042$  and  $0.016$  for the MCE and McC bridging models, respectively. These values of  $\mu$  were based on  $\tau$  deduced at 23°C prior to the heat-up. The prediction of  $\tau$  made by assuming  $\mu$  is temperature independent is close to the deduced  $\tau$  for temperatures up to  $\approx 400^\circ\text{C}$  within  $\pm$

15%. The value of  $\mu$  shown in Figs. 5 and 6 are similar to the values reported by Larsen et al. (3) and also are in agreement with the range  $0.014 \leq \mu \leq 0.054$  reported by Cox et al. (26) for other titanium matrix composites.

The prediction based on temperature independent  $\mu$  underestimates  $\tau$  deduced from COD for temperatures  $> 400^\circ\text{C}$ . This difference can be attributed to the oxidation of the carbon coating existing on the SCS-6 fibers. Dacic and Marinkovic (27) reported the onset of oxidation induced degradation of the carbon coating on the SCS-6 fibers at temperatures  $\geq 440^\circ\text{C}$ . The damage to the carbon coating would increase the apparent friction between the fiber and the matrix, thus increasing the deduced  $\tau$ .

The results shown in Figures 5 and 6 show that  $\tau$  decreases with increasing temperature and that the decrease in  $\tau$  is proportional to the decrease in the radial residual stresses at the fiber/matrix interface. A friction law given by Equation (5) can be used to predict the variation in  $\tau$  with temperature for temperatures up to the onset of the oxidation of the carbon coating on the fibers. The above analysis assumed that  $\sigma_r$  does not change during mechanical load cycling at room and elevated temperatures. Additional analysis is required to verify this assumption.

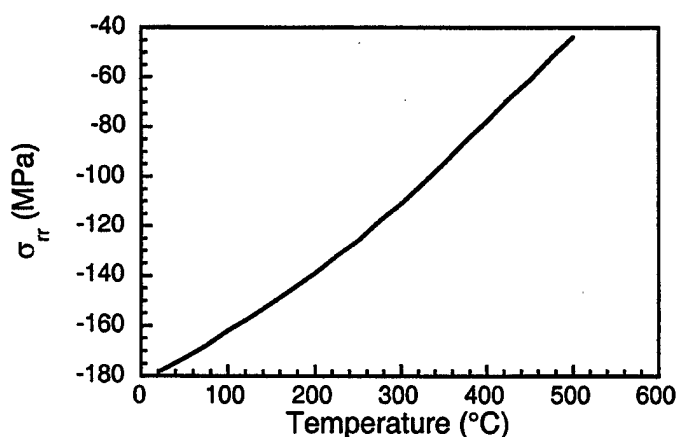


Figure 7. Effect of temperature on residual clamping stress,  $\sigma_r$ , around the fiber.

greater than that corresponding to the onset of oxidation of the carbon coating on the fibers.

### Conclusions

A technique based on crack opening displacements along the crack wake was developed to deduce the *in situ* fiber/matrix interfacial shear stress ( $\tau$ ) as a function of temperature.  $\tau$  decreases with increase in temperature. A friction law, in which  $\tau$  is proportional to the radial residual stress, was found to successfully predict the temperature effect on the effective  $\tau$  for a bridged crack. This friction law underestimates the deduced  $\tau$  for temperatures

### Acknowledgment

This research was conducted at the Materials and Manufacturing Directorate, Air Force Research Laboratory (AFRL/MLLN), Wright-Patterson Air Force Base, OH, USA. A. Hutson was supported under on-site contract number F33615-94-C-5200. The authors also gratefully acknowledge technical discussions with Dr. J. M. Larsen of AFRL/MLLN, Wright-Patterson Air Force Base, OH.

### References

1. J.G. Bakuckas Jr. and W.S. Johnson, Application of Fiber Bridging Models to Fatigue Crack Growth in Unidirectional Titanium Matrix Composites, NASA TM 107588, NASA Langley, Hampton, VA (1992).
2. J.M. Larsen, J.R. Jira, R. John, and N.E. Ashbaugh, Life Prediction Methodology for Titanium Matrix Composites ASTM STP 1253, W.S. Johnson, J.M. Larsen, and B.N. Cox, Eds., American Society for Testing and Materials, West Conshohocken, PA, p. 114, (1996).
3. J.M. Larsen, J.R. Jira, R. John, and D. Blatt, TMS Annual meeting: Mechanisms and Mechanics of MMC Fatigue Rosemont, IL (1994).
4. J. Telesman, L.J. Ghosn, and P. Kantzos, Journal of Composites Technology & Research, 15, 234 (1993).
5. R. John, S.G. Kaldon, and N. E. Ashbaugh, P.R. Smith and W.C. Revelos, Eds., Titanium Metal Matrix Composites II, WL-TR-93-4105, p. 270, Wright Laboratory, Wright Patterson AFB, OH (1993).
6. B.N. Cox and D.B. Marshall, Fatigue and Fracture of Engineering Materials and Structures, 14, 847 (1991).
7. D.P. Walls, G. Bao, and F.W. Zok, Acta Metallurgica et Materialia, 41, 2061 (1993).
8. D.L. Davidson, Metallurgical Transactions A, 23A, 865 (1992).
9. B.N. Cox, W.S. Johnson, J.M. Larsen, and B.N. Cox, Eds., Life Prediction Methodology for Titanium Matrix Composites ASTM STP 1253, p.552, American Society for Testing and Materials, West Conshohocken, PA (1996).
10. J.M. Larsen, S.M. Russ, and J.W. Jones, Metallurgical Transactions A, 26A, 3211 (1995).
11. L.J. Ghosn, P. Kantzos, and J. Telesman, M.R. Mitchell and O. Buck, Eds., Cyclic Deformation, Fracture, and Nondestructive Evaluation of Advanced Materials: Second Volume ASTM STP 1184, p. 64, American Society for Testing and Materials, Philadelphia, PA (1994).
12. S.J. Connell and F.W. Zok, Acta Materialia, 45, 5203 (1997).
13. R. John, J.R. Jira, and J.M. Larsen, TMS Materials Week '97, Fatigue and Creep of Composite Materials Indianapolis, IN (1997).
14. R. John, J.R. Jira, and J.M. Larsen, Composite Materials: Fatigue and Fracture ASTM STP 1330, R.B. Bucinell, Ed., American Society for Testing and Materials, West Conshohocken, PA, p. 122, (1998).
15. D. Zheng and H. Ghonem, W.S. Johnson, J.M. Larsen, and B.N. Cox, Eds., Life Prediction Methodology for Titanium Matrix Composites ASTM STP 1253, p. 137, American Society for Testing and Materials, West Conshohocken, PA (1996).
16. R.M. McMeeking and A.G. Evans, Mechanics of Materials, 9, 217 (1990).
17. A. Hutson, in A Summary of Various Materials Research Experiments, W. Vogler, Ed., WL-TR-97-4037, Air Force Research Laboratory, Wright Patterson AFB, OH 45433, p. 489, (1997).
18. L.N. McCartney, Mechanics of Matrix Cracking in Brittle-Matrix Fibre-Reinforced Composites, Proceedings of Royal Society of London A, A409, 329 (1987).
19. D.B. Marshall, B.N. Cox, and A.G. Evans, Acta Metallurgica et Materialia, 33, 2013 (1985).
20. Sharpe, W.N., Jira, J.R., and Larsen, J.M., J.M. Larsen and J.E. Allison, Eds., Small-Crack Test Methods ASTM STP 1149, p. 92, American Society for Testing and Materials, Philadelphia, PA (1992).
21. H. Tada, P.C. Paris, and G.R. Irwin, The Stress Analysis of Cracks Handbook, Del Research Corporation, St. Louis, MO (1985).
22. J.M. Larsen, J.L. Moran, J.R. Jira, and D. Blatt, Titanium '95, p. 2803, The Institute of Materials, UK (1996).

23. P. Kantzos, J. Eldridge, D.A. Koss, and L.J. Ghosn, The Effect of Fatigue Loading on the Interfacial Shear Properties of SCS/Ti-Based MMC's, Materials Research Society, Materials Research Society Symposium Proceedings, 273, 135 (1992).
24. D. Coker, N.E. Ashbaugh, and T. Nicholas, H. Sehitoglu, Ed., Thermomechanical Fatigue Behavior of Materials ASTM STP 1186, p. 50, American Society for Testing and Materials, Philadelphia, PA (1993).
25. D. Coker, F. Boller, J.L. Kroupa, and N.E. Ashbaugh, FIDEP2 User Manual to Micromechanical Models for Thermoviscoplastic Behavior of Metal Matrix Composites, University of Dayton Research Institute, Dayton, OH (1995).
26. B.N. Cox, M.S. Dadkhak, M.R. James, D.B. Marshall, W.L. Morris, and M. Shaw, Acta Metallurgica et Materialia, 38, 2425 (1990).
27. B. Dacic and S. Marinkovic, Carbon, 25, 409 (1987).



Reference: John, R., Buchanan, D., Larsen, J., "Prediction of Transverse Fatigue Behavior of Unidirectionally Reinforced Metal Matrix Composites," *Scripta Metallurgica et Materialia*, Vol. 39, No. 11, 1998, pp. 1529-1536.

## Prediction of Transverse Fatigue Behavior of Unidirectionally Reinforced Metal Matrix Composites

Reji John\*, Dennis J. Buchanan\*, and James M. Larsen

Materials and Manufacturing Directorate, Air Force Research Laboratory (AFRL/MLLN),  
WPAFB, OH 45433-7817.

\*Structural Integrity Division, University of Dayton Research Institute, Dayton, OH 45469-0128.

### Introduction

Unidirectionally reinforced metal matrix composites (MMC) are targeted for use in many aerospace applications which require high specific strength and stiffness at elevated temperatures [1,2]. Such applications include blisks and disks. The primary weakness of a component made of unidirectionally reinforced MMC is its susceptibility to transverse loads. The strength of the component in the transverse direction is significantly lower than that in the longitudinal direction under monotonic, sustained and fatigue loading conditions [1-12]. Figure 1 shows the effect of orientation of the reinforcement on the fatigue behavior of unidirectionally reinforced SCS-6/Ti-24Al-11Nb [10,11]. Note that [0] and [90] imply longitudinal and transverse loading, respectively. The data correspond to tests conducted at room temperature with load ratio (=minimum

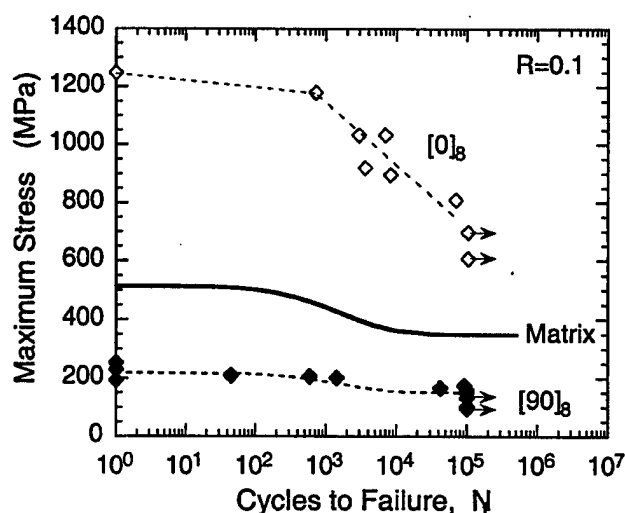


Figure 1. Effect of orientation of reinforcement on fatigue behavior of SCS-6/Ti-24Al-11Nb. Data from Refs. [10] and [11]. Fiber volume fraction,  $V_f \approx 0.32$ .

load/maximum load) = 0.1 in lab air. The tensile strength under transverse loading is  $\approx 20\%$  of tensile strength under longitudinal loading and  $\approx 43\%$  of the matrix tensile strength. Similarly, the threshold stress under transverse loading is also significantly lower than the [0]<sub>8</sub> MMC and the matrix. Hence, replacement of monolithic components with MMC components requires that the transverse strength of the MMC should be predicted accurately. This paper discusses the applicability of a net-section based model to predict the fatigue behavior of [90] MMC under transverse loading.

### Materials and Experimental Results

The data analyzed in this paper were obtained from Buchanan et al. [9], Gambone [10] and Hall et al. [11]. Two types of MMC are discussed in this paper: (1) Ti-24Al-11Nb (wt%) unidirectionally reinforced with silicon carbide fibers (SCS-6™), SCS-6/Ti-24Al-11Nb [10,11] and (2) Ti-6Al-2Sn-4Zr-2Mo (wt%) unidirectionally reinforced with silicon carbide fibers (Trimarc-

1<sup>TM</sup>), Trimarc-1/Ti-6Al-2Sn-4Zr-2Mo [9]. SCS-6<sup>TM</sup> is a silicon carbide fiber with a carbon core and two layers of exterior carbon coating ( $\approx 1\mu\text{m}$  thick/layer). The diameter of SCS-6<sup>TM</sup> fiber is  $\approx 142\mu\text{m}$ . Trimarc-1<sup>TM</sup> is also a silicon carbide fiber with a Tungsten core and three layers of exterior carbon coating ( $\approx 1\mu\text{m}$  thick/layer). The diameter of Trimarc-1<sup>TM</sup> fiber is  $\approx 127\mu\text{m}$ . SCS-6/Ti-24Al-11Nb is an 8-ply composite fabricated using a foil/fiber/foil technique through hot isostatic pressing (HIP) [10,11]. The average thickness of the SCS-6/Ti-24Al-11Nb specimens was  $\approx 1.9\text{ mm}$  and the volume fraction of fibers,  $V_f \approx 0.32$ . Trimarc-1/Ti-6Al-2Sn-4Zr-2Mo is a 10-ply composite fabricated using the wire winding technique [9]. The average thickness of the Trimarc-1/Ti-6Al-2Sn-4Zr-2Mo specimens was  $\approx 2.26\text{ mm}$  and the volume fraction of fibers,  $V_f \approx 0.29$ . SCS-6/Ti-24Al-11Nb was tested in laboratory air at  $21^\circ\text{C}$  with frequency = 1-5 Hz and load ratio (=minimum load/maximum load)  $R=0.1$ . Trimarc-1/Ti-6Al-2Sn-4Zr-2Mo was tested in laboratory air at  $163^\circ\text{C}$  with frequency = 3 Hz and  $R=0.1$ .

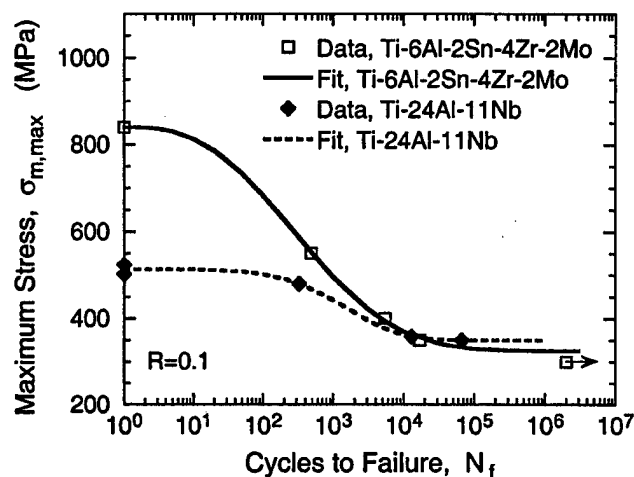


Figure 2. Fatigue behavior of fiberless Ti-6Al-2Sn-4Zr-2Mo and Ti-24Al-11Nb.

The prediction of the fatigue behavior of the MMC requires the characterization of the fatigue behavior of the corresponding matrix. In Refs. [9-11], fatigue data from fiberless (neat) matrices were reported. These matrix plates were fabricated using the procedure identical to that used for the MMC. Accordingly, Ti-24Al-11Nb foils and Ti-6Al-2Sn-4Zr-2Mo wires used to make the matrix plates. The matrix specimens were cut from the plate consistent with the direction of the layup of the matrix in the MMC. For Ti-6Al-2Sn-4Zr-2Mo, the length of the specimens was aligned perpendicular to the wire winding direction. Figure 2 shows the data for Ti-24Al-11Nb [11] and Ti-6Al-2Sn-4Zr-2Mo [9] from tests conducted at  $R=0.1$  in laboratory air. Ti-24Al-11Nb was tested at  $21^\circ\text{C}$  and Ti-6Al-2Sn-4Zr-2Mo at  $163^\circ\text{C}$ . The following equation was used to describe the fatigue behavior of the matrix.

$$\sigma_{m,max} = \sigma_{m,th} + (\sigma_{m,u} - \sigma_{m,th}) e^{C_1(\log N_f)^{C_2}} \quad (1)$$

where  $\sigma_{m,max}$  = maximum matrix stress,  $\sigma_{m,th}$  = matrix threshold stress,  $\sigma_{m,u}$  = matrix ultimate tensile strength,  $N_f$  = cycles to failure, and  $C_1$  and  $C_2$  are constants. These values are shown in Table I for the two fiberless matrices. The constants  $C_1$  and  $C_2$  were obtained based on data from relatively few fatigue tests as shown in Fig. 2. Since, fatigue data are typically associated with significant scatter (2-3X), additional tests are required to adequately characterize the fatigue behavior of the neat matrices.

**Table I. Constants used to describe fatigue behavior of fiberless matrix.**

Matrix	$\sigma_{m,u}$ (MPa)	$\sigma_{m,th}$ (MPa)	$C_1$	$C_2$
Ti-24Al-11Nb (21°C, R=0.1)	512.6	349.8	-0.001761	5.254
Ti-6Al-2Sn-4Zr-2Mo (163°C, R=0.1)	840.0	325.0	-0.05367	2.751

Typical fracture profiles of failed SCS-6/Ti-24Al-11Nb and Trimarc-1/Ti-6Al-2Sn-4Zr-2Mo specimens are shown in Figures 3 and 4, respectively. These figures show that the failure surface corresponds to the narrowest matrix

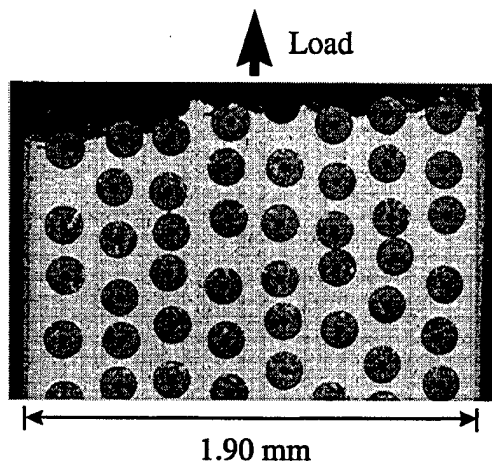


Figure 4. Fracture profile of  $[90]_8$  SCS-6/Ti-24Al-11Nb.

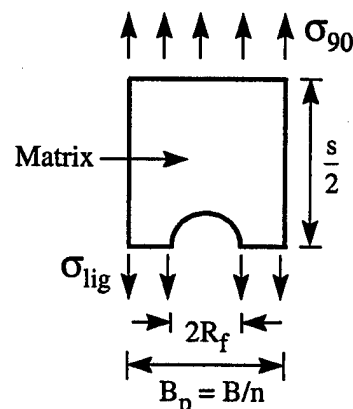


Figure 3. Schematic of the net-section model.

ligament between the fibers. The surfaces of the failed matrix ligaments between the fibers are approximately perpendicular to the loading direction. Based on these observations, a net-section based model was used to predict the fatigue behavior of transversely loaded MMC as described next.

### Net-Section Model

The schematic of a unit cell for a rectangular arrangement of fibers is shown in Fig. 5 [8,9]. In this figure,  $R_f$  = radius of fiber,  $B$  = thickness of composite,  $B_p$  = average ply thickness =  $B/n$ ,  $n$  = number of plies, and  $s$  = center-to-center fiber spacing along the length of the specimen. Using load equilibrium, the far-field applied stress for the composite,  $\sigma_{90}$ , can be related to the stress in the matrix ligament,  $\sigma_{lig}$  as ,

$$\sigma_{90} = \sigma_{lig} F_n , \quad (2)$$

where,

$$F_n = 1 - \frac{2R_f}{B_p} . \quad (3)$$

Using the geometry parameters shown in Fig. 5, the volume fraction of fibers,  $V_f$  can be derived as,

$$V_f = \frac{\pi R_f^2}{B_p s} \quad (4)$$

Note that  $s = 0.197$  and  $0.195$  mm for SCS-6/Ti-24Al-11Nb and Trimarc-1/Ti-6Al-2Sn-4Zr-2Mo, respectively. Substituting Eqn. (4) in Eqn. (3), we obtain,

$$F_n = 1 - \sqrt{\frac{4V_f s}{\pi B_p}} \quad (5)$$

For a square arrangement of fibers with  $s = B_p$ , Eqn. (4) becomes identical to that proposed by Walls et al. [6]. The net-section based model has been used to successfully predict the transverse creep-rupture [8] and fatigue crack growth parallel to fibers [13,14] in various MMC systems.

Thus, combining Eqns. (1) and (2), the composite maximum stress,  $\sigma_{90,max}$  versus  $N_f$  can be predicted using Eqn. (6).

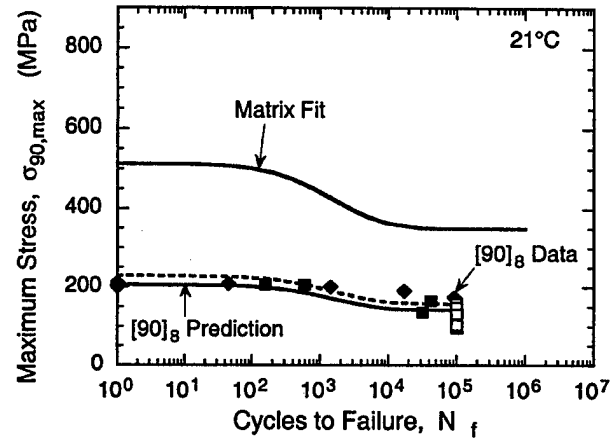


Figure 5. Fatigue behavior of  $[90]_\theta$  SCS-6/Ti-24Al-11Nb. ◆ from Hall et al. ■ & □ from Gambone. □ = specimens stopped prior to failure.

$$\sigma_{90,max} = \left\{ \sigma_{m,th} + (\sigma_{m,u} - \sigma_{m,th}) e^{C_1 (\log N_f)^2} \right\} F_n \quad (6)$$

Using the same approach, the MMC ultimate tensile strength,  $\sigma_{90,u}$  and the MMC threshold stress,  $\sigma_{90,th}$  can be predicted using Eqn. (7).

$$\sigma_{90,u} = \sigma_{m,u} F_n \quad \text{and} \quad \sigma_{90,th} = \sigma_{m,th} F_n \quad (7)$$

### Results and Discussion

The transverse fatigue behavior of the MMC predicted using Eqn. (6) is compared with the data from SCS-6/Ti24Al-11Nb and Trimarc-1/Ti-6Al-2Sn-4Zr-2Mo in Figs. 6 and 7, respectively. The proposed model predicts the following features satisfactorily:

- (1) Average tensile strength of the  $[90]$  MMC ( $=\sigma_{90}$  at  $N_f=1$ ),
- (2) The threshold stress of the  $[90]$  MMC, and
- (3) The overall trend of the maximum stress versus cycles (S-N) behavior, i.e. near-flat S-N behavior relative to that of the matrix.

The proposed model assumed that (1) the matrix ligament between the fibers is always perpendicular to the loading axis and (2) the fibers are arranged in perfectly aligned rows. As shown in Figs. 3 and 4, some of the matrix fracture surfaces are not perpendicular to the loading axis and the fibers show a staggered arrangement. The influence of these features can be estimated assuming an increase in the matrix net-section. The prediction based on 10% increase in the matrix ligament surface is shown as dashed lines in Figs. 6 and 7. The dashed lines appear to correlate better with the data at low stresses or longer lives. This implies that the orientation of the fracture surface with respect to the loading axis could depend on the maximum stress or stress range. Detailed fractographic studies (similar to that discussed in Ref. [14]) are required to determine these effects.

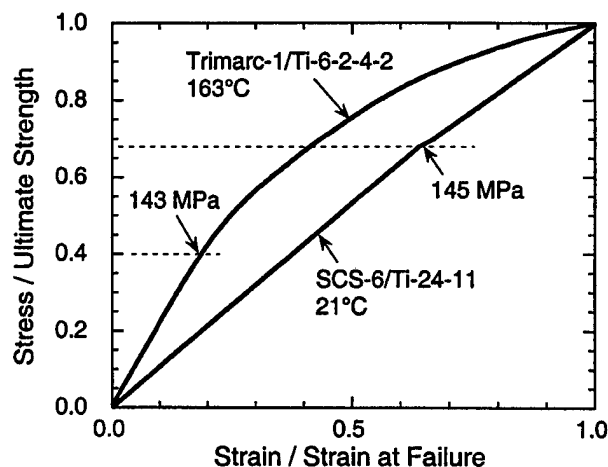


Figure 6. Normalized stress versus normalized strain curve for the two MMC systems. Data from Hall et al. [11] and Buchanan et al. [9].

Comparing the difference between  $\sigma_u$  and  $\sigma_{th}$  for the matrix and the corresponding composite, we conclude that the fatigue range ( $=\sigma_u - \sigma_{th}$ ) for the composite loaded in the  $[90]_0$  orientation is only  $\approx 40\%$  of that of the fiberless matrix. The resulting near-flat S-N trend is correctly predicted by the model as shown in Figs. 6 and 7. This S-N behavior of the  $[90]_0$  MMC is also associated with significant scatter ( $\approx 5X$ ) in the measured  $N_f$  for  $\sigma_{90} \leq 200$  MPa. Hence, a damage tolerance based design for transverse loading may be impractical for some MMC systems. In these components, the transverse stresses should always be less than  $\sigma_{90,th}$  predicted by Eqn. (7).

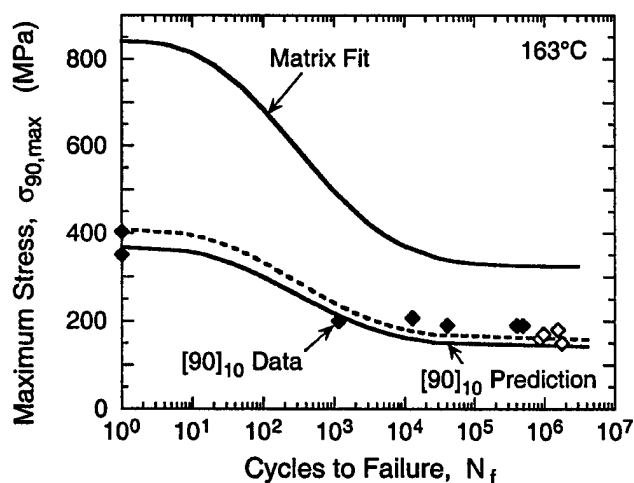


Figure 7. Fatigue behavior of  $[90]_0$  Trimarc-1/Ti-6Al-2Sn-4Zr-2Mo.  $\blacklozenge$  &  $\diamond$  from Buchanan et al.  $\diamond$  = specimens stopped prior to failure.

For typical MMC with  $V_f \approx 0.3$ , the stress-correction term  $F_n \approx 0.40$  implying that  $\sigma_{90,u} \approx 0.4 \sigma_{m,u}$  and  $\sigma_{90,th} \approx 0.4 \sigma_{m,th}$ , i.e. the transverse tensile strength and threshold stress (and other parameters such as creep-rupture strength) of the MMC component is  $\approx 60\%$  lower than that of the corresponding monolithic component. Consequently, the use of unidirectionally reinforced MMC is restricted to components with low transverse loads.

The proposed approach

neglected the:

- (1) load-carrying capacity of the fibers,
- (2) influence of residual stresses due to processing,
- (3) non-uniform stress distribution in the matrix ligament between the fibers,
- (4) potential for cracks emanating from the fiber/matrix interface, and
- (5) influence of non-uniform fiber distribution.

These issues are discussed next.

The normalized tension stress-strain curve for the two MMC systems [11,15] under transverse loading is shown in Fig. 8. A "knee" (onset of change in slope) in the curve occurs at  $\approx 68\%$  of ultimate strength for SCS-6/Ti-24Al-11Nb and  $\approx 40\%$  of ultimate strength for Trimarc-1/Ti-6Al-2Sn-4Zr-2Mo. Interestingly, these stresses are close to the MMC threshold stress indicated by the data and predicted by the model in Figs. 6 and 7. The onset of the change in slope corresponds to the stress required to exceed the residual stresses and the fiber-matrix bond strength [4,16]. Using edge replicates, Johnson et al. [4] showed that this change in slope was also associated with beginning of the separation between the fiber and the matrix. Hence, the proposed method of neglecting the fibers can be expected to be valid for all composite stress levels greater than the stress corresponding to the onset of debonding at the fiber/matrix interface.

The mismatch of coefficient of thermal expansion between the matrix and the fiber results in significant residual stresses in the MMC after consolidation [2,17]. The residual stresses in the hoop direction are typically tensile in the matrix and range from 250 to 450 MPa depending on the properties of the fiber and the matrix [17]. Hall et al. [11] reported that the residual stresses decrease during fatigue loading. This decrease in residual stress will depend on the applied stress and stress range. The tensile residual stresses will increase the effective mean stress and load ratio in the matrix ligament in the MMC. If the effective mean stresses exceed the yield stress of the matrix, the processing-induced residual stresses will be zeroed during the first load/unload cycle. In addition, the stress distribution in the matrix ligament may not be constant as assumed in the proposed model (see Fig. 5). These various issues require a detailed micromechanical analysis of a unit cell [16] under various loading conditions.

The fiber packing factor,  $2^*R_f / B_p = 0.55-0.60$  for the TMC systems studied during this investigation. The stress concentration at the hole edge (=maximum stress /  $\sigma_{lig}$ ) is  $\approx 1.4-1.5$  for this fiber packing factor [18]. Hence, in some TMC systems cracks could emanate from the fibers/matrix interface during transverse fatigue loading, as reported by Castelli [19] of SCS-6/Ti-15V-3Cr-3Al-3Sn. The proposed model does not account for such crack growth. If crack growth occurs during fatigue loading, the measured fatigue life of the composite can be expected to be lower than the life predicted by the proposed model. Buchanan et al. [15] reported that the global fracture surface is not always perpendicular to the loading axis as shown in Figs. 3 and 4. The orientation of the fracture surface with respect to the loading axis appeared to be sensitive to the non-uniformity of the fiber distribution and features such as fiber touching. Work is in progress to analyze the influence of the fiber distribution on the observed scatter in the transverse fatigue life of the MMC [15].

### Summary

A net-section based model was used to successfully predict the overall isothermal fatigue behavior of unidirectionally reinforced MMC subjected to transverse loading. The model correctly predicts the relatively flat transverse fatigue behavior (S-N) of the MMC including the ultimate strength during tension loading and the threshold stress. The threshold stress is close to the stress corresponding to the onset of debonding between the fiber the matrix during transverse tension loading. The near-flat transverse fatigue behavior (S-N) implies that a

damage tolerance based approach may be inapplicable under transverse loading for some MMC systems.

### Acknowledgments

This research was conducted at the Materials and Manufacturing Directorate, Air Force Research Laboratory (AFRL/MLLN), Wright-Patterson Air Force Base, OH, USA. R. John and D.J. Buchanan were supported under on-site contract number F33615-94-C-5200. The authors gratefully acknowledge the assistance of Mike Shepard in obtaining the fracture profiles.

### References

1. Larsen, J. M., Russ, S. M., and Jones, J. W., *Metallurgical and Materials Transactions A*, 26A, pp. 3211 (1995).
2. Life Prediction Methodology for Titanium Matrix Composites, ASTM STP 1253, W.S. Johnson, J.M. Larsen, and B.N. Cox, Eds., American Society for Testing and Materials, Philadelphia, PA, (1996).
3. Castelli, M.G. and Gayda, J., in Reliability, Stress Analysis, and Failure Prevention, DE-55, ASME, pp. 213 (1993).
4. Johnson, W.S., Lubowski, S.J., and Highsmith, A.L., in Thermal and Mechanical Behavior of Metal Matrix and Ceramic Matrix Composites, ASTM STP 1080, J.M. Kennedy, H. Moeller, and W.S. Johnson, Eds., American Society for Testing and Materials, Philadelphia, PA, pp. 193 (1990).
5. John, R. and Ashbaugh, N.E., in Elevated Temperature Crack Growth, MD-Vol. 18, ASME, S. Mall and T. Nicholas, Eds., pp. 149 (1990).
6. Walls, D.P., Bao, G., and Zok, F.W., *Acta Metallurgica et Materialia*, 41, pp. 2061 (1993).
7. Venkateswara Rao, K.T., Siu, S.C., and Ritchie, R.O., *Metall. and Matls. Transactions A*, 24A, pp. 721 (1993).
8. John, R., Khobaib, M., and Smith, P.R., *Metallurgical and Materials Transactions A*, 27A, pp. 3074 (1996).
9. Buchanan, D.J., John, R. and Goecke, K. E., in Seventh Symposium on Composites: Fatigue and Fracture, ASTM STP 1330, R. B. Bucinell, Ed., American Society for Testing and Materials, Philadelphia, PA (1998).
10. Gambone, M.L., Fatigue and Fracture of Titanium Aluminides, WRDC-TR-89-4145, Air Force Research Laboratory (AFRL), Wright-Patterson Air Force Base, OH 45433-6533 (1990).
11. Hall, J.A., Peralta, A., Hollars, R.L., Harmon, D., Finefield, M.A., James, M.R., and Marshall, D.B., Damage Tolerance Concepts for Titanium-Aluminide Composites, WL-TR-95-4089, Air Force Research Laboratory (AFRL), Wright-Patterson Air Force Base, OH 45433-6533 (1995).
12. Cotterill, P.J. and Bowen, P., *Journal of Materials Science*, 31, pp. 5897 (1996).
13. John, R., Ashbaugh, N.E., and Lackey, A.F., *Scripta Metallurgica et Materialia*, 35, pp. 711 (1996).
14. John, R., Ashbaugh, N.E., and Lackey, A.F., *Jnl. of Comp. Tech. and Res.*, To be submitted, (1998).
15. Buchanan, D.J., John, R., and Larsen, J.M., *Materials Science and Engineering*, To be submitted (1998).
16. Koupa, J.L. and Ashbaugh, N.E., *Composites Engineering*, 5, pp. 569 (1995).
17. Coker, D., Boller, F., Kroupa, J.L., and Ashbaugh, N.E., FIDEP2 User Manual to Micromechanical Models for Thermoviscoplastic Behavior of Metal Matrix Composites, Univ. of Dayton Res. Institute, Dayton, OH, (1995).
18. Peterson, R.E., Stress Concentration Factors, Wiley, New York, 1974, pp. 188.
19. Castelli, M.G., Thermomechanical and Isothermal Fatigue Behavior of a [90]<sub>2</sub> Titanium Matrix Composite, NASA Contractor Report 191196, NASA Lewis Research Center, Cleveland, OH, October 1993.

**This page intentionally left blank.**



Reference: Kroupa, J.L. and Bartsh, M., "Influence of Viscoplasticity on Residual Stress and Strength of a Titanium Matrix Composite After Thermomechanical Fatigue," *Composites Engineering*, Vol. 29B, No. 5, pp. 633-642, 1998.

## **Influence of Viscoplasticity on the Residual Stress and Strength of a Titanium Matrix Composite After Thermomechanical Fatigue**

**J.L. Kroupa<sup>a</sup> and M. Bartsch<sup>b</sup>**

<sup>a</sup> Research Applications Inc., 11772 Sorrento Valley Road, Suite 145, San Diego, CA 92121, USA (Formerly of University of Dayton Research Institute, Dayton, OH 45469-0165, USA)

<sup>b</sup> Southwestern Counsel for Higher Education, Dayton, OH 45420, USA

(Received 24 April 1997; accepted 24 May 1998)

Modifications to the Bodner-Partom (B-P) constitutive equations provide improved flexibility in fitting a larger strain-rate range than previously available. Using the modified B-P equations, the importance of good matrix characterization becomes apparent for an SCS-6/Timetal®21S composite under thermomechanical and isothermal fatigue, as well as sustained loading. An interesting observation is that the residual stress after thermomechanical fatigue (TMF) can be significantly different than those found in the as-received composite. This phenomenon is caused by prestraining the fiber at high loads and temperatures during TMF. This phenomenon also provides an excellent opportunity to compare the predictive capabilities between the older and newer B-P models. When the maximum and minimum strains during TMF are obtained with the two models and compared to experimental measurements, the difference between the two models is minimal. However, inspection of the shifts in residual stress from the as-received condition shows significant difference between the older and newer B-P formulation. Lastly, pre-strained fibers caused by thermomechanical loading can cause a loss of room temperature tensile strength. To show this, a rudimentary fiber failure model is defined. This model is used to show that the loading type strongly influences residual strength. The loss of residual strength is significantly more sensitive to loading type, rather than the viscoplastic characterization.

(Keywords: Bodner-Partom equations; B. Thermomechanical fatigue; titanium matrix composites)

### **INTRODUCTION**

Under thermal and mechanical loads, the response of titanium matrix composites (TMC) is complex in nature due to the viscoplastic matrix response as well as the mismatch between the coefficient of thermal expansion between the fiber and the matrix. A variety of methods have been explored in the past to accurately characterize the strain-rate sensitivity, and time dependent (viscoplastic) response of a Timetal®21S matrix<sup>1</sup>. Using the material constants of Neu, the analysis of Zuiker and Sanders<sup>2</sup> found that the viscoplastic behavior was not well characterized at lower stress levels. Although, the lower stress ranges could be accurately modeled with a new set of constants, the new set of constants would then be less accurate in characterizing the higher strain-rate cases. To address that issue, Neu and Bodner<sup>3</sup> proposed an improved model to better capture a wider range of strain-rates. Unfortunately, Neu and Bodner only provided improved constants for Timetal®21S at two temperatures, 482°C and 650°C. A complete set of constants is determined for the temperature range of interest, from 23°C to 815°C, and is presented later.

Thermomechanical fatigue (TMF) loading on the SCS-6/Timetal®21S composite is chosen to demonstrate the differences between the newer and the older matrix characterization. Residual stresses within the composites after TMF are of interest because of experimental observations made by Nicholas *et al.*<sup>4</sup> They found that after in-phase (IP) TMF,

the residual stresses in a titanium matrix composites were significantly different than those within the as-received composite. In the as-received condition, the fiber residual stresses are predicted to be compression. However, after IP-TMF, the room temperature fiber stresses are predicted to be in tension.

Our investigation will expand beyond the IP-TMF case to see if room temperature residual stresses change during other types of load conditions. In particular, the types of loading are thermal cycling, isothermal fatigue, out-of-phase (OP) TMF, and sustained (creep) loading. This paper will also investigate how the viscoplastic characterization influences the shift in residual stress.

The shifting of residual stresses from those in the as-received condition is a result of pre-straining of fibers at load and temperature. If a tensile test was performed on a composite with tensile pre-strained fiber, one might expect the fiber to reach its failure strain quicker than the as-received composite. This would appear as a loss of strength in the composite. This paper investigates the loss of strength phenomena after several types of fatigue loading, as well as the differences between a new and an old set of material constants.

### BODNER-PARTOM THEORY

For the temperature and time dependence, as well as the strain-rate sensitivity, the response of the Timetal®21S was characterized with the viscoplastic theories of Bodner and Partom. The original theory for Timetal®21S proposed by Neu<sup>1</sup> is similar to the isotropic nonisothermal theory of Chan *et al.*<sup>5</sup> Given here is a brief description of the theory. Additional modifications to the theory are presented later as well as a complete set of material constants for Timetal®21S.

#### Basic Bodner-Partom equations

The first assumption in this analysis is the additive decomposition of the total strain,  $\epsilon_{ij}^{tot}$ , into elastic, thermal, and inelastic components.

$$\epsilon_{ij}^{tot} = \epsilon_{ij}^{el} + \epsilon_{ij}^{th} + \epsilon_{ij}^{in} \quad (1)$$

The elastic strains,  $\epsilon_{ij}^{el}$ , depend on the current stress state, elastic modulus  $E$ , and Poisson's ratio  $\nu$ . The thermal strain components,  $\epsilon_{ij}^{th}$ , equal the product of the coefficient of thermal expansion and the difference between the current and reference temperatures. The Bodner-Partom (B-P) flow rule governs the evolution of the inelastic strains,  $\epsilon_{ij}^{in}$

$$\dot{\epsilon}_{ij} = D_0 \exp \left\{ -\frac{1}{2} \left( \frac{(Z^I + Z^D)^2}{3J_2} \right)^n \right\} \frac{S_{ij}}{J_2} \quad (2)$$

with the two hardening variables,  $Z^I$  and  $Z^D$ , for the isotropic and directional hardening, respectively.  $D_0$  is the limiting strain rate,  $s_{ij}$  are the components of deviatoric stress with  $J_2$  equal to  $(s_{ij}s_{ij})/2$ .

The evolution of  $Z^I$  and  $Z^D$  has similar empirical forms. Each equation consists of a hardening, thermal recovery and temperature rate term. The isotropic hardening evolution equation with these three terms is:

$$\dot{Z}^I = m_1 (Z_1 - Z^I) \dot{W}^{in} - A_1 Z_1 \left( \frac{Z^I - Z_2}{Z_1} \right)^{n_1} + \left( \frac{Z_1 - Z^I}{Z_1 - Z_2} \right) \frac{\delta Z_2}{\delta T} \dot{T}, \quad (3)$$

where the inelastic work rate is:

$$\dot{W}^{in} = \sigma_{nm} \dot{\epsilon}_{nm}^{in} \quad (4)$$

The initial value of the isotropic hardening,  $Z^I(0)$ , is  $Z_0$ . The material parameters associated with the isotropic hardening evolution are  $m_1$ ,  $Z_0$ ,  $Z_1$ ,  $A_1$ , and  $r_1$ . The thermal differential term  $\delta Z_2/\delta T$  appropriately scales  $Z^I$  when inelastic deformation and thermal recovery occur under nonisothermal conditions. The thermal differential term prevents  $Z^I$  from passing through maximum and minimum values,  $Z_1$  and  $Z_2$ , respectively.

The scalar product of a state variable,  $\beta_{nm}$ , and a unit stress vector  $u_{nm}$  yields the magnitude of the directional hardening term;

$$Z^D = \beta_{nm} u_{nm}, \quad (5)$$

Where:

$$\dot{\beta}_{ij} = m_2 (Z_3 u_{ij} - \beta_{ij}) \dot{W}^{in} - A_2 Z_1 \left( \frac{\sqrt{\beta_{nm} \beta_{nm}}}{Z_1} \right)^{r_2} v_{ij} + \frac{\beta_{ij} \delta Z_3}{Z_3 \delta T} \dot{T}, \quad (6)$$

$$u_{ij} = \frac{\sigma_{ij}}{\sqrt{\sigma_{nm} \sigma_{nm}}}, \quad (7)$$

and

$$v_{ij} = \frac{\beta_{ij}}{\sqrt{\beta_{nm} \beta_{nm}}}. \quad (8)$$

The initial directional hardening variable,  $Z^D(0)$  is set to zero. The material constants associated with the directional hardening evolution equation are  $m_2$ ,  $Z_3$ ,  $A_2$ , and  $r_2$ . The temperature differential term  $\delta Z_3/\delta T$  appropriately scales the directional hardening variable when inelastic deformation and thermal recovery occur under nonisothermal conditions.

#### Improvements to Bodner-Partom equations

Using the basic B-P formulation of Chan *et al.*<sup>5</sup>, the original set of material parameters for Timetal®21S were determined by Neu<sup>1</sup> using a limited amount of monotonic, cyclic, and creep test data<sup>6</sup>. At the time, these constants were determined to be sufficiently accurate. However, the study of Zuiker and Sanders<sup>2</sup> found that the parameters did not accurately characterize Timetal®21S response at very low stress levels. Noting the inadequacies of the original set of constants, Neu and Bodner<sup>3</sup> revisited the viscoplastic characterization of Timetal®21S and surmised that strain hardening occurred over a much larger range of strain-rates than previously proposed by Chan *et al.*<sup>6</sup> The proposed changes are similar to other approaches<sup>7,8</sup>. The hardening rate term  $m_1$  is proposed to be exponential functions of the state variables for hardening,  $Z^I$ , as follows:

$$m_1 = m_{1b} + (m_{1a} - m_{1b}) \exp[-m_{1c} (Z^I - Z_2)] \quad (9)$$

The two new material constants,  $m_{1a}$  and  $m_{1b}$ , represent, respectively, the initial and final (saturated) values of  $m_1$ . The material constant  $m_{1c}$  controls the saturation rate of  $m_1$ .

The second modification was made in the constant value of  $A_1$ , which also becomes a function of the hardening variable  $Z^I$ :

$$A_1 = A_{1b} + (A_{1a} - A_{1b}) \exp[-A_{1c} (Z^I - Z_2)] \quad (10)$$

where  $A_{1a}$  and  $A_{1b}$  are, respectively, the initial and saturated values of  $A_1$ . Similar to  $m_{1c}$ ,  $A_{1c}$  controls the saturation rate of  $A_1$ .

In summary, two temperature dependent material constants are transformed into six constants. The increased number of material constants allows much more flexibility in representing the viscoplastic, time- and temperature-dependent response. Although a similar

form for  $m_2$  and  $A_2$  could be proposed, no experimental evidence or rational supports such a form.

#### *Timetal@21S material parameters*

Unfortunately, Neu and Bodner<sup>3</sup> only reported constants at 482°C and 650°C for the new form of the equations. The remaining temperature properties, from 23°C to 815°C, were determined by us for use here. The combined series of constants are provided in *Table 1*. Only a handful of constants are chosen as temperature dependent:  $n$ ,  $Z_2$ ,  $A_{1a}$ ,  $A_{1b}$  and  $A_2$ . For simplicity,  $A_{1b}$  is one-twentieth of  $A_{1a}$ , and  $A_2$  is equal to  $A_{1b}$ .

For simplicity, the original set of material parameters proposed by Neu<sup>1</sup> is referred to as 'old' B-P constants. The material parameters given above are referred to as 'new' B-P constants. The temperature-dependent elastic constants for both models are the same.

**Table 1** New Bodner-Partom parameters

Temperature-independent constants					
$m_{1a}=20 \text{ (MPa)}^{-1}$			$m_{1b}=2 \text{ (MPa)}^{-1}$		
$m_{1c}=0.001 \text{ (MPa)}^{-1}$			$m_2=4 \text{ (MPa)}^{-1}$		
$r_1=r_2=3.5$			$Z_1=3500 \text{ MPa}$		
$D_0=1 \times 10^4 \text{ s}^{-1}$			$Z_3=180 \text{ MPa}$		
$A_{1c}=0.005 \text{ (MPa)}^{-1}$					
Temperature-dependent constants					
T(C)	n	$Z_0=Z_2$ (MPa)	$A_{1a}$ (1/s)	$A_{1b}$ (1/s)	$A_2$ (1/s)
23.0	1.5	3000	0.0	0.0	0.0
260.0	1.31	2700	0.0	0.0	0.0
482.0*	1.15	300	0.01	2.0 X 10-4	2.0 X 10-4
566.0	1.025	200	1.0	0.1	0.1
650.0*	0.94	100	100.0	2.0	2.0
760.0	0.87	90	600.0	150.0	150.0
815.0	0.82	75	650.0	200.0	200.0

## COMPOSITE MODELING

The unidirectional SCS-6/Timetal@21S composite system is modeled in our investigation. Since the loading is applied in the fiber direction, the concentric cylinder model is well suited for the analysis. The concentric cylinder geometry is solved with the FIDEP2 program provided by Coker *et al.*<sup>9</sup> The fiber volume content of 0.35 is used, unless otherwise noted. The analysis assumes a thermal elastic stress-strain response for the fiber. The temperature-dependent elastic properties are provided by Lara-Curzio and Sternstein.<sup>10</sup> The longitudinal thermal expansion data was measured by Hillmer.<sup>11</sup> For the fiber, isotropic response for both elastic properties and thermal expansion is assumed.

## ANALYSIS AND RESULTS

### *Neat Timetal@21S matrix response*

Before addressing the composite response, the differences between the two sets of material constants are easily shown with neat (fiberless) matrix material. In the neat matrix, the differences between the older and new constants can be seen in *Figure 1*. The data in the figure show the correlation of steady-state response from B-P models to experimental creep and tensile data. In creep, the model is matched to minimum creep rate. In tension, the model is matched to the saturation or ultimate stress.

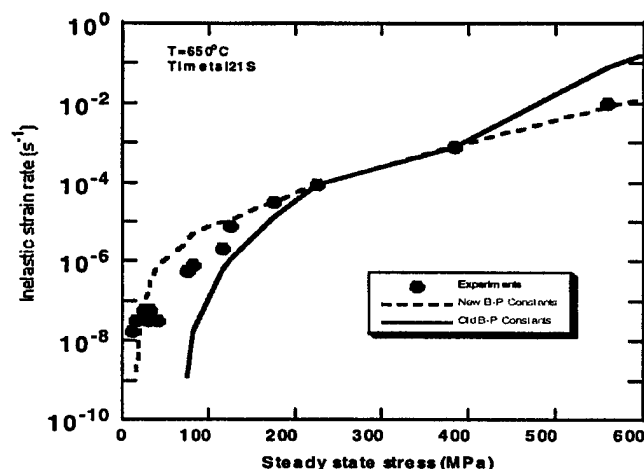
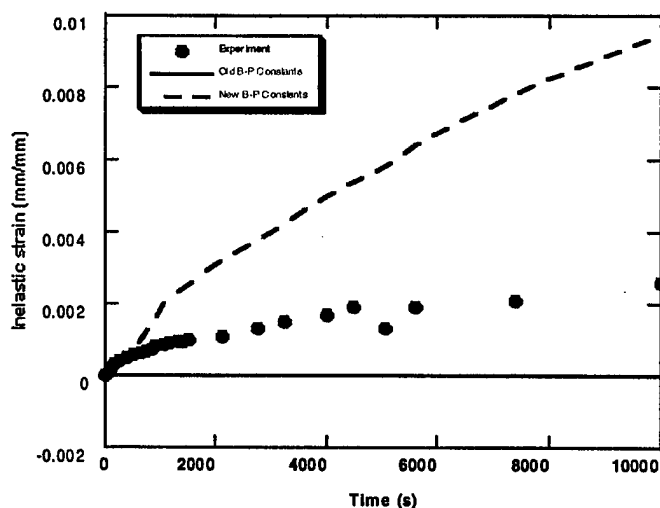


Figure 1 Saturation stresses for two different B-P material parameters

Figure 1 shows that the new B-P material parameters characterize a larger range of strain-rates than the old constants. Note the stress level in which the strain-rates drop off toward zero. That is, no inelastic deformation will occur below this lower limit stress. The limiting stress is about 80 MPa for the old constants, whereas the limiting stress is 25 MPa for the new constants.

The better ability to capture the lower stress ranges is shown in comparisons of the predictions to creep measurements in Figure 2. At 40 MPa load, the old constants predict no inelastic deformation, whereas the new constants predict excessive inelastic strains. Between the two predictions, it is hard to determine whether one fit is better or worse, however, a factor of two in minimum creep rate obtained by the newer model is within the generally acceptable scatter for experiments. The primary creep response is not modeled the best with either constant as both models are calibrated to the minimum creep rate.

For a unidirectional composite under the types of loading discussed in this paper, stress relaxation is more realistic than creep for the matrix response. The comparison of the two models in stress-relaxation is shown in Figure 3. The differences between cut off stress for both models are also seen here. For the older model, the stress saturates at 75 MPa, whereas the new model better matches the experiment by saturating at 25 MPa. Overall, the new constants do a better job at predicting the response than the old constants.



**Figure 2** Comparison of two models in creep at 650°C and 40 MPa

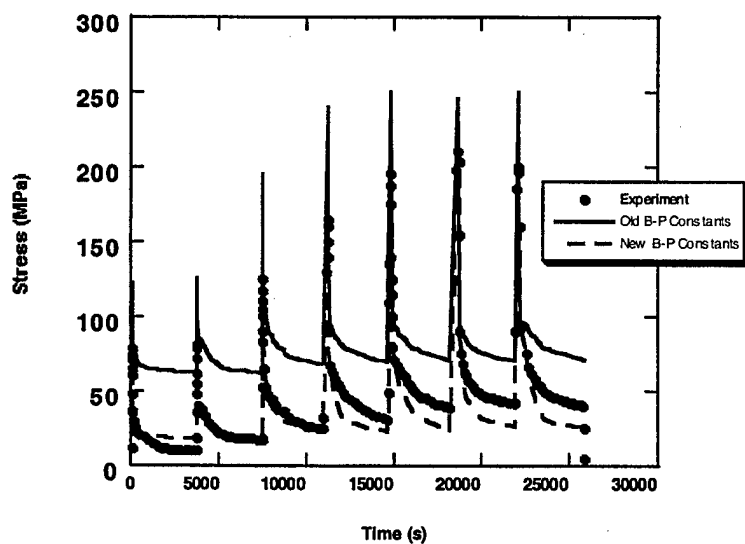


**Figure 3** Comparisons of two models in stress-relaxation at 650°C

#### *Residual Stresses within the as-received composite*

Process-induced residual stresses are commonly found in the as-received composites. The residual stresses are caused by the composite cooling to room temperature after consolidation at high temperature. During the cool-down processing and the mismatch of the CTE between the fiber and the matrix cause residual stresses. For this analysis, the SCS-6/Timetal®21S composite processing consisted of a linear 10 h cool-down from 900°C, which is fairly representative of the actual processing condition.

For both models, the predicted matrix stress throughout the composite is fairly close to the measurements of James,<sup>12</sup> as well as those of Rangaswamy and Jayaraman,<sup>13</sup> as illustrated in *Figure 4*. The difference between the two models is evident in that the new

constants exhibit more inelastic strains during cool-down, and predict lower stress magnitudes. Since the thermal strain difference between the fiber and matrix must be balanced between the elastic and inelastic strains, more inelastic strains result in less elastic strains and hence, lower stresses.

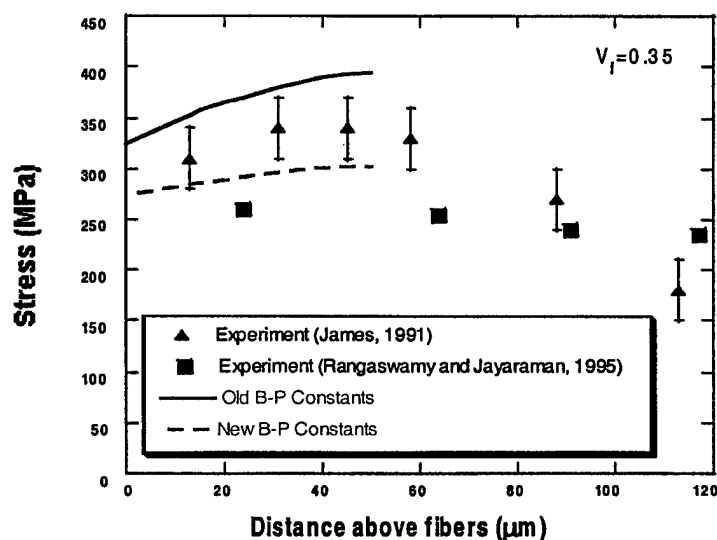
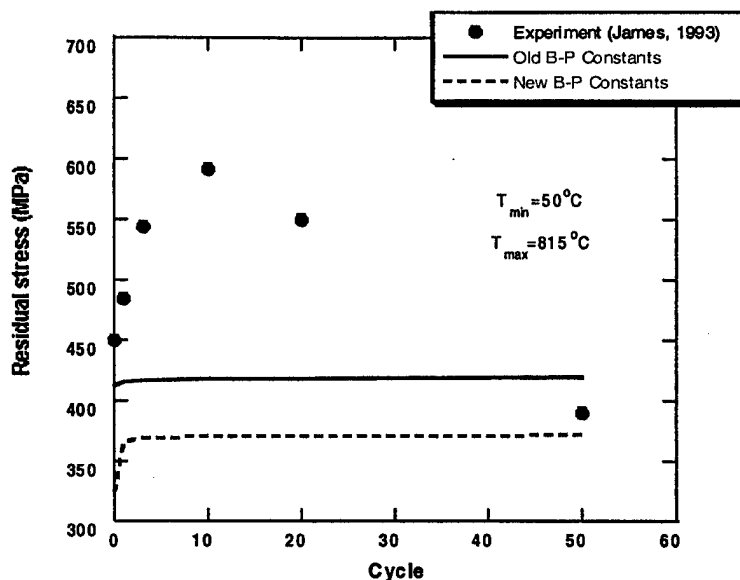


Figure 4 Room temperature residual matrix stresses in the as-received composite

#### *Residual stress after thermal cycling*

As noted by Ghonem *et al*<sup>14</sup> and Sherwood and Quimby,<sup>15</sup> thermal cycling of a metal matrix can change the room temperature residual stresses from those predicted after processing. Experimental measurements for James, M.R. (1993, pers. comm.) confirm these observations. By using the two sets of material constants, the room temperature residual stresses are computed after thermal cycling (see Figure 5). The experimental measurements are significantly higher than previously reported (in Figure 4), which may be a consequence of the higher fiber-volume content of 0.38. Both viscoplastic models exhibit an increase in stress with the old constants shifting 2 MPa, while the new constants shift 80 MPa. In the first 10 cycles, the experimental data exhibit a significant increase in matrix stress, nearly 150 MPa, which could be caused by a change in microstructure. For this experiment, the maximum temperature of 815°C is nearly 200°C higher than the beta-transus, the temperature of a microstructure phase change between hex-close pack and body-centered cubic. After 10 cycles, the drop in matrix stress of 200 MPa could be caused by matrix crack initiation, which was observed for the same composite and loading conditions.<sup>16</sup> In short, the comparison of both models to experiments is not all that great, which is not a surprise, since both sets of material constants do not account for either the phase-change or matrix cracking.



**Figure 5** Room temperature residual longitudinal matrix stress after thermal cycling

#### *Isothermal loading*

During isothermal fatigue at 650°C, the numerically predicted response agrees well with the experimental measurements of the maximum and minimum strains shown in *Figure 6*. The one major difference between the old and new models can be illustrated in this figure. Note that the old model results are not shown beyond 25 cycles. The numerical solution refused to converge for the high strain rates imposed during 1 Hz isothermal fatigue test at 650°C. The lack of convergence is an intrinsic problem with the selection of material constants. In particular,  $Z_3$  (4300 MPa) is larger than  $Z_2$  (100 MPa) at 650°C. The trouble starts when the variable  $\beta_{ij}$  exceeds the isotropic hardening variable  $Z$ . This is not a problem, unless the same component of stress  $\sigma_{ij}$  changes sign from tensile to compressive. When the stress changes sign with large  $\beta_{ij}$ , the resulting instantaneous change in  $Z^D$  causes havoc in the FIDEP2 solver. The new model does not have this problem and matches the experimental measurements fairly well.



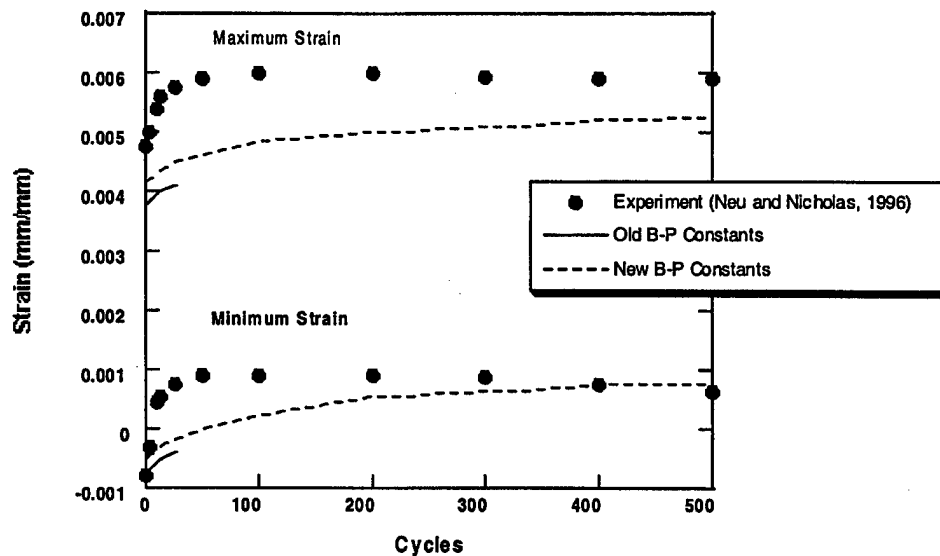


Figure 6 Maximum and minimum strains predicted during isothermal fatigue at 650°C

#### Thermomechanical loading

Both the new and old sets of B-P constants provide reasonable predictions of the maximum and minimum strains measured from IP-TMF experiments<sup>17</sup> as seen in Figure 7. The difference in strain between the two sets of constants is not particularly great. Neither model predicted as much strain ratcheting as measured from experiments. The experiments may have exhibited fiber fracture during cycling. In addition, more primary creep may have occurred in the experiments than the models predicted.

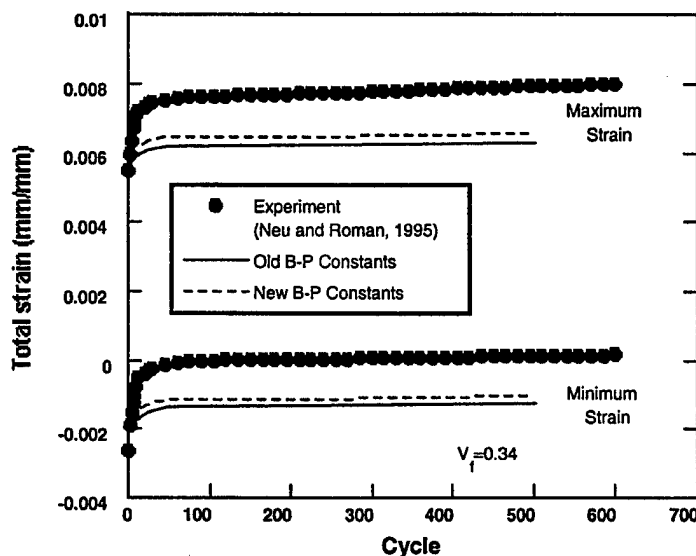
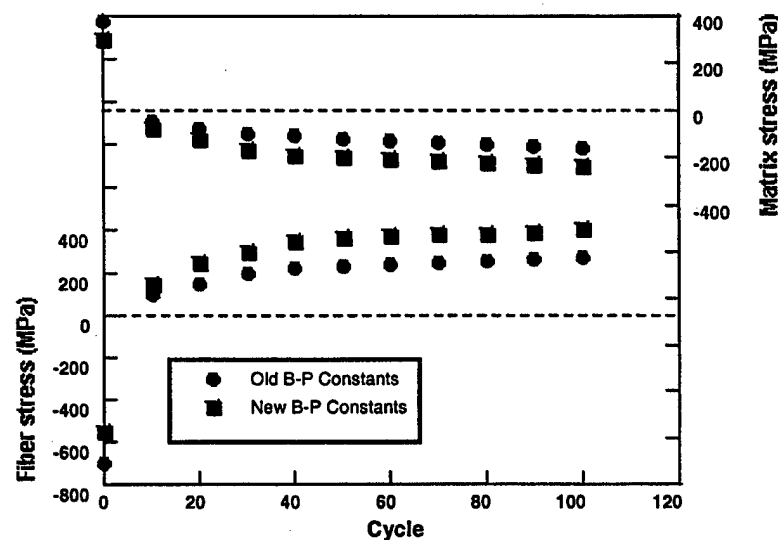


Figure 7 Maximum and minimum strains predicted during IP-TMF

One interesting prospect, proposed by Nicholas *et al.*<sup>4</sup>, was whether IP-TMF significantly changes the as-received residual fiber stress from compressive to tensile. To evaluate this phenomenon, an in-phase simulation was interrupted with regular cooling cycles to room temperature. During the cool-down cycle, the composite is rapidly cooled and heated in 1 s

periods while the applied load is held at zero. The influence of the cooling cycle is assumed not to influence the remaining TMF response.

As speculated, the room temperature residual stresses change significantly after 100 cycles of IP-TMF, as shown in *Figure 8*. Much of the redistribution occurs during the first 10 Cycles; however, the stresses do not reach saturation until cycle 50. Consistent with hypotheses of Nicholas *et al.*, the residual longitudinal stresses in the fiber changes sign from compression to tension. The difference between the two matrix models is not intrinsically obvious from strains; however, signification difference can be seen in the predicted stress levels (nearly 100 MPa difference in the fiber).



**Figure 8** Room temperature residual stresses during an interrupted IP-TMF test

During OP-TMF, a significant difference between the two models is observed in the measured maximum and minimum strain<sup>18</sup> as shown in *Figure 9*. At first glance, both models do not seem to predict the experimental measurement as well as the in-phase case. The difference between the in- and out-of-phase cases is the magnitude of measured strains. The strain range measured in IP-TMF (0.008 mm/mm) is four times larger than from OP-TMF (0.002 mm/mm). Plotted on the same scale as IP-TMF, the difference between the two predictions and experiments would not seem as great.

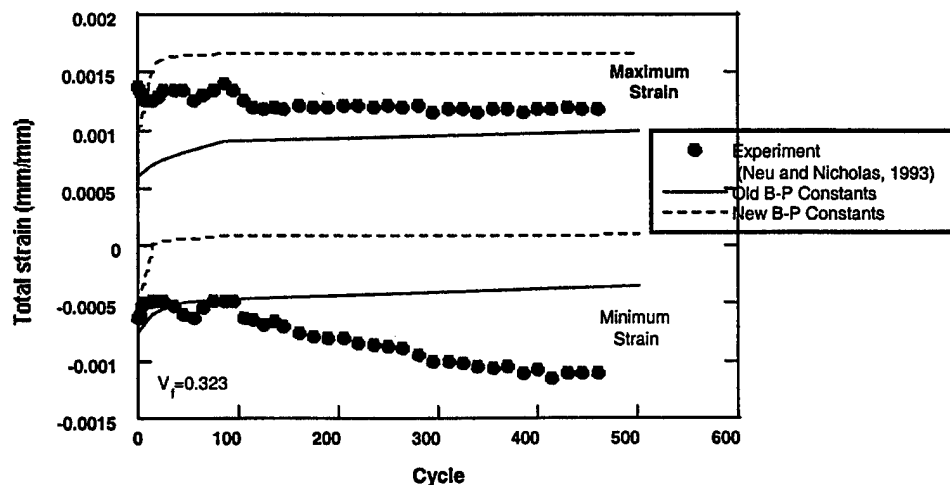


**Figure 9** Maximum and minimum strains predicted during OP-TMF

In OP-TMF, the difference between the two sets of constants is more obvious by inspection of room temperature residual stresses, as shown in *Figure 10*. Conducting the same interrupted fatigue simulation as above, the old model constants predicted a final residual stress in fiber of -600 MPa, where as the new constants predict a stress of -300 MPa. This difference in predicted stress states is significant. Given that neither model predicted maximum and minimum strains particularly well, it is difficult to decide which one is more accurate. Since the range of measured strains is so narrow, the experimental measurements are more susceptible to experimental scatter. A repeat of the experiment would be highly desirable.

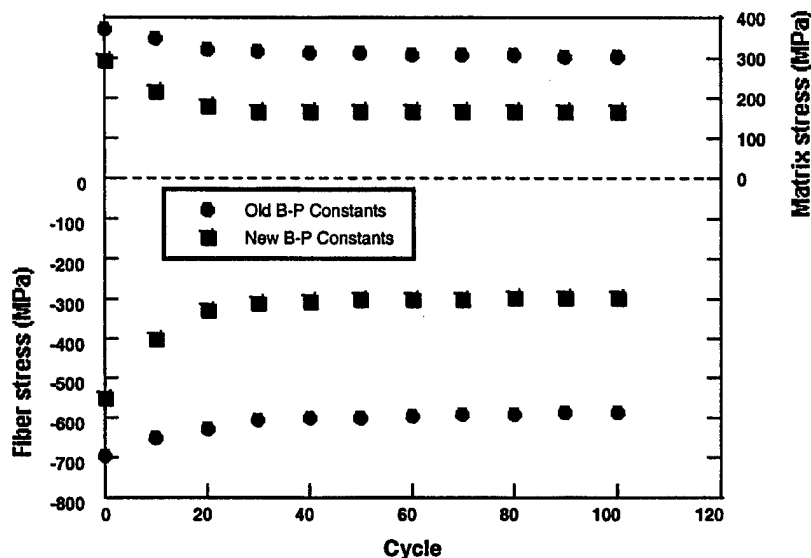


**Figure 10** Room Temperature residual stresses during an interrupted OP-TMF test

#### *Residual strength predictions*

As noted above, the residual stress after 100 cycles of fatigue loading can significantly change from that found in the as-received composite. The fundamental question becomes whether pre-straining of fibers during TMF could influence residual strength. To investigate what types of fatigue is more susceptible to the shifting of residual stress common levels for mechanical and thermal loads are chosen, as shown in *Table 2*. For the types of loading shown in *Table 2*, the resultant residual fiber stress at room temperature is presented in *Table 3*. The most obvious feature is that high loads at elevated temperatures, IP-TMF and sustained load at 1000 MPa, resulted in a significant shift in the residual stress. This significant shift is caused by the straining of fibers at high load and temperature.

To determine the influence of pre-strained fibers on residual strength, a criterion of composite failure is defined. The residual strength of the composite is defined with a simple fiber failure criterion during a room temperature tension simulation. In this study, the fiber failure strain of 0.007 mm/mm is assumed. As an example, the composite and fiber tensile stress-strain response is illustrated in *Figure 11*. In this case, the tensile response was obtained after 100 cycles of IP-TMF. Note that the strain fiber is pre-strained about 0.001 mm/mm at a stress of 250 MPa. The tensile load increases until the fiber strain is 0.007 mm/mm at which time the analysis is stopped, and the composite stress of 1250 MPa is defined as the strength.

As expected, the composites with more tensile pre-strained fibers exhibited a greater reduction of residual strength, as illustrated in *Table 3*. Consistent with that, the IP-TMF and sustained load at 1000 MPa cases show significant reductions in residual strength. The other cases show lesser amounts of strength reduction. Overall, the difference between the two sets

of viscoplastic constants is small compared to influence of the loading types. The largest difference between the two models is 10%, found for the OP-TMF case.

**Table 2** Fatigue conditions prior to residual strength analysis

Condition	Peak stress (MPa)	Minimum stress (MPa)	Peak temp. (°C)	Minimum temp. (°C)
Thermal cycles*	0	0	815	150
Isothermal fatigue	1000	100	650	—
In-phase TMF	1000	100	650	150
Out-of-phase TMF	1000	100	650	150
Sustained loading	500 and 1000	—	650	—

**Table 3** Post-fatigues residual fiber stress and room-temperature composite strength

	Residual fiber stress (MPa)		Residual composite strength (MPa)	
	Old constants	New constants	Old constants	New constants
As processed	-692	-544	1681	1690
Thermal fatigue	-702	-658	1682	1703
OP-TMF	-574	-291	1677	1585
Creep at $\sigma=500$ MPa	-153	-87	1504	1473
Isothermal fatigue	-10	-15	1428	1436
Creep at $\sigma=1000$ MPa	N.A.	372	N.A.	1230
IP-TMF	268	413	1281	1210

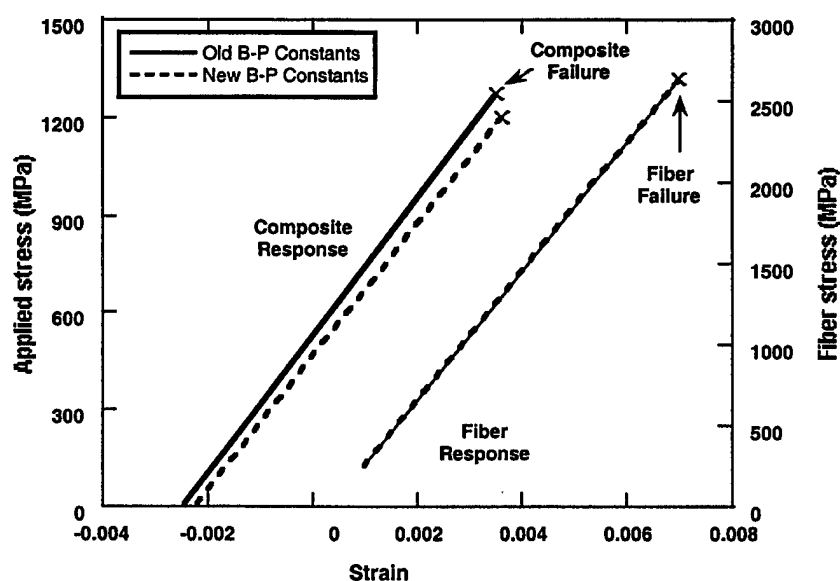


**Figure 11** Stress-strain response of residual strength computation

#### Computational efficiency

Given that the improved model with new constants is more complex than the old model, one could expect that the computer algorithms would require more CPU time to solve the equations. For the analysis conducted here, the algorithms associated with the new B-P formulation generally took twice as long to solve the equations. However, 100 cycles of TMF could be completed in less than half an hour on a Convex-Metaseries2 computer. Using a two-bar model would dramatically decrease the time; however, the solutions would generally be 5% to 10% different from the concentric cylinder model.

## DISCUSSION

For this investigation, the influence of viscoplasticity on TMF response and residual strength is a subtle point since the effects of strain-rate sensitivity and time-dependent response were not directly shown. However, the comparison between the old and new viscoplastic characterizations did show significant differences. Even more subtle, the differences in predicted responses are not evident in all cases for TMF. The differences can be illustrated with the results of *Table 3*. In the case of thermal fatigue and isothermal fatigue, the viscoplastic characterization did not significantly influence the predicted stress state. In other cases, such as IP-TMF, the differences are larger. The biggest difference (nearly 100%) is found with the out-of-phase case. Overall, the type of loading influences the shift in residual stress more than the difference between the two sets of constants. For practical matters, both models are accurate enough to capture the shifting of residual stress phenomena.

Not necessarily viscoplastic, the influence of plasticity, in the pre-straining of fibers, can result in the loss of strength. An amazing observation is that the theories used here do not account for any formal treatment of damage, yet predict a loss of strength. Solely on the pre-strained fibers, certain types of thermal mechanical fatigue result in lower residual strength. Both sets of B-P constants predicted the phenomenon, with very little difference between the two. Once again, the predicted loss of residual strength is more sensitive to loading type than viscoplastic model.

Some experimental residual strength data exist for two loading types – thermal fatigue and OP-TMF. In both cases, experimental measurements have found residual strength to be significantly less than the as-received composite. For thermal cycling, Nicholas and Updegraff<sup>16</sup> measured a 70% loss of strength after 1500 cycles. For OP-TMF, Castelli<sup>19</sup> measured up to a 40% loss of strength after 90% of life under certain conditions. In both cases, significant matrix cracking was observed. Since neither viscoplastic model accounts for any form of matrix cracking, the predicted residual strength does not reflect the influence of this damage. In fact, for the thermal cycling case, the strength actually increased slightly (10 MPa). Such shortcomings of our current models indicate the need to couple a damage accumulation model with our viscoplastic approach, as proposed by Neu and Nicholas.<sup>20</sup>

## CONCLUSIONS

This investigation introduces an improved formulation for the viscoplastic response of Timetal®21S matrix. In the neat matrix form, the improved model produces better agreement with the experimental creep and stress-relaxation data. Under many types of thermomechanical loading, the differences between the two models vary. Some cases show no difference, while others show significant difference. For OP-TMF, the difference between the two models is nearly a factor of 2. Both models do predict the phenomenon of shifting residual stresses from the as-received state. Both models also predict the loss of residual strength due to pre-strained fibers. Both models fail to predict the loss of residual strength measured after thermal cycling and OP-TMF. In this regard, both models require additional modifications to account for matrix cracking damage.

## ACKNOWLEDGEMENTS

This research was conducted at the Materials Behavior Branch, Metals and Ceramics Division, Materials and Manufacturing Directorate, Air Force Research Laboratory (AFRL/MLLN) Wright-Patterson AFB, OH, under Contract no. F33615-94-C-5200. The authors would also like to give personal thanks to Drs Noel Ashbaugh and Theodore Nicholas for continued technical support.

## REFERENCES

1. Neu, R.W., Nonisothermal material parameters for the Bodner-Partom model, MD-Vol. 43. In *Material Parameter Estimation for Modern Constitutive Equations*, ed. L.A. Bertram, S.B. Brown, and A.D. Freed. ASME, New York, 1993, pp. 211-225.
2. Zuiker, J.R. and Sanders, B.P., Analysis of pinned joints in viscoplastic monolithic plates, ASME AMD Vol. 213/MD Vol. 63. In *Proceedings of the Symposium on Numerical Implementation and Application of Constitutive Models in the Finite Element Method*, 1995, pp. 37-48.
3. Neu, R.W. and Bodner, S.R., Contributive research and development, Vol. 6. In *Determination of the Material Constants of Timetal@21S for a Constitutive Model*, SYSTRAN report under contract no. F33615-94-C05804 for Wright Laboratory, Wright-Patterson AFB, OH, 45433, 1995.
4. Nicholas, T., Castelli, M.G., and Gambone, M.L., Fiber breakage in metal matrix composites – reality or artifact?. *Scripta Materialia*, 1997, **36**, 585-592.
5. Chan, K.S., Bodner, S.R. and Lindholm, U.S., Phenomenological modeling of hardening and thermal recovery in metals. *ASME Journal of Engineering Materials and Technology*, 1988, **110**, 1-8.
6. Khobaib, M. and Ashbaugh, N.E., Tensile, creep, and LCF behavior of fiberless Timetal@21S alloy. In *Fatigue 93*, ed. J.-P. Baille and J.I. Dickson. EMAS, Chameleon Press, London, 1993, pp. 909-910.
7. Bodner, S.R. and Lindenfeld, A., Constitutive modeling of the stored energy of cold work under cyclic loading. *European Journal of Mechanics and Solids*, 1995, **14**(3), 333-348.
8. Bodner, S.R. and Rubin, M.B., On the representation of rate dependence of hardening and non-proportional loading effects by a viscoplastic model, ICES, 1995.
9. Coker, D., Ashbaugh, N.E. and Nicholas, T., Analysis of thermomechanical cyclic behavior of unidirectional metal matrix composites. In *Thermomechanical Fatigue Behavior of Materials, ASTM STP 1186*, ed. H. Sehitoglu. American Society for Testing and Materials, Philadelphia, 1993, pp. 50-69.
10. Lara-Curzio, E. and Sternstein, S.S., Thermalelastic analysis of composite CVD SiC fibers. *Composites Science and Technology*, 1993, **46**, 265-275.
11. Hillmer, J.J., Thermal expansion of chemically vapor deposited silicon carbide figures. In *Symposium on High Temperature Composites, Proceedings of the American Society of Composites*. Technomic Publishing Company, 1989, pp. 206-213.
12. James, M.R., Behavior of residual stresses during fatigue of metal matrix composites. In *Residual Stresses III Science and Technology*, ed. H. Guiwara, T. Abe and K. Tanaka. Elsevier, Oxford, 1991, pp. 555-560.
13. Rangaswamy, P. and Jayaraman, N., Residual stresses in SCS-6/Beta-21S composites. *Journal of Composites Technology and Research*, 1995, **17**(1), 43-49.

14. Ghonem, H., Wen, Y. and Zheng, D., An interactive simulation technique to determine the internal stress states in fiber reinforced metal matrix composites. *Materials Science and Engineering*, 1994, **A177**, 125-134.
15. Sherwood, J.A. and Quimby, H.M., Optimization of the manufacturing process of a titanium aluminide metal matrix composite using a viscoplastic constitutive theory. *ASME Journal of Engineering Materials and Technology*, 1996, **118**(2), 235-240.
16. Nicholas, T. and Updegraff, J.J., Modeling thermal fatigue damage in metal-matrix composites. *Composites Engineering*, 1994, **4**(7), 775-795.
17. Neu, R.W. and Roman, I., Acoustic emission monitoring of damage in metal matrix composites subjected to thermomechanical fatigue. *Composites Science and Technology*, 1995, **52**, 1-8.
18. Neu, R.W., and Nicholas, T., Methodologies for predicting the thermomechanical fatigue life of unidirectional metal matrix composites. In *Advances in Fatigue Lifetime Predictive Techniques*, Vol. 3, ASTM STP 1292, ed. M.R. Mitchell and R.W. Landgraf. American Society for Testing and Materials, Philadelphia, 1993, pp. 1-23.
19. Castelli, M.G., Characterization of damage progression in SCS-6/Timeal®21s [0]<sub>4</sub> under thermomechanical fatigue loading. In *Life Prediction Methodology for Titanium Matrix Composites*, ASTM STP 1253, ed. W.S. Johnson, J.M. Larsen and B.N. Cox. American Society for Testing and Materials, Philadelphia, 1996, pp. 412-431.
20. Neu, R.W. and Nicholas, T., Thermomechanical fatigue of SCS-6/Timetal®21S under out-of-phase Loading, AD-Vol. 34. In *Thermomechanical Behavior of Advance Structural Materials*, ed. W.J. Jones, 1993, pp. 97-111.

**This page intentionally left blank**



Reference: Kramb, V.A., John, R., and Zawada, L.P., "Fracture Behavior of an Oxide/Oxide Ceramic Matrix Composite," submitted for publication J. American Ceramic Society, May 1998.

## Notched Fracture Behavior of an Oxide/Oxide Ceramic Matrix Composite

Victoria A. Kramb<sup>1</sup>, Reji John and Larry P. Zawada

Materials and Manufacturing Directorate, Air Force Research Laboratory, (AFRL/MLLN), Wright-Patterson Air Force Base, OH 45433-7817, USA.

<sup>1</sup> University of Dayton Research Institute, 300 College Park, Dayton, OH 45469-0128, USA.

### Abstract

The fracture behavior of an oxide/oxide ceramic matrix composite, alumina/alumina-silica (Nextel610/AS), was investigated at 23°C and 950°C using a single edge notched specimen geometry with clamped ends. Crack growth and damage progression was monitored during the tests using optical microscopy, ultrasonic C-scans, and crack mouth opening displacement. Nextel610/AS was found to be notch sensitive, with net section failure stresses below the unnotched ultimate tensile strength. The failure mode was nonbrittle with considerable nonlinear deformation prior to and after the peak load at 23°C and 950°C. The effect of temperature on the notched strength was significant. Net section failure stress decreased 50% when temperature was increased from 23°C to 950°C. Observations of damage progression indicated that the reduction in notch strength with temperature was associated with a change in damage mechanism. Ultrasonic C-scans were found to be an effective method of monitoring damage progression. Ultrasonic attenuation ahead of the notch tip was correlated with surface matrix cracks and exposed fiber lengths on the fracture surface.

### 1. Introduction

Ceramic matrix composites (CMC) consisting of an oxide matrix and oxide fibers with no engineered fiber-matrix interphase are currently under consideration for high temperature aerospace applications due to their inherent resistance to oxidation. The CMC produced by General Electric Aircraft Engines (GEAE) consisting of alumina fibers and an 87% alumina-13% silica matrix (Nextel610/AS) exhibits excellent room temperature fatigue and tensile strength (170 MPa and 205 MPa respectively) [1, 2]. When tested at 1000°C, fatigue and tensile strength decreased by only 15% [1, 2]. Current component designs, however, include stress concentration sites such as bolted attachment points and cooling holes. Local stresses in these regions often exceed the proportional limit of the composite, thus acting as crack and damage initiation sites. Component design using Nextel610/AS composites will therefore require knowledge of the notched fracture behavior and damage progression at room temperature and expected service temperatures.

Fracture studies of other CMC systems [3-9] have shown that damage mechanisms such as multiple matrix cracking, fiber bridging and fiber pullout act to redistribute stresses in the vicinity of a notch. John et al. [3], Cady et al. [4] and Mall et al. [5] showed that Nicalon™ fiber reinforced glass matrix composites exhibit multiple matrix cracking around notches and holes resulting in notch insensitive behavior at room temperature. Fiber dominated CMC, including some C/C composites, show a nearly linear unnotched stress-strain response in the [0/90] orientation. However, increasing nonlinearity with increasing notch length was observed for edge notched specimens [8, 9]. For these composite systems, damage ahead of the notch was found to extend as a narrow zone normal to the notch plane. The damage zone effectively redistributed the stresses away from the notch tip, thus increasing fracture toughness at room

temperature. Similarly, the oxide/oxide CMC Nextel610/AS exhibits nearly linear unnotched stress-strain behavior [1, 2]. However, the notched behavior of Nextel610/AS has not been examined.

For CMC to be used effectively in aerospace applications with sites of stress concentration, the decrease in fracture toughness at elevated temperatures must be minimized. For most of the CMC systems studied thus far, the enhanced fracture toughness relies on the existence of a weak fiber/matrix interphase which allows fiber debonding and sliding during fracture. At elevated temperature, oxidation of the fiber/matrix interphase resulted in embrittlement of these composites as the matrix became tightly bonded to the fiber [3, 6]. Consequently, the fracture toughness at elevated temperature was significantly lower than that at room temperature [3, 7]. Oxidation occurring at the fiber/matrix interface and degradation of the fiber itself must therefore be prevented to maintain fracture toughness in these CMC systems. A new approach to enhanced CMC fracture toughness utilizes a very weak, porous matrix bonded to the fiber with no engineered interphase. Oxide based CMC are inherently oxidation resistant at elevated temperature and are expected to show damage tolerance when produced using a strong interface and weak matrix [10]. The limited experimental data available in the open literature on the notched fracture behavior of an oxide/oxide CMC is restricted to room temperature [11]. This paper discusses the results of a study of the fracture behavior and damage progression of an oxide/oxide composite (Nextel610/AS) at room temperature and 950°C.

## II. Material

The Nextel610/AS CMC used in this investigation was produced by GEAE under the trade name Gen IV. The Nextel610 fibers, produced by the 3M Company [10], consist of fine grained ( $<0.5 \mu\text{m}$ ) polycrystalline alpha alumina. These fibers were woven into an eight harness satin weave (8HSW) cloth. The resulting cloth consists of fibers primarily in the warp direction on one side of the ply and fill fibers on the other. The plies were warp aligned during lay-up, but alternating plies were rotated about the warp direction so that fill fibers were matched with fill fibers, warp fibers matched with warp fibers. This lay-up provides better nesting of the plies and minimizes panel warpage. The resulting panel contained primarily fill fibers on the exposed outer plies. The composite panel used in this study contained 12 plies. Sections of the Nextel610 cloth were prepregged with alumina powder and a silica forming polymer before stacking. No coating was applied to the fibers before prepregging. The laminate was then warm molded to produce the green state ceramic tile. Sintering the green tile in air at 1000°C removed the organic binders and produced a porous alumina-silica matrix. The resulting matrix contains approximately 87 wt.% alumina and 13 wt.% silica. Image analysis of polished cross sections (Fig. 1) was used to obtain a fiber volume fraction of 33%. Extensive microcracking present throughout the matrix is a result of the shrinkage which occurs during the pyrolysis processing. These microcracks are distributed throughout the interior matrix as well as on the specimen surface.

## III. Experimental Procedure

### (1) Test Procedure

Unnotched tension tests were conducted using an automated, servo-controlled, hydraulic, horizontal test system [13, 14]. The tests were conducted under load-line displacement control at a rate ( $\dot{\delta}$ ) of 0.05 mm/s. Specimen endpoint displacement was increased monotonically to specimen failure. Tension tests were conducted at 23 and 1000°C. Further discussion of the unnotched tension test procedures and results are described elsewhere [2].

Fracture tests were conducted using an automated, servo-controlled, hydraulic, horizontal test system [13, 14]. The single edge notched specimen geometry with clamped ends, MSE(T) [15] shown in Fig. 2, was used for all the tests. The specimen ends were rigidly

clamped resulting in rotationally constrained end conditions. The overall dimensions of the specimens were: width ( $W$ ) = 19.0 mm or 25.4 mm, thickness ( $B$ ) = 2.9 mm and height to width ratio ( $H/W$ ) = 4.0. The notches were cut using a diamond saw to produce an initial notch height of 0.4 mm, and length ( $a_0$ ) equal to  $0.2W$  for all specimens. Crack mouth opening displacement (CMOD) was measured continuously using a high resolution knife edge extensometer at room temperature and a high temperature extensometer with alumina rods at  $950^\circ\text{C}$ . Optical measurements of matrix crack extension were made on both sides of the specimen during testing.

## (2) Elevated Temperature Testing

Heating of the test specimen was achieved with closed-loop controlled, 4 zone quartz lamps. The heated section of the specimen was approximately 3 inches in length centered on the specimen notch. Slotted windows in the center of the quartz lamps allowed for visual inspection of crack growth from the notch tip during testing. Further details of the test equipment have been described elsewhere [13, 14].

Various methods of thermocouple attachment were investigated. The method which produced the most repeatable temperature measurements with minimal damage to the specimen surface was chosen for use in testing. Platinum-10%Rhodium, S-type, beaded thermocouples were first wire tied to the specimen with the thermocouple bead in contact with the specimen surface. A small drop of Ceramabond™ (Ceramabond 503, Aremco Products, Inc., 23 Snowden Ave., Ossining, NY 10562) ceramic adhesive was then placed over the thermocouple bead and spread to cover the bead surface. The adhesive was cured for 30 minutes at  $300^\circ\text{C}$  resulting in a hard, adhesive, insulating cover for the thermocouple bead while assuring contact with the specimen surface during testing. The adhesive was white in color, matching the color of the Nextel610/AS specimen, which eliminated temperature errors due to differential radiant heat absorption. The Ceramabond™ was also easily removed from the specimen surface after testing.

A thermal map of the temperature distribution across the specimen length, width and thickness was obtained using a notched Nextel610/AS specimen with  $W = 25.4$  mm and  $a_0 = 0.2W$ . The temperature variation was  $\leq \pm 2.9\%$  across the gage length, and  $\leq \pm 1.0\%$  through the thickness. During testing, 6 thermocouples were attached to the top and 1 to the bottom surfaces. Four thermocouples controlled the quartz lamp output and 3 monitored temperature near the notch plane.

## (3) Fracture Test Parameters

Fracture tests were conducted under load-line displacement control at a rate of 0.001 mm/s and 0.01 mm/s. During the tests conducted at 0.001 mm/s, load-line displacement was periodically held constant for crack length measurements. During this hold time, the specimen was also unloaded and reloaded to determine residual CMOD and changes in specimen compliance. The fracture test conducted at 0.01 mm/sec was loaded monotonically (without unloading loops or hold times) to specimen failure. Applied load, CMOD and load-line displacement ( $\delta$ ) were recorded continuously as a function of time during all tests. Whenever possible, specimens were unloaded and removed from the test machine after attaining the peak load for ultrasonic and optical evaluation. Mode I stress intensity factor ( $K_I$ ), and elastic modulus ( $E$ ), from specimen compliance ( $= \text{CMOD}/P$ ), were calculated using isotropic expressions [15] given by Eqn. (1). Assuming crack length ( $a$ ) equal to the saw-cut notch length, elastic modulus was calculated from the initial loading compliance below a far-field applied stress ( $\sigma_a$ ) = 15 MPa. Applied stress was calculated as  $\sigma_a = P/(BW)$  where  $P$  = applied load, and  $B$  and  $W$  are shown in Fig.2.

$$K_I = \sigma_a \sqrt{\pi a} F(a/W) \quad \text{and} \quad E = \frac{2\sigma_a a}{\text{CMOD}} G(a/W), \quad (1)$$

where  $F(a/W)$  and  $G(a/W)$  are given in [15].

#### (4) *Damage Characterization*

Ultrasonic C-scans of the test specimens were recorded before testing and during interrupted tests. The C-scans were obtained using a through transmission, reflector plate scanning technique described elsewhere [16, 17]. Each ultrasonic C-scan was calibrated, and referenced to a calibrated ultrasonic attenuation scale. During the C-scan, the ultrasonic signal passing through the specimen was acquired at regularly spaced x-y locations, digitized, and color coded. A 12.7 mm diameter, 10 MHz, 76 mm focused transducer produced by KB Aerotech was used to emit and receive the ultrasonic energy. The C-scan technique required immersion of the test specimen in water during the scan. After each C-scan, excess moisture was removed during a 1 hour bake out at 70°C. Zawada and Lee [2, 18] showed that water exposure did not result in a change in the mechanical behavior of Nextel610/AS.

Optical inspection of the notch tip region was performed on both sides of the specimen during testing. Due to the extensive preexisting matrix cracking on the specimen surface, the notch tip region appeared cracked before testing. Crack growth from the notch tip was identified as a clearly observable opening of a pre-existing surface crack (identified as the dominant crack), or the appearance of a new crack at the notch tip. Post test inspection of the crack growth and fracture surfaces was performed using optical and scanning electron microscopy (SEM). Specimens were sputter coated with gold/palladium before SEM imaging. Backscatter electron imaging was used to minimize charging effects and highlight microcracks. Destructive evaluation of interrupted test specimens was performed by sectioning and polishing using a diamond impregnated lapping film. Polishing the specimens with light pressure removed surface layers slowly enough to prevent damage to fibers within the underlying layers.

### IV. Results and Discussion

#### (1) *Notched Fracture Behavior*

The experimental results of the notched fracture tests are shown in Figs. 3-5 and summarized in Table I. Each experimental condition listed in the table represents a single test result. For each fracture test a low load ( $< 1.0$  kN) check out cycle was used to determine the initial loading compliance. Elastic modulus calculated using Eqn. (1) and the initial loading compliance ranged from 69-71 GPa for all fracture tests (Table I). No dependence of elastic modulus on temperature was observed.

The load-CMOD response for room temperature fracture tests conducted on 19.0 mm and 25.4 mm wide specimens is shown in Fig. 3. Unloading the specimen from applied loads within the initial linear region resulted in no residual CMOD or loop hysteresis. Beyond the linear region, loading behavior was increasingly nonlinear and associated with increasing residual CMOD ( $CMOD_{res}$ ) and measurable hysteresis in the unloading loops.

The onset of nonlinear loading behavior was determined by fitting a linear curve to the initial load/displacement data. Measured load deviation from the linear fit exceeding 5% was defined as the onset of nonlinear loading behavior. Fracture tests conducted at room temperature exhibited linear loading behavior up to an applied stress intensity factor ( $K_a$ ) = 6 MPa $\sqrt{m}$ , corresponding to an applied load,  $P = 2.8$  kN for the 25.4 mm wide specimen. Unloading the specimen from  $K_a$  levels above 6 MPa $\sqrt{m}$  resulted in measurable  $CMOD_{res}$  and hysteresis in the load-CMOD loops. Residual CMOD and unloading loop hysteresis increased with applied load up to the peak load. After reaching the peak load, CMOD continued to increase under increasing load-line displacement, while the applied load remained nearly constant (Fig. 3).

The stress intensity factor ( $K_{peak}$ ) based on the peak load and initial notch length was calculated to be 16.8 MPa $\sqrt{m}$  and 15.5 MPa $\sqrt{m}$  for the 19.0 mm and 25.4 mm wide specimens respectively. The 19.0 mm wide specimen failed abruptly after reaching a  $CMOD = 0.10$  mm. The 25.4 mm wide specimen reached the peak load when  $CMOD = 0.08$  mm and was removed

from the test frame when  $\text{CMOD} = 0.10$  mm for ultrasonic and optical evaluations. Although the current data is limited, the fracture results indicate that within the range of specimen widths examined, the effect of width on  $K_{\text{peak}}$  at room temperature is minimal.

The load versus CMOD responses for fracture tests conducted at 23°C and 950°C on 25.4 mm wide specimens are shown in Fig. 4. Unloading loops for the 23°C test were eliminated from Fig. 4 for clarity. Loading behavior at 950°C was linear to  $K_a = 4$  MPa $\sqrt{\text{m}}$  ( $P = 1.7$  kN) which is  $\approx 33\%$  lower than that at 23°C. Similar to the 23°C fracture test, unloading the specimen from applied loads within the initial linear region at 950°C resulted in no  $\text{CMOD}_{\text{res}}$  or loop hysteresis. Increase in applied load beyond the linear region resulted in sudden decrease in specimen compliance.

Nonlinear loading behavior can be compared for the two fracture tests by examining the residual  $\text{CMOD}_{\text{res}}$ . Figure 5 shows the  $\text{CMOD}_{\text{res}}$  after unloading the specimen from a maximum load with corresponding maximum CMOD ( $\text{CMOD}_{\text{max}}$ ). For the room temperature specimen,  $\text{CMOD}_{\text{res}}$  increased slowly as  $\text{CMOD}_{\text{max}}$  increased. Prior to the peak load,  $\text{CMOD}_{\text{res}}$  remained below 0.01 mm, corresponding to 13% of the  $\text{CMOD}_{\text{max}}$  at the peak load. This result is consistent with  $\text{CMOD}_{\text{res}}$  due primarily to distributed matrix cracking with minimal 0° fiber breakage. In contrast, the 950°C specimen showed a sudden rapid increase in  $\text{CMOD}_{\text{res}}$  prior to the peak load with values  $\approx 5\text{X}$  higher than that at room temperature. The sudden rapid increase in  $\text{CMOD}_{\text{res}}$  indicates a change in damage mode, consistent with observations of dominant crack growth discussed later in section 3. The increase in  $\text{CMOD}_{\text{res}}$  and dominant crack growth at 950°C are consistent with the onset of 0° fiber breakage. However, additional interrupted tests are required to determine if 0° fiber breakage occurred prior to the peak load at 950°C.

As a result of the enhanced nonlinear deformation prior to the peak at 950°C, a decrease in peak load  $\approx 50\%$ , compared to that at 23°C, was observed. The decrease in peak load corresponded to a decrease in  $K_{\text{peak}}$  from 16 MPa $\sqrt{\text{m}}$  at 23°C to 7.9 MPa $\sqrt{\text{m}}$  at 950°C. The higher  $\text{CMOD}_{\text{res}}$  at 950°C, and decrease in notch strength, indicated a change in damage mechanism from 23°C.

## (2) Effect of Loading Rate on 950°C Fracture Behavior

The effect of loading rate and unloading loops on the fracture behavior at 950°C was examined by conducting an additional fast-rate monotonic fracture test. The load versus CMOD responses for the slow and fast rate tests are shown in Fig. 4. The load-line displacement rate ( $\dot{\delta}$ ) used during the fracture test with unloading loops was  $\dot{\delta} = 0.001$  mm/s, resulting in a total elapsed time to peak load ( $t_p$ ) of 668 s. The test without unloading loops was conducted at a rate of  $\dot{\delta} = 0.01$  mm/s, resulting in  $t_p = 15$  s. As shown in Fig. 4, the overall load versus CMOD response was nearly the same for both tests, indicating that loading rate and unloading loops had no effect on the peak stress intensity factor or overall fracture behavior. However, a complete assessment of time at temperature effects on the notched behavior must be examined under sustained load conditions.

## (3) Damage Accumulation

### Ultrasonic Evaluation

Due to the extensive pre-existing matrix cracks present throughout the Nextel610/AS composite, characterization of damage accumulation based on surface matrix crack growth alone was determined to be inappropriate. A nondestructive ultrasonic C-scan technique [16, 17] was therefore adapted for use with the Nextel610/AS composite system [19]. Some of the Nextel610/AS specimens were scanned prior to testing. Due to the extensive pre-existing matrix cracks and porosity C-scans of the untested composite showed regions of varying

ultrasonic attenuation. These regions typically varied from 0-50% attenuation, with isolated regions of high porosity which attenuated the signal up to 75%. These regions were consistent and reproducible across a given specimen. C-scans of specimens which had been loaded to sufficiently high stress, showed levels of ultrasonic attenuation near the notch tip region which exceeded 75%. Specimens which were tested and showed increased attenuation in the notch tip region showed no change in the level of ultrasonic attenuation of the undamaged regions far from the notch tip. Therefore, attenuation of the ultrasonic signal exceeding 75% was identified as that which indicated damage accumulation during testing. For clarity in this publication, the original color scale used for the C-scans, was mapped into the gray scale image shown in Fig. 8. With reference to the gray scale, white indicates that the ultrasonic signal through the specimen was attenuated less than 75%, gray shades indicate attenuation of 75-100%. Further discussion of the ultrasonic test technique and detailed color C-scan images can be found in Ref. [19].

The room temperature fracture tests were conducted with periodic unloading, but without interruption until clearly beyond the peak load. Optical inspection of the notch tip region during testing did not reveal the formation of either new matrix cracks or a dominant matrix crack. The lack of dominant matrix crack extension prior to the peak load correlated with the small  $CMOD_{res}$  after unloading (Fig. 5). Although  $CMOD_{res}$  increased more rapidly after the peak load, clear dominant surface crack growth was not observed. However, nonlinear loading behavior prior to and after the peak load indicated that a progressive damage mechanism was operative. Therefore, subsurface damage was examined using ultrasonic C-scans. The ultrasonic C-scan of the specimen after the peak load showed a region of enhanced ultrasonic attenuation approximately 10 mm in length and 10 mm in height (Fig. 6a). The extent of ultrasonic attenuation indicated that the damage progression from the notch tip at room temperature was distributed away from the notch plane, consistent with the absence of primary crack growth from the notch.

During the 950°C fracture test with periodic unloading, optical inspection of the notch tip region first identified the formation of a dominant matrix crack at an applied load of 3.0 kN. Unloading the specimen from this applied load resulted in the significant  $CMOD_{res}$  (Fig. 5). Increasing load-line displacement resulted in extension of the dominant crack as it grew and linked with other preexisting surface matrix cracks. When the test was stopped, the continuous matrix crack extension from the notch tip was equal to 9 mm (Fig. 6c). Fig. 6b shows the corresponding ultrasonic C-scan at the same point of unloading. The region of ultrasonic attenuation was 5 mm in height and extended 11 mm beyond the notch, slightly longer than the surface matrix crack extension. The dominant crack extension at 950°C was associated with a more narrow damage zone compared to that observed at room temperature.

Fracture surface profiles of the 23 and 950°C specimens are shown in Fig. 7. Note that the specimen in Fig. 7a corresponds to that in Fig. 6a, and the specimen in Fig. 7b was monotonically loaded to failure as shown in Fig. 4. The 23°C fracture specimen exhibited fiber bundles which extend 2-3 mm in either direction from the notch plane (Fig. 7a). In contrast, fibers extended a maximum of 1.0 mm from the crack plane of the fracture surface on the 950°C specimen (Fig. 7b). These relative fiber lengths are consistent with the C-scan attenuation regions which indicated a damage zone which was more concentrated in the notch plane at 950°C. For both temperatures the height of the C-scan damage zone is approximately 2X larger than the maximum length of exposed fibers. This result can be attributed to matrix damage which extends beyond the point where fiber breakage occurs. Hence, fibers do not necessarily break at the end of the damage zone, and exposed fiber lengths on the fracture surface underestimate the extent of damage above and below the notch plane.

#### Observed Damage Modes

Micrographs of the room temperature specimen fracture surface are shown in Fig. 8. A cross-sectional view of the crack growth from the machined notch tip showed the primary failure

plane advanced from the notch along 90° tows and matrix rich regions (Fig. 8a). Multiple matrix cracks *within* the 90° tows allowed those fibers to be pulled away from the fracture surface at the notch tip and cannot be seen in Fig. 8a. The 0° fiber tows extend from the failure plane as fiber bundles. Farther from the failure plane, the bundles separated into individual fibers with uncorrelated fiber failure locations.

Matrix cracking throughout the 90° fiber tows, resulted in long unbroken lengths of exposed 90° fibers and a peeling type failure mode. This damage mode lead to disintegration of the 90° tows (Fig. 8b and 7a). Matrix degradation *within* 90° tows was also observed above and below the primary failure plane. The distributed damage resulting from degradation of the matrix *within* 90° tows resulted in the enhanced ultrasonic attenuation away from the notch plane in the room temperature specimen [19, 20].

The observed damage indicated that crack growth from degraded 90° tows and pre-existing matrix cracks was dissipated in the crack plane by the 0° fiber tows as a whole. Near the primary crack plane, broken matrix remained attached to the fiber tows as shown in Fig. 8c. Away from the crack plane, matrix crack growth parallel to individual fibers further promoted energy dissipation. This mechanism of stress redistribution is in contrast to the debonding/sliding mechanism operating in CMC with an engineered interphase. The matrix remaining within the tow >1 mm away from the primary failure plane was effectively disintegrated as fibers broke during the final fast fracture. As a result of the matrix disintegration, no matrix sockets were observed on the fracture surfaces as are observed in CMC which exhibit a fiber/matrix sliding mechanism. The absence of sockets is similar to the observations of damage in an all oxide CMC by Levi, et al. [11]. As a result of matrix cracking and disintegration along 0° fibers, exposed fibers far from the primary crack plane are relatively smooth and nearly devoid of matrix (Fig. 8d). These damage mechanisms associated with extensive matrix cracking, result in redistribution of stresses at the notch tip, thus decreasing notch sensitivity and increasing fracture toughness at room temperature.

Observations of surface and subsurface damage occurring at 950°C were obtained from fracture surfaces and polished sections of two specimens. The fracture surface images were obtained from the specimen loaded monotonically to failure. The polished sections were obtained from the specimen shown in Fig. 6c, which was unloaded after reaching the peak load. Fig. 9a shows a cross-sectional view of the machined notch tip in the unloaded specimen. The micrograph shows that the primary failure plane grew from the notch within the matrix rich regions and 90° tows. The residual crack opening displacement ( $COD_{res}$ ) within the 90° tows is clearly seen in the micrograph. The average 90° tow  $COD_{res} \approx 40 \mu m$ , which is comparable to the  $CMOD_{res}$  after final unloading = 42  $\mu m$  (Fig. 5). A cross-sectional view of the notch tip region of the failed specimen is shown in Fig. 9b. As observed on the unloaded specimen, crack growth within the 90° tows and matrix rich regions was restricted to a single plane. However, both micrographs in Fig. 9 show that the primary crack was initially deflected in the notch plane by matrix cracking along 0° tows. This initial crack deflection allowed 0° fiber failure to occur away from the crack plane. Unlike the room temperature specimen however, distributed matrix cracking *within* both the 0° and 90° tows was greatly reduced. Within the 0° tows, the lack of distributed matrix cracking along 0° fibers resulted in failure locations significantly closer to the crack plane than at 23°C. Within the 90° tows, individual fibers remained bonded to the matrix and were broken in the crack plane as the crack advanced (Fig. 9b and 7b). Thus, individual 90° fibers were not pulled away from the crack plane as was observed on the room temperature fracture surface. Similarly, polished sections of the unloaded specimen showed matrix degradation within 90° fiber tows was limited. Thus, the lack of distributed matrix cracking between fibers *within* the 0 and 90° tows at 950°C resulted in a change in damage mechanism from that observed at 23°C.

Further details of the 0° tow behavior at 950°C were obtained by closer examination of crack propagation from the notch tip. Figure 10 shows the notch tip region of the specimen in

Fig. 6c after polishing the specimen surface to remove the top matrix layer and some of the 90° fibers. At 950°C, matrix cracking between fibers within the 0° tows was minimal, resulting in 0° fibers breaking as bundles. Broken 0° fibers were observed along the entire length of the surface crack. A comparison of Fig. 8c and 10 shows the differences in 0° fiber bundle behavior at 950°C and 23°C. At 23°C, multiple matrix cracking *within* fiber tows allowed individual fibers to fail independently. This damage mode resulted in fiber failure far from the primary crack plane and long exposed individual 0° fibers on the fracture surface. In contrast, at 950°C, energy dissipation through matrix cracking along individual 0° fibers *within* the tow did not occur. As a result, 0° fibers were broken as bundles near the crack plane as the crack propagated through the 0° tow. The observed differences in matrix cracking behavior at 23 and 950°C may be related to changes in the alumina-silica matrix with temperature. Glassy grain boundary phases have been shown to affect the behavior of alumina at temperatures near 1000°C [22, 23]. Further studies are currently underway to investigate the mechanisms.

The assessment of damage progression in Nextel610/AS discussed above, indicated there was a change in damage mode as temperature was increased from 23 to 950°C. The lack of distributed damage at 950°C resulted in a higher stress concentration at the notch tip than at room temperature, and the propagation of a single dominant crack. This change in damage mode, coupled with the decrease in fiber strength at 950°C ( $\approx 15\%$ ) [21], resulted in significant decrease ( $\approx 50\%$ ) in apparent fracture toughness.

The applicability of linear elastic fracture mechanics (LEFM) to characterize the notched behavior has not been established for the present CMC system. The large post-peak damage zone size indicated in the C-scans (Fig. 6) implies LEFM may not be applicable. Further interrupted testing is required to determine damage progression prior to the peak load. The damage zone size at the peak load can then be used to assess the applicability of LEFM. In addition, variation in  $K_{peak}$  with notch length and specimen size must be examined to determine the applicability of  $K_{peak}$  to predict failure. However, independent of LEFM, notch sensitivity of the Nextel610/AS system can be studied in terms of the net section strength ( $\sigma_n$ ) as discussed in the next section.

#### (4) Comparison of Notched and Unnotched Behavior

Table I summarizes the results for the notched fracture tests and unnotched tensile tests [1, 2]. The elastic moduli of 73 GPa and 77 GPa at 23°C and 1000°C, respectively, were close to the average value of 70 GPa for the notched specimens. The unnotched tensile stress-strain response is shown in Fig. 11. At room temperature the tensile behavior was nearly linear to the ultimate failure stress (UTS) (Fig. 11). In contrast, the notched specimens exhibited nonlinear loading behavior prior to the peak stress, and non-brittle failure after reaching the peak load (Fig. 4). The unnotched tensile response at 1000°C was slightly nonlinear before abrupt failure at the ultimate stress (Fig. 11). This is in sharp contrast to the notched fracture behavior at 950°C which resulted in extensive nonlinear loading prior to and after reaching the peak load.

The net section failure strength ( $\sigma_n$ ) of the notched specimens was significantly less than the UTS (Table 1). At room temperature, the average  $\sigma_n$  was 138 MPa; 34% lower than the unnotched UTS of 208 MPa. At 950°C,  $\sigma_n$  was 62 MPa; 65% lower than the UTS at 1000°C of 176 MPa. Thus, notch sensitivity was exhibited at 23 and 950°C. The notched strength decreased  $\approx 50\%$  as temperature was increased from 23 to 950°C. In contrast, the unnotched UTS decreased by only 15% as temperature was increased from 23 to 1000°C. Hence, the relative decrease in notch strength with increasing temperature was significantly greater than the corresponding decrease in unnotched tensile strength. The time to peak stress,  $t_p \approx 9$  s in both tensile tests, was close to  $t_p \approx 15$  s in the notched fracture test without unloading loops. A similar time to peak stress in the tension and fracture tests implies that the



observed decrease in fracture toughness between 23°C and 950°C was not due to time at temperature.

The room temperature unnotched tensile specimen fracture surfaces showed that failure was associated with interply delamination and 0° fiber failure far from the fracture plane (Fig. 12a). The absence of a stress concentration in the unnotched specimen distributed the applied stress across the entire width and gage length allowing the composite plies to fail on different planes. Examination of the 0° fiber tows on the fracture surface showed that close to the ply failure plane matrix remained attached to the fibers (Fig. 12c). This is similar to the observed failure features near the crack plane of the notched specimen (Fig. 8c). Far from the ply failure plane, relatively smooth fiber surfaces nearly devoid of matrix were observed, similar to the notched specimen (Fig. 12c and Fig. 8d). The smooth appearance of fibers in both the notched and unnotched specimens is a direct result of matrix cracking and disintegration during fracture, not due to a debonding/sliding mechanism as occurs in CMC with an engineered interphase. Multiple matrix cracking within the 90° fiber tows in the unnotched specimen resulted in long exposed 90° fiber lengths, similar to the notched specimen (Fig. 12a and Fig. 8b). Although overall features of the fracture surfaces are similar in the notched and unnotched specimens, exposed 0° fiber lengths were considerably longer (2-3X) in the unnotched tension specimen.

Unnotched tensile failure at 1000°C resulted in a more localized fracture zone with 0° fiber breaks closer to the crack plane than at 23°C (Fig. 12b). Similar to the notched specimen at 950°C, matrix cracks within 90° tows were restricted to a single plane. Matrix remained bonded to the fibers resulting in 90° fiber failure within the crack plane (Fig. 9b and Fig. 12d). Although the failure locations of exposed 0° tows were close to the failure plane, fracture was not planar. This result indicated that propagation of pre-existing matrix cracks was initially deflected by the 0° tows. In contrast to the observed room temperature fracture behavior, close examination of the 0° fiber tows showed no evidence of the extensive matrix cracking within the tows. As a result of the change in matrix cracking behavior at 1000°C, most fibers failed as bundles rather than individual fibers. These observations showed that the elevated temperature fracture surfaces for notched and unnotched specimens exhibited similar features. Hence, the average length of exposed 0° fibers was also similar  $\approx 0.5$  mm. Although the fracture surfaces of the notched and unnotched specimens exhibited similar features, the overall tensile behavior was dramatically different for the two test geometries. Apparently the lack of matrix cracking within fiber tows at temperatures near 1000°C increased notch sensitivity without greatly affecting unnotched tensile strength.

#### IV. SUMMARY AND CONCLUSION

Fracture tests conducted at 23 and 950°C showed that the Nextel610/AS composite was notch sensitive. The net section strength of the notched specimens was  $\approx 0.65$  and  $0.35$  of UTS at 23°C and 950°C respectively. The net sections strength decreased 50% with an increase in temperature from 23°C to 950°C. Fracture behavior was nonlinear prior to the peak load. The post-peak behavior was characterized by non-brittle failure with considerable retained load bearing capacity. Load-line displacement rate and unloading loops were found to have no effect on the fracture behavior at 950°C. Exposed fiber lengths on the fracture surface were reduced at elevated temperature with fiber bundle failure significantly closer to the primary crack plane than at room temperature. At room temperature individual fibers failed away from the matrix crack plane with distributed matrix cracking within the 0° and 90° fiber tows. A comparison between the notched fracture behavior and the unnotched tensile response of Nextel610/AS showed that the effect of temperature is significantly different.

Ultrasonic C-scans were shown to be an effective method of measuring the extent of damage accumulation. Post-peak room temperature test specimens showed no evidence of damage on the specimen surface, however, the attenuated zone indicated by the C-scan provided a measure of the extent and distribution of damage. Dominant matrix crack growth

was observed on the specimen surface during testing at 950°C. The surface crack length correlated well with the length of the C-scan damage zone. C-scans indicated that, at 950°C, the height of the damage zone was approximately half that at 23°C. The reduction in damage zone height correlated with the reduction in exposed 0° fiber lengths on fracture surfaces.

Observations of damage on fracture surfaces and polished sections revealed a change in matrix crack behavior between 23 and 950°C. At 23°C, extensive matrix cracking *within* fiber tows allowed for stress redistribution around the notch. Evidence of this damage mechanism was indicated by exposed 0° fiber lengths, matrix cracking between fibers, and the extent of ultrasonic C-scan attenuation. At 950°C, a change in failure mode to self-similar crack growth occurred. Examinations of exposed 0° fibers revealed at 950°C matrix cracking between fibers *within* the tows was greatly reduced resulting in a higher stress concentration in the notch tip area. Exposed 0° fiber lengths and the extent of ultrasonic C-scan attenuation verified that the damage zone was confined to the notch plane at 950°C. Crack growth beyond the peak load was characterized by fiber breakage. Although load-bearing capacity decreased slightly after the peak load, clearly fiber breakage in the crack wake did not immediately result in catastrophic failure at 950°C.

**Acknowledgments:** This research was conducted at the Materials and Manufacturing Directorate, Air Force Research Laboratory (AFRL/MLLN), Wright-Patterson Air Force Base, OH 45433-7817. V. A. Kramb was supported in part by the Dayton Area Graduate Studies Institute (DAGSI) and in part by AFOSR/AASERT Program (Contract No. F49620-95-1-0500). L. P. Zawada received partial financial support from Dr. W. S. Coblenz at DARPA under contract no: in-house and order number A565.

## References

1. L. P. Zawada and S. S. Lee, "The Effect of Hold Times on the Fatigue Behavior of an Oxide/Oxide Ceramic Matrix Composite," Thermal and Mechanical Test Methods and Behavior of Continuous-Fiber Ceramic Matrix Composites, ASTM STP 1309, Michael G. Jenkins, Stephen T. Gonczy, Edgar Lara-Curzio, Noel E. Ashbaugh, and Larry P. Zawada, Eds., American Society for Testing and Materials, Philadelphia, PA, 1996.
2. Lee, S. S., Zawada, L. P., Hay, R. S. and Staehler, J., "High Temperature Mechanical Behavior and Characterization of an Oxide/Oxide Composite," submitted for publication *J. Am. Ceram. Soc.*, Oct. 1998.
3. R. John and N. E. Ashbaugh, "Fatigue Crack Growth in Ceramics and Ceramic Matrix Composites"; pp 28-50 in *Cyclic Deformation, Fracture and Nondestructive Evaluation of Advanced Materials*, ASTM STP 1157. Edited by M.R. Mitchell and O. Buck, American Society for Testing and Materials, Philadelphia, PA, 1992.
4. C. M. Cady, T. J. Mackin and A. G. Evans, "Silicon Carbide/Calcium Aluminosilicate: A Notch -Insensitive Ceramic-Matrix Composite," *J. Am. Ceram. Soc.*, **78** [1] 77-82 (1995).
5. S. Mall, D. E. Bullock and J. J. Pernot, "Tensile Fracture Behaviour of Fibre-Reinforced Ceramic-Matrix Composite with Hole," *Composites*, **25** [3] 273-242 (1994).
6. A. G. Evans, F. W. Zok, R. M. McMeeking and Z. Z. Du, "Models of High-Temperature, Environmentally Assisted Embrittlement in Ceramic-Matrix Composites," *J. Am. Ceram. Soc.*, **79** [9] 2345-52 (1996).
7. R. F. Allen, C. J. Beevers and P. Bowen, "Fracture and Fatigue of a Nicalon/CAS Continuous Fibre-Reinforced Glass-Ceramic Matrix Composite," *Composites*, **24** [2] 150-156 (1993).
8. F. E. Heredia, S. M. Spearing, T. J. Mackin, M. Y. He, A. G. Evans, P. Mosher, and P. Brondsted, "Notch Effects in Carbon Matrix Composites," *J. Am. Ceram. Soc.*, **77** [11] 2817-27 (1994).

9. K. R. Turner, J. S. Speck, and A. G. Evans, "Mechanisms of Deformation and Failure in Carbon-Matrix Composites Subject to Tensile and Shear Loading," *J. Am. Ceram. Soc.*, **78** [7] 1841-48 (1995).
10. W. C. Tu, F. F. Lange and A. G. Evans, "Concept for a Damage-Tolerant Ceramic Composite with "Strong" Interfaces," *J. Am. Ceram. Soc.*, **79** [2] 417-24 (1996).
11. C. G. Levi, J. Y. Yang, B. J. Dalgleish, F. W. Zok and A. G. Evans, "Processing and Performance of an All-Oxide Ceramic Composite," *J. Am. Ceram. Soc.*, **81** [8] 2077-86 (1998).
12. 3M Company Product Data Sheet, 3M Ceramic Fiber Products, 3M Center-Building 207-1W-11, St. Paul, MN 55144-1000.
13. G. A. Hartman and D. J. Buchanan, "Methodologies for Thermal and Mechanical Testing of TMC Materials," Characterization of Fibre Reinforced Titanium Matrix Composites, 77<sup>th</sup> Meeting of the AGARD Structures and Materials Panel, AGARD Report 796, Bordeaux, France, 27-28 September 1993.
14. G. A. Hartman S. M. Russ, "Techniques for Mechanical and Thermal Testing of Ti3Al/SCS-6 Metal Matrix Composites," *Metal Matrix Composites: Testing, Analysis, and Failure Modes, ASTM STP 1032*, Edited by W. S. Johnson, American Society for Testing and Materials, Philadelphia, PA, 1989.
15. R. John and B. Rigling, "Effect of Height to Width Ratio on K and CMOD Solutions For A Single Edge Cracked Geometry With Clamped Specimen Ends," *Eng. Frac. Mech.* **60** [2] 147-56 (1997).
16. D. A. Stubbs and G. S. Clemons, "Screening Metal Matrix Composites Using Ultrasonic Reflector Plate and X-ray Radiography Nondestructive Evaluation Techniques," in *Characterization of Titanium Matrix Composites, Vol. VII - Mechanical Behavior and Damage Tolerance of TMCs*, NASP Technical Memorandum 1199 (1995).
17. D. A. Stubbs and G. S. Clemons, "Guidelines for Standardizing the Gain of Ultrasonic Inspection Systems used to Acquire Ultrasonic Reflector Plate C-scans," in *Characterization of Titanium Matrix Composites, Vol. VII - Mechanical Behavior and Damage Tolerance of TMCs*, NASP Technical Memorandum 1199 (1995).
18. L. P. Zawada and S. S. Lee, "Evaluation of Four CMCs for Aerospace Turbine Engine Divergent Flaps and Seals," *Ceram. Eng. Sci. Proc.*, **16** [4] 337-39 (1995).
19. V. Kramb, R. John and D. Stubbs, to be submitted for publication, *Mat. Eval.*, (1998).
20. V.A. Kramb and R. John, "Room Temperature Fracture Behavior of an Oxide/Oxide CMC," to be submitted: *J. Comp. Sci. Tech.*, (1998).
21. D. M. Wilson, S. L. Lieder and D. C. Lueneburg, "Microstructure and High Temperature Properties of Nextel 720 Fibers," *Ceram. Eng. Sci. Proc.*, **16** [5] 1005-14 (1995).
22. K. Y. Donaldson, A Venkateswaran and D. P. H. Hasselman, "Observations on the Crack-Enhanced Creep-Fracture of a Polycrystalline Alumina with a Glassy Grain-Boundary Phase," *J. Mat. Sci.* **27** [16] 4501-10 (1991).
23. S. R. Choi and V. Tikare, "Crack Healing of Alumina with a Residual Glassy Phase: Strength, Fracture Toughness and Fatigue," *Mat. Sci. Eng.* **A171** 77-83 (1993).

Table I. Notched and Unnotched Test Results

Temperature (°C)	Width (mm)	$\dot{\delta}$ (mm/s)	Elastic Modulus (GPa)	Unnotched Peak Stress (MPa)	Notched Peak Net Section Stress (MPa)	Peak Stress Intensity Factor (MPa $\sqrt{m}$ )	Time to Peak Stress (s)
<u>Unnotched</u>							
23*	10.1	0.05	73	205			9.4
1000*	13.6	0.05	77	173			8.9
<u>Notched</u>							
23	19.0	0.001	69		151	16.8	736
23	25.4	0.001	71		124	15.5	665
950	25.4	0.001	71		62	7.9	668
950	25.4	0.01	70		62	7.9	15

\* Reported values are an average from 3 tests conducted at 23°C and 2 tests at 1000°C

## Figures

- Figure 1 Nextel610/AS composite polished section optical micrograph.
- Figure 2 Schematic of single edge notched specimen with clamped ends, MSE(T).  $W = 19.0$  &  $25.4$  mm,  $B = 2.9$  mm and  $H/W = 4$ .
- Figure 3 Load versus crack mouth opening displacement for load-line displacement controlled fracture tests at room temperature,  $W = 19.0$  and  $25.4$  mm.
- Figure 4 Effect of temperature, loading rate and unloading loops on the load versus crack mouth opening displacement response for load-line displacement controlled fracture tests,  $W = 25.4$  mm.
- Figure 5 Effect of temperature on residual CMOD after unloading from a maximum load with corresponding  $CMOD_{max}$ .  $CMOD_{max}$  at the peak load is also indicated on the plot.
- Figure 6 (a) Ultrasonic C-scan of entire gage section, room temperature specimen. (b) Ultrasonic C-scan of entire  $950^{\circ}C$  specimen gage section. The saw-cut notch region is indicated by the solid white bar in both C-scans. (c) Optical micrograph of  $950^{\circ}C$  fracture test specimen unloaded after peak load.
- Figure 7 Optical fracture surface profiles for specimens tested at (a)  $23^{\circ}C$  and (b)  $950^{\circ}C$  monotonically loaded to failure.
- Figure 8 Scanning electron micrographs of room temperature fracture surface. (a) cross-sectional view of machined notch tip (b) top view of fracture surface ( $15^{\circ}$  tilt from normal) (c)  $0^{\circ}$  fibers near matrix crack plane (d)  $0^{\circ}$  fibers  $\approx 1$  mm from primary crack plane.
- Figure 9 Cross-sectional view of machined notch tip region in  $950^{\circ}C$  specimens: (a) interrupted after the peak load (b) monotonically loaded to failure.
- Figure 10 Notch tip region of  $950^{\circ}C$  specimen shown in Fig. 6c, after removing the top matrix layer and some  $90^{\circ}$  fibers. Failed  $0^{\circ}$  fibers were identified along the length of the dominant crack.
- Figure 11 Tensile stress/strain response for unnotched Nextel610/AS at  $23^{\circ}C$  and  $1000^{\circ}C$ .
- Figure 12 Nextel610/AS unnotched tension fracture surfaces: (a)  $23^{\circ}C$  (b)  $1000^{\circ}C$  and details of matrix and  $0^{\circ}$  fiber behavior (c)  $23^{\circ}C$  (d)  $1000^{\circ}C$ .

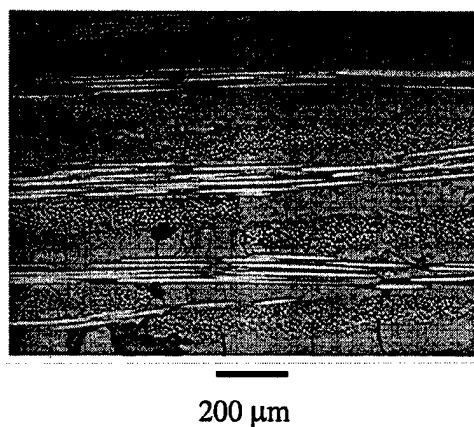


Figure 1. Nextel610/AS composite polished section optical micrograph.

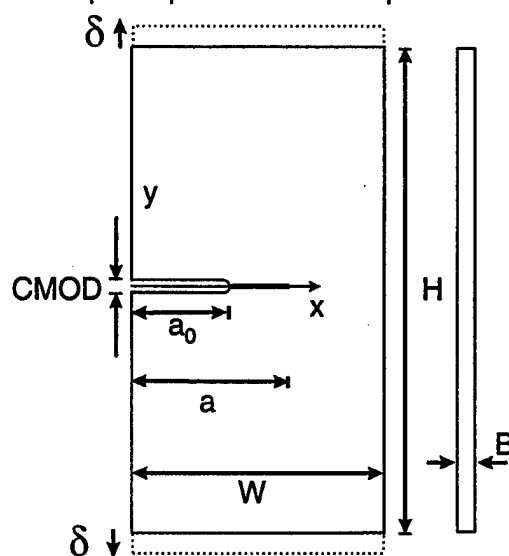


Figure 2. Schematic of single edge notched specimen with clamped ends, MSE(T).  $W = 19.0$  &  $25.4$  mm,  $B = 2.9$  mm and  $H/W = 4$ .

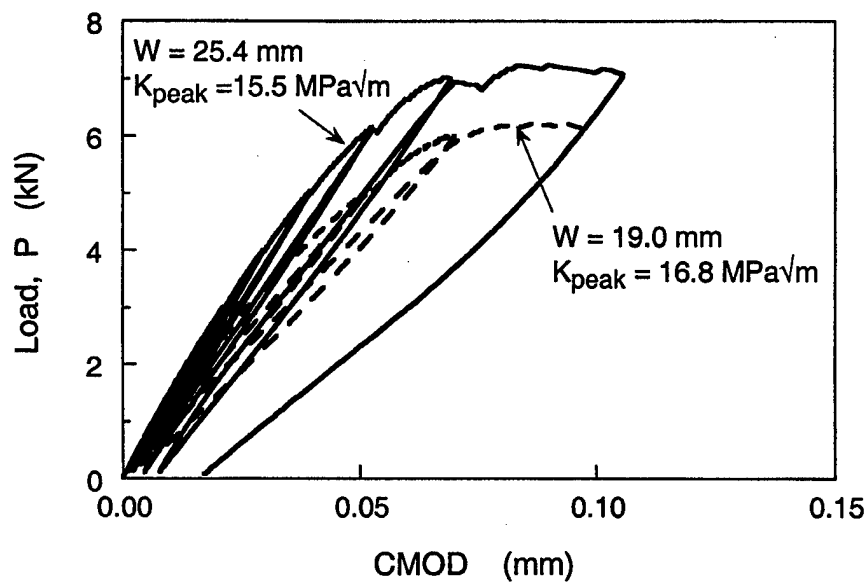


Figure 3. Load versus crack mouth opening displacement for load-line displacement controlled fracture tests at room temperature,  $W = 19.0$  and  $25.4$  mm.

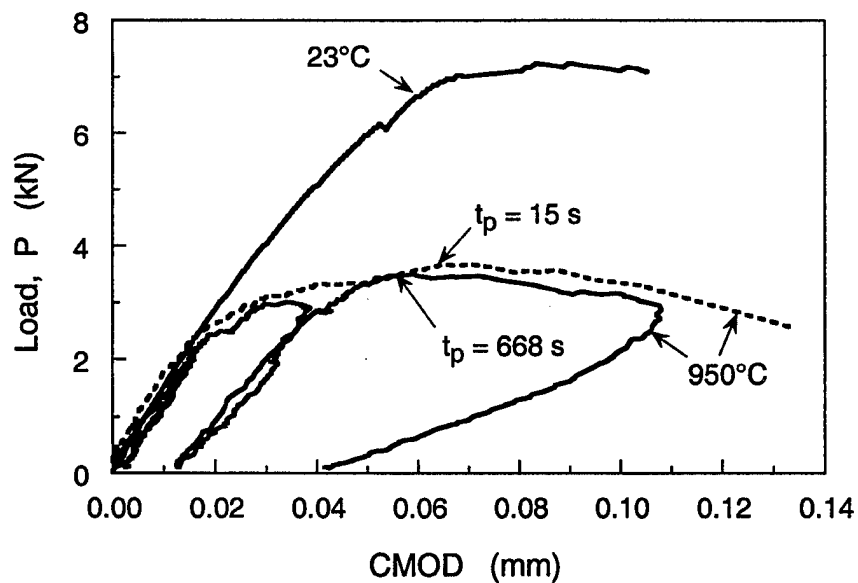


Figure 4. Effect of temperature, loading rate and unloading loops on the load versus crack mouth opening displacement response for load-line displacement controlled fracture tests,  $W = 25.4$  mm.

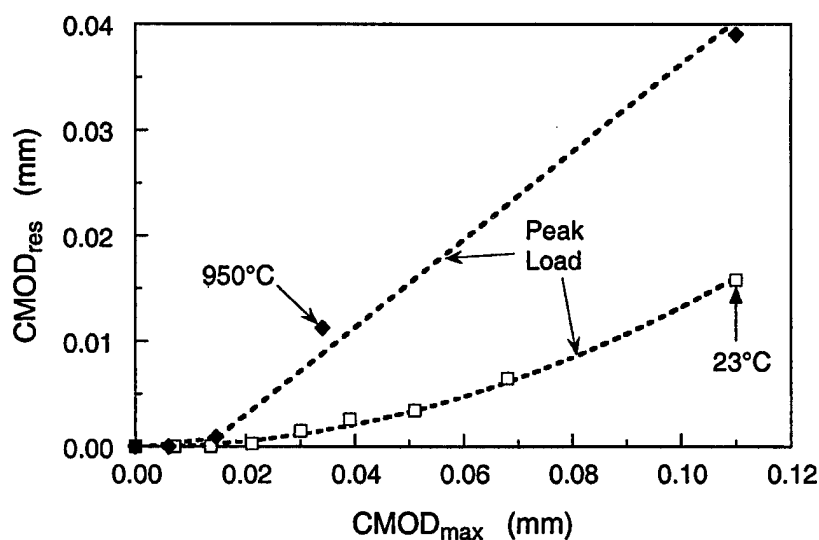


Figure 5. Effect of temperature on residual CMOD after unloading from a maximum load with corresponding  $CMOD_{max}$ .  $CMOD_{max}$  at the peak load is also indicated on the plot.

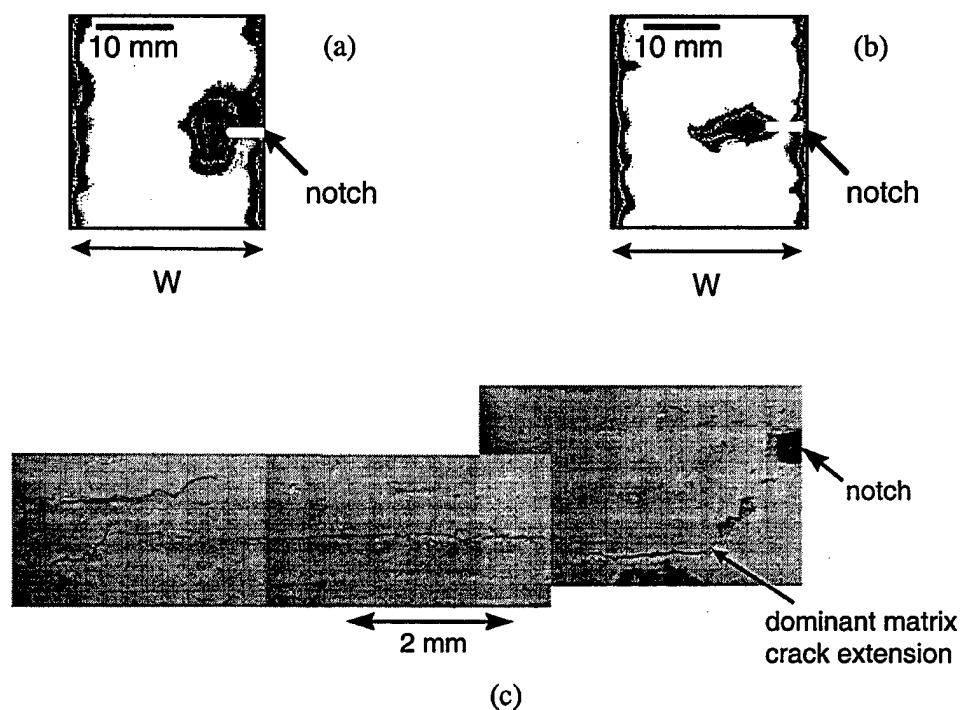
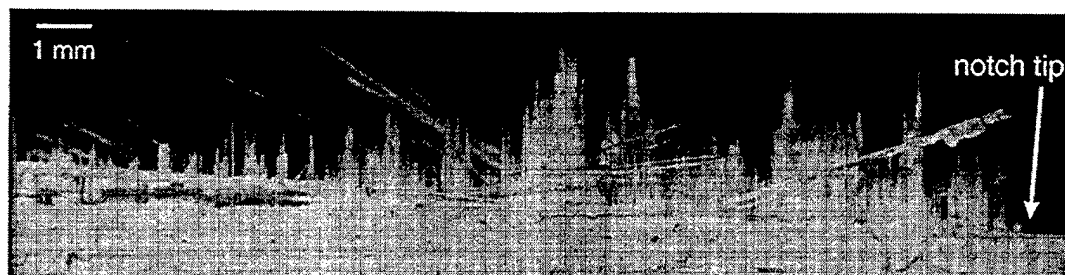
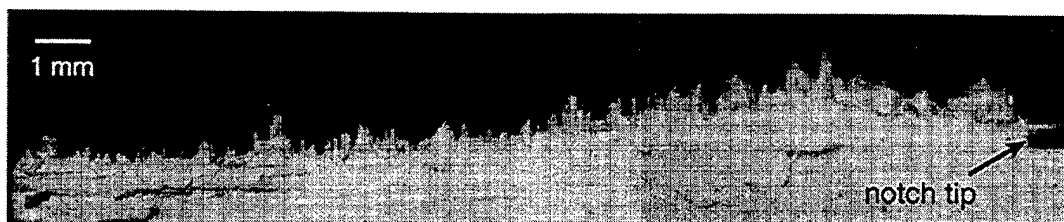


Figure 6. (a) Ultrasonic C-scan of entire gage section, room temperature specimen. (b) Ultrasonic C-scan of entire 950°C specimen gage section. The saw-cut notch region is indicated by the solid white bar in both C-scans. (c) Optical micrograph of 950°C fracture test specimen unloaded after peak load.





(a)



(b)

Figure 7. Optical fracture surface profiles for specimens tested at (a) 23°C and (b) 950°C monotonically loaded to failure.

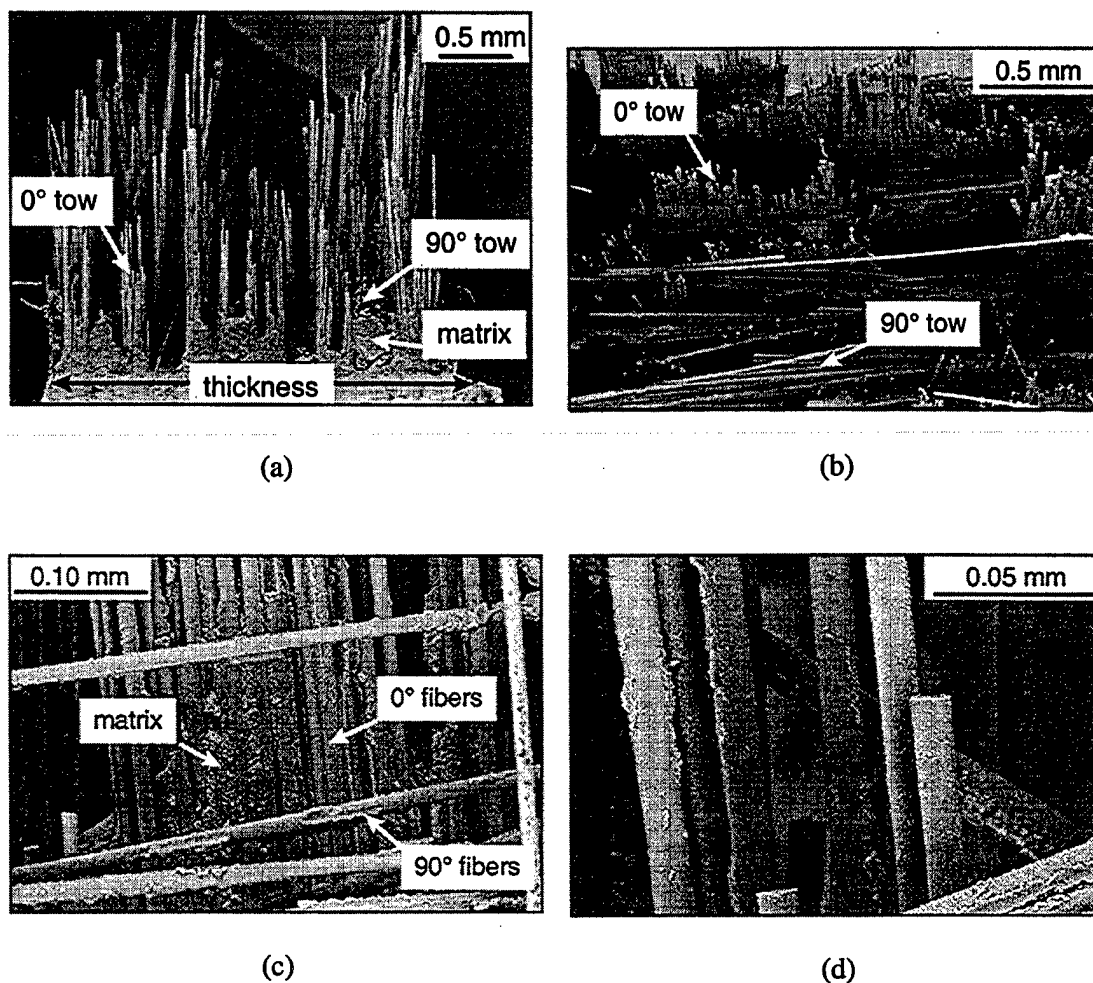


Figure 8. Scanning electron micrographs of room temperature fracture surface. (a) cross-sectional view of machined notch tip (b) top view of fracture surface (15° tilt from normal) (c) 0° fibers near primary crack plane (d) 0° fibers  $\approx$  1 mm from primary crack plane.

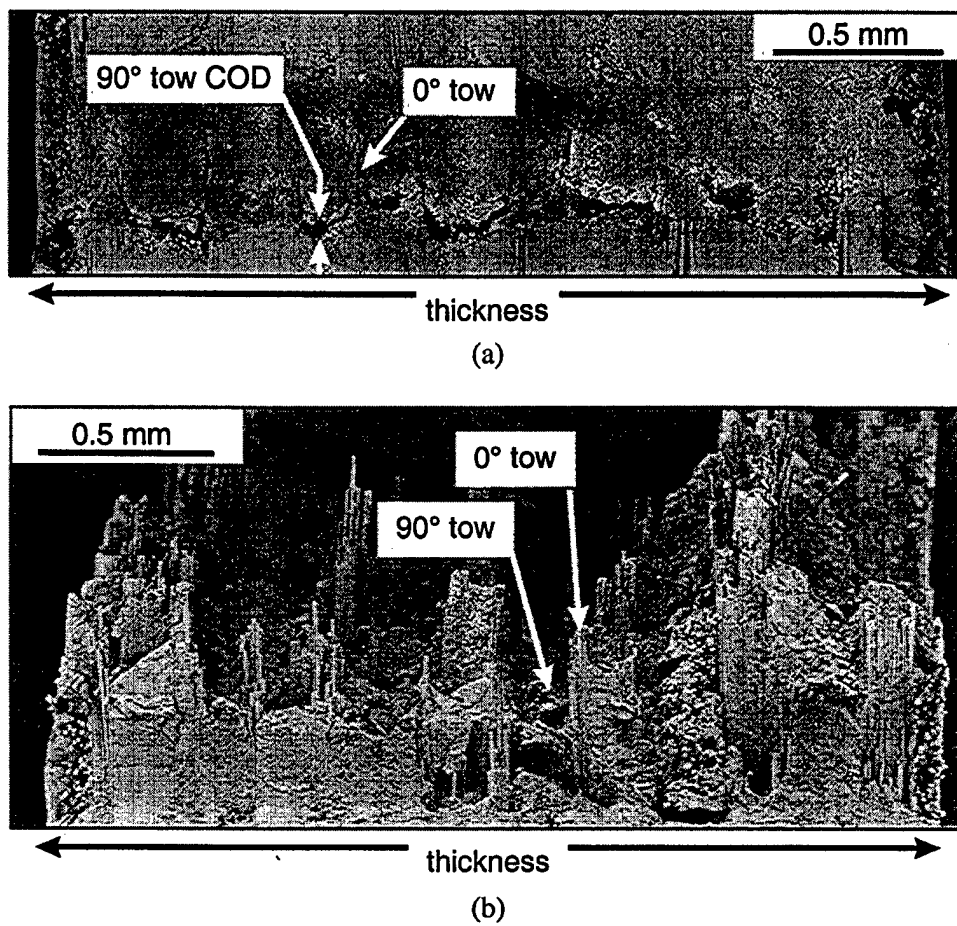


Figure 9. Cross-sectional view of machined notch tip region in 950°C specimens: (a) interrupted after the peak load (b) monotonically loaded to failure.

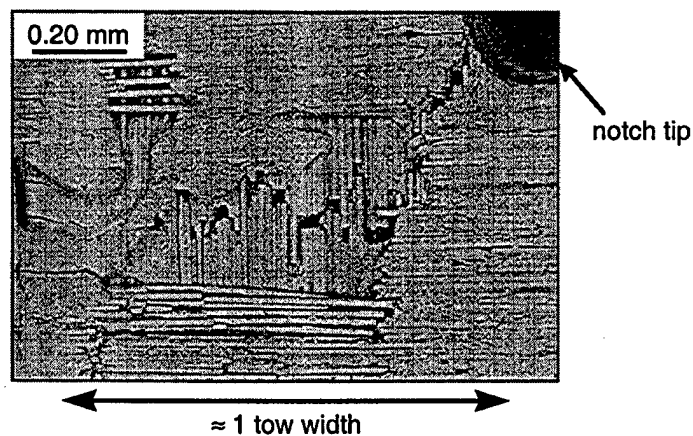


Figure 10. Notch tip region of 950°C specimen shown in Fig. 6c, after removing the top matrix layer and some 90° fibers. Failed 0° fibers were identified along the length of the dominant crack.

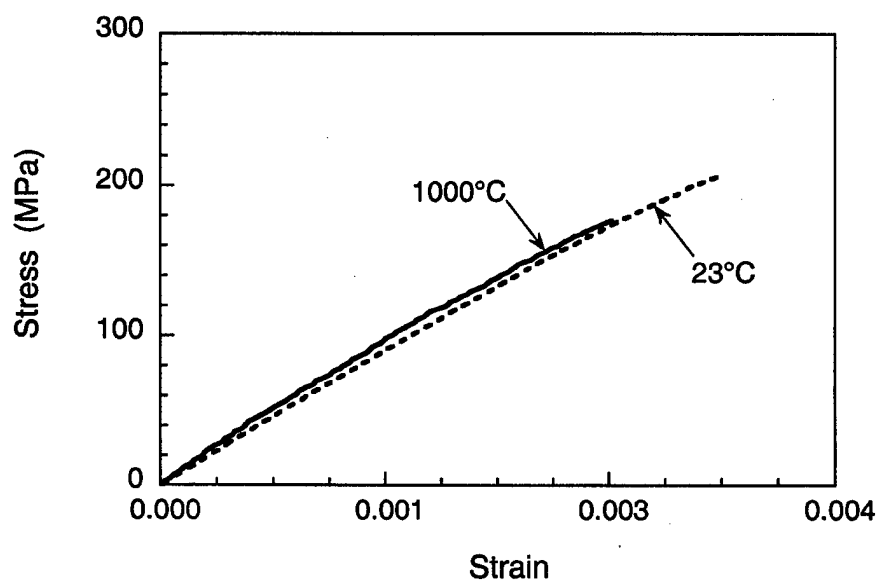


Figure 11. Tensile stress/strain response for unnotched Nextel610/AS at 23°C and 1000°C.

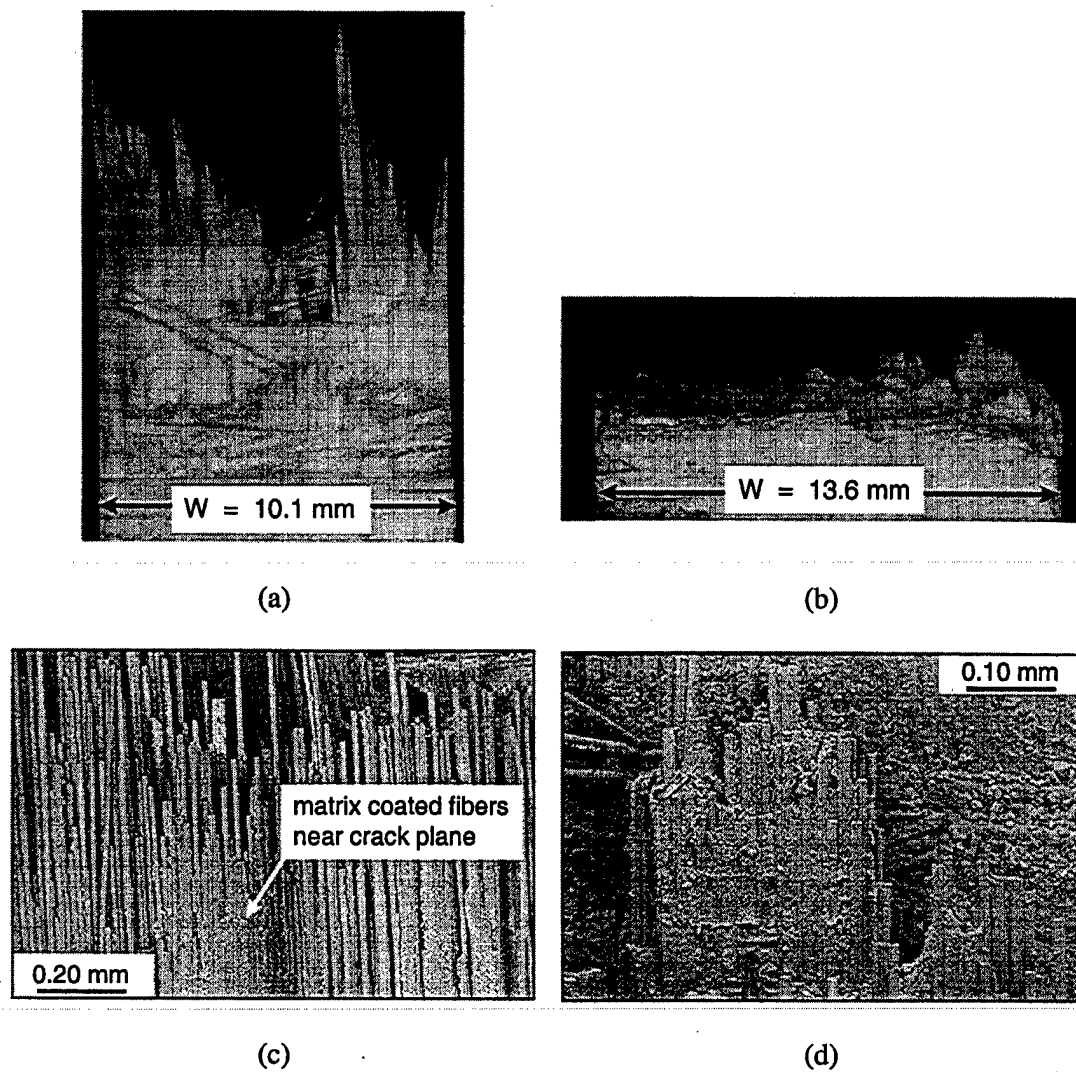


Figure 12. Nextel610/AS unnotched tension fracture surfaces: (a) 23°C (b) 1000°C and details of matrix and 0° fiber behavior (c) 23°C (d) 1000°C.

**This page intentionally left blank**

## A RAPID METHOD FOR GENERATION OF A HAIGH DIAGRAM FOR HIGH CYCLE FATIGUE

---

**REFERENCE:** Maxwell, D.C. and Nicholas, T., "A Rapid Method for Generation of a Haigh Diagram for High Cycle Fatigue," *Fatigue and Fracture Mechanics: 29<sup>th</sup> Volume, ASTM STP 1332*, T.L. Panontin and S.D. Sheppard, Eds., American Society for Testing and Materials, 1998, pp. 626-641.

**ABSTRACT:** A rapid test method is described for generating data points for a Haigh diagram for Ti-6Al-4V at a constant life of  $10^7$  cycles at room temperature. It involves subjecting specimens to loading blocks of  $10^7$  fatigue cycles and progressively increasing the load until failure occurs. An equivalent stress is obtained for each test specimen for plotting on the Haigh diagram. The method is applied to tests conducted at stress ratios (ratio of minimum to maximum stress) from  $R=-1$  to  $R=0.9$ . The validity of the method is confirmed by comparing data with those obtained using the conventional S-N interpolation approach at values of  $R=0.1$ ,  $0.5$ , and  $0.8$ . The rapid testing technique is then extended to the generation of a Haigh diagram for the same material subjected to prior low cycle fatigue (LCF) for ten percent of its LCF life. No degradation of the fatigue limit is observed from subsequent HCF testing using the rapid testing technique.

**KEY WORDS:** high cycle fatigue, test methods, Haigh diagram, titanium, fatigue limit, Ti-6Al-4V

---

Testing materials to failure under high cycle fatigue (HCF), as the name suggests, takes considerable time in the laboratory because of the very large number of cycles involved, typically in excess of  $10^6$ . Further, most engineering applications involving HCF require data at more than one stress ratio,  $R$  (ratio of minimum to maximum stress). To represent HCF data at different values of  $R$ , a Haigh diagram<sup>1</sup> (often referred to incorrectly as a modified Goodman diagram) is used, which is a plot of alternating stress versus mean stress for constant life. In turn, the individual data points for constant life at a given mean stress or value of  $R$  are obtained by interpolating data from an S-N curve. For long lives such as  $10^7$  cycles, which is used in design of rotating engine components, obtaining data points both below and above  $10^7$  cycles to failure and then interpolating to  $10^7$  cycles is extremely time consuming. One method for reducing the testing time is to use very high frequency testing apparatus which, unfortunately, is not widely available. A second method is to use a single specimen to obtain each data point for the Haigh diagram. The objective of this study is to develop and validate such a technique and to evaluate its applicability to fatigue limit testing for cases where only a limited number of specimens are available and where many different types of damage may have

---

<sup>1</sup> Materials test specialist, University of Dayton Research Institute, Dayton, OH 45469

<sup>2</sup> Senior scientist, Air Force Research Laboratory, Materials and Manufacturing Directorate, Wright-Patterson AFB 45433

<sup>1</sup> The attribution of a diagram to Goodman or Haigh is historically inaccurate. The use of a constant fatigue life diagram of some type using maximum stress, minimum stress, stress ratio, alternating stress, or mean stress in some combination predates either of these individuals. The alternating stress amplitude, the shape of the curve, the equation describing the curve, or the specific axes used can be attributed to various individuals including, but not limited to (in chronological order), Rankine (1864), Mueller (1873), Launhardt (1873), Gerber (1874), Schaffer (1874), Weyruch (1877), Smith (1880), Unwin (1888), and Johnson (1897). [1]

to be evaluated for a single test condition. A brief review of conventional as well as prior methods and a critique of their validity is also presented.

## Background

Standard methods for determination of the fatigue or endurance limit require both a large number of fatigue tests but also statistical analysis to establish their reliability [2]. Fatigue data corresponding to a given life or what is termed the greatest number of cycles,  $N_g$ , e.g.  $10^7$ , can be grouped into three categories according to applied stress level. At high stresses, all specimens fracture before  $N_g$  is reached. These stresses correspond to the range of finite life. Over a range of lower stresses, at least one but not all of the specimens fail before  $N_g$ ; this region is called the transition region. Finally, at some lower stress level and below, no failures are obtained before  $N_g$ ; this is called the range of infinite endurance. Testing is usually performed to identify the boundary between the transition and infinite endurance regions. For each stress level, a minimum of ten specimens are usually required, and four stress levels are recommended [2]. The data are treated statistically to identify the endurance limit corresponding to a probability of failure of less than some small amount like 1%, depending on the scatter in the data and the width of the transition region. This approach, while both scientifically based and statistically sound, requires an extensive amount of testing which is prohibitive for many investigations, particularly when  $N_g$  is a large number like  $10^7$ . Whilst other non-standard or accelerated methods are available for determining the endurance limit, the number of specimens and testing time are too large for practical engineering applications where a large data base, such as a Haigh diagram, which requires data at a number of mean stress or stress ratio conditions, is necessary.

By early in this century, numerous accelerated tests for endurance limit had been proposed and rejected because they did not prove to be reliable. These tests depended on inelastic behavior or mechanical hysteresis, rise of temperature, strain accumulation with cycles, energy absorbed, or changes in electrical resistance (due to cracks forming) or magnetic properties. Among these early accelerated tests was that of Moore and Wishart [3] who developed an "overnight" test based on application of a fixed number of HCF cycles followed by determination of tensile strength. The basis of this test was that fatigue testing below the endurance limit increases the tensile strength and endurance limit,<sup>2</sup> while above the endurance limit, cracks form and ultimately degrade the tensile strength. In a discussion of this paper, H.J. Gough, who studied fatigue and published extensively on the subject in the 1920's and 30's, stated that "I have arrived definitely at the conclusion that no reliable form of short-time test known has yet been devised." Further, he saw "no fundamental reason why any short-time test can be *expected* to prove reliable. I make this remark because it seemed to be inferred that the fatigue limit marks the dividing line between two essentially different behaviors of the material under test. This *may* prove to be so, but it is certainly not known at the present time. I cannot accept that such a dividing line exists. I think that the general effect on the material is essentially the same at stress ranges inferior and superior to the endurance limit." Little was done subsequently to develop rapid test techniques to establish the fatigue limit based solely on properties obtained at stresses above and below that limit.

One of the earliest attempts at developing a rapid test for determining the fatigue limit without using constant stress tests is attributed to Prot [4]. His technique involved starting at a stress below the estimated fatigue limit and increasing the stress at a constant rate until failure occurs. Each successive test is conducted at a reduced rate of increase, thereby producing a series of endurances associated with each rate of stress increase. Prot shows that a plot of square root of rate of stress increase against final stress at fracture produces a straight line which, if extrapolated, intersects the stress axis at a value equal to the fatigue limit. In the approach of Prot, one test specimen is required for each rate of increase in stress. Still, it was claimed that this method reduces testing time by nine-tenths. The major concern with an

<sup>2</sup> This phenomenon is often referred to as a "coaxing" effect and is discussed later



increasing load method of determining a fatigue limit is the effect that understressing might have in increasing the true fatigue limit, that is, the coxing effect. The Prot method was validated by Ward, et al [5] on welded SAE 4340 steel and found to be applicable to ferrous metals with a well-defined endurance limit [6]. However, Corten et al. [6] noted that for ferrous metals that are susceptible to coxing, the Prot procedure appreciably raises the endurance limit compared to that obtained by conventional methods. In a discussion of their paper, they pointed out the following: "Only if coxing is absent and the number of cycles in each step is sufficiently large (possibly  $10^7$  cycles), does it appear reasonable to expect that the fracture stress data obtained from the step-up method will agree with the endurance limit obtained from conventional tests." Subsequent work found that the Prot approach was reasonably reliable for a titanium alloy [7]. The existence of a coxing effect, while important in establishing the validity of an accelerated test procedure of the type due to Prot, does not appear to have an established scientific basis.

### A Proposed New Rapid Test Method

The method proposed for generating data points for a Haigh diagram for Ti-6Al-4V at a constant life of  $10^7$  cycles at room temperature involves subjecting a specimen to  $10^7$  fatigue cycles at a stress level which is below the anticipated level to cause failure. This can be performed at a particular value of R or, alternately, at a constant value of mean stress. The latter condition is recommended when sufficient data at various values of R are available to define the shape of the curve on the Haigh diagram. If failure does not occur within the block of  $10^7$  cycles, the stress level is increased by five percent and the test is repeated on the same specimen<sup>3</sup>. The procedure is repeated until failure occurs within a block of loading before  $10^7$  cycles is reached. The number of cycles to failure in that block, and the stress level of that and the prior block, are used in an interpolative formula to determine the effective stress to cause failure in  $10^7$  cycles. This number is obtained by assuming a linear damage law and has the form:

$$\sigma_{N-H} = \sigma_{pr} + \frac{N_f}{10^7} (\sigma_f - \sigma_{pr}) \quad (1)$$

where  $\sigma_{N-H}$  is the value of maximum stress to be plotted on the Nicholas-Haigh diagram (discussed later) corresponding to a life of  $10^7$  cycles,  $\sigma_f$  is the maximum stress level of the final block of cycles where failure occurred before reaching  $10^7$  cycles,  $N_f$  is the number of cycles to failure within that block, and  $\sigma_{pr}$  is the maximum stress level of the prior block of cycles where no failure occurred. If failure occurs on the first block of cycles, the stress chosen was too high and the method fails. The method depends, therefore, on being able to choose a stress level which is slightly below the stress corresponding to  $10^7$  cycles to failure. Prior testing at the same or similar conditions helps in making a good choice of starting stress level without having to retest too many cycle blocks. If the Haigh diagram is being developed for a number of cycles to failure other than  $10^7$  as chosen here, the denominator of  $10^7$  in Eqn. (1) is replaced by the appropriate number of cycles. In general, the procedure is not recommended for values below  $10^7$  and for stress increments of more than several percent<sup>4</sup>. The method can be continued using additional specimens for various values of R covering the range from R=-1 to R=0.9 to generate a Haigh diagram corresponding to a life of  $10^7$  cycles.

<sup>3</sup> With the current availability of increasing numbers of high frequency machines, which reduce testing times, we recommend increases of load as low as two percent to better establish the value to be plotted as stress to reach  $10^7$  cycles to failure.

<sup>4</sup> A more conservative approach which depends less on the percent increase of load is to use the last stress value at which no failure occurred as the endurance stress.

There are some advantages to the use of the proposed technique other than the considerable savings in testing time. The proposed technique results in failure in each specimen, contrary to conventional fatigue testing where some use of specimens fail and others do not because the test is terminated after a large number of cycles (runout). This results in two populations of specimens, one failed and the other unfailed, which are difficult to analyze statistically. Another justification for a non-constant load to determine the fatigue limit is, as Prot [3] points out, "in practice, fatigue loads are not regularly variable, but they are not uniform amplitude loads."

One of the disadvantages of the use of the proposed method is the potential existence of a coxing effect. Coxing implies that testing at a stress level below the endurance limit alters the material in such a manner that the endurance limit will be raised above that which would be obtained on the uncoaxed material. Such a phenomenon has been attributed to strain aging by Sinclair [8] who shows a direct correlation between a strong coxing effect and the ability of the material to undergo strain aging. In Ref. [9], it is shown that the strain aging process is of minor significance in commercially pure titanium at stresses near the fatigue limit. Another possible explanation of the coxing effect is one which is purely statistical in nature. Epremian and Mehl [10] point out that elimination of the weaker specimens during fatigue testing below the fatigue limit biases the population of specimens tested at higher stress levels. Because of the statistical selectivity, specimens subsequently tested above the fatigue limit tend to show longer lives. For either of the proposed explanations, it is not felt that coxing is a real phenomenon in titanium alloys and, therefore, the step loading test procedure introduced here is valid for determination of the fatigue limit.

### **Experimental**

The material used in this study is random length 45 mm diameter Ti-6Al-4V bar forgings. The material was processed in accordance with ASM 4928L. The material was heat treated at 705°C in vacuum for two hours followed by a static argon gas cooling to below 149°C. The material was then stress relieved at 549°C in vacuum for two hours followed by a static argon gas cooling to below 149°C. The resulting microstructure (Fig. 1) consists of wide, plate-like alpha with intergranular beta and is typical of Ti-6Al-4V in the mill annealed condition. The high aspect ratio (about 4:1) of the alpha plates in the longitudinal direction is the result of forging at or above the beta transus (~830°C) and subsequent slow cooling. Test specimens were machined from the heat treated bars in the longitudinal orientation using wire electro-discharge machining to produce the blanks.

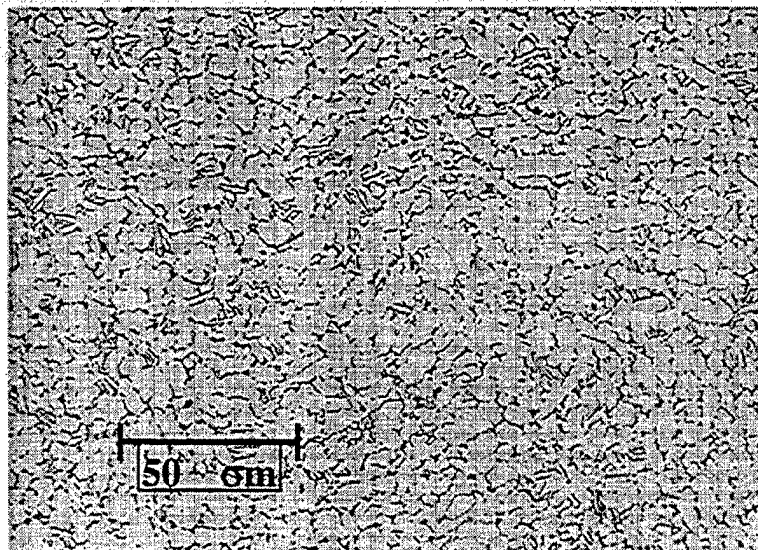


**Figure 8. Microstructure of Ti-6Al-4V.**

The specimens were cylindrical with a 6.35 mm diameter gage section 19 mm in length which tapered gradually to a grip section of 12.7 mm diameter. The large difference between cross-sectional area between the grip and gage sections was required to prevent fretting in the grip during fatigue testing. All specimens were finish machined using standard low stress grind procedures for titanium followed by polishing with 600 grit paper to a 15  $\mu\text{m}$  finish. Tension tests produced values for modulus of 109 GPa, yield strength of 990 MPa and ultimate strength of 1035 MPa. The stress/strain diagram is shown in Fig. 2.

Fatigue tests were conducted under constant stress conditions using a closed-loop computer controlled servo-hydraulic test machine. All high frequency tests were conducted at room temperature in laboratory air at a frequency of 70 Hz. The choice of 70 Hz as the frequency for the HCF testing was dictated primarily by machine capability coupled with practical considerations such as testing time and noise levels generated in the testing laboratory. At 70 Hz, the machine was capable of producing a sine wave with minimal distortion. To achieve  $10^7$  cycles corresponding to a single block at any load level required almost 40 hours. A typical test requiring 3 or 4 blocks of loading would, therefore, take approximately one week in order to obtain one data point on the Haigh diagram. As the number of data points obtained increased, the ability to predict the load level for any subsequent test got better and the number of load steps needed decreased accordingly. The low cycle fatigue testing to produce damage prior to HCF testing was accomplished in laboratory air at 1 Hz. The test procedure was applied to a number of test specimens to establish the shape of the Haigh diagram corresponding to  $10^7$  cycles over the range of stress ratios from -1 to 0.90. At each stress ratio, a specimen was fatigued to a limit of  $10^7$  cycles at a stress lower than the expected fatigue limit. After each runout of  $10^7$  cycles, the stress was increased by a maximum of 5% until failure occurred at less than  $10^7$  cycles. The fatigue limit stress was then determined using the linear interpolation scheme described in the previous section.

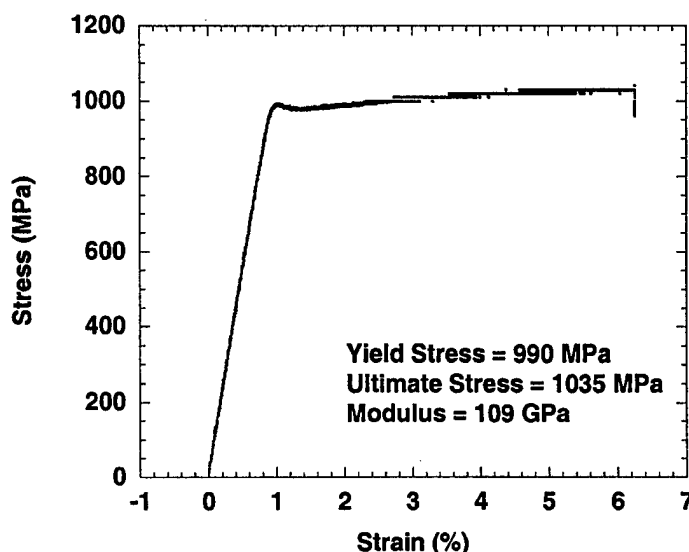


**Figure 9. Stress-Strain diagram for Ti-6Al-4V**

To evaluate the validity of the method, which is based on an underlying assumption that cycling at lower stress levels for an extended number of cycles has a minimum effect on HCF life, tests were conducted to develop conventional S-N plots at stress ratio values of  $R=0.1$ ,  $0.5$ , and  $0.8$ . In general, the method should provide the best results when the number of cycles to failure for the Haigh diagram is high enough so that the S-N curve has a very shallow slope or the endurance limit has been reached. A minimum of 4 samples were used at each stress ratio value and data were obtained over the range of  $10^4$  to  $10^8$  cycles. The slopes of the S-N curves at these lives were shallow and the data were fit with a straight line on a semi-logarithmic plot to determine the stress associated with failure at  $10^7$  cycles at each value of stress ratio.

The rapid testing technique developed herein was extended to the generation of a Haigh diagram for the same material and conditions described above, but including the addition of prior low cycle fatigue (LCF) damage. Five specimens were first subjected to LCF at values of either  $R=0.1$  or  $R=-1$  under load control at a frequency of  $1\text{ Hz}$  for a fraction of LCF life. The LCF life was determined approximately from S-N data which were generated at  $1\text{ Hz}$  using stress levels corresponding to total lives approximately in the range  $10^4$  to  $10^5$ . Specimens were subjected to a number of LCF cycles at a given stress level and then subjected to HCF under constant mean load conditions to determine the points on a Haigh diagram for material which has undergone potential damage under LCF. By comparing the Haigh diagrams for HCF and combined LCF/HCF, the effects of prior LCF loading upon subsequent HCF life was established. The test conditions for the LCF testing are summarized in Table 1. For each test case, the number of cycles applied was estimated to be approximately 10 percent of the LCF life at the test frequency of  $1.0\text{ Hz}$ .

**Table 1. LCF conditions prior to HCF testing.**

Stress Ratio	Stress (Mpa√m)	LCF Cycles
0.1	950	1,000
0.1	900	10,000
0.1	950	1,000
0.1	900	10,000
-1	590	10,000

### Results and Discussion

There are three considerations that should be addressed in presenting HCF data. First, the type of data, e.g., number of cycles to failure, endurance limit, etc. In this paper, we address constant life which will be defined, arbitrarily, as  $10^7$  cycles. Second, the quantities used to represent the data points requiring two of the following: maximum stress, minimum stress, alternating stress, mean stress, or stress ratio (ratio of minimum to maximum stress). In this paper, we will present alternating stress against mean stress as well as maximum stress against mean stress. Third, the nature of the line or curve, if any, which is used to represent the data. Here, as suggested by many of the authors who proposed equations, laws, or "diagrams", the actual data points are used with no attempt to fit them by any functional form.

The plot of both alternating stress and maximum stress against mean stress will be referred to as a Nicholas-Haigh diagram. At the possible expense of duplicating past efforts as well as confusing future historians, we introduce this plot to present data for engineering design in two fashions. For low values of mean stress or low  $R$  ( $R < 0.5$ ), the alternating stress is the crucial allowable quantity, particularly for aeroengine applications where mean stresses are relatively predictable and well defined. For high values of mean stress or high  $R$  ( $R > 0.5$ ), the maximum stress becomes a critical parameter in design. It is proposed that margins of safety be imposed on both parameters (alternating stress and maximum stress) in order to insure a safe design. The Nicholas-Haigh diagram is an attempt to present data in a form that will allow a designer to recognize the importance of both quantities. Such a plot may not be totally new, but the following features may make it unique:

- It is a method of representing experimental data. There is no equation or formula intended or implied to represent the data.
- There is no specific value of a y-axis intercept (zero mean stress or  $R = -1$ ) which is related to any material property such as yield or ultimate stress.
- There is no value, experimental or theoretical, associated with an x-axis intercept ( $R = 0$ ).

This last condition differs from most previous diagrams or laws which have attempted to pin the data to the ultimate strength for theoretical reasons, or to yield stress for engineering purposes. One of the main reasons for avoiding an intercept such as ultimate strength is that ultimate strength depends on the strain rate at which a test is conducted since most metals exhibit some degree of strain rate hardening [11]. Data plotted on a Nicholas-Haigh diagram are conducted at a given frequency which produce a different strain rate for each differing value of alternating stress. For increasing values of mean stress, as  $R$  approaches 1, the strain rate approaches zero, which is equivalent to a stress-strain curve to ultimate at an arbitrarily slow rate of loading. Thus, we introduce a fourth condition which defines a Nicholas-Haigh diagram, namely, that the frequency of loading for all data points be specified<sup>5</sup>. As a further condition, it is recommended that all data points be included, particularly those obtained at high values of  $R$  ( $R \rightarrow 1$ ). In this region, many materials tend to exhibit creep behavior which may lead to a creep rather than a fatigue failure (see, for example, Ref. [12]). Nonetheless, if the frequency is specified, the time to failure can be easily deduced. Data of this type should be appended with a footnote if necessary, but they are still valid design data, even though the mode of failure is not pure fatigue<sup>6</sup>.

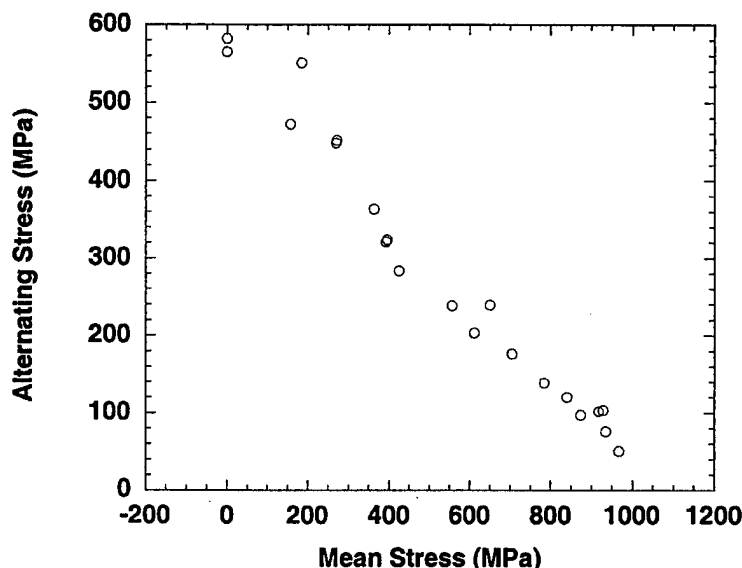


**Figure 10. Haigh Diagram for Ti-6Al-4V at 70 Hz and  $10^7$  cycles**

The data for all of the tests are plotted on a Haigh diagram as shown in Fig. 3. It can be seen that the scatter in the stresses obtained using the rapid test procedure is not unreasonable, especially when one considers that each data point is obtained from a single specimen. Some of

<sup>5</sup> It should be noted that because data for the Nicholas-Haigh diagram are obtained at high frequencies, the strain rates associated with the tests are not quasi static. For this reason, maximum stress values obtained under fatigue testing at high  $R$  and high frequency can be above the quasi-static ultimate strength of the material and, further, will not produce a smooth plot on a Nicholas-Haigh diagram if a quasi-static ultimate strength is used to anchor the plot to the x-axis.

<sup>6</sup> In the limit, a "fatigue" test at very high values of  $R$  becomes a creep or sustained load test. Any strain hardening which occurs due to strain rate effects, therefore, is influenced by the rate of loading which is used in going from zero to mean stress at the start of the test. This rate of loading should be recorded, particularly if data are to be compared with an ultimate stress value. The ultimate stress, consequently, should be obtained from a test at the same rate of loading for consistency.

the scatter, particularly a few "high" points, can be attributed to the magnitude of the stress jumps used in the rapid test method and the linear damage interpolation scheme used to determine the stress corresponding to  $10^7$  cycles. There is no fundamental basis for this scheme at the present time and it was used only for convenience.

A major concern was the effect that understressing the material might have in increasing the true fatigue limit. To help shed light on the possible existence of a coxing effect, data for a Haigh diagram were compared using two approaches. First, data were obtained from S-N curves at values of  $R=0.1$ ,  $0.5$ , and  $0.8$ . The S-N data at  $70$  Hz appear as the three highest curves in Fig. 4. The stresses obtained corresponding to  $10^7$  cycles are plotted on the Haigh diagram to compare the S-N and rapid test method HCF data for lives of  $10^7$  cycles and the resulting plot is shown in Fig. 5. The S-N data at  $R=0.1$ ,  $0.5$  and  $0.8$  show that there is no discernable difference in life times between the S-N data and data obtained using the increasing load method when determining a fatigue limit. S-N data to  $10^7$  cycles were not generated at  $70$  Hz for negative stress ratios, but if the  $R=-1$  data in Fig. 4, obtained at  $1$  Hz, are extrapolated out to  $10^7$  cycles, a value of fatigue limit of slightly less than  $600$  MPa is obtained. Assuming little difference between data at  $1$  Hz and  $70$  Hz, there appears to be no effect on life times at negative stress ratios when comparing results using the S-N approach with the rapid test method (see Fig. 5).

The data representing the fatigue limit for specimens subjected to prior LCF for several conditions are shown in Fig. 6. The LCF conditions, summarized in Table 1, correspond to approximately 10 percent of the fatigue life under LCF at  $1$  Hz. The specimens subjected to LCF at  $R=0.1$  were tested under HCF using the rapid test method at constant values of mean stress of  $600$  and  $900$  MPa. The results, shown in Fig. 6, show that these data points indicate no difference in HCF fatigue stress than specimens that had and also tested at  $R=-1$  at  $70$  Hz using the rapid test procedure, also shows no degradation in fatigue limit compared to the baseline data in fig. 6. From these very limited series of tests, it can be concluded in a preliminary manner, that LCF testing up to 10 percent of LCF life has no detrimental effect on the subsequent HCF fatigue limit. This observation is limited to smooth bar testing and the particular values of stress and life for the LCF tests used in this investigation. Clearly, additional testing is required to substantiate this preliminary finding.

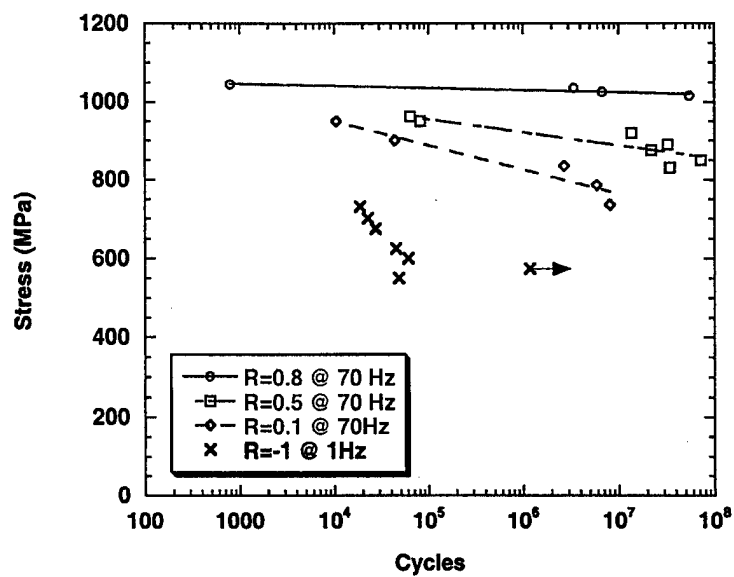


Figure 11. *Ti-6Al-4V Stress-life diagram.*

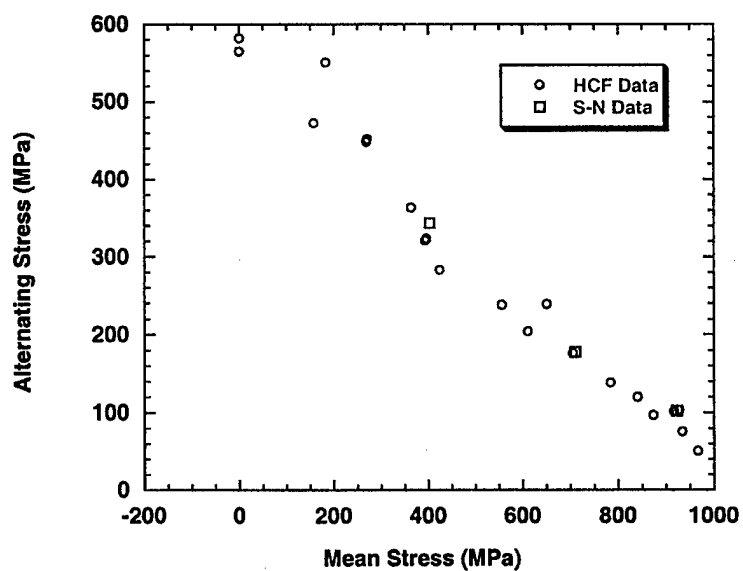
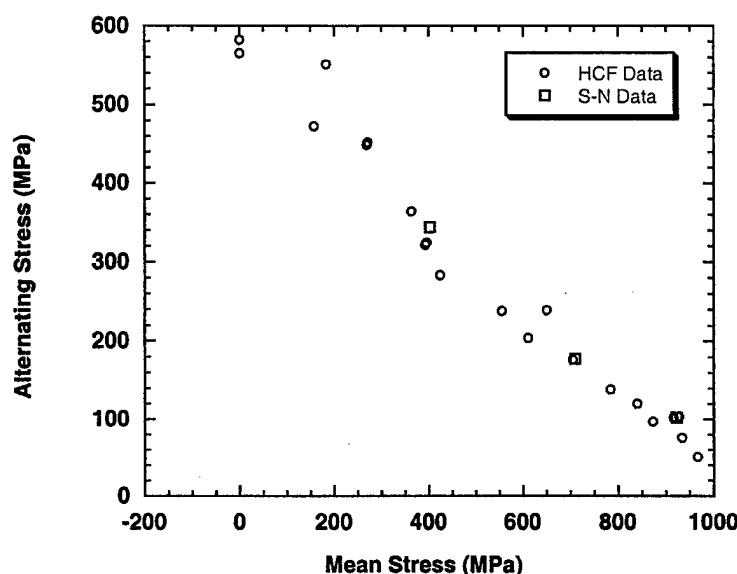


Figure 12. *Comparison of HCF and S-N data*





**Figure 13. Comparison of prior LCF data with HCF data.**

The data for alternating and maximum stresses are represented by a straight line in Fig. 7. To illustrate the importance of considering the maximum as well as the alternating stress in a Nicholas-Haigh diagram, consider what happens if the maximum stress is limited, for design purposes, to approximately 80 percent of the yield stress. Taking 800 MPa as the maximum design allowable stress, the alternating stress is limited as shown in Fig. 8 by the line denoted by "allowable alternating stress". Alternately, a design allowable based on a fraction of the alternating stress, taken as 60 percent for illustrative purposes, as shown in Fig. 9. If both criteria are considered together, as in Fig 10, it can be seen that for high values of mean stress (above 660 MPa), the maximum stress criterion of 800 MPa will govern the allowable alternating stress. At lower values of mean stress, the 60% criterion governs. The point where the transition occurs from a 60 percent criterion to a maximum stress criterion corresponds to a value of  $R=0.65$  and a mean stress which is 67 percent of the yield stress (990 MPa) for this material. If a maximum criterion for allowable vibratory stress is chosen as  $\pm 140$  MPa ( $\pm 20$  ksi), then this criterion along with the 60 percent vibratory or 800 MPa maximum stress limitation (see Fig 10) will dictate that the material cannot be used when the mean stress exceeds 660 MPa (67 percent of the yield stress).

### Conclusions

A proposed new rapid test technique based on testing at increasing stress levels for  $10^7$  cycles is shown to provide data for a Haigh diagram within a reasonable amount of testing time. The results obtained at various values of  $R$  seem to be in good agreement with limited data obtained using conventional test techniques where each sample is tested at only one stress level. The new technique provides a data point on fatigue limit for each test specimen.

Prior LCF testing up to 10 percent of anticipated LCF life appears to have no detrimental effect on the subsequent fatigue limit corresponding to  $10^7$  cycles within the constraints of the test conditions evaluated

Presentation of data in the format of a Nicholas-Haigh diagram, where both maximum and alternating stress are plotted as a function of mean stress, sheds light on the role of maximum stress in determining material allowables. Margins of safety at high values of mean stress are shown to be affected when maximum stress is considered as a design criterion. Finally, we close with some thoughts on why this work is being presented. When Moore and Wishart [3] presented results demonstrating a method for determining the endurance limit in a single overnight test in 1933 to ASTM, they did so with the understanding that "it is a good policy to describe the test before a technical society so that it may be criticized, and so that other laboratories may be encouraged to try it out, and if it be found at all reliable, to develop modifications and improvements." It is with this same spirit in mind, some 64 years later, that we present the results of this current investigation of a rapid test technique for determining the endurance limit of a material from a single test.

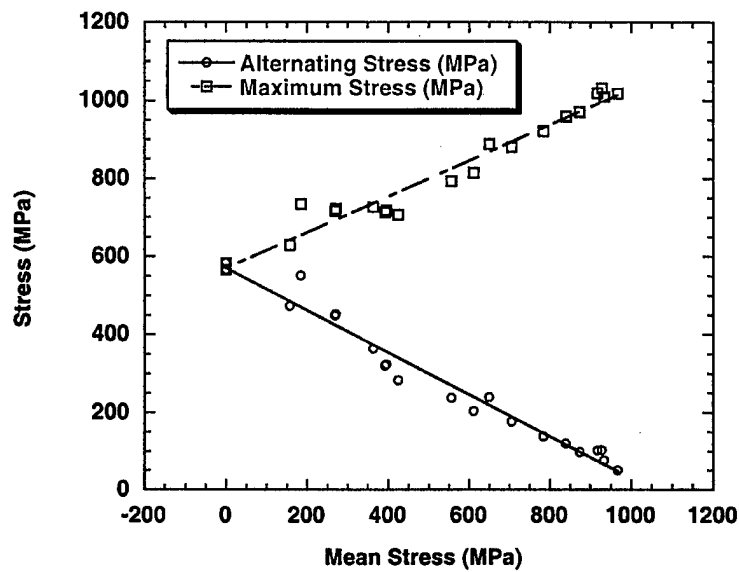


Figure 14. *Nicholas-Haigh Diagram*

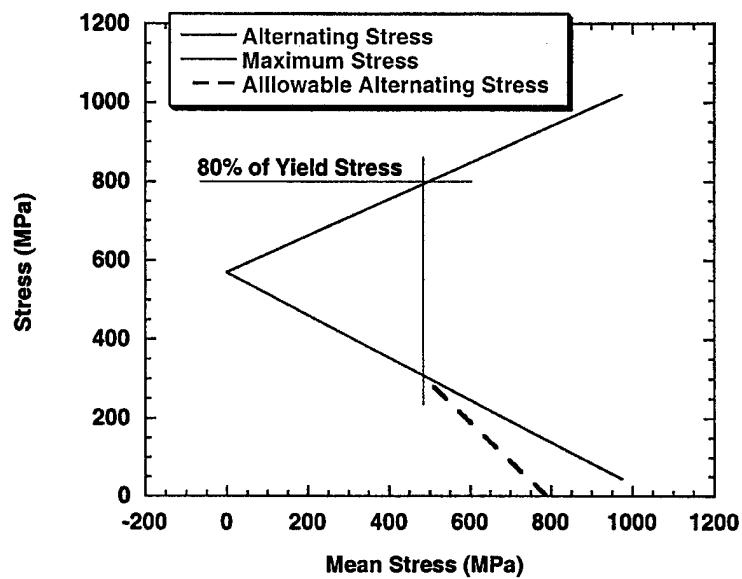


Figure 15. Effect of limiting maximum stress to 80% of yield stress.

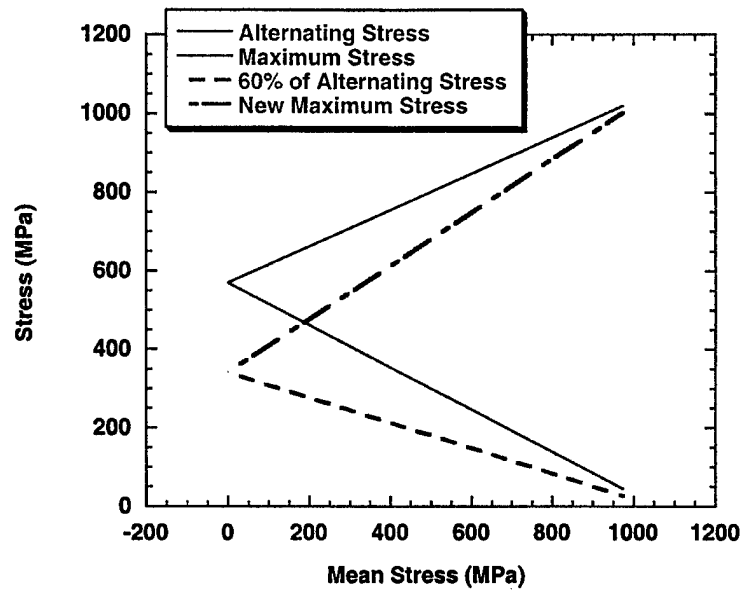


Figure 16. Effect of limiting alternating stress to 60% of allowable.

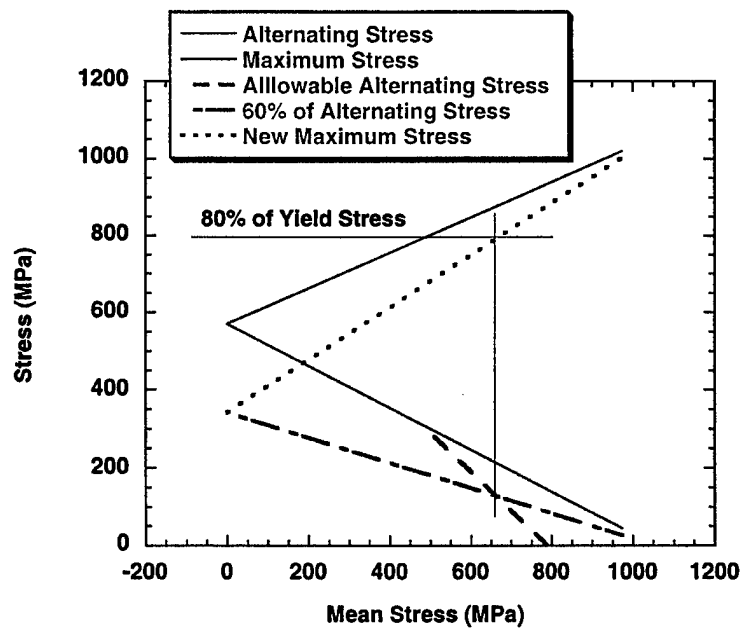


Figure 17. Combination of design limitations.

## References

- 1 Sendeckyj, G.P., "History of Constant Life Diagrams," *High Cycle Fatigue of Structural Materials*, T.S. Srivatsan and W.O. Soboyejo, Eds., TMS, 1998, pp. 95-107.
- 2 Maennig, W.-W., "Planning and Evaluation of Fatigue Tests," ASM Handbook, Volume 19, Fatigue and Fracture, ASM International, Materials Park, 1996, pp. 303-313.
- 3 Moore, H.F. and Wishart, H.B., "An 'Overnight' Test for Determining Endurance Limit," Proc. Amer. Soc. Test. Mater., Vol. 33, Part II, 1933, pp. 334-347.
- 4 Prot, M., "Un Nouveau Type de Machine D'Essai des Metaux a la Fatigue par Flexion Rotative," Rev. Metall., Vol. 34, 1937, pp. 440: see also: Prot, M., matériaux [Fatigue tests under progressive load. A new technique for testing materials], Rev. Metall., Vol. 45, No. 12, Dec.1948, pp. 481-489. English translation: Wright Air Development Centre Tech. Report No. 52-148, Sept. 1952. Italian Abstract: Metallurg. Ital., Vol. 41, No. 4, July-Aug. 1949, pp. 211-212.
- 5 Ward, E.J., Schwartz, R.T., and Schwartz, D.C., "An Investigation of the Prot Accelerated Fatigue Test," Proceedings ASTM, vol. 53, 1953, pp. 885-891.
- 6 Corton, H.T., Dimoff, T. and Dolan, T.J., "An Appraisal of the Prot Accelerated Fatigue Test," Proceedings ASTM, Vol. 54, 1954, pp. 875-894.
- 7 Vitovec, F.H. and Lazan, B.J., "Strength, Damping and Elasticity of Materials Under Increasing Reversed Stress with Reference to Accelerated Fatigue Testing," Proceedings ASTM, Vol. 55, 1955, pp 844-862.
- 8 Sinclair, G.M., "An Investigation of the Coaxing Effect in Fatigue of Metals," ASTM Proceedings, Vol. 52, 1952, pp. 743-758.
- 9 Turner, N.G. and Roberts, W.T., "Fatigue Behavior of Titanium," AIME Trans., Vol. 242, 1968, pp. 1223-1230.
- 10 Epremian, E. and Mehl, R.F., "A Statistical Interpretation of the Effect of Understressing on Fatigue Strength," Fatigue with Emphasis on Statistical Approach, ASTM STP 137, 1952, pp. 58-69.
- 11 Nicholas, T., "Material Behavior at High Strain Rates," Impact Dynamics, Chap. 8, J. Zukas et al., Eds., Wiley, New York, 1982, pp. 277-332.
- 12 Haigh, B.P., "Experiments on the Fatigue of Brasses," Journal of the Institute of Metals, Vol. 18, 1917, pp. 55-86.

This page intentionally left blank

Reference: Hutson, A.L. and Nicholas, T., "Fretting Fatigue of Ti-6Al-4V Under a Flat-on-Flat Contact," Proceeding of the National Conference on High Cycle Fatigue, San Antonio, TX, U.S. Air Force, Feb. 1998.

### **Fretting Fatigue of Ti-6Al-4V Under a Flat-on-Flat Contact**

Mrs. Alisha Hutson\*

Advanced Materials Characterization Group, Structural Integrity Division  
University of Dayton Research Institute, Dayton, OH 45469-0128, USA.

Dr. Ted Nicholas

Air Force Research Laboratory (AFRL/MLLN), Materials & Manufacturing Directorate; Wright-Patterson Air Force Base, OH 45433-7817, USA.

#### **Introduction**

Fretting fatigue is the damage caused by localized relative motion between components under load, and results in premature crack initiation and failure. Such damage has been indicated as the cause of many premature disk and blade failures in turbine engines, and as a result, has been the focus of numerous studies over the years. The applicability of the results of these studies is questionable because the geometries are not directly comparable. Turbine engine blade roots experience fretting in a flat-on-flat contact with rather large radii at the edges of contact. Most research has been conducted on cylinder-on-flat, punch-on-flat, or Hertzian (ball-on-flat) geometries because of the availability of closed form analytical solutions for the resulting stress distributions. While analytical solutions allow the researcher to correlate test results and ultimately predict laboratory behavior, no accurate life prediction models for complex components have resulted from these efforts. The modeling of a more representative geometry is required to develop a life prediction model that bridges the gap between laboratory and service conditions.

The purposes of this study were to evaluate the feasibility of modifying an existing test system to conduct fretting fatigue experiments with a flat-on-flat geometry, and to evaluate the effects of normal contact stress, contact radius, contact length, and load ratio on fretting fatigue of Ti-6Al-4V against Ti-6Al-4V. The axial stresses yielding specimen failure at 10 million cycles for different fretting pad contact radii, applied normal contact (fretting) stresses, and axial stress ratios were quantified. Metallography and fractography were used to qualify fretting damage and to evaluate failure mechanisms. Results and conclusions of this study will call for a more detailed investigation of parameters and correlation of results with analysis.

#### **Experimental Approach**

The fretting experiment was designed to simulate the loading conditions under which fretting fatigue damage occurs in turbine engine blade attachments, for which a typical loading condition is shown in Figure 1a. This loading condition includes a normal and a shear load against the blade-disk interface, and a bending moment induced by the dovetail flank angle. The two contacting surfaces are flat-on-flat with blending radii on both the blade root and the disk slot. The test apparatus for this study simulates the blade root geometry by employing flat fretting pads, with a radius at the edge of contact, against a flat specimen. The imposed normal and internal shear loads are reproduced in the test apparatus, as shown in Figure 1b. The bending moment could not be reproduced in this apparatus.

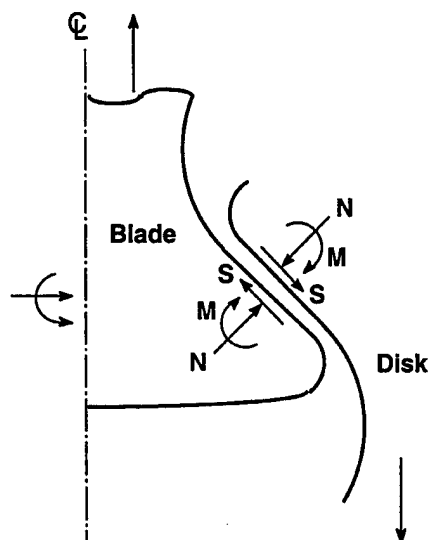


Figure 1a. Representation of blade root loading condition.

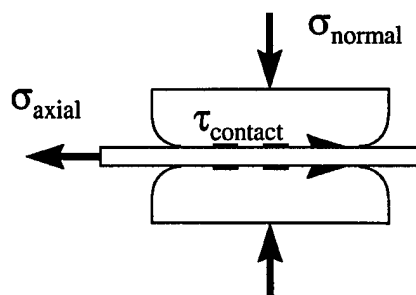


Figure 1b. Representation of test configuration designed to simulate blade root loading condition.

The test system used to conduct fretting fatigue tests for this study was modified from an existing axial fatigue test machine that experienced frequent specimen grip failures due to fretting in the grips. In an effort to capitalize on the machine's capacity to produce fretting fatigue failures, the gripping system was modified to allow control of critical fretting parameters. The resulting design (Figure 2) features removable fretting pads to facilitate control of the surface conditions, and bolts instrumented with strain gages in the shank to quantify static normal loads. A specific torque pattern permits symmetric normal loading of the specimen. The load train is shown in Figure 3. The axial fretting fatigue specimen is sandwiched in the grips, the normal (or clamping) load is applied via the instrumented bolts, the mean axial load is applied via closed loop pneumatic control, and a dynamic axial load is applied with an electromagnetic shaker. The specimen configuration produces two fretting fatigue tests per specimen. In this study, the contact conditions were nominally identical at both ends of each test specimen, and fretting pads were replaced for each test. This procedure facilitated comparison of test data by having each test to start from the same initial conditions. Fretting damage occurred at the edge of contact, shown in the magnified view in Figure 2.

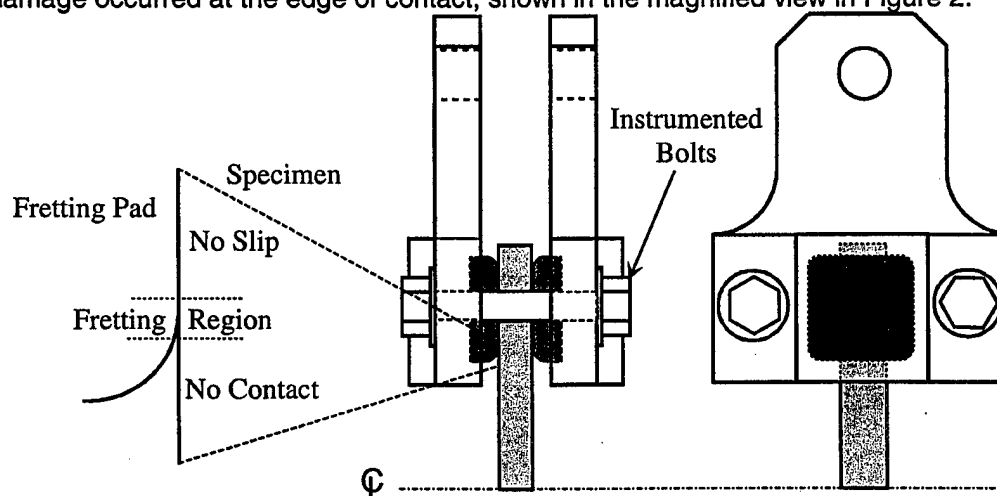


Figure 2. Fretting fatigue gripping system and stress state induced in contact region.



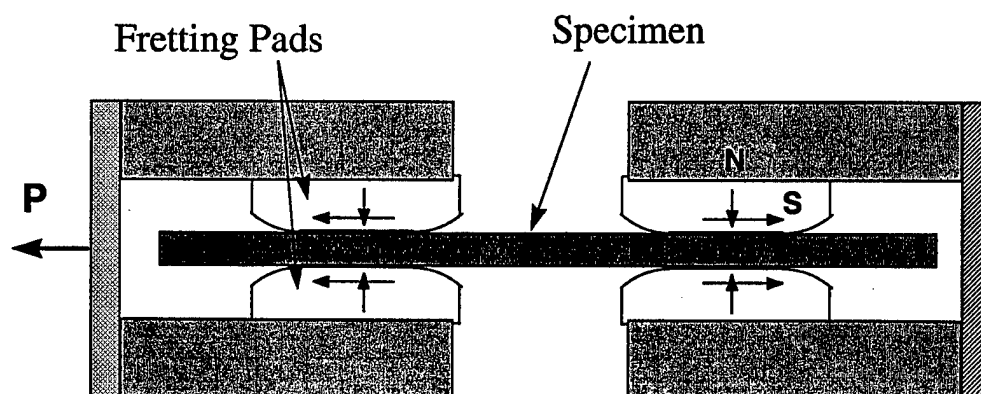


Figure 3. Test load train schematic. The apparatus produces two nominally identical regions of fretting for each test specimen.

In the study of fretting fatigue, slip length is considered to be a controlling parameter. Presumably, various slip lengths can be achieved by changing the shear stress distribution. To achieve a range of shear stress distributions in this test system, contact length, contact radius, and normal contact load were varied, resulting in eight test conditions. The eight test conditions were investigated for two load ratios, as in Figure 4. This test matrix was developed as a preliminary study of fretting parameters, therefore, only two values of each parameter were selected to determine if changing the parameters would produce trends in the test results. Nominal contact lengths were 25.4 mm and 12.7 mm; static normal loads were 70 kN and 42 kN; and contact radii were 3.2 mm and 0.4 mm. All tests were conducted at 300 Hz in lab air at room temperature.

	Contact Area			
PHASE 1	115 mm <sup>2</sup>	250 mm <sup>2</sup>	60 mm <sup>2</sup>	220 mm <sup>2</sup>
Normal Load = 70 kN	$\sigma_{\text{axial}} = 150 \text{ MPa}$ $R = 0.1$	$\sigma_{\text{axial}} = 150 \text{ MPa}$ $R = 0.1$	$\sigma_{\text{axial}} = 150 \text{ MPa}$ $R = 0.1$	$\sigma_{\text{axial}} = 150 \text{ MPa}$ $R = 0.1$
	$\sigma_{\text{axial}} = 220 \text{ MPa}$ $R = 0.5$	$\sigma_{\text{axial}} = 220 \text{ MPa}$ $R = 0.5$	$\sigma_{\text{axial}} = 270 \text{ MPa}$ $R = 0.5$	$\sigma_{\text{axial}} = 220 \text{ MPa}$ $R = 0.5$
Normal Load = 42 kN	$\sigma_{\text{axial}} = 100 \text{ MPa}$ $R = 0.1$	$\sigma_{\text{axial}} = 170 \text{ MPa}$ $R = 0.1$	$\sigma_{\text{axial}} = 135 \text{ MPa}$ $R = 0.1$	$\sigma_{\text{axial}} = 80 \text{ MPa}$ $R = 0.1$
	$\sigma_{\text{axial}} = 220 \text{ MPa}$ $R = 0.5$	$\sigma_{\text{axial}} = 220 \text{ MPa}$ $R = 0.5$	$\sigma_{\text{axial}} = 220 \text{ MPa}$ $R = 0.5$	$\sigma_{\text{axial}} = 220 \text{ MPa}$ $R = 0.5$

Figure 4. Phase 1 test matrix indicating normal loads, calculated contact areas, load ratios, and initial axial stresses

Testing was conducted using the stepped loading approach developed by Maxwell and Nicholas<sup>1</sup>. This technique employs constant amplitude loading blocks (see Figure 5) where the initial axial stress is set below the limit stress for a given fatigue life. Each loading block is run for the given design life, which is ten million cycles in this case, or until the specimen fails. If the specimen doesn't fail in the first load block, the axial stress is raised by a percentage of the initial axial stress, and run for another ten million cycles. This process is repeated for each subsequent block until the specimen fails. The design stress, or Goodman stress is interpolated from the failure stress, the number of cycles at the failure stress, and the stress from the previous step.

Axial specimens and some of the fretting pads were machined from vacuum annealed and stress relieved Ti-6Al-4V. The balance of the fretting pads were machined from forged

AMS4928 Ti-6Al-4V with TE01 heat treatment. All specimens and fretting pads were low stress ground to an RMS 16 surface finish.

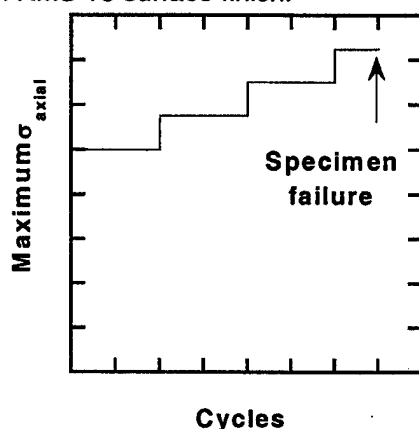


Figure 5. Step loading pattern used for Goodman stress determination.

### Results / Discussion

The test matrix in Figure 4 has been completed and scanning electron microscopy (SEM) has been performed. Results indicate that the test apparatus has successfully produced fretting fatigue failures. Axial specimen failures occurred near the edge of contact, usually less than 250  $\mu\text{m}$  from the lower edge of the fretting pad. Characteristic fretting damage was also observed on the unfailed ends of the tested specimens. A fretting scar typical of those observed in the test specimens is shown in Figure 6. Fretting damage appears on the left half of

the image, while the right half of the image shows a typical undamaged surface. The diagonal texture is a result of the low stress grind process used in manufacturing the specimen.

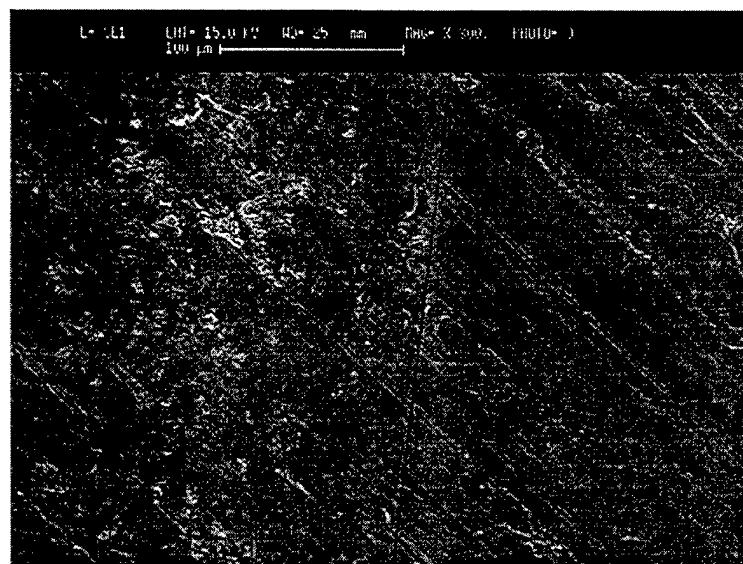
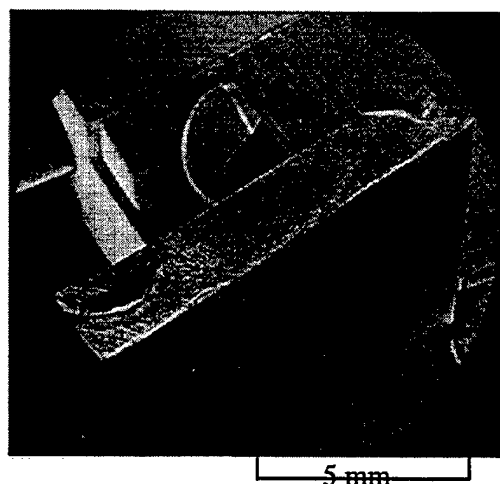


Figure 6. A representative fretting scar from the unfailed end of a typical test specimen is shown to the left of the dashed line. The loading axis is approximately horizontal.

The fractography conducted on selected specimens also provides evidence of fretting fatigue induced failures. In the macro photo in Figure 7, indications of fatigue crack growth can be seen across the center of the specimen thickness, with an obvious fast fracture region on the right side. Crack initiation begins at the middle back face of the fracture surface, and the crack front appears almost semi-elliptical in the early

stages of crack growth. The left side shows features which are probably evidence of rapid fatigue crack growth. One particular point of interest is the flake on the upper left-hand corner of the fracture surface, which may be an indication of multiple crack initiation sites, perhaps on different planes.



*Figure 7. Typical fretting fracture surface. The loading axis is perpendicular to the crack plane.*

In addition to the qualitative data provided by the SEM, quantitative results indicate an effect of fretting fatigue on specimen fatigue strength. The results are designated as Goodman stresses, which refer to the fatigue stress as defined by the maximum stress and the stress ratio. The values for the Goodman stress under fretting fatigue, as shown in Figure 8, are much lower than those for uniaxial fatigue. Typical Goodman stress values for  $R = 0.1$  and  $R = 0.5$  are 600 MPa and 825 MPa, respectively. Comparison to average fretting Goodman stress values from this study reveal a knockdown factor of approximately 3.

Trends in the data for this study also appear in Figure 8, which shows Goodman stress versus average normal contact stress. The average normal contact stress is determined by dividing the applied normal load by the contact area. The contact area used in the calculation excluded the part of the radius that did not contact the specimen. The average normal contact stress is used strictly for comparison purposes, since it is well known that the normal stress distribution in the contact region is highly non-uniform, with very high stress concentrations near the edge of contact. A remarkable feature of this data is that no trend appears as a function of normal stress. Many references<sup>2-9</sup> indicate the dependence of fretting fatigue on slip length, and casual observation suggests that a change in normal stress would produce a change in slip length. However, the results in Figure 8 indicate that changes in normal stress do not result in appreciable changes in Goodman stress. That Goodman stresses are unaffected by changes in normal stress would seem to imply that the normal stress does not affect slip length, at least in the stress range encompassed by this study. Any relationship between normal stress and Goodman stress may be obscured by other parameters, or by scatter in the data for this stress range.

The data in Figure 8 also point to an increase in Goodman stress with an increase in stress ratio; however, such a trend is expected based on results from uniaxial fatigue. Yet another trend observed in the figure is a decrease in contact radius appears to produce higher allowable Goodman stresses. The authors suggest that such a trend may point toward a possible effect of contact radius on the slip length. Since slip lengths were not measured for these tests, additional testing is required to confirm this hypothesis.

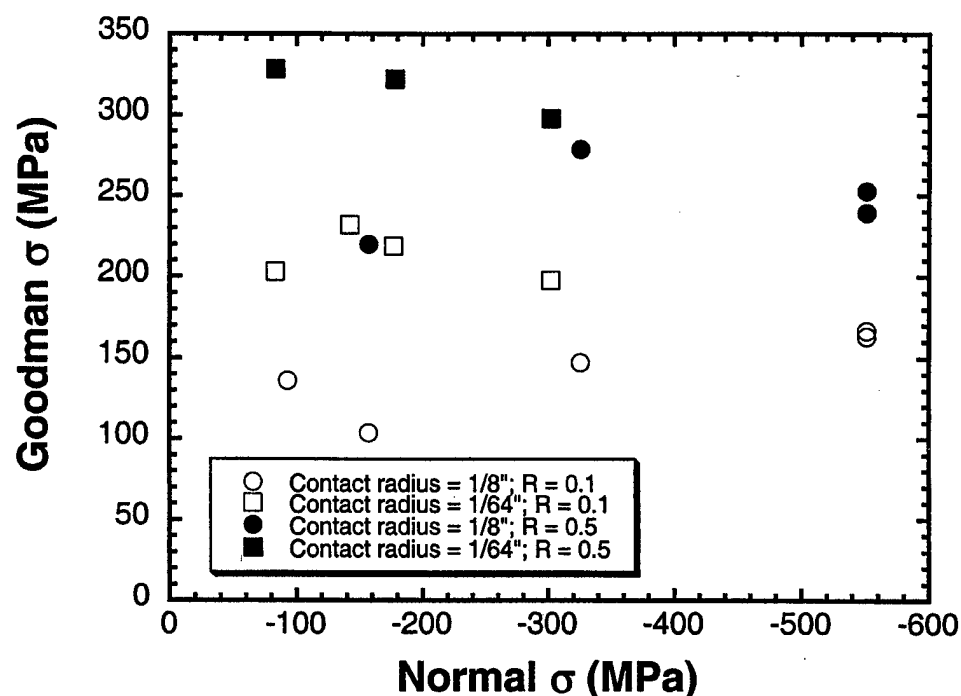


Figure 8. Fretting fatigue test results; all tests conducted at 300 Hz in lab air at room temperature

Analysis is currently being performed to gain insight into the experimental observations. A finite element analysis (FEA) of a typical blade under 7500 rpm rotational load has been provided, courtesy of AFRL/PRTC (Figure 9), for comparison to our test geometry. No aerodynamic loads were considered in the FEA. The blade stresses in the dovetail peak at approximately 70 MPa compressive for the specified rotational load. Calculation of average normal stresses as indicated above for different conditions in this study reveal test apparatus capability range from 40 MPa to 550 MPa compressive. These are average normal stresses; as yet, no attempt has been made to quantify the stress concentrations at the edge of contact or the distributions throughout the contact region. However, the rough comparison appears to indicate that the test system can generate loading conditions that are useful for comparison to engine conditions.

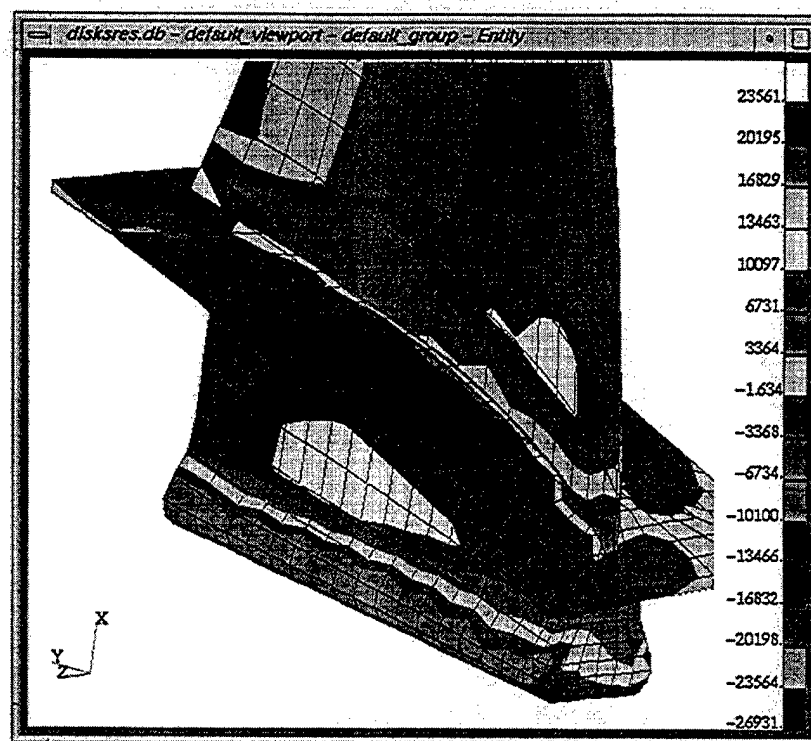


Figure 9. Finite element results for a blade under a rotational load of 7500 rpm.

### Future Work

A great deal of additional work is required to fully characterize fretting fatigue. The next step in testing for this study involves conducting interrupted fretting tests to evaluate the effect of prior fretting fatigue on uniaxial fatigue life. Stress ratios of 0.5 and 0.8 will be investigated for two normal contact stresses, 100 MPa and 275 MPa. The variation in normal contact stress will be achieved by varying the contact length between 25.4 mm and 12.7 mm. Specimens will be tested under fretting fatigue conditions for 1E5, 1E6, and 5E6 cycles, which correspond to 1%, 10%, and 50% of design life. Then, the specimens will be removed, and one end will be failed in constant amplitude uniaxial fatigue to quantify the reduction of fatigue life due to fretting damage, while the other half is used for metallographic characterization. The one eighth inch radius will be used for these tests, because it more closely simulates a typical dovetail geometry. In addition, some of the test conditions from the matrix for this study may be repeated to facilitate slip length measurement, which will provide additional insight to some of the conclusions from this study. A few S-N tests will also be run at selected Goodman stress and stress ratio conditions to confirm that that previous load steps do not produce appreciable fretting damage.

A 2D finite element analysis of the contact region is being conducted to evaluate the stress concentration that occurs at the edge of contact, and possibly to quantify the magnitude of the slip length in the fretting region.

### Conclusions

Successful fretting fatigue tests have been conducted as evidenced by the characteristic fretting damage and failure locations observed in test specimens. In addition, trends in data based on variation of different parameters have been observed. Specifically, higher allowable Goodman stresses were observed by either increasing the stress ratio, or decreasing the contact radius.

The test technique appears to produce stress states similar to those seen in turbine engine blade attachments, based on a rough comparison. Although this fretting fatigue experiment does not reproduce the bending moment, no other fretting fatigue studies where bending moment is applied in an experimental apparatus have been encountered in the literature, except where a dovetail shape was tested. An analysis to characterize the stress states in the test configuration is currently being performed.

The test apparatus developed for this study incorporates small, removable fretting pads of a simple geometry. This feature could facilitate the generation of low cost fretting fatigue data for various surface treatments, assuming the dovetail attachment is well represented by this test apparatus.

#### Acknowledgment

This research was conducted at the Materials Directorate, Air Force Research Laboratory (AFRL/MLLN), Wright-Patterson Air Force Base, OH, USA. A. Hutson was supported under on-site contract number F33615-94-C-5200.

#### References

1. Maxwell, D.C. and Nicholas, T., "A Rapid Method for Generation of a Haigh Diagram for High Cycle Fatigue," *Fatigue and Fracture Mechanics: 29th Volume*, ASTM STP 1321, T.L. Panontin and S.D. Sheppard, Eds., American Society for Testing and Materials, 1998, submitted for publication.
2. Blanchard, P., Colombie, C., Pellerin, V., Fayeulle, S., and Vincent, L., "Material Effects in Fretting Wear: Application to Iron, Titanium, and Aluminum Alloys," *Metallurgical Transactions A*, vol. 22A, pp. 1535-1544, 1991.
3. Fayeulle, S., Blanchard, P., and Vincent, L., "Fretting Behavior in Titanium Alloys," *Tribology Transactions*, vol. 36, no. 2, pp. 267-275, 1993.
4. Fouvry, S., Kapsa, Ph., and Vincent, L., "Analysis of Sliding Behavior for Fretting Loadings: Determination of Transition Criteria," *Wear*, vol. 185, pp. 35-46, 1995.
5. Hills, D.A., Nowell, D., and Sackfield, A., "Surface Fatigue Considerations in Fretting," *Interface Dynamics*, Proc. 14<sup>th</sup> Leeds-Lyon Symposium on Tribology, Lyon, September 1987, Elsevier, Amsterdam, 1988.
6. Hoepfner, D.W., "Mechanisms of Fretting Fatigue," *Fretting Fatigue*,ESIS 18 (R.B. Waterhouse and T.C. Lindley, eds.), Mechanical Engineering Publications, London, pp. 3-19, 1994.
7. Kuno, M., Waterhouse, R.B., Nowell, D., and Hills, D.A., "Initiation and Growth of Fretting Fatigue Cracks in the Partial Slip Regime," *Fatigue Fract. Engng. Mater. Struct.*, vol. 12, no. 5, pp. 387-398, 1989.
8. Waterhouse, R.B., "Fretting Fatigue," *International Materials Review*, vol. 37, no. 2, pp. 77-97, 1992.
9. Dobromirski, J.M., "Variables of Fretting Processes: Are There 50 of Them?," *Fretting Fatigue*,ESIS 18 (R.B. Waterhouse and T.C. Lindley, eds.), Mechanical Engineering Publications, London, pp 60-66, 1994.

R. Sunder<sup>1</sup>, W. John Porter<sup>1</sup>, and Noel E. Ashbaugh<sup>1</sup>

## STRESS-LEVEL-DEPENDENT STRESS RATIO EFFECT ON FATIGUE CRACK GROWTH

**REFERENCE:** Sunder, R., Porter, W. J., and Ashbaugh, N. E., "Stress-Level-Dependent Stress Ratio Effect on Fatigue Crack Growth," *Fatigue and Fracture Mechanics: 29th Volume, ASTM STP 1332*, T. L. Panontin and S. D. Sheppard, Eds., American Society for Testing and Materials, 1998, pp.426-437.

**ABSTRACT:** Fractographic measurements of fatigue crack growth rate for small cracks reveal stress-ratio effects even when fatigue crack closure is absent. These effects are restricted to low fatigue crack growth rates and become significant with increase in net stress levels. To characterize the effect, experiments and analyses were conducted on notched coupons of an Al alloy at stress levels producing inelastic conditions on initial loading. As a reference, fatigue crack growth rates were obtained for a long crack tested under fully elastic loading well below yield stress. The results indicate that for fatigue growth associated with low applied stress intensity range, minor changes in stress ratio can cause substantial variation in crack growth rate. A model is proposed for the small crack fatigue growth rate as a function of applied stress intensity and stress ratio. The model is based on crack growth rates obtained under several stress levels with crack size as small as 0.03 mm.

**KEYWORDS:** fractography, fatigue crack growth, stress ratio, crack closure, small cracks

This research effort was motivated by several issues: a) spectrum load or load history effects, b) interest in high cycle fatigue which can lead to stress ratio,  $R$ , values approaching unity, and c) application of life prediction methodology to structures which invariably have notches or stress risers present.

Load history effects in metal fatigue under random service loading are closely linked with mean stress effects in crack formation and stress ratio effects in fatigue crack growth. Most predictive models would indicate that in the absence of mean stress or stress ratio effects, cumulative fatigue damage will be load sequence (history) insensitive. In general, stress ratio effects in fatigue crack growth [1-6] have been associated with fatigue crack closure [1]. Crack growth rate ( $da/dN$ ) equations also account for the rapid increase in  $da/dN$  as  $K_{max}$  approaches  $K_{Ic}$  [2,3].

Several mechanisms may be responsible for the stress ratio effect on fatigue crack growth rate [4-6]. Of these, fatigue crack closure has emerged as the most "popular" one to explain the effect in terms of truncation of applied stress intensity range,  $\Delta K$ , to an effective range,  $\Delta K_{eff}$ . This reduction in  $\Delta K$  is a consequence of closure in the wake of the crack, effectively working like a wedge that does not allow stress intensity to drop below a certain level. The closure of the fatigue crack can be attributed to one or more mechanisms - crack tip plasticity, roughness, asperities, oxide layer formation, etc. [1,7]. The first three of these are load history sensitive, making crack closure a widely accepted phenomenon to model load interaction effects in fatigue life prediction for random, service load conditions [3]. Oxide layer formation can have a major influence on stress ratio effects on threshold stress intensity,  $\Delta K_{th}$ .

High cycle fatigue is related to history effects in the sense that difficulties in predicting the life of a structure [8] usually result when high frequency load cycles are superimposed on low frequency cycles. In applications, the low frequency load is the service load with high amplitude. While the high frequency load is thought to be of low amplitude, the high frequency





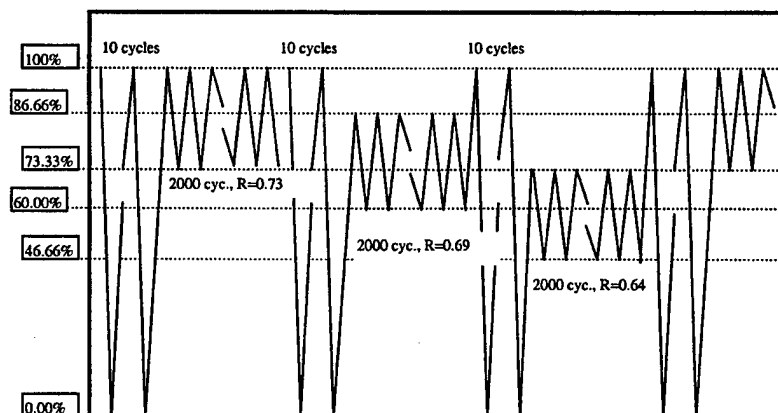


FIG. 2--Schematic of load sequence used in testing; actual waveform was sine with nominal loading rate of 200 kN/s.

cycles is the same as  $S_{max}$  during the first step at  $R = 0.73$ . This precludes any load interaction effects associated with overloads. Even the cycles at the lowest stress ratio of  $R = 0.64$  see an overload ratio of just 36% due to the markers. Overloads under 50% of baseline loading have generally been found to cause only negligible retardation effects on crack growth.

Approximate calculations of plane strain plastic zone size suggest fatigue crack extension in a single step of 2 000 cycles would be under 5% of the plastic zone size due to the preceding markers. This calculation also supports the possibility that plasticity induced retardation effects if any, would apply uniformly to all three steps.

All three sets of marker loads contain ten cycles. This number was selected to ensure discernible marker bands on the fracture surface even at very low crack growth rates of  $10^{-5}$  mm/cycle due to the marker cycles. The step size of 2 000 cycles for each of the stress ratios was selected to improve chances of measurable crack extension even at growth rates as low as  $10^{-7}$  mm/cycle. Step size serves as a "resolution amplifier" in microscopy. At very low growth rates, individual striations may be too fine to be picked up under the microscope. Reference 10 noted that striation spacings indicating crack growth rates under  $10^{-4}$  mm/cycle have not been observed. However, a band of multiple such striations are more readily identified when spaced with marker cycles that leave behind their own bands with contrasting morphology.

In the process of ensuring minimum load interaction effects and absence of fatigue crack closure, variation of applied stress ratio was restricted to between 0.64 and 0.73. This interval was assumed to be wide enough to show any stress ratio effect on crack growth rate.

Three test conditions were used. Applied load levels and estimated stress responses are listed in Table 1. Test 1 was on an SE(T) specimen with a 3 mm saw cut serving as the crack initiator. The test was at  $S_{max} = 100$  MPa to simulate long crack fully elastic conditions.

Tests 2 and 3 were conducted on the notched coupon (see Fig. 1 for details) with  $K_t = 2.5$ . The purpose of these tests was to simulate the behavior of real engineering components with stress riser and associated stress gradient. The specimen was designed with a notch enforcing natural crack initiation under conditions of controlled local inelasticity. Due to inelastic response, the effective stress ratios in these tests were different from applied stress ratios. When the material yields under the initial tensile loading, subsequent local stress cycles are totally elastic. The effective stress ratio will be less than applied stress ratio. Stress levels were estimated as notch surface local stresses after Neuber conversion.

The maximum applied load (50 kN) in Test 2 was selected to induce notch root yield, with estimated notch root maximum stress reaching 515 MPa compared to the material yield stress of 420 MPa. This maximum load caused limited residual stresses upon unloading, thereby reducing the applied stress ratios at the notch root. Test 3 used a higher maximum applied load (75 kN), thereby producing considerable inelastic deformation of the notch root, leading to formation of significant residual stresses and considerable reduction in the stress ratios at the notch root.

TABLE 1-- Loading conditions and estimated stress response. Refer to Fig. 2 for load sequence.

Test:	1	2	3
<b>Specimen geometry:</b>	SE(T) W45/T5 mm	Notched Spec. ( $K_t = 2.5$ ) W23/T10 mm	Notched Spec. ( $K_t = 2.5$ ) W23/T10 mm
<b>Reference loading (100%)</b>	100 MPa	50 kN	75 kN
Maximum net stress, MPa	100	217	326
Max. notch local stress, MPa	-	515	670
<b>Step #1 (2 000 cycles)</b>			
Applied stress ratio	R = 0.73		
Effective stress ratio	0.73	0.718	0.676
$S_{max}$ , MPa	100	515	670
$\Delta S$ , MPa	26.7	145	217
Mean stress, MPa	113	458	562
<b>Step #2 (2 000 cycles)</b>			
Applied stress ratio	R = 0.69		
Effective stress ratio	0.69	0.672	0.615
$S_{max}$ , MPa	86.7	443	564
$\Delta S$ , MPa	26.7	145	217
Mean stress, MPa	100	370	456
<b>Step #3 (2 000 cycles)</b>			
Applied stress ratio	R = 0.64		
Effective stress ratio	0.64	0.608	0.526
$S_{max}$ , MPa	73.3	370	458
$\Delta S$ , MPa	26.7	145	217
Mean stress, MPa	86.7	298	350

Table 1 summarizes the estimated stress response of the test coupons for the three test conditions. The maximum stress varied from 100 to 670 MPa to cover both fully elastic and inelastic loading conditions. As mentioned earlier, subsequent cycling after initial inelastic deformation produced a purely elastic response.

## Results and Discussion

### Small-Crack Growth Behavior

The growth rates for small cracks obtained from test conditions 2 (50 kN) and 3 (75 kN) are plotted versus crack length in Fig. 3. The growth rates were obtained for crack lengths from about two to ten grain sizes. Two distinct regions of growth rates appear. The data just beyond

the characteristic grain size on the left side of Fig. 3 have a more rapidly increasing growth rate than the data on the right side which have a slowly increasing growth rate. Since the growth data were acquired from crack surfaces which lead to failure of the specimen, the growth rates can be associated with the least resistant path after initiation in the notch root vicinity.

From observations of crack growth after initiation [11], the crack encounters a high resistance in traversing the grain boundary which would diminish the growth rate and even arrest the crack if conditions are appropriate. As the crack has found favorable growing conditions after being slowed by the initial grain boundary, it begins to grow at an increasing rate after passing through the first grain boundary. Ultimately, this increasing growth rate begins to slow as the crack encounters more grains that offer more resistance to its growth. The growth rates of the crack with the higher stress and stress range will be higher. From the data, the rate of change of the growth rates decreases after two to four grains have been traversed. This transition appears to happen at about  $10^{-6}$  mm/cycle.

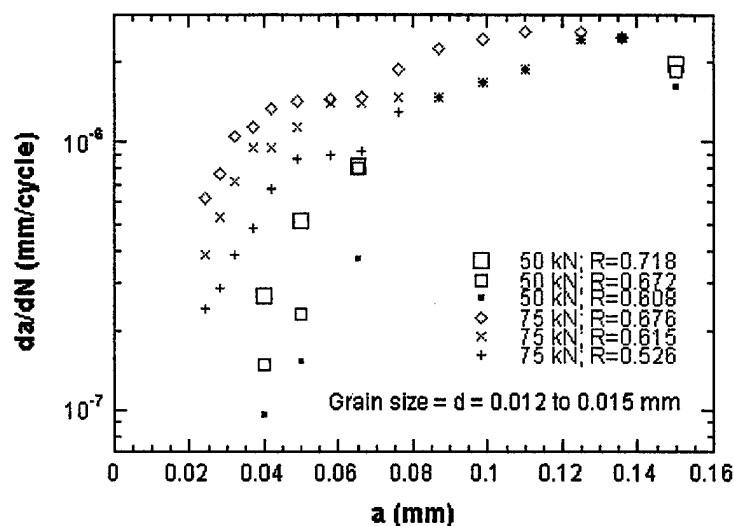


FIG. 3--Small-crack growth rates versus crack length.

Since the stress excursions in the notch root are essentially elastic after the initial loading cycle, the crack driving force can reasonably be expressed in terms of the elastic stress intensity factor range,  $\Delta K$ . The same small-crack growth rates have been plotted in Fig. 4 versus  $\Delta K$ . As expected the data show a transition in the rate of growth at about  $10^{-6}$  mm/cycle. However, a stratification among the growth rates has emerged. For a fixed  $\Delta K$  in the first growth region, the growth rates increase with increasing  $R$ , generally, irrespective of the applied load. Also, the slopes of the growth rates for the various data sets in the first growth region are similar.

In the second region, which exhibits a lower change in growth rates than the first, this stratification is still apparent but not as obvious as the growth rates begin to coalesce at higher  $\Delta K$  values. In both of these regions, the conditions of the loading sequence and the known response of the material [12] suggest that the minimum stress levels are above the closure level.

In referring to Table 1, note that two sets of loading conditions exist where the effective  $R$  values are very similar. The 75 kN load at the highest applied  $R$  and the 50 kN load at the

intermediate applied  $R$  have effective  $R = 0.676$  and  $0.672$ , respectively. The second set of loading conditions is the 75 kN load at the intermediate applied  $R$  and the 50 kN load at the lowest applied  $R$  have effective  $R = 0.615$  and  $0.608$ , respectively. A plot of the small-crack growth rates for each of these sets of loading conditions is shown in Fig. 5a and Fig. 5b. For each set of data, the growth rates for approximately the same value of effective  $R$  are very similar even though significant differences exist between the mean stress values shown in the figures and in Table 1. Apparently, similar values of the local  $R$  are sufficient to coalesce the growth rate data.

As previously discussed, the values of  $R$  for the low- $R$  blocks were selected to minimize load interactions. Fractographic evidence indicates that negligible crack growth or crack tip stretching are associated with a markerband block when the crack is small. The growth of small cracks during a low- $R$  block is several orders of magnitude larger than that for a markerband block. Thus, a damage zone at the crack tip due to the markerband block is not sufficient to disturb the majority of crack growth associated with a low- $R$  block. From a slightly different view, if load interactions are present, they are likely to affect all low- $R$  blocks similarly. Hence, their effects would be qualitatively subtractable.

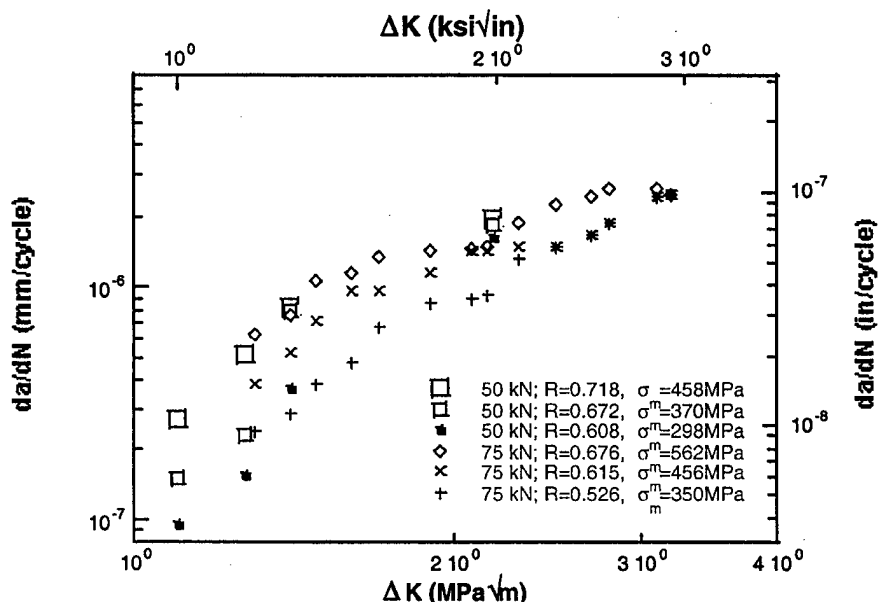
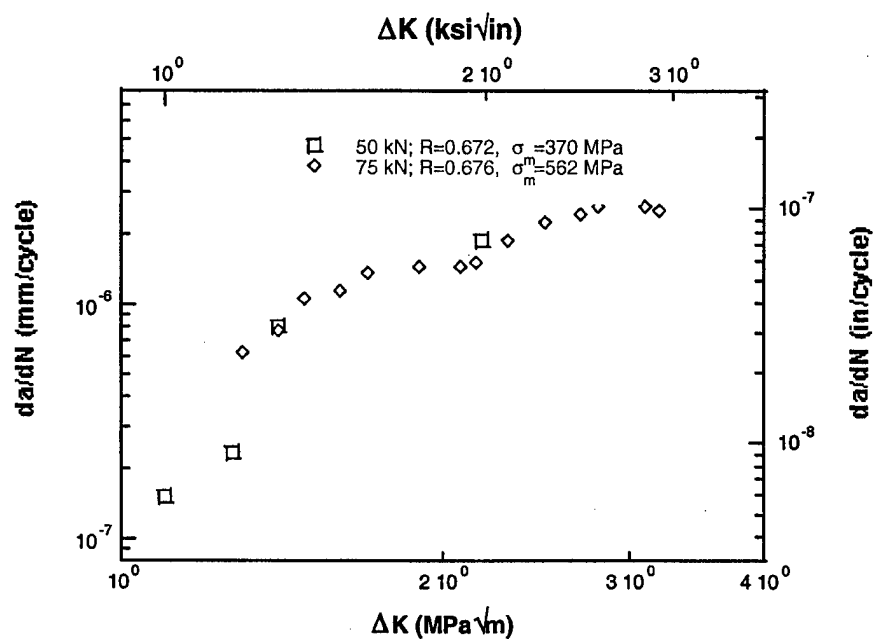


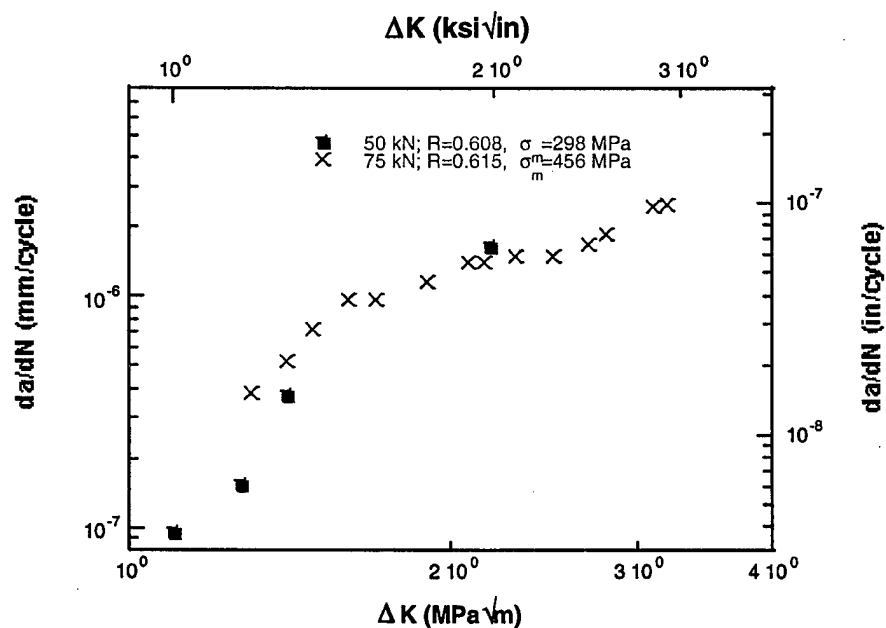
FIG. 4--Small-crack growth rates versus range of stress intensity factor.

#### Long-Crack Growth Behavior

The combined long- and small-crack growth data are shown in Fig. 6. Threshold stress intensity ranges for long cracks [13] vary from 2 to 3  $\text{MPa}\sqrt{\text{m}}$  for values of  $R$  considered in this study. A small-crack growth rate effect, where small cracks are growing at  $\Delta K$  values lower than long crack thresholds, is apparent for Al 2014T651. Note the good coalescence of the long-crack growth rates at the various high- $R$  levels. This result is consistent with the condition that closure is not occurring at  $R$  values used in these tests. For the long crack, the applied stress and stress range are the same as those experienced by the crack. However, some discrepancy as discussed in Ref. 9 exists between the long-crack growth rates produced by the load sequence in Fig. 2 and long-crack growth rates produced by constant amplitude applied



(a)



(b)

FIG. 5--Influence of mean stress on small-crack growth rates: (a)  $R=0.67$  and (b)  $R=0.61$ .

load [13]. Since the fatigue crack growth portions of failure surfaces at the low- $R$  value and the high- $R$  values are yielding topographical features that are similar to features associated with

crack front incompatibility [14], the difference in growth rates are attributed to incompatibility of crack front orientation when transitioning from low-R to high-R loading conditions and visa-versa.

Equal striation bands in long crack fractography largely confirmed the absence of all types of closure including roughness induced closure. Available empirical evidence and models suggest that given similar loading conditions, less closure is present as crack size diminishes. However, Mode II roughness induced closure may be present even when Mode I closure is not seen. As early crack growth is Mode II, roughness may possibly impede Mode II sliding. However, the clarity of striation bands on fractographs suggests the absence of Mode II closure which would have had an abrasive action on the fracture surface.

#### *Modeling Small-Crack Growth Behavior*

The small-crack growth rate at high R can be reasonably characterized by  $\Delta K$  and R in the two growth rate regions by using

$$da/dN = C(\Delta K)^m$$

where C and m are material parameters. In the first region of rapidly increasing growth rates,  $m \approx 3.6$  independent of R for the test conditions used in this investigation and C is a function of R or, equivalently, the mean stress. In the second region of slowly changing and converging growth rates, m becomes a function of R with values between 1.2 and 2.4 and C is also a function of R. This characterization in both of the two growth rate regions where either C or both m and C are dependent on R is contrary to the influence of crack closure where  $\Delta K$  can be modified to fit the data.

For long-crack growth behavior under constant amplitude applied load and for  $\Delta K$  occurring in this investigation,  $m \approx 3.3$  independent of R and C is independent of R.

#### **Concluding Remarks**

In summary, the results from the study suggest the following conclusions. A small crack effect is observed in Al 2014T651. Small-crack growth rate can be partitioned into two regimes. In the first regime, the crack length is greater than the grain size and less than a factor of the grain size. The factor is between 2 and 4 and appears to depend on a critical value of crack growth rate. In the second regime, the crack length is greater than this factor of the grain size and less than about 10 times the grain size. These two regimes reflect different material response to small-crack growth propagation. Small-crack growth propagation in the presence of a notch are influenced by  $\Delta K$  and R or equivalently,  $\Delta K$  and  $K_{max}$ . These effects noted at small-crack lengths disappear when the crack length is greater than 10 times the grain size.

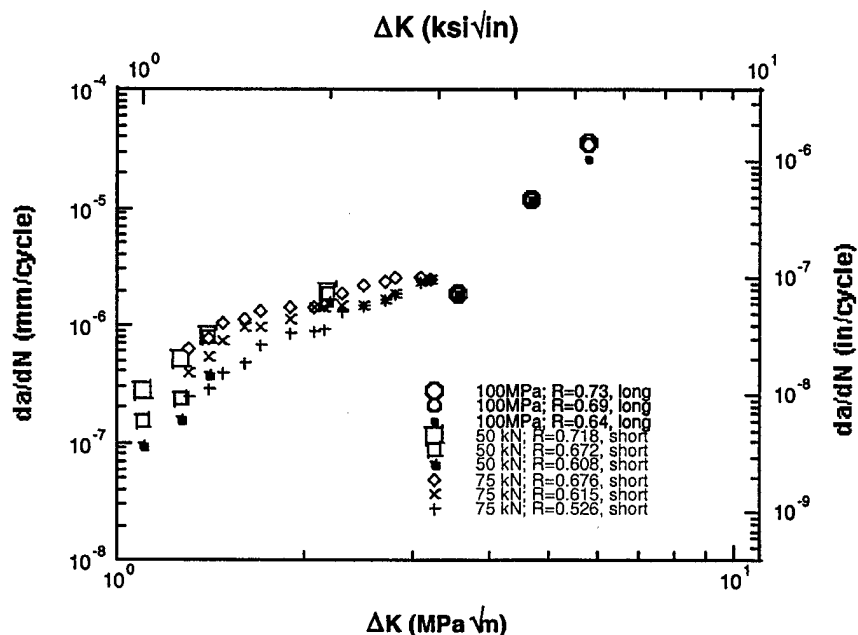


FIG. 6--Long- and small-crack growth rates versus range of stress intensity factor.

#### Acknowledgments

This research was performed at the Air Force Research Laboratory Materials and Manufacturing Directorate with support from AF Contract F33615-94-C-5200. The authors would like to acknowledge the helpful technical guidance and support provided by Dr. Jim Larsen of the Materials and Manufacturing Directorate, Wright-Patterson Air Force Base. The first author also appreciates the useful discussions with Dr. Raghu V. Prakash of the National Aerospace Laboratories, Bangalore, India.

#### References

- [1] Elber, W., "The Significance of Fatigue Crack Closure," *Damage Tolerance in Aircraft Structures, ASTM STP 486*, American Society for Testing and Materials, Philadelphia, 1971, pp. 230-242.
- [2] Forman, R. G., Kearney, V. E., and Engle, R. M., "Numerical Analysis of Crack Propagation in Cyclic Loaded Structures," *Journal Basic Engineering, Transactions ASME, Vol. 89*, 1967, pp. 459-464.
- [3] Newman, J. C. "A Crack-Closure Model for Predicting Fatigue Crack Growth under Aircraft Spectrum Loading," *Methods and Models for Predicting Fatigue Crack Growth under Random Loading, ASTM STP 748*, J. B. Chang and C. M. Hudson, Eds., American Society for Testing and Materials, 1981, pp. 53-84.
- [4] Booth, G. S. and Maddox, S. J., "Correlation of Fatigue Crack Growth Data Obtained at Different Stress Ratios," *Mechanics of Fatigue Crack Closure, ASTM STP 982*, J. C. Newman, Jr. And W. Elber, Eds., American Society for Testing and Materials, Philadelphia, 1988, pp. 516-527.

- [5] Walker, K., "The Effect of Stress Ratio During Crack Propagation and Fatigue for 2024-T3 and 7075-T6 Aluminum," *Effects of Environment and Complex Load History on Fatigue Life*, ASTM STP 462, American Society for Testing and Materials, Philadelphia, 1970, pp. 1-14.
- [6] Maddox, S. J., "The Effect of Mean Stress on Fatigue Crack Propagation: A Literature Review," *International Journal of Fracture*, Vol. 11, No. 3, June 1975, pp. 389-408.
- [7] Elber, W., "Fatigue Crack Closure Under Cyclic Tension," *Engineering Fracture Mechanics*, Vol. 2, 1970, pp. 37-45.
- [8] Nicholas, T. and Zuiker, J. R., "On the Use of the Goodman Diagram for High Cycle Fatigue Design," *International Journal of Fracture*, Vol. 80, 1996, pp. 219-235.
- [9] Sunder, R., Porter, W. J., and Ashbaugh, N. E., "The Effect of Stress Ratio on Fatigue Crack Growth Rate in the Absence of Closure," *International Journal of Fatigue*, Vol. 19, Supp. No. 1, 1997, pp. S211-S221.
- [10] Davidson, D. L. and Lankford, J., "Fatigue Crack Growth in Metals and Alloys: Mechanisms and Micromechanisms," *International Materials Reviews*, Vol. 37, No. 2, 1977, pp. 45-76.
- [11] Miller, K. J., "The Three Thresholds for Fatigue Crack Propagation," *Fatigue and Fracture Mechanics: 27th Volume*, ASTM STP 1296, R. S. Piascik, J. C. Newman, and N. E. Dowling, Eds., American Society for Testing and Materials, 1997, pp. 267-286.
- [12] Ashbaugh, N. E., Dattaguru, B., Khobaib, M., Nicholas, T., Prakash, R. V., Ramamurthy, T. S., Seshadri, B. R., and Sunder, R., "Experimental and Analytical Estimates of Fatigue Crack Closure in an Aluminum-Copper Alloy Part I: Laser Interferometry and Electron Fractography," *Fatigue & Fracture of Engineering Materials & Structures*, Vol. 20, No. 7, 1997, pp. 951-961.
- [13] Sunder, R., Prakash, R. V., and Mitchenko, E. I., "Calculation of Spectrum Load Notch Root Crack Growth Rate Under Elastic and Inelastic Conditions," *Advances in Fatigue Lifetime Predictive Techniques: Second Volume*, ASTM STP 1211, M. R. Mitchell and R. W. Landgraf, Eds., American Society for Testing and Materials, Philadelphia, 1993, pp. 30-44.
- [14] Schijve, J., "Fatigue Damage Accumulation and Incompatible Crack Front Orientation," *Engineering Fracture Mechanics*, Vol. 6, 1974, pp. 245-252.



Reference: John, R., DeLuca, D., Nicholas, T., and Porter, W.J., "Near-Threshold Crack Growth Behavior of a Single Crystal Ni-Base Superalloy Subjected to Mixed Mode Loading," Mixed-Mode Crack Behavior, ASTM STP1359, 1999.

## Near-Threshold Crack Growth Behavior of a Single Crystal Ni-Base Superalloy Subjected to Mixed Mode Loading

Reji John, Dan DeLuca<sup>1</sup>, Ted Nicholas, and John Porter<sup>2</sup>

Metals, Ceramics & NDE Division (AFRL/MLLN), Materials and Manufacturing Directorate,  
Air Force Research Laboratory, Wright-Patterson AFB, OH

<sup>1</sup> Pratt&Whitney, Mechanics of Materials, West Palm Beach, FL

<sup>2</sup> University of Dayton Research Institute, Dayton, OH

### ABSTRACT

Ni-base single crystal superalloys, which are used in applications such as gas turbine engine blades, are primarily loaded along the  $\langle 001 \rangle$  direction. Mode II (crystallographic shear) type cracking along the (111) plane is frequently the mode of growth in the early stages of fatigue failure of these components. Disks with a middle crack were used to characterize crystallographic shear crack growth from machined flaws oriented parallel to a (111) plane of a single crystal alloy. Automated crack growth experiments were conducted at constant stress ratio in the near threshold regime. Various combinations of mode I and mode II loading were achieved by orienting the machined flaw at different angles ( $\theta$ ) to the loading axis. Loading angle  $\theta=0^\circ$  (pure mode I loading) resulted in crystallographic crack extension along alternating (111) slip systems producing a zig-zag pattern. This orientation exhibited significant resistance to self-similar crack growth from the machined flaw. In contrast, self-similar crack growth was achieved with relative ease for loading angles,  $\theta \neq 0^\circ$  (mixed mode). In the mixed mode tests with  $K_I > 0$ , the crack growth rate was 10 to 50 times higher than that under mode I loading. Preliminary results indicate that crack growth is non-crystallographic at 593°C.

**Keywords** Fatigue crack growth, high temperature, microstructure, mixed mode, mode I, mode II, single crystal, superalloy, threshold

## **BACKGROUND**

Ni-base single crystal superalloys, which are used in applications such as turbine engine blades, are primarily loaded along the  $\langle 001 \rangle$  direction. A significant cause of failure of such components is high cycle fatigue (HCF) [1]. Two basic types of fatigue fracture occur at the root of the engine blades subjected to HCF loading: non-crystallographic mode I cracking normal to the principal load axis and crystallographic shear fracture parallel to (111) crystallographic planes. Mode II (crystallographic shear) type cracking along the (111) plane is frequently the mode of growth in the early stages (stage I) of fatigue. The crystallographic initiation and crack growth mechanism ensures that the local conditions at the tip of a stage I microcrack are mixed mode regardless of the remote loading mode mixity [2]. Hence, prior to successful application of fracture mechanics for solving such HCF problems, we need to understand issues including the near-threshold behavior under mixed mode loading and the influence of crystallographic initiation sites [1]. Nicholas and Zuiker [3] used a fracture mechanics based analysis to evaluate the applicability of the Goodman diagram for high cycle fatigue design including low-cycle and high-cycle fatigue (LCF/HCF) interactions. Although mode I threshold stress intensity factor range,  $\Delta K_{I,th}$  was used during the analysis, Nicholas and Zuiker [3] identified the need to account for mode II or near-mode II induced HCF crack initiation and subsequent mixed mode crack growth. This requirement implies that the near-threshold mixed mode crystallographic crack growth behavior should be characterized under all possible combinations of mode mixity and flaw orientation.

Many investigators [4-16] have addressed the issue of mixed mode crack growth in various materials. Recently, John et al. [16] investigated the crack growth behavior of Ti-6Al-4V under mixed mode loading using a centrally notched disk geometry. The loading angle (=angle between the flaw and the load-line) was chosen such that pure mode II loading conditions existed at the tips of the starter flaw. The crack initiated at an angle of  $\approx 70^\circ$  with respect to the starter flaw and propagated along a curved path towards the loading point. Similar curved crack propagation paths have been observed in most materials with isotropic properties [4,6-8]. Limited results [9-15] are available for addressing mixed mode crack growth in superalloys. Telesman and Ghosn [12-14] investigated the crystallographic crack growth resulting in local mixed mode conditions at the crack tip. The remote applied loading was always mode I. Reed et al. [9-11] investigated the effects of remote mixed mode loading using asymmetric four point bend specimens with an edge crack. The starter flaw was oriented along the (001) plane and the crack growth was in the  $\langle 110 \rangle$  direction. Mode mixity ratios ( $= K_{II}/K_I$ ) of 0, 0.6 and 1.4 were studied. In this geometry,  $K_{II}/K_I$  remained near-constant during the test. The results showed that the crack growth rate under mixed mode loading was significantly faster than that under mode I loading. The best correlation of the data from the different tests was obtained using  $\Delta K_I$ . These tests were conducted at room temperature. Cunningham et al. [17] reported that the failure mode changed from crystallographic at room temperature to non-crystallographic at elevated temperature. In addition, the mode mixity can be expected to change continuously during crack extension and mode I loading could be either tensile or compressive. Hence, a program was initiated by the US Air Force to characterize crystallographic shear crack growth from machined flaws oriented parallel to a (111) plane of a single crystal superalloy subjected to mode I and mixed mode (modes I + II) loading. This paper discusses the effects of mode mixity, microstructure and temperature on the fatigue crack growth from machined flaws which were oriented near-parallel to a (111) plane.

## **EXPERIMENTAL PROCEDURE**

### **Test Geometry**

The geometry adapted for testing under mixed mode loading was the "Brazilian" Disk with a Middle crack subjected to Compressive loading, DM(C), as shown in Fig. 1. The DM(C) geometry has been used to investigate the mixed mode fracture of polymethylmethacrylate [18], graphite [19] and sintered carbide [20], and mixed mode fatigue crack growth in the high strength steel, 35NCD16, and 316 stainless steel [21]. The DM(C) geometry is ideal for testing under a wide range of mode I and mode II loading conditions. Mode I stress intensity factor,  $K_I$  and mode II stress intensity factor,  $K_{II}$ , solutions are available [18-20] for this geometry for crack length to width ratio, ( $\alpha = 2a/W$ ) up to 0.6 and loading angle ( $\theta$ ) ranging from 0 to 90°. Recently, John and Johnson [22] extended the solutions up to  $2a/W=0.8$  in the range  $0 \leq \theta \leq 90^\circ$  using finite element analysis.

Various ratios of mode II stress intensity factor to mode I stress intensity factor,  $K_{II}/K_I$  can be achieved at the crack tip by orienting the crack at different angles ( $\theta$ ) to the loading axis (Fig. 1). Figure 2 shows the effect of flaw orientation on  $K_I$  and  $K_{II}$  for  $\alpha = 0.30$ . When  $\theta = 0$ ,  $K_{II} = 0$ , resulting in pure mode I loading conditions, and when  $\theta \approx 27^\circ$ ,  $K_I = 0$ , resulting in pure mode II loading conditions. For  $\theta > 27^\circ$ ,  $K_I < 0$ , implying that the crack surfaces could be in contact with each other depending on the initial notch width and the applied load ratio. Figure 3 shows that for a constant load and  $\theta = 25^\circ$ ,  $K_I$  decreases and  $K_{II}$  increases with increase in  $\alpha$ . Hence, if a test is started with  $\theta = 25^\circ$  and  $\alpha = 0.3$ , as the crack extends in a self-similar path, the loading condition at the crack tip changes from pure mode II to mixed mode loading with  $K_I < 0$ . The typical dimensions of the specimens used during this study were: diameter,  $W \approx 30$  mm, thickness,  $B \approx 2.2$  mm, and initial crack length to width ratio,  $2a_0/W \approx 0.3$ . The initial starter flaw was created using an electrical discharge machining (EDM) technique. The width of the EDM flaw was typically  $\approx 0.3$  mm.

### Material

The material used was the columnar grain Ni-base superalloy (PWA1422) cast as a single crystal for purpose of this study. The composition of the material is (in weight percent): 9 Cr, 10Co, 12.5 W, 5 Al, 2 Ti, 1.6 Hf, 1 Cb, 0.14 C, 0.015 B and the balance in Ni. The specimens were prepared from cylindrical stock of the superalloy material such that the starter flaw was parallel to a (111) plane, i.e. the mode I loading was in the  $\langle 111 \rangle$  direction and the mode II loading was in the  $\langle 110 \rangle$  direction. The notch orientation with respect to the slip planes is shown in Fig. 1. The disk specimens were machined such that the flat surfaces were normal to the  $\langle 112 \rangle$  direction. Two microstructures identified as "standard" and "bimodal", as shown in Fig. 4, were investigated during this study. The standard microstructure consisted of  $\gamma'$  phase ranging in size from 0.5-1.0  $\mu\text{m}$  in a  $\gamma$  matrix. In contrast, the bimodal microstructure consisted of  $\gamma'$  phase sizes with two distinct populations: 0.2  $\mu\text{m}$  and  $\approx 1\text{-}4$   $\mu\text{m}$ . Most of the tests were conducted using specimens with the standard microstructure. Additional tests were conducted using specimens with bimodal microstructure to characterize the microstructure and temperature effects on the mixed mode crack growth behavior.

### Test Setup and Procedure

The DM(C) specimens were loaded in compression using ceramic anvils as shown in Fig. 5. The elevated temperature tests were conducted using an oven as indicated by the dashed line. Most of the tests were conducted in laboratory air at a frequency of 10-20 Hz with a load ratio,  $R$ , of 0.1 ( $=K_{\min}/K_{\max}$  at crack tip). The loading angles included  $\theta = 0, 16$  and  $27^\circ$ . The specimens were typically precracked under constant maximum load until crack initiation corresponding to  $\approx 1$ mm crack extension from the starter flaw was achieved. Following precracking, the applied load was shed simulating a threshold-type decreasing  $K_{\max}$  test. After the crack reached near-arrest conditions or  $2a/W \approx 0.8$ , all the mixed mode specimens were

rotated back to  $\theta = 0^\circ$  and loaded under mode I conditions with  $R=0.5$ . This high  $R$  testing ensured that the crack extended to failure with minimum contact between the crack surfaces, thus protecting the fracture surfaces for fractographic studies. In some cases the specimens were pulled apart after the crack had reached about 90-95% of the width. One test at  $\theta = 16^\circ$  was conducted under constant maximum load conditions up to failure. A test was also conducted at  $R=0.5$  to observe the influence of  $R$  on the fracture surface.

The direct current electric potential (DCEP) technique was used to monitor the crack growth during the above tests. The DCEP measurements were verified and/or corrected using periodic optical crack length measurements. The DCEP solution for a center-cracked geometry was used during the tests, consistent with the observed self-similar crack propagation in the DM(C) specimens. The DCEP measurements were within 10% of the optical measurements for  $0.3 \leq 2a/W \leq 0.8$ . Using the measured crack length versus cycles response,  $K_I$ ,  $K_{II}$ , and the crack growth rate,  $da/dN$ , were calculated as a function of crack length. Note that the  $K_I$  and  $K_{II}$  solutions were based on isotropic elasticity.

During the early stages of the test program, we noticed that the high stresses at the loading points resulted in failure at these locations prior to crack extension from the starter flaws. This problem was overcome by using aluminum and steel pads ( $\approx 3.2$  mm thick) at room and elevated temperatures, respectively, to distribute the contact load. The contact length was typically  $\approx 3.6$  mm along the circumference. Awaji and Sato [19] reported that the decrease in  $K_I$  and  $K_{II}$  is  $\approx 10\%$  compared to the solutions obtained assuming point-loads at the loading points. Hence,  $K_I$  and  $K_{II}$  solutions corresponding to point-loads [22] were considered applicable and used during this study.

## **RESULTS AND DISCUSSION**

### **Crack Growth Under Mixed Mode Loading**

The observed crack propagation paths for PWA1422 with standard microstructure tested under different combinations of  $K_{II}/K_I$  are shown schematically in Fig. 6. Note that these paths correspond to the specific orientation of the flaw as described earlier. Under pure mode I loading ( $\theta = 0^\circ$ ), the crack propagated along multiple crystallographic planes resulting in a zig-zag crack pattern. The crack growth rate ( $=da/dN$ ) was very low ( $\approx 6 \times 10^{-10}$  m/cycle) and the test was stopped when failure at the loading points was observed. The total crack extension from the starter flaw was  $\approx 1$  mm as shown in Fig. 7(a). Under mixed mode loading ( $\theta = 16$  and  $27^\circ$ ), the crack extension from the starter flaw was self-similar as shown in Figs. 6 and 7(b). The crystallographic crack propagation under mixed mode loading was essentially planar in contrast to that observed under mode I loading. In these tests, the cracks grew up to 80-90% of the width of the specimen when the test was stopped. As illustrated in Fig. 2,  $\theta = 16^\circ$  corresponds to a test initiating with  $K_I > 0$  and  $\theta = 27^\circ$  to a test initiating with  $K_I = 0$ . Both of these conditions exhibited planar crystallographic crack growth as shown in Fig. 6.

The observed crack pattern in PWA1422 (Fig. 6) under mixed mode loading is contrary to the curvilinear path commonly observed [4,6-8,16] in materials with isotropic properties. As discussed earlier, the crack growth behavior of Ti-6Al-4V under mixed mode loading was investigated using the DM(C) geometry [16]. This Ti-6Al-4V consisted of a duplex microstructure with  $\approx 60\%$  equiaxed primary alpha. The equiaxed primary alpha and the transformed regions were  $\approx 1 \mu\text{m}$  in diameter. The observed crack propagation path for  $\theta = 27^\circ$  in the Ti-6Al-4V is shown in Fig. 8. The loading angle  $\theta = 27^\circ$  was chosen such that pure mode II loading conditions existed at the tips of the starter flaw. Crack initiation occurred at an angle of  $\approx 70^\circ$  with respect to the starter flaw. The subsequent crack propagation occurred along a

curved path towards the loading point. The initiation angle is consistent with the mixed mode initiation theories proposed by Erdogan and Sih [23], Hussain et al. [24] and Sih [25]. The predicted propagation path for an isotropic material is also shown in Fig. 8. The prediction was obtained using the interactive PC-based finite element code, FRANC2DL [26]. The predicted path agrees well with the observed curved crack propagation path.

In addition to differences in propagation paths, mode I loading of PWA1422 did not facilitate planar crystallographic crack growth. Hence, the current results clearly show that the combination of mixed mode loading and orientation of the initial flaw used in this study (parallel to (111) plane) resulted in crack propagation along a (111) plane contrary to that observed in isotropic materials.

#### Mode Mixity Effects on Crack Growth Rate Behavior

The crack growth behavior of PWA1422 with the standard microstructure under three types of mixed mode loading conditions is discussed next. The variation of the applied  $K_I$  and  $K_{II}$  with increasing crack length for these tests is shown in Fig. 9.  $\theta = 16^\circ$  corresponded to an initial  $K_{II}/K_I \approx 2.0$  and  $\theta = 27^\circ$  to an initial  $K_I = 0$ . The main features of these tests are:

- (a)  $\theta = 16^\circ$  and constant maximum load:  
In this case,  $\Delta K_I$  was maintained near-constant ( $\approx 6.4 \text{ MPa}\sqrt{\text{m}}$ ) and  $\Delta K_{II}$  increased with increasing crack length.
- (b)  $\theta = 16^\circ$  and decreasing maximum load:  
In this case,  $\Delta K_{II}$  was maintained near-constant ( $\approx 10 \text{ MPa}\sqrt{\text{m}}$ ) and  $\Delta K_I$  decreased with increasing crack length.  $\Delta K_I$  was  $> 0$  during about 80% of the crack growth and  $< 0$  towards the end of the test. This implies that crack surface contact most likely occurred during the final stages of the test.
- (c)  $\theta = 27^\circ$  and decreasing maximum load:  
In this case,  $\Delta K_{II}$  was maintained near-constant ( $\approx 11 \text{ MPa}\sqrt{\text{m}}$ ) and  $\Delta K_I$  decreased with increasing crack length.  $\Delta K_{II}$  is close to that used for the previous test but  $\Delta K_I$  was  $< 0$  throughout the test. This implies that crack surface contact should have occurred during the entire test in contrast to the previous test (b), in which contact was expected only during the last part of the test.

The  $\theta = 16^\circ$  tests correspond to  $\Delta K_{II}/\Delta K_I \geq 2$  when  $\Delta K_I > 0$  in contrast to  $\Delta K_{II}/\Delta K_I \leq 1.4$  reported by Wu and Reed [11]. The data from the above tests (Fig. 9) are shown in Fig. 10 highlighting the effect of mode mixity on the crack growth rate ( $da/dN$ ) versus the applied stress intensity factor range,  $\Delta K$ , behavior. Note that the x-axis is shown linear to enable the plotting of  $\Delta K_I$  data for all the tests including the tests with  $\Delta K_I < 0$ . During this study,  $\Delta K_I < 0$  implies that the applied  $\Delta K_I$  is associated with  $K_{I,\text{max}} < 0$ . While we recognize that  $\Delta K_I$  being negative has no formal meaning, negative  $\Delta K_I$  is used to represent the relative magnitude of the compressive loading applied to the crack surfaces. The crack growth rate for the tests conducted at  $\theta = 16^\circ$  is almost 10-100X faster than that for the tests at  $\theta = 27^\circ$ . This can be attributed to the significant negative  $K_I$  during the  $\theta = 27^\circ$  tests as shown in Fig. 9. As discussed earlier,  $K_I < 0$  implies that the crack surfaces were in contact thus generating a frictional component which decreased the effective  $\Delta K_{II}$ ,  $\Delta K_{II,\text{eff}}$  at the crack tip, i.e.,

$$\Delta K_{II,\text{eff}} = \Delta K_{II} - \Delta K_{II,\text{friction}} \quad (1)$$

Equation (1) is consistent with Smith and Smith's [6] observation that mode II cracks in a compressive stress field can be modeled based on the Coulomb friction law.

The crack growth rate behavior for the  $27^\circ$  test is nearly vertical suggesting a near-threshold type behavior since the variation of the applied  $\Delta K_I$  and  $\Delta K_{II}$  is insignificant. This

trend, however, could be primarily due to the frictional component from the crack surface contact behind the crack tip. Note that the frictional component can be expected to increase with increase in crack length since  $\Delta K_I$  is negative throughout this test. Hua, Brown and Miller [5] reported that co-planar mode II growth can be expected to end in crack arrest, unless the crack flanks are separated by a mode I load. This trend can be compared to the  $\theta = 16^\circ$  tests in Fig. 10. The slope of the  $16^\circ/\text{Const. } P_{\max}$  test at low  $\Delta K_{II}$  values suggests a mode II threshold lower than that implied by the  $27^\circ$  data. Note, however, that  $\Delta K_I > 0$  for this threshold level. In contrast, the data from the  $16^\circ/\text{Dec. } P_{\max}$  test suggest an apparent mode II threshold similar to that obtained at  $\theta = 27^\circ$ . In this case,  $\Delta K_I < 0$  in the threshold regime, similar to the  $27^\circ$  test.

Comparison of Fig. 9(b) and 9(c) indicate that the  $K_I$  is  $< 0$  for the  $16^\circ/\text{Dec. } P_{\max}$  and  $27^\circ/\text{Dec. } P_{\max}$  tests at  $a \geq 10$  and  $5.5$  mm, respectively. The data from the  $27^\circ/\text{Dec. } P_{\max}$  test show a near-vertical trend of decreasing crack growth rate implying significant decrease in  $\Delta K_{II, \text{eff}}$ . This range of data corresponds to a crack extension of  $\approx 5$  mm under  $K_I < 0$ , as shown in Fig. 9(c). The  $da/dN$  vs.  $\Delta K_{II}$  data from the  $16^\circ/\text{Dec. } P_{\max}$  test show a sudden near-vertical decrease in crack growth rate when  $K_I$  becomes  $\leq 0$ . This range of data corresponds to a crack extension of  $\approx 1$  mm under  $K_I < 0$ , as shown in Fig. 9(b). Thus, comparison of the  $16^\circ/\text{Dec. } P_{\max}$  and  $27^\circ/\text{Dec. } P_{\max}$  tests shows clearly that a short surface contact zone behind the crack tip is sufficient to decrease or retard the crack growth under mode II conditions. The magnitude of the growth rate near threshold, however, seems to depend on the crack extension. The growth rate at longer crack extension ( $27^\circ/\text{Dec. } P_{\max}$ ) is slower than that at shorter crack extension ( $16^\circ/\text{Dec. } P_{\max}$ ) by  $\approx 2$  orders of magnitude.

The above results imply that if the mode mixity of the component changes unfavorably during service, i.e.  $K_{II}/K_I$  changes from  $< 0$  to  $> 0$ , then rapid crack growth can occur. Hence, reliable damage tolerance based design of components susceptible to crystallographic crack growth under mixed mode loading requires accurate characterization of the mixed mode loading conditions.

Numerous investigators [9-16] have attempted to model the crack tip driving parameter under mixed mode loading using an equivalent stress intensity factor range,  $\Delta K_{\text{eq}}$ , defined as,

$$\Delta K_{\text{eq}} = \sqrt{(\Delta K_I)^2 + (\Delta K_{II})^2} \quad \text{if } \Delta K_I \geq 0, \text{ and} \quad (2)$$

$$\Delta K_{\text{eq}} = \Delta K_{II} \quad \text{if } \Delta K_I < 0. \quad (3)$$

Equation (2) is based on the summation of the mode I and mode II energy components. A similar approach was considered during this study. This approach does not consider the increasing contribution of crack length to reduction in the effective driving force due to friction as discussed earlier. Figure 11 shows the data from Fig. 10 plotted using  $\Delta K_{\text{eq}}$ . For the loading cases with  $K_I < 0$ ,  $K_I$  was set  $= 0$ , based on a closure type correction. The data from the distinctly different  $16^\circ$  tests nearly collapse into a single curve. The magnitude of  $\Delta K_{\text{eq}}$  is close to  $\Delta K_{II}$  because  $\Delta K_I \ll \Delta K_{II}$ . The data from the  $16^\circ$  tests imply that  $\Delta K_{\text{eq}}$  could be a valid correlating parameter for  $\Delta K_{II}/\Delta K_I > 2$  with  $K_I > 0$ . The  $\Delta K_{\text{eq}}$  correlation based on tests with varying  $\Delta K_{II}/\Delta K_I$  is contrary to the  $\Delta K_I$  correlation reported by Reed et al. [11] based on constant  $\Delta K_{II}/\Delta K_I (\leq 1.4)$  tests. The data from the  $27^\circ$  test does not correlate with the data from the  $16^\circ$  tests. As discussed earlier, this lack of correlation can possibly be attributed to the significant friction occurring along the crack wake.

The limited data from the mode I test is also plotted in Fig. 11. A range is shown to highlight the range of possible values of applied  $\Delta K_I$  because of the non-self-similar crack extension. Figure 11 clearly shows that crystallographic crack growth along (111) planes under mixed mode loading could be 10-50X faster than that under pure mode I loading. A similar increase in crack growth rate under mixed mode loading compared to that under mode I loading was also reported by Wu and Reed [11]. This increase in crack growth rate implies that any damage tolerance based design using only mode I data can lead to overestimation of crack growth life when actual service conditions produce mixed mode loading along a potential failure plane. In addition, the presence of surface or near surface defects in the region of mixed mode loading (e.g. at the root of the blades) could result in crystallographic initiation and rapid growth under loads lower than that expected under mode I loading.

#### Mode Mixity Effects on Fracture Surface

Figure 12 shows the fracture surface of a specimen tested with  $\theta = 27^\circ$  as illustrated in Fig. 9(c). This specimen was tested under mixed mode loading at  $R=0.1$  up to near-arrest conditions. At the end of the test, the specimen was rotated to  $\theta = 0^\circ$  and fatigued under pure mode I loading at high  $R (=0.5)$ . The fracture surface under mixed mode loading is distinctly different from that under mode I loading. The mixed mode fracture surface is planar throughout the test, which is typical of crystallographic fracture. In contrast, the mode I fracture surface is non-planar, which is consistent with crystallographic fracture along multiple planes (also shown in Fig. 7(a)). Mixed mode tests conducted at  $R=0.5$  also showed planar crystallographic fracture surface similar to the test at  $R=0.1$ . The non-planar crystallographic fracture is also consistent with low crack growth rates observed under mode I loading as shown in Fig. 11. No distinct difference was observed between the fractures surfaces of the specimens tested at  $16^\circ$  and  $27^\circ$ .

#### Effect of Microstructure and Temperature

Figure 13 compares the mixed mode crack growth behavior from the specimens with standard and bimodal microstructures. The microstructures were shown earlier in Fig. 4. The data in Fig. 13 were obtained from room temperature tests conducted at  $\theta = 16^\circ$  and  $R=0.1$ . The crack propagation in the specimen with bimodal microstructure was similar to that shown in Figs. 6 and 7(b). Only the data corresponding to  $K_I > 0$  are shown in the Fig. 13. The crack growth rate in the standard microstructure is  $\approx 10X$  faster than that in the bimodal microstructure. Examination of the fracture surfaces did not reveal any obvious differences. Both the fracture surfaces exhibited planar crystallographic crack growth similar to that shown in Fig. 12.

Figure 14 shows the crack propagation observed in the specimen with bimodal microstructure which was tested at  $593^\circ\text{C}$  ( $\theta = 16^\circ$ ,  $R=0.1$ ). The observed crack path is similar to the curved path seen in isotropic materials as shown in Fig. 8. This propagation path is in sharp contrast to the self-similar crystallographic crack extension observed at  $21^\circ\text{C}$  as shown in Fig. 6. The change in the crack extension path from a (111) flaw at elevated temperatures could be attributed to an environmental effect. The observed change in crack path with increase in temperature is consistent with observations of Cunningham et al. [17]. Tests are in progress to characterize the temperature effects on the mixed mode crack growth from (111) flaws.

### CONCLUSIONS

The centrally notched disk geometry, DM(C), can be used to characterize the mixed mode crack growth behavior in single crystal superalloys using the DCEP technique to monitor self-similar crack growth. A particular flaw orientation with respect to the primary loading axis of the

single crystal geometry can result in self-similar crack growth when the material is subjected to mixed mode loading, contrary to that observed in isotropic materials. Mixed mode loading with  $K_I > 0$  can produce crack growth rates 10 to 50 times faster than that under mode I loading. Mixed mode loading with  $K_I < 0$  can produce threshold type crack growth behavior implying an apparent arrest. Data obtained with  $K_I > 0$ , show that the bimodal microstructure is significantly more damage tolerant than the standard microstructure under mixed mode loading. In the bimodal microstructure, mixed mode loading at 593°C did not produce planar crystallographic crack extension as did the tests at room temperature.

### **ACKNOWLEDGMENT**

This research was conducted at Air Force Research Laboratory (AFRL/MLLN), Materials and Manufacturing Directorate, Wright-Patterson Air Force Base, OH 45433-7817, USA. Reji John and John Porter were supported under on-site contract number F33615-94-5200. The damage tolerant material described in this publication is the property of United Technologies and is covered under U.S. Patents 5605584 and 5725692. The authors gratefully acknowledge the extensive testing support provided by Mr. Andrew Lackey from the University of Dayton Research Institute.



## REFERENCES

1. Cowles, B.A., "High Cycle Fatigue in Aircraft Gas Turbines - An Industry Perspective," *International Journal of Fracture*, Vol. 80, 1996, pp. 147-163.
2. McDowell, D.L., "Basic Issues in the Mechanics of High Cycle Fatigue," *International Journal of Fracture*, Vol. 80, 1996, pp. 103-145.
3. Nicholas, T. and Zuiker, J.R., "On the Use of the Goodman Diagram for High Cycle Fatigue Design," *International Journal of Fracture*, Vol. 80, 1996, pp. 219-235.
4. Multiaxial Fatigue, ASTM STP 853, K.J. Miller and M.W. Brown, Eds., American Society for Testing and Materials, West Conshohocken, PA, 1985.
5. Hua, G., Brown, M.W., and Miller, K.J., "Mixed-Mode Fatigue Thresholds," *Fatigue of Engineering Materials and Structures*, Vol. 5, 1982, pp. 1-17.
6. Tong, J., Yates, J.R., and Brown, M.W., "The Formation and Propagation of Mode I Branch Cracks in Mixed Mode Fatigue Failure," *Engineering Fracture Mechanics*, Vol. 56, No. 2, 1997, pp. 213-231.
7. Qian, J. and Fatemi, A., "Mixed Mode Fatigue Crack Growth: A Literature Survey," *Engineering Fracture Mechanics*, Vol. 55, No. 6, 1996, pp. 969-990.
8. Tong, J., Yates, J.R., and Brown, M.W., "The Significance of Mean Stress on the Fatigue Crack Growth Threshold for Mixed Mode I + II Loading," *Fatigue and Fracture of Engineering Materials*, Vol. 17, No. 7, 1994, pp. 829-838.
9. Reed, P.A.S. and King, J.E., "Mixed Mode Effects in Ni-Base Single Crystals - Preliminary Results," *Scripta Metallurgica*, Vol. 26, 1992, pp. 1829-1834.
10. Reed, P.A.S. and King, J.E., "Orientation Effects on Fatigue Crack Growth in Udimet 720 Single Crystals," *Fatigue '93*, J.-P. Bailon and J.I. Dickson, Eds., Engineering Materials Advisory Services Ltd., West Midlands, U.K., 1993, pp. 841-846.
11. Wu, X.D. and Reed, P.A.S., "Mode I and Mixed Mode I/II fatigue of Ni-Base Single Crystal Udimet 720 in Air and in Vacuum," *Fatigue '96*, G. Lütjering and H. Nowack, Eds., Elsevier Science Ltd., Oxford, U.K., 1996, pp. 855-860.
12. Telesman, J. and Ghosn, L.J., "The Unusual Near-Threshold FCG Behavior of a Single Crystal Superalloy and the Resolved Shear Stress as the Crack Driving Force," *Engineering Fracture Mechanics*, Vol. 34, No: 5/6, 1989, pp. 1183-1196.
13. Telesman, J. and Ghosn, L.J., "Effect of Crystal Orientation Effects on the Fatigue Crack Growth Behavior of a Single Crystal Alloy," *Fatigue '93*, J.-P. Bailon and J.I. Dickson, Eds., Engineering Materials Advisory Services Ltd., West Midlands, U.K., 1993, pp. 835-840.
14. Telesman, J. and Ghosn, L.J., "Fatigue Crack Growth Behavior of PWA 1484 Single Crystal Superalloy at Elevated Temperatures," *ASME*, 95-GT-452, 1994, pp. 1-11.
15. John, R., Nicholas, T., Lackey, A.F., and Porter, W.J., "Mixed Mode Crack Growth in a Single Crystal Ni-Base Superalloy," *Fatigue '96*, G. Lütjering and H. Nowack, Eds., Elsevier Science Ltd., Oxford, UK, May 1996, pp. 399-404.
16. John, R., Nicholas, T., Lackey, A.F., and Johansen, K., "Mixed-Mode Fracture Behavior of Ti-6Al-4V," To be published, 1998.
17. Cunningham, S.E., DeLuca, D.P., and Haake, F.K., "Crack Growth and Life Prediction in Single Crystal Nickel Superalloys," *WL-TR-94-4089*, Vol. I, Materials and Manufacturing Directorate, Air Force Research Laboratory (AFRL), Wright-Patterson Air Force base, OH, February 1996.
18. Atkinson, C., Smelser, R.E. and Sanchez, J., "Combined Mode Fracture via the Cracked Brazilian Disk Test," *International Journal of Fracture*, Vol. 18, 1982, pp. 279-291.
19. Awaji, H. and Sato, S., "Combined Mode Fracture Toughness Measurement by the Disk Test," *Journal of Engineering Materials and Technology*, Vol. 100, April 1978, pp. 175-182.
20. Yarema, S. Ya., Ivanitskaya, G.S., Maistrenko, A.L., and Zboromirskii, A.I., "Crack Development in a Sintered Carbide in Combined deformation of Types I and II," *Problemy Prochnosti*, No. 8, August 1984, pp. 51-56.

21. Louah, M., Pluvinage, G., and Bia, A., "Mixed Mode Crack Growth Using the Brazilian Disc," *Fatigue 87*, Editors: R.O. Ritchie and E.A. Starke, Jr., Engineering Materials Advisory Services, Ltd., West Midlands, U.K, 1987, pp. 969-977.
22. John, R., and Johnson, D.A., " $K_I$  and  $K_{II}$  Solutions for a Centrally Notched Disk," To be published, 1998.
23. Erdogan and Sih G., "On the Crack Extension in Plates Under Plane Loading and Transverse Shear," *Journal of Basic Engineering*, ASME, Vol. 85, 1963, pp. 519-527.
24. Hussain, M.A., Pu, S.L., and Underwood, J.H., "Strain Energy Release Rate for a Crack Under Combined Mode I and Mode II," *Fracture Analysis, ASTM STP 560*, American Society for Testing and Materials, West Conshohocken, PA, 1974, pp. 2-28.
25. Sih, G.C., "Strain Energy Density factor Applied to Mixed Mode Crack Problems," *International Journal of Fracture*, Vol. 10, No. 3, 1987, pp. 305-321.
26. James, M. and Swenson, D., "FRANC2D/L: A Crack Propagation Simulator for Plane Layered Structures," Kansas State University, Manhattan, KS, U.S.A., Available through the Internet at <http://www.mne.ksu.edu/~franc2d/>, 1997.

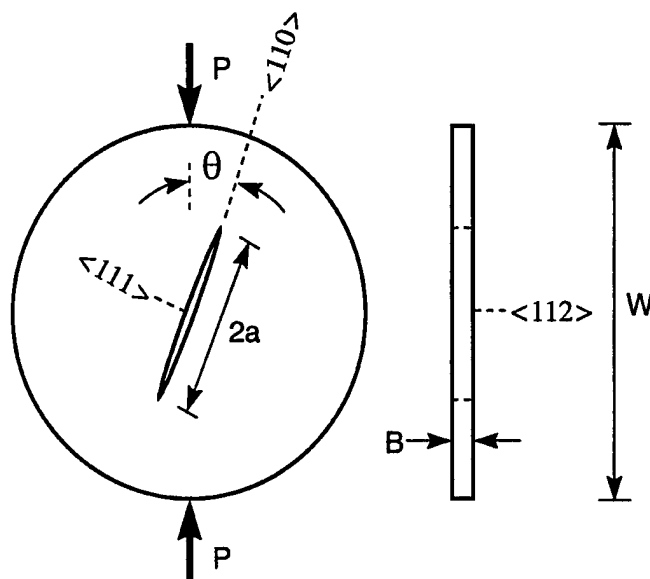


Fig. 1. Schematic of a centrally notched disk subjected to compression.

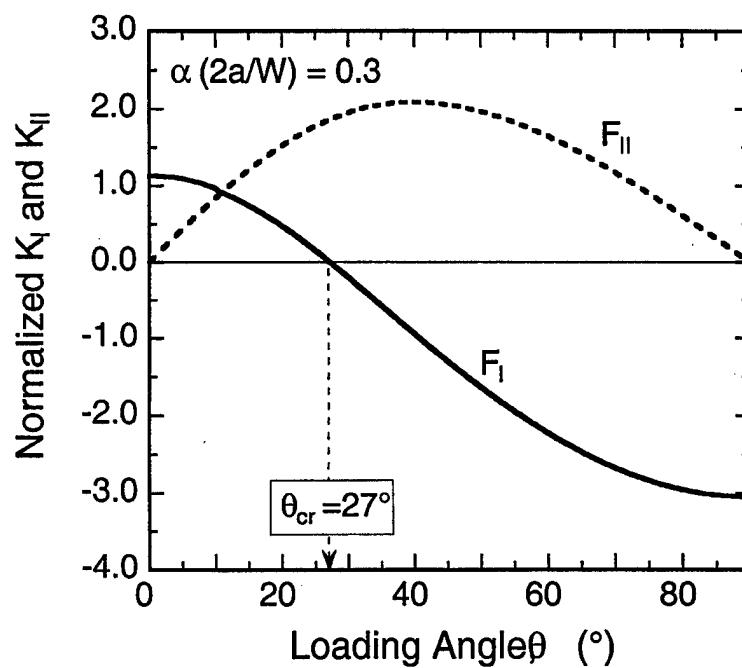


Fig. 2. Effect of flaw orientation ( $\theta$ ) on normalized  $K_I$  and  $K_{II}$ .  
 $(F = K / [\sigma \sqrt{a}], \sigma = 2P / [\pi BW])$

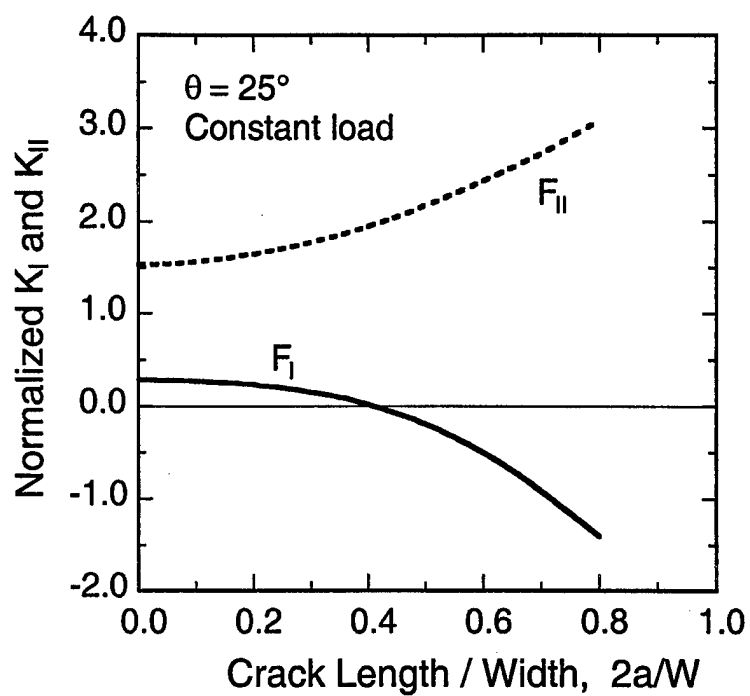
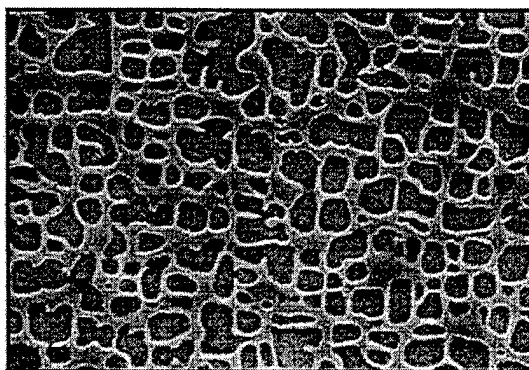
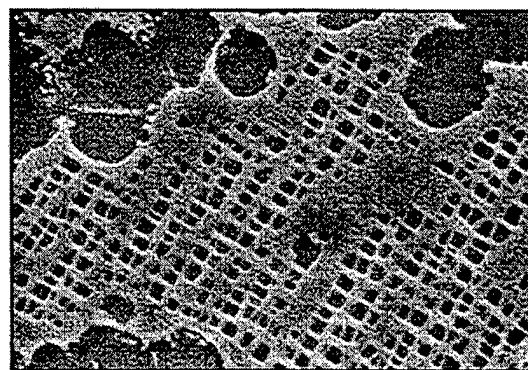


Fig. 3. Variation of  $K_{II}$  and  $K_I$  with normalized crack length.  
 $(F = K / [\sigma \cdot (\cdot a)], \cdot \cdot \sigma = 2P / [\pi BW])$



1  $\mu\text{m}$

(a) Standard microstructure



1  $\mu\text{m}$

(b) Bimodal microstructure

Fig. 4. Standard and bimodal microstructures investigated during this study.

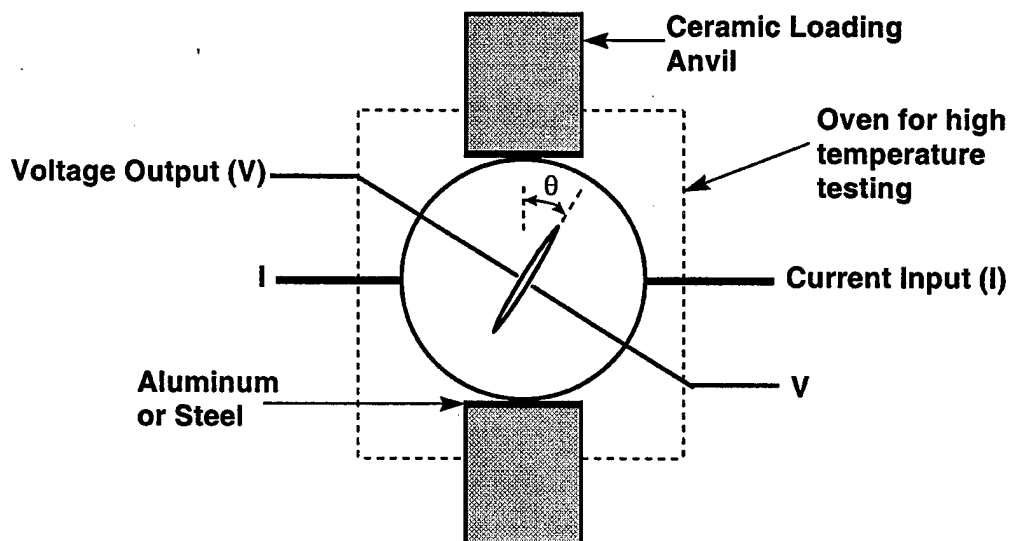


Fig. 5. Schematic of test set-up.

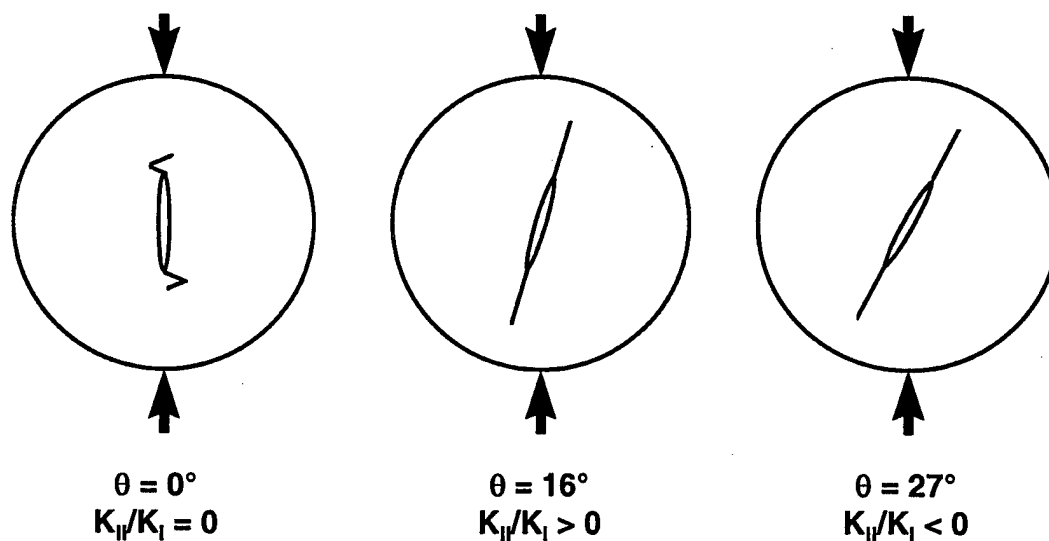
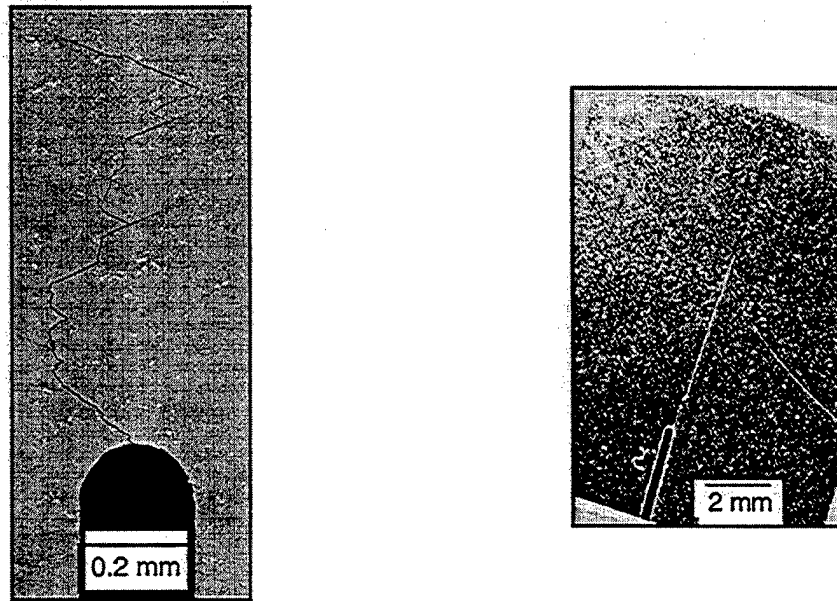


Fig. 6. Propagation paths of cracks emanating from a (111) flaw in PWA1422 with standard microstructure. Note that mode I and mode II loading was applied in the  $\langle 111 \rangle$  and  $\langle 110 \rangle$  directions, respectively.



(a)  $\theta = 0^\circ$  with  $K_{II} = 0$  and  $K_I > 0$  (Mode I)

(b)  $\theta = 16^\circ$  with  $K_I \geq 0$  (Mixed Mode)

Fig. 7. Mode mixity effects on the propagation paths of cracks emanating from a (111) flaw in PWA1422 with standard microstructure. The loading-line is vertical. (a)  $\theta = 0^\circ$  with  $K_{II} = 0$ , and (b)  $\theta = 27^\circ$  with  $K_I \leq 0$ .

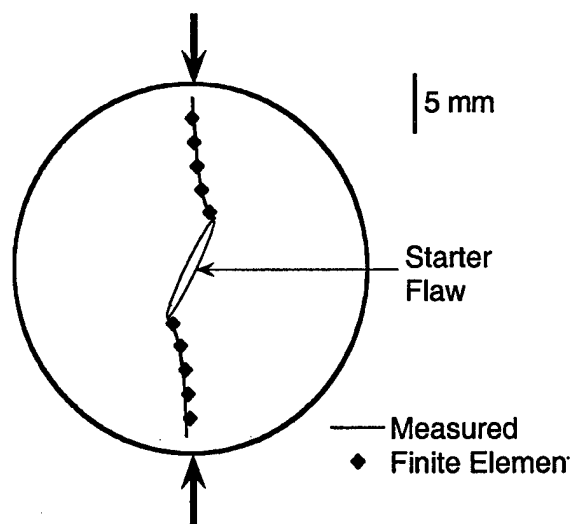


Fig. 8. Measured and predicted mixed mode crack propagation path in a material with isotropic properties (Ti-6Al-4V).

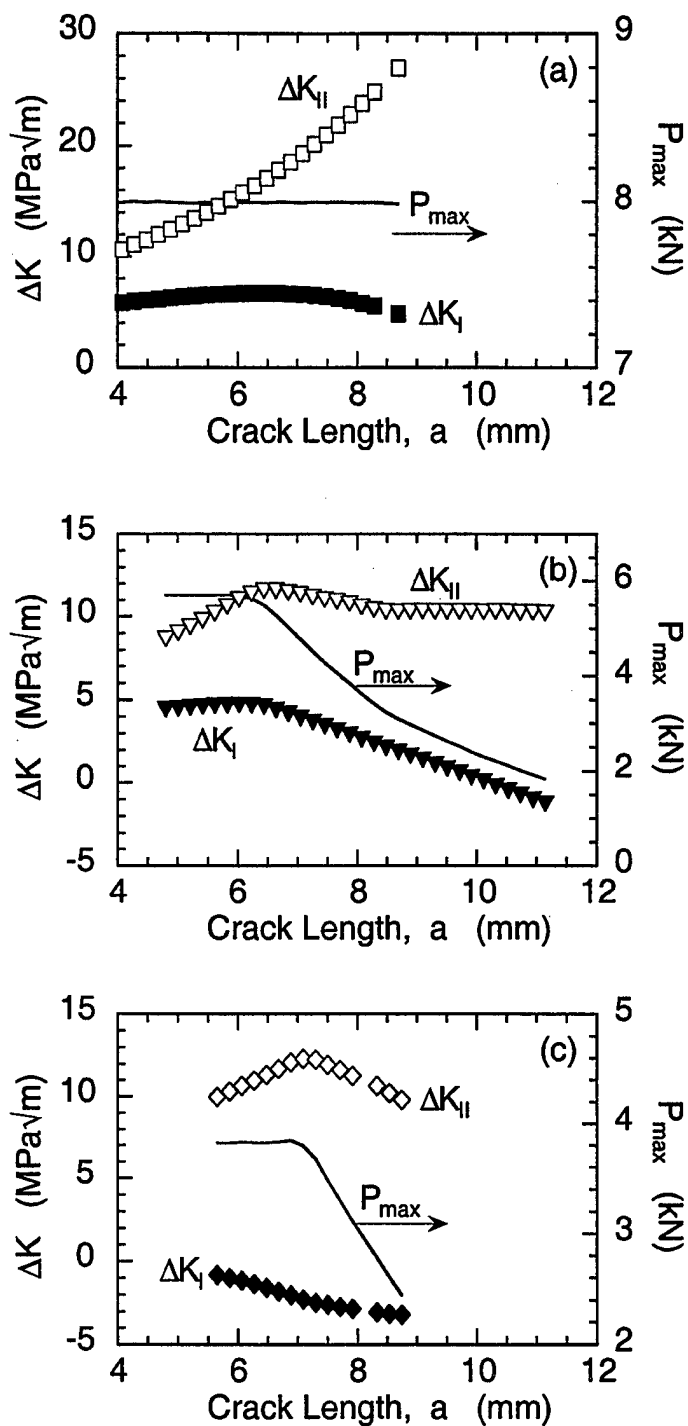


Fig. 9. Effect of loading angle ( $\theta$ ) and crack length on applied  $K_I$  and  $K_{II}$  at the crack tip.  
 (a)  $\theta = 16^\circ$  and  $P_{max}$  constant, (b)  $\theta = 16^\circ$  and  $P_{max}$  decreasing, and (c)  $\theta = 27^\circ$  and  $P_{max}$  decreasing. Note that  $\Delta K_I < 0$  implies that  $K_{I,max} < 0$ .

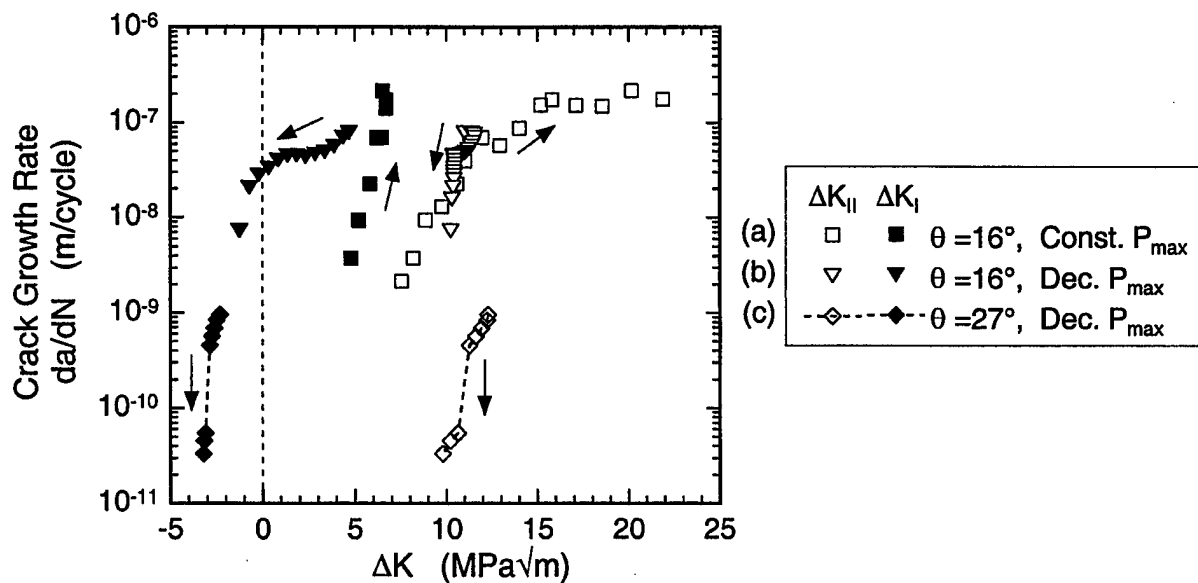


Fig. 10. Mode mixity effects on crack growth rate behavior of PWA1422 with standard microstructure. (a), (b) and (c) correspond to the loading histories shown in Fig. 9. Arrows indicate relationship with respect to crack growth direction.

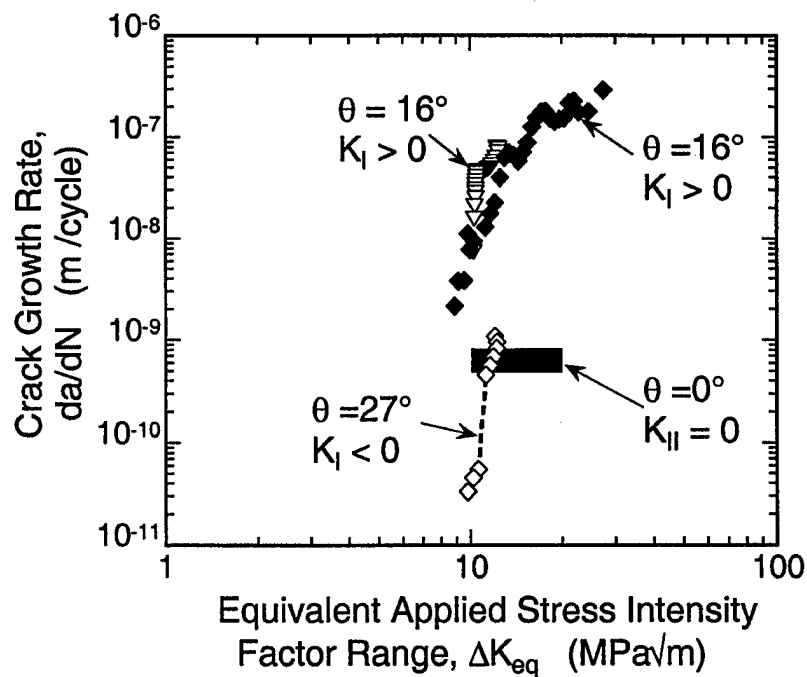


Fig. 11. Correlation of mixed mode crack growth behavior.



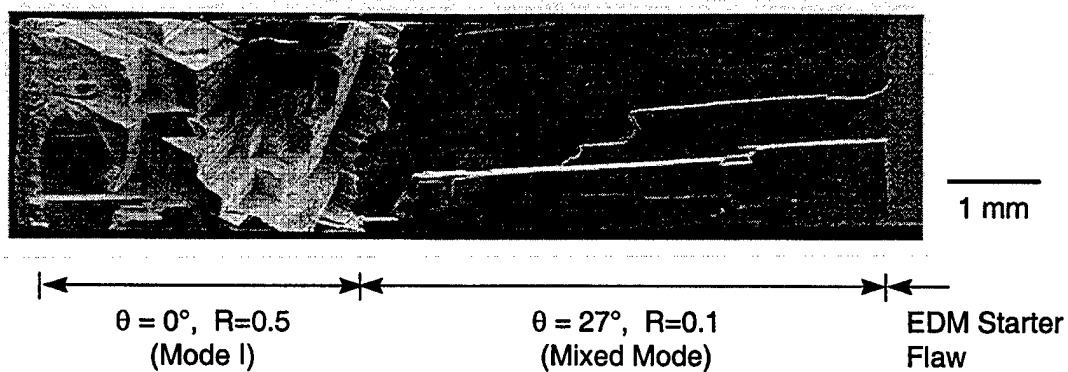


Fig. 12. Effect of mode mixity on the fracture surface.

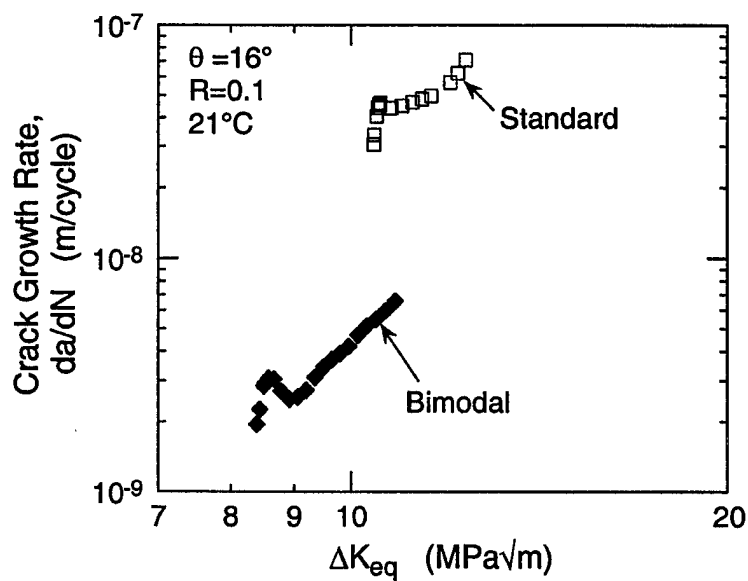


Fig. 13. Effect of microstructure on mixed mode crack growth at  $21^\circ\text{C}$ .  
Data shown correspond to  $K_{I,max} > 0$ . ( $\theta = 16^\circ, R=0.1$ ).

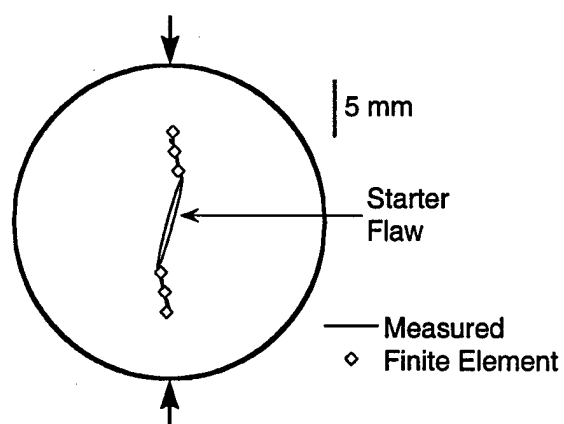


Fig. 14. Propagation path of a crack emanating from a (111) flaw in PWA1422 (bimodal microstructure) tested at 593°C.

Reference: Larsen, J.M., S.M. Russ, D.C. Maxwell, and B.D. Worth, "The Role of Threshold Fatigue Crack Growth in Life Prediction of the Alloy Ti-6Al-4Sn-2Zr-6Mo Under High Cycle Fatigue Spectra," Analysis and Design Issues for Modern Aerospace Vehicles - 1997, G.J. Simitses, Ed., AD Vol 55, The American Society of Mechanical Engineers, New York, NY, pp. 443-448.

# **THE ROLE OF THRESHOLD FATIGUE CRACK GROWTH IN LIFE PREDICTION OF THE ALLOY Ti-6Al-2Sn-4Zr-6Mo UNDER HIGH CYCLE FATIGUE SPECTRA**

**James M. Larsen and Stephan M. Russ**

Materials Directorate, Air Force Research Laboratory (WL/MLLN)  
Wright-Patterson Air Force Base, OH 45433, U.S.A.

**David C. Maxwell and Brian D. Worth**

The University of Dayton Research Institute  
Dayton, OH 45419-0128, U.S.A.

## **ABSTRACT**

Damage tolerance methods are widely used to assure reliability of fracture critical components in advanced gas turbine engines. Although low cycle fatigue often determines component lifetime, high cycle fatigue of airfoils and airfoil attachment regions is a growing concern. Crack-growth-rate behavior tends to dominate life under low cycle fatigue, but crack formation and the threshold crack growth condition,  $\Delta K_{th}$ , are crucial under high cycle fatigue. In addition to material-dependent effects, key factors controlling fatigue crack growth thresholds in titanium alloys used in turbine engines include effects of load spectra, crack geometry, crack size, and residual stress. The utility of  $\Delta K_{th}$  as a life prediction criterion is examined under load histories that contain both low and high cycle fatigue. These results are discussed with respect to life management methods used for titanium-alloy fan and compressor components in high performance turbine engines.

## **INTRODUCTION**

Major rotating components in gas turbine engines are exposed to low-frequency, low-cycle fatigue (LCF) produced by variations in engine speed. Each flight involves one major fatigue cycle, produced by the ground-air-ground excursion, and numerous additional low-frequency fatigue cycles of less severe amplitude caused by routine in-flight maneuvers. In some instances, selected components may also experience occasional transient intervals of high-cycle fatigue (HCF) at frequencies up to several kilohertz.

Turbine engine components are defined as "fracture critical" if their failure would result in loss of

the aircraft. To assure engine reliability, since 1984 the Air Force has required that fracture critical components be designed and life-managed according to a damage tolerant approach specified by the Engine Structural Integrity Program (ENSIP) (U. S. Air Force, 1984). Under this specification a component must be capable of achieving its design lifetime in the presence of realistic intrinsic material defects and service-induced damage. The damage tolerance requirement has been applied primarily to engine disks and spacers, while airfoils, which are not normally fracture critical, have typically been exempt.

The high-cycle fatigue performance of turbine engine components has been the focus of recent attention (Nicholas and Zuiker, 1996; Cowles, 1996; and Larsen et al., 1996), and efforts are underway to develop improved life prediction methods to address this aspect of turbine engine fatigue spectra. Appreciable levels of high cycle fatigue appear to be confined to engine airfoils and airfoil attachment regions. Moreover, high cycle fatigue appears to be significant only in conjunction with some other form of service-induced damage. Such damage may result from low-cycle fatigue, high-velocity impacts by foreign objects in the gas flow path (Haake et al., 1989), and fretting fatigue in airfoil attachment regions. Accurate prediction of the effects of combinations of these factors should improve overall engine reliability.

This paper examines the damage-tolerance capability of a high-strength aerospace titanium alloy under fatigue spectra that may contain high cycle fatigue. The role of the fatigue-crack-growth-rate threshold is examined for alloy usage conditions that

are likely to be life-limiting for turbine engine components.

## MATERIAL

The experimental results to be presented are for the high-strength titanium alloy Ti-6Al-2Sn-4Zr-6Mo (weight %) (Ti-6246), which has been used in turbine engine airfoils and disks. The actual composition of the alloy is listed in Table I, along with its monotonic tensile properties. This material was forged into the shape of a disk and heat treated to produce a fine duplex microstructure of equiaxed primary  $\alpha$  phase (hexagonal close packed) in a matrix of Widmanstätten  $\alpha + \beta$  (body centered cubic) phase as shown in Fig. 1. The figure also shows the primary directions in the alloy forging.

Table I: Actual chemical composition (weight %) and tensile properties of the titanium alloy Ti-6Al-2Sn-4Zr-6Mo.

Al	Sn	Zr	Mo	$\sigma_y$	$\sigma_u$	Elong.	R. A.
				(MPa)	(MPa)	(%)	(%)
6.33	2.07	3.93	5.76	1158	1232	10.9	24.2

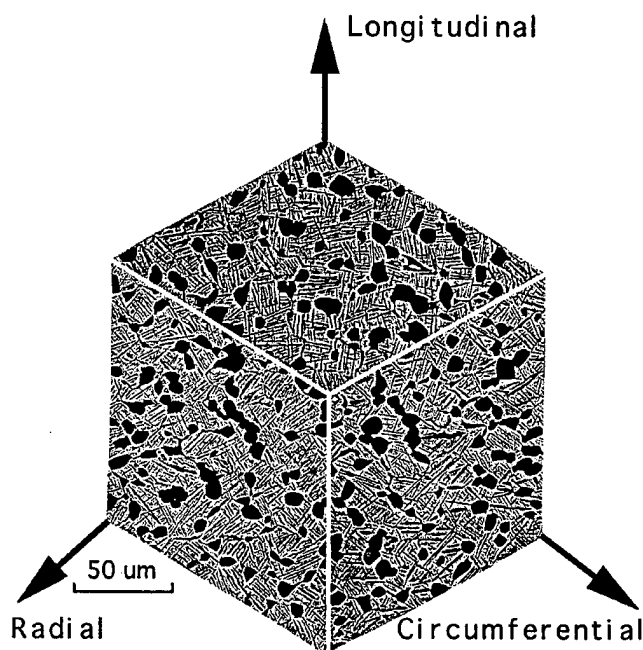


Fig. 1. Equiaxed microstructure of Ti-6246, after solution heat treatment and aging, showing primary directions in the disk forging.

## EXPERIMENTAL RESULTS AND DISCUSSION

### Fatigue

Smooth-bar fatigue experiments were performed at room temperature to characterize the high-cycle fatigue endurance limit of the Ti-6246 over a range of stress ratios,  $R = \sigma_{min}/\sigma_{max}$ . Tests were performed at 60 Hz on hourglass-shaped specimens that had been electropolished to remove surface residual stresses. Using a step-stress method previously shown to be effective in similar tests of the alloy Ti-6Al-4V (Maxwell and Nicholas, 1997), blocks of  $10^7$  cycles of constant amplitude fatigue were applied. If the specimen survived a given block of cycles, the maximum stress was increased, and another  $10^7$  block of cycles was applied. This procedure was repeated until specimen failure occurred. Data obtained by this method were found to be in good agreement with more traditional S-N test results that did not involve step loading.

The results of the endurance fatigue tests are presented in Fig. 2 in the form of a constant-life plot, sometimes known as a "Goodman" diagram. The historical precedence for this diagram has recently been reviewed in detail by Sendekyj (1997). This presentation of the data, which plots the fatigue endurance limit in terms of stress amplitude and mean stress, represents the  $10^7$ -cycle fatigue capability of nominally defect-free material. This fatigue capability represents the upper limit of expected performance, and structural damage to actual components from sources other than HCF would be expected to reduce this capability. One approach for assessing the reduction in fatigue capability due to the combined effects of the various damage mechanisms involves characterization and analysis by fracture mechanics methods.

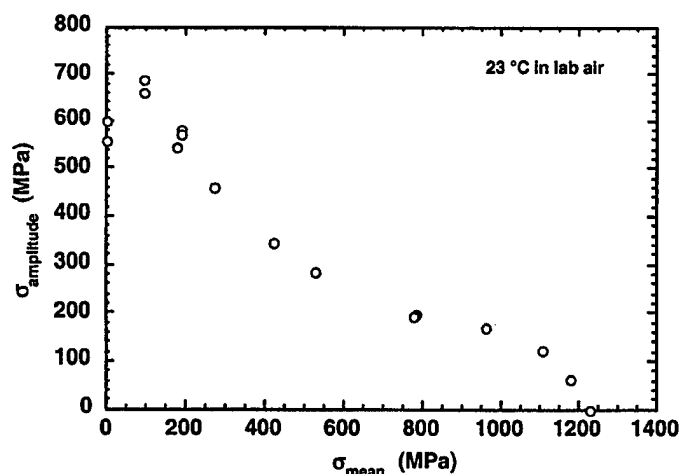


Fig. 2. Constant-life plot for  $10^7$  fatigue cycles for tests of smooth electropolished samples tested at 60 Hz in air at room temperature.

### Fatigue Crack Propagation

Fatigue crack growth experiments were performed using standard procedures given by ASTM E-647 (1997) and compact type, C(T), specimens of width 40 mm and thickness 10 mm. These tests were conducted at 60 Hz in laboratory air at room temperature under stress ratios ranging from 0.1 to 0.8. The crack growth data were acquired under decreasing stress-intensity-factor-range,  $\Delta K$ , fatigue followed by constant-load-amplitude fatigue. The resulting fatigue crack growth rate data are shown in Fig. 3, along with lines representing a regression analysis performed using the equation

$$\log(da/dN) = C_1 \{ \operatorname{arctanh}(C_2 [\log(\bullet K) + C_3]) \} + C_4 \quad (1)$$

which provided a good representation of the crack growth rate behavior.

### Residual Crack Propagation Lifetime

As established by ENSIP, the damage tolerance approach to life management of turbine engines requires the assumption that fracture critical components contain initial defects or damage. Generally, the scale of the assumed damage is defined by the detection limit of some nondestructive inspection method. In this case the detection limit is the *maximum* crack size,  $a_i$ , that can be *missed* by the inspection. Damage tolerance life predictions

are performed by calculating the number of cycles required to propagate a crack of initial size  $a_i$  to failure. This crack propagation lifetime is given by

$$N_p = \int_{a_i}^{a_c} \frac{da}{f(\Delta K)} \quad (2)$$

where  $a_c$  is the critical crack length corresponding to the material's effective fracture toughness in fatigue ( $K_Q$ ),  $f(\Delta K)$  is a crack-growth-rate function such as Eq. 1, and  $\Delta K$  is defined for a specific crack geometry and loading history. In the example to follow, the crack was assumed to be a semicircular surface flaw of depth  $a$ , which is a crack geometry typical of those experienced in actual components.

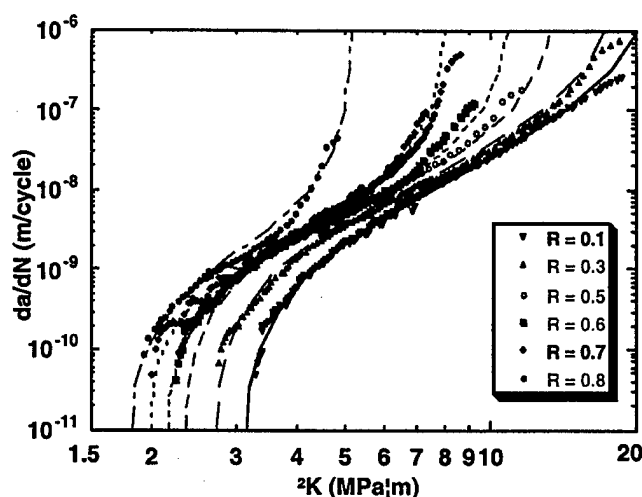


Fig. 3. Fatigue crack growth behavior as a function of stress ratio for tests of C(T) specimens performed in air at room temperature.

To examine the effect of the assumed initial crack size on the calculated crack propagation lifetime, Eq. 2 was solved numerically to construct the remaining-life plots shown in Figs. 4 and 5. For a given crack size,  $a_i$ , the remaining fatigue crack propagation life,  $N_p$ , is given by the ordinate on these plots. Figure 4 illustrates the effect of the level of maximum stress on the remaining lifetime for a stress ratio of 0.1. The three curves shown have features common to all similar life calculations performed using the crack growth data of Fig. 3. For combinations of  $a_i$  and loading conditions that result in  $\Delta K$  less than  $\Delta K_{th}$ ,  $N_p$  in Fig. 4 is infinite. When  $\Delta K_{th}$  is exceeded, however, there is an abrupt transition from infinite predicted lifetimes to finite

lifetimes. The threshold crack depths,  $a_{th}$ , corresponding to  $\Delta K_{th}$  for the three cases of  $\sigma_{max} = 300, 500$ , and  $700$  were  $0.091, 0.033$ , and  $0.017$  mm, respectively. As shown in the figure, for crack sizes exceeding these threshold values the total remaining life in fatigue crack growth in each case was less than about  $5 \times 10^5$  cycles. Such a short crack propagation life would almost certainly be exceeded under a realistic number of HCF cycles.

**Effects of Stress Ratio.** Figure 5 presents the results of similar calculations performed for a maximum stress of  $500$  MPa and stress ratios ranging from  $0.1$  to  $0.8$ . Again, a distinct threshold crack growth behavior is evident. The critical crack sizes for threshold crack growth at  $R = 0.1, 0.5, 0.7$ , and  $0.8$  were  $0.033, 0.062, 0.125$ , and  $0.230$  mm, respectively. For initial crack sizes greater than the threshold value, the crack propagation lives for the four curves decrease continuously with increasing  $a_i$ , converging to a common critical crack size, which is determined by  $K_{max}$  approaching  $K_Q$ .

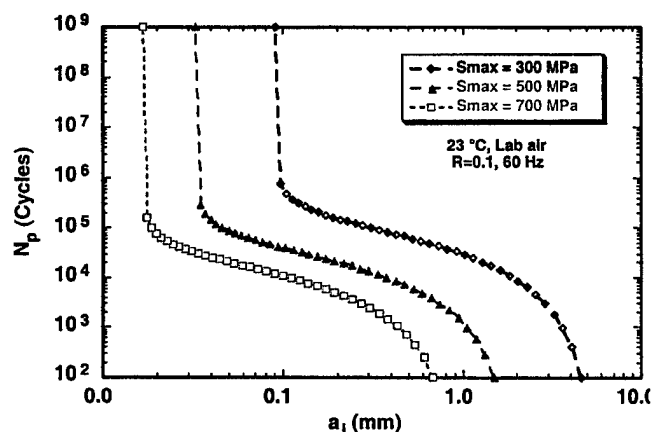


Fig. 4. Remaining crack propagation lifetime,  $N_p$ , plotted versus initial crack size,  $a_i$ , for fatigue under conditions of  $R = 0.1$  and a range of maximum-stress levels.

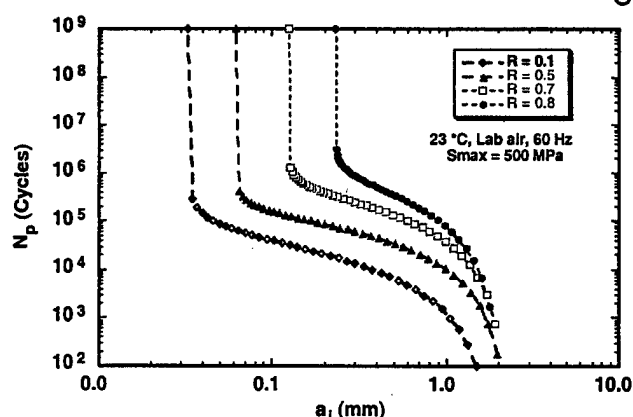


Fig. 5. Remaining crack propagation lifetime,  $N_p$ , plotted versus initial crack size,  $a_i$ , for a maximum stress of  $500$  MPa and a range of stress ratios.

For turbine engine components that are life-limited by low cycle fatigue, the maximum number of fatigue cycles is typically less than  $10,000$ , and routine engine overhaul intervals permit component inspections to be performed well before the design lifetime is reached. Thus, a component of Ti-6246 could spend much of its fatigue life propagating a crack, depending on the applied maximum stress and stress ratio. The situation is considerably different for components that experience high cycle fatigue, however, since these structures may be expected to experience fatigue loadings well in excess of  $10^7$  cycles. The general trends of the remaining-life curves indicate that  $\Delta K_{th}$  should be the dominant consideration for life management under spectra containing significant levels of high-cycle fatigue, if a damage-tolerance-based approach to life management approach is to be adopted.

**HCF/LCF Spectrum Loading.** The utility of Fig. 5 is also evident when considering a combination of low- and high-cycle fatigue. For example, assume that low cycle fatigue is represented by the  $R = 0.1$  curve, while the  $R = 0.8$  curve represents crack growth under a possible high cycle fatigue condition. The number of HCF cycles per LCF cycle in a typical spectrum may be expected to be in the approximate range of  $100$  to  $10,000$ . Under these circumstances, according to the curves of Fig. 5, a small crack could propagate under low cycle fatigue for an extended period but still be sufficiently small to resist propagation under high cycle fatigue. In this instance, the threshold

crack depth under HCF would be 0.230 mm. Assuming no synergism between LCF and HCF, cracks greater than this size would be expected to alternate between the  $R=0.1$  and  $R=0.8$  curves during crack growth, as the loading alternated between low- and high-cycle fatigue conditions. If the ratio of HCF-to-LCF cycles was on the order of 100 to 10,000 as suggested, then for this hypothetical case, high cycle fatigue would dominate the crack propagation life for cracks greater than 0.230 mm, and the ultimate failure would probably occur under high cycle fatigue. The relationship between LCF and HCF crack growth behavior obviously depends on a number of factors including stress ratio, maximum stress, and the ratio of HCF to LCF cycles, and a synergistic interaction between these two modes of fatigue could complicate the behavior. The potential LCF/HCF problem in Ti-6Al-4V has recently been discussed by Zuiker and Nicholas (1996).

### Fatigue Life Maps

Although it may be attractive to use the large-crack  $\Delta K_{th}$  as a life-management criterion, it is well known that data of large fatigue cracks may not accurately represent the behavior of small fatigue cracks (Ritchie and Lankford, 1986; Miller and de los Rios, 1992). One view of this issue follows from the original work of Kitagawa and Takahashi (1976) who showed that threshold crack growth rate data display a dependence on crack size that is related to the material's fatigue strength,  $\Delta S_e$ , and  $\Delta K_{th}$ . As shown schematically in Fig. 6, a plot can be constructed that combines fatigue crack initiation and propagation concepts. Considering crack initiation, and disregarding the possibility of a preexisting crack, specimen failure should occur only if the applied stress range exceeds  $\Delta S_e$ , which is represented by the horizontal line in the figure. Alternatively, considering a fracture mechanics approach, crack growth should occur only if the applied  $\Delta K$  exceeds  $\Delta K_{th}$ , which is represented by the solid line of slope  $-1/2$  on the figure. Thus, the utility of  $\Delta K_{th}$  as a "material property" appears to be limited to cracks of approximate length greater than that given by the intersection of the two lines ( $a_0$ ). For many materials,  $a_0$  appears to provide a rough approximation of the crack size below which small-crack effects become potentially significant.

Alternatively, when  $a_i$  is greater than  $a_0$  the large-crack threshold should be largely applicable.

Using a format representing maximum stress as a function of crack size ( $a_i$ ), fatigue life maps were generated for stress ratios of 0.1, Fig. 7, and 0.8, Fig. 8. The maps include boundaries between which a sample is predicted to have a limited lifetime, and below the lower boundary the life is assumed infinite. The case of a semicircular surface flaw in an infinite solid was used again for all calculations. The lower boundary was established by the fatigue limit, determined from Fig. 2, and  $\Delta K_{th}$ . In an analogous fashion the upper limit was established by the ultimate tensile strength (UTS) and  $K_Q$ . The applicable values for  $\Delta K_{th}$  and  $K_Q$  were derived from the model predictions, Fig. 3 and Eq. 1, from the  $\Delta K$  associated with crack growth rates of  $10^{-14}$  and  $10^{-2}$  m/cycle, respectively. The curves of constant life between the boundaries represent crack propagation lives calculated by numerical integration of Eq. 2 utilizing Eq. 1 as the form for  $f(\Delta K)$ . Of course, this assumes the large-crack data from Fig. 3 appropriately represent crack growth rates for smaller surface flaws. This assumption was previously shown to be correct in experiments on naturally initiated small surface cracks in this alloy (Larsen and Jira, 1991; Larsen et al., 1988; Jira et al., 1988; and Jira et al., 1987). Moreover, since  $a_0$  in Figs. 7 and 8 was approximately 2 and 6 times the grain size of the material, 0.014 and 0.038 mm respectively, and the small-crack effect has been noted to cease when the crack size is "3 to 10 grain diameters" (Taylor and Knott, 1981; McDowell, 1996), this seems a reasonable assumption.

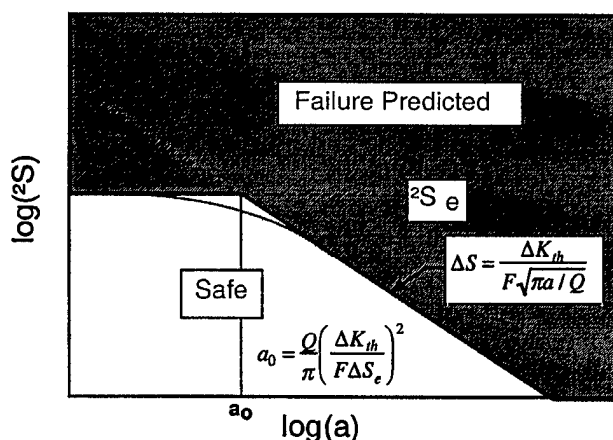


Fig. 6. Schematic "Kitagawa plot" of threshold fatigue conditions in terms of crack size and stress range.

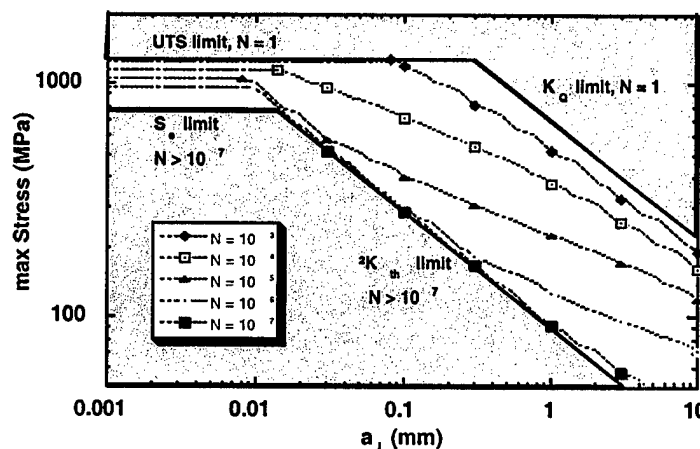


Fig. 7. Fatigue-life map plotted in terms of maximum stress and initial crack size for a surface flaw in an infinite solid under constant amplitude fatigue and a stress ratio of  $R = 0.1$ .

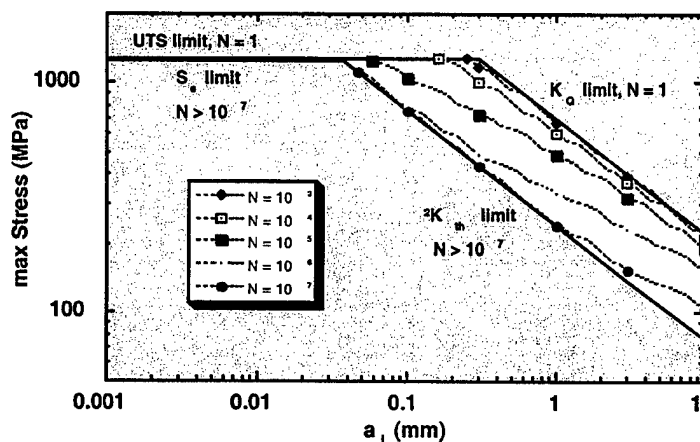


Fig. 8. Fatigue-life map plotted in terms of maximum stress and initial crack size for a surface flaw in an infinite solid under constant amplitude fatigue and a stress ratio of 0.8.

These fatigue maps represent a useful tool to visualize the conditions (stress level and flaw size) under which a material can be used (Ti-6246 in this case). The maps also highlight again the utility of  $\Delta K_{th}$  when designing for fatigue lives of  $10^7$  cycles and higher, especially if the assumed initial flaw depth is greater than approximately 0.040 mm. This

flaw size range is of significance since it agrees well with the depths of foreign object damage observed in service (Haake et al., 1989; Larsen et al., 1996) and includes current detection limits currently used for some engine components.

The fatigue-life maps also represent an alternative method for visualizing the HCF/LCF interactions. As an example, assume a mission spectrum with a maximum stress of 600 MPa, which is slightly less than half the UTS, contains 1000 HCF cycles at  $R = 0.8$  for every one LCF cycle at  $R = 0.1$ . According to the  $R = 0.1$  fatigue-life map, a flaw size of approximately 0.2 mm would be acceptable to achieve the LCF life of 10,000 cycles. However, this flaw size is greater than the threshold from the  $R = 0.8$  fatigue-life map, and failure would be predicted is less than  $10^6$  HCF cycles. Assuming, therefore, that the crack growth would be dominated by the HCF portion of the load spectrum, failure in less than 1000 missions would be predicted. From further inspection of the  $R = 0.8$  fatigue-life map, an initial flaw size of less than 0.16 mm would be required to stay below the threshold condition at a maximum stress of 600 MPa.

#### CONCLUDING REMARKS

Life prediction under high cycle fatigue spectra must address a variety of potentially interactive effects. Possible damage events include crack formation from slip bands, surface fretting fatigue, combinations of low- and high-cycle fatigue, and damage growth from intrinsic material defects and foreign objects, the latter of which may produce relatively large damage sites (Haake et al., 1989; Larsen et al., 1996). The results of the present effort address a key aspect of the life prediction process – the role of the crack growth rate threshold based on data from large fatigue cracks. The data and analyses presented pertain specifically to the titanium alloy Ti-6Al-2Sn-4Zr-6Mo with a fine equiaxed  $\alpha+\beta$  microstructure, but the findings are probably reflective of the behavior of other high strength titanium alloys (Larsen et al., 1996).

The current results show that a crack growth approach is useful for life management of Ti-6246 under low cycle fatigue, but the typical crack propagation lifetimes available from this alloy under realistic loading conditions are insufficient to permit crack growth to occur under high cycle fatigue, given the large number of cycles that are expected. Recognizing that crack formation due to a variety of



potential mechanisms cannot be avoided, it appears that an effective damage tolerance life prediction system must focus on the conditions necessary for threshold crack growth. Because the crack growth analyses presented were based on the behavior of large fatigue cracks, which exhibited a distinct  $\Delta K_{th}$ , the predicted crack growth behavior probably represents a *best case*. Although load-spectrum interaction effects, for example, might result in reduced crack growth rates, small cracks may propagate faster than predicted by the large-crack trends.

Under realistic fatigue loads, the crack sizes corresponding to  $\Delta K_{th}$  were quite small and would be difficult to detect by conventional methods of nondestructive evaluation. Thus, it appears that effective life management of titanium-alloy turbine-engine components that experience significant levels of high cycle fatigue must address both the detection and near-threshold crack propagation behavior of small fatigue cracks. This will require understanding the small-crack  $\Delta K_{th}$  as a function of residual stress, mode of crack formation, mission spectra, crack geometry, temperature, and material and microstructural characteristics. Compared with the more general small-crack problem, however, understanding crack size effects in this particular instance should be simplified by the combination of limited stresses and refined microstructures that pertain to the high cycle fatigue problem for titanium-alloy turbine-engine components. In the future, a thorough understanding of the effects of alloy microstructure and composition on high cycle fatigue performance, including effects of fretting and foreign object damage, will probably be needed to optimize the performance of future titanium airfoil materials.

#### ACKNOWLEDGMENTS

This research was performed in the Materials Directorate, Air Force Research Laboratory, Wright-Patterson Air Force Base, OH and was supported by the Air Force Office of Scientific Research under Task 2302BW1. The authors would like to acknowledge the thoughtful comments of Mr. Jay R. Jira and the assistance of Mr. Kevin Gross and Mr. Michael Shepherd.

#### REFERENCES

ASTM E-647-95a, 1997, Standard Test Method for Measurement of Fatigue Crack Growth Rates," 1997

Annual Book of ASTM Standards, Vol. 03.01, ASTM, Philadelphia, PA, pp. 557-593.

Cowles, B. A., 1996, "High Cycle Fatigue in Aircraft Gas Turbines - An Industry Perspective," International Journal of Fracture, Vol. 80, pp. 147-163.

Haake, F. K., Salivar, G. C., Hindle, E. H., Fischer, J. W., and Annis, C. G., Jr., 1989, "Threshold Fatigue Crack Growth Behavior," U. S. Air Force Technical Report WRDC-TR-89-4085, Wright-Patterson Air Force Base, OH.

Jira, J. R., Weerasooriya, T., Nicholas, T., and Larsen, J. M., 1988, "Effects of Closure on the Fatigue Crack Growth of Small Surface Cracks in a High-Strength Titanium Alloy," Mechanics of Fatigue Crack Closure, ASTM STP 982, J. C. Newman, Jr. and W. Elber, ed., American Society for Testing and Materials, Philadelphia, pp. 617-635.

Jira, J. R., Nicholas, T., and Larsen, J. M., 1987, "Fatigue Thresholds in Surface Flaws in Ti-6Al-2Sn-4Zr-6Mo," Fatigue 87, Vol. IV, E. Starke and R. O. Ritchie, ed., Engineering Materials Advisory Services, Ltd., West Midlands, U. K., pp. 1851-1860.

Kitagawa, H. and Takahashi, S., 1976, "Applicability of Fracture Mechanics to Very Small Cracks or the Cracks in the Early Stage," Proceedings of the Second International Conference on Mechanical Behavior of Materials, Boston, MA, pp. 627-631.

Larsen, J. M. and Jira, J. R., March 1991, "Small-Crack Closure Measurements in Titanium Alloys," Experimental Mechanics, pp. 82-87.

Larsen, J. M., Jira, J. R., and Weerasooriya, T., 1988, "Crack Opening Displacement Measurements on Small Cracks in Fatigue," Fracture Mechanics: Eighteenth Symposium, ASTM STP 945, D. T. Read and R. P. Reed, ed., American Society for Testing and Materials, Philadelphia, PA, pp. 896-912.

Larsen, J. M., Worth, B. D. Worth, Annis, C. G., Jr., and Haake, F. K., 1996, "An Assessment of the Role of Near-Threshold Crack Growth in High-Cycle-Fatigue Life Prediction of Aerospace Titanium Alloys Under Turbine Engine Spectra," International Journal of Fracture, Vol. 80, pp. 237-255.

Maxwell, D. C. and Nicholas, T., 1997, "A Rapid Method for Generation of a Haigh Diagram for High Cycle Fatigue," submitted for publication, ASTM STP, National Symposium on Fatigue and Fracture, American Society for Testing and Materials, Philadelphia, PA.

McDowell, D. L., 1996, "Basic Issues in the Mechanics of High Cycle Metal Fatigue," International Journal of Fracture, Vol. 80, pp. 103-145.

Miller, K. J. and de los Rios, E. R., 1992, Short Fatigue Cracks, Mechanical Engineering Publications Limited, London, UK.

Nicholas, T. and Zuiker, J. R., 1996, "On the Use of the Goodman Diagram for High Cycle Fatigue Design," *International Journal of Fracture*, Vol. 80, pp. 219-235.

Ritchie, R. O. and Lankford, J., eds., 1986, *Small Fatigue Cracks, The Minerals, Metals, and Materials Society*, Warrendale, PA.

G. P. Sendeckyj, 1997, "History of Constant Life Diagrams," to be published in *High Cycle Fatigue of Structural Materials: Paul C. Paris Symposium*, TMS/ASM International, Warrendale, PA.

Taylor, D. and Knott, J. F., 1981, "Fatigue Crack Propagation Behaviour of Short Cracks; The Effect of Microstructure," *Fatigue of Engineering Materials and Structures*, Vol. 4, No. 2, pp. 147-155.

U.S. Air Force, Engine Structural Integrity Program., 1984, *Military Standard 1783, Aeronautical Systems Division*, Wright-Patterson Air Force Base, OH.

Zuiker, J. R. and Nicholas, T., 1996 "Observations and Limitations of the Use of The Goodman Diagram for Combined HCF/LCF Loading," *FATIGUE '96*, Elsevier Science Ltd., Oxford, U.K., pp. 467-472.

Reference: Larsen, J.M., S.M. Russ, R. John, and D.C. Maxwell, "The Role of Threshold Fatigue Crack Growth in Life Prediction for Two Titanium Alloys Under High Cycle Fatigue Spectra," Proceedings of the National Conference on High Cycle Fatigue, San Antonio, TX, U.S. Air Force, Feb. 1998.

**The Role of Threshold Fatigue Crack Growth  
in Life Prediction for Two Titanium Alloys  
Under High Cycle Fatigue Spectra**

Dr. James M. Larsen\*, Mr. Stephan M. Russ  
Dr. Reji John<sup>†</sup>, and Mr. David C. Maxwell<sup>†</sup>

Materials and Manufacturing Directorate  
Air Force Research Laboratory (AFRL/MLLN)  
Wright-Patterson Air Force Base, OH 45433-7817, U.S.A.

<sup>†</sup> The University of Dayton Research Institute  
Dayton, OH 45419-0128, U.S.A.

Life prediction under fatigue spectra that contain combinations of low cycle fatigue (LCF) and high cycle fatigue (HCF) must address a variety of potentially interactive damage events. These events include fatigue crack formation at slip bands and intrinsic material defects, surface fretting fatigue, and foreign object impacts, the latter of which may produce relatively large damage sites [1,2]. The present effort addresses a key aspect of the life prediction process – the role of the conventional crack growth rate threshold,  $\Delta K_{th}$ , based on data from large fatigue cracks. The data and analyses are for two representative titanium alloys, used in turbine engines blades and disks, for which a substantial fatigue and fracture database was available [e.g., 1-10]. The microstructures of these alloys, Ti-8Al-1Mo-1V (Ti-811) and Ti-6Al-2Sn-4Zr-6Mo (Ti-6246) (weight %), are shown in Figs. 1 and 2, respectively. The  $10^7$ -cycle fatigue lives of these materials tested over a range of stress ratios ( $R = \sigma_{min}/\sigma_{max}$ ) are plotted in Fig. 3 in terms of stress amplitude ( $S_a = (\sigma_{max} - \sigma_{min})/2$ ) versus mean stress ( $S_m = (\sigma_{max} + \sigma_{min})/2$ ). The data on Ti-811 were obtained from tests at 260°C, while the data on Ti-6246 are from tests at room temperature. In spite of the differences in temperature and the obvious differences in fatigue strength between the two alloys, the basic findings on the two materials were similar. Thus, to achieve brevity, the following discussion will address the Ti-6246 alone.

Figure 4 presents crack growth rate data as a function of stress ratio for Ti-6246, and Figs. 5-7 show typical results of crack propagation life analyses performed for this material, assuming that the crack propagation behavior of Fig. 4 is valid for all crack sizes. These figures plot remaining crack propagation lifetime,  $N_p$ , as a function of initial crack size,  $a_i$ , for a range of stresses and stress ratios. The overall results of these analyses may be illustrated in the form of a fatigue life map, which is shown schematically in Fig. 8 and presented in Figs. 9 and 10 for fatigue at  $R = 0.1$  and 0.8, respectively. These two stress ratios were chosen to reflect conditions representative of low cycle fatigue and high cycle fatigue, respectively.

The results of the life analyses indicate that, for the Ti-6246 at room temperature, a crack growth methodology is useful for life management under low cycle fatigue (lives  $\delta 10^4$  cycles). However, the typical crack propagation lifetimes available from this alloy under realistic loading conditions are insufficient to permit crack growth under high cycle fatigue, given the large number of cycles that may be expected under HCF (lives  $\tau 10^7$  cycles). Recognizing that crack formation due to a variety of potential mechanisms cannot be avoided, it appears that an effective damage tolerance life prediction system must focus on the conditions necessary for threshold crack growth. Moreover, because the crack growth analyses presented here were based on the behavior of large fatigue cracks, which exhibited a distinct  $\Delta K_{th}$ , the predicted crack growth behavior probably represents a *best-case* scenario. For example, it is well known that, under certain conditions, small cracks may propagate faster than predicted by large-crack trends, which could render the analyses non-conservative.

Under realistic fatigue loads, the crack sizes corresponding to  $\Delta K_{th}$  were quite small, and cracks of the indicated sizes would be difficult to detect by conventional methods of nondestructive evaluation. The threshold crack sizes may be increased substantially, however, by the imposition of a state of surface residual stress. This may be accomplished by a variety of surface treatments, such as shot peening, which produce compressive residual stresses in a surface layer of material. Figure 11 shows representative residual stress profiles for Ti-6246 after a variety of surface treatments, and Fig. 12 presents calculations of the effects of these residual stresses on the stress intensity factor of a semicircular surface crack. As shown, the residual stress can have a dramatic effect on the magnitude of  $K$ . The effects of the various residual stress states on  $\Delta K_{th}$  are illustrated in the Figs. 13 and 14, which show examples representative of LCF ( $R = 0.1$ ) and HCF ( $R = 0.8$ ) loading, respectively. It is interesting to note that the benefits of the residual stresses are much more significant under the LCF condition than under the HCF loading. This is due to the fact that the residual stresses reduce both  $\Delta K_{eff}$  and  $R_{eff}$  under  $R = 0.1$  fatigue, but the residual stresses only reduce  $R_{eff}$  under  $R = 0.8$  fatigue.

In general, it appears that effective life management of titanium-alloy turbine-engine components that experience significant levels of high cycle fatigue must address both the detection and near-threshold crack propagation behavior of small fatigue cracks. This will require understanding the small-crack  $\Delta K_{th}$  as a function of the mode of crack formation, crack geometry, residual stress, mission spectra, temperature, and material and microstructural characteristics. Compared with the general small-crack problem, however, understanding crack size effects in this particular instance should be simplified by the combination of limited stresses and refined microstructures that pertain to high cycle fatigue of titanium-alloy turbine-engine components. In the future, a thorough understanding of the effects of alloy microstructure and composition on high cycle fatigue performance, including resistance to fretting and foreign object damage, will probably be needed to optimize the performance of future titanium airfoil materials.

#### Acknowledgments

This research was performed in the Materials and Manufacturing Directorate, Air Force Research Laboratory, Wright-Patterson Air Force Base, OH. The authors would like to acknowledge the thoughtful comments of Mr. Jay R. Jira and the technical assistance of Mr. Kevin Gross and Mr. Michael Shepherd.

#### References

1. Haake, F. K., Salivar, G. C., Hindle, E. H., Fischer, J. W., and Annis, C.G., Jr., "Threshold Fatigue Crack Growth Behavior," U. S. Air Force Technical Report WRDC-TR-89-4085, Wright-Patterson Air Force Base, OH, 1989.
2. Larsen, J. M., Worth, B. D., Annis, C. G., Jr., and Haake, F. K., "An Assessment of the Role of Near-Threshold Crack Growth in High-Cycle-Fatigue Life Prediction of Aerospace Titanium Alloys Under Turbine Engine Spectra," *International Journal of Fracture*, Vol. 80, 1996, pp. 237-255.
3. Salivar, G. C., Heine, J. E., and Haake, F. K., "The Effect of Stress Ratio on the Near-Threshold Fatigue Crack Growth Behavior of Ti-8Al-1Mo-1V at Elevated Temperature," *Engineering Fracture Mechanics*, Vol. 32, No. 5, 1989, pp. 807-817.
4. Salivar, G. C. and Haake, F. K., "A Comparison of Test Methods for the Determination of Fatigue Crack Growth Rate Threshold in Titanium at Elevated Temperature," *Engineering Fracture Mechanics*, Vol. 37, No. 3, 1990, pp. 505-517.
5. Jira, J. R., Nicholas, T., and Larsen, J. M., "Fatigue Thresholds in Surface Flaws in Ti-6Al-2Sn-4Zr-6Mo," *Fatigue 87*, Vol. IV, E. Starke and R. O. Ritchie, Eds., Engineering Materials Advisory Services, Ltd., West Midlands, U. K., 1987, pp. 1851-1860.
6. Jira, J. R., Weerasooriya, T., Nicholas, T., and Larsen, J. M., "Effects of Closure on the Fatigue Crack Growth of Small Surface Cracks in a High-Strength Titanium Alloy," *Mechanics of Fatigue Crack Closure*, ASTM STP 982, J. C. Newman, Jr. and W. Elber, Eds., American Society for Testing and Materials, Philadelphia, 1988, pp. 617-635.

7. Jira, J. R., Nicholas, T. and Larsen, J. M., "Crack Closure Development and its Relation to the Small-Crack Effect in Titanium Alloys," *FATIGUE 90, Vol. II*, H. Kitagawa and T. Tanaka, Eds., Materials and Components Engineering Publications Ltd., Birmingham UK, 1990, pp. 1295-1300.
8. Larsen, J. M. and Jira, J. R., "Small-Crack Closure Measurements in Titanium Alloys," *Experimental Mechanics*, March, 1991, pp. 82-87.
9. Ravichandran, K. S. and Larsen, J. M., "An Approach to Measure the Shapes of Three Dimensional Surface Cracks During Fatigue Crack Growth," *Fatigue of Engineering Materials and Structures*, Vol. 16, 1993, pp. 909-930.
10. Larsen, J. M., Russ, S. M., Maxwell, D. C., and Worth, B.D., "The Role of Threshold Fatigue Crack Growth in Life Prediction of the Alloy Ti-6Al-2Sn-4Zr-6Mo Under High Cycle Fatigue Spectra," *Analysis and Design Issues for Modern Aerospace Vehicles - 1997*, G. J. Simitses, Ed., AD Vol. 55, The American Society of Mechanical Engineers, New York, NY, pp. 443-448.

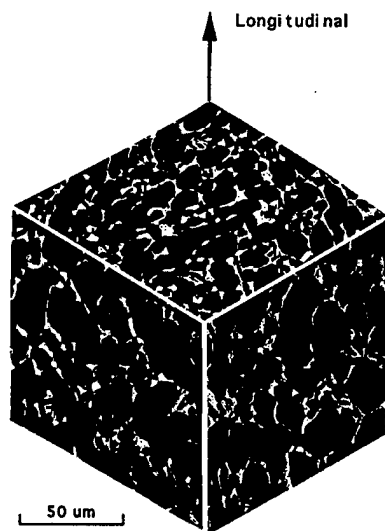


Fig. 1. Microstructure of Ti-8Al-1Mo-1V bar after solution treatment plus aging. This material was composed of equiaxed and acicular  $\alpha$  with a small amount of grain boundary  $\beta$  phase.

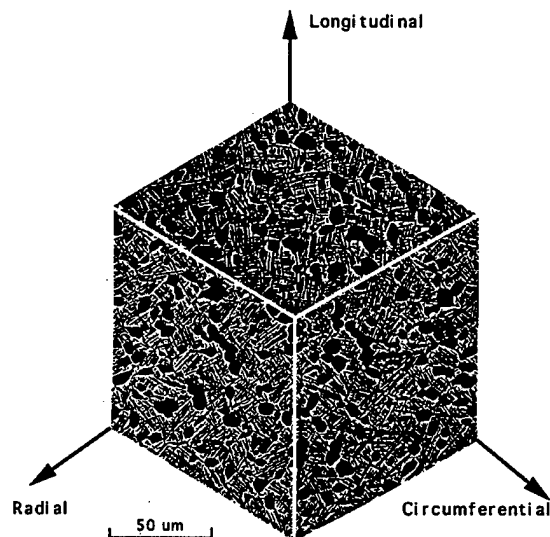


Fig. 2. Fine, equiaxed  $\alpha+\beta$  microstructure of Ti-6Al-2Sn-4Zr-6Mo after heat treatment, showing primary directions in the disk forging. This microstructure consists of islands of primary  $\alpha$  phase in a matrix of transformed  $\beta$  phase.

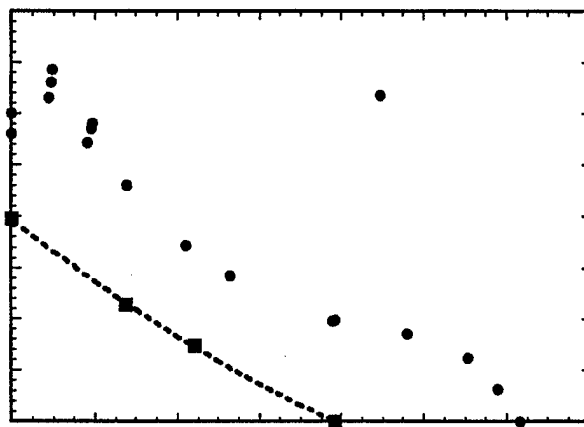


Fig. 3. Constant-life plot for  $10^7$  fatigue cycles for tests of smooth specimens. The Ti-811 was tested at 20 Hz in air at 260°C, and the Ti-6246 was tested at 60 Hz in air at room temperature.

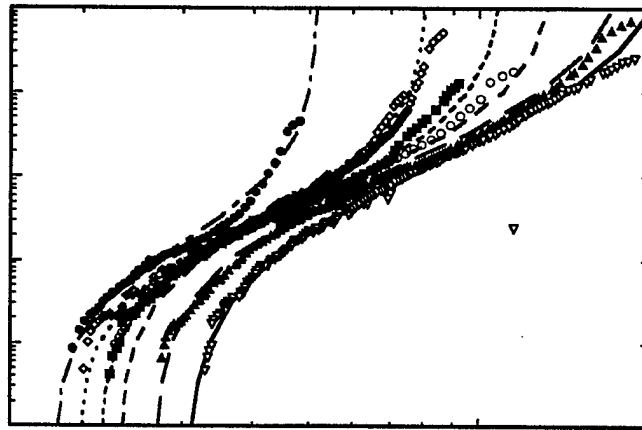


Fig. 4. Fatigue crack growth behavior of Ti-6246 as a function of stress ratio for tests of C(T) specimens performed in air at room temperature.

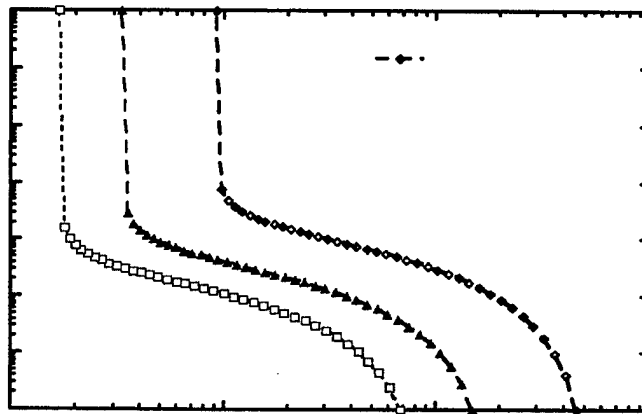


Fig. 5. Remaining crack propagation lifetime,  $N_p$ , plotted versus initial crack size,  $a_i$ , for fatigue under conditions of  $R = 0.1$  and a range of maximum-stress levels for Ti-6246. The threshold crack depths,  $a_{th}$ , corresponding to  $\Delta K_{th}$  for the three cases of  $\sigma_{max} = 300, 500$ , and  $700$  were  $0.091, 0.033$ , and  $0.017$  mm, respectively.

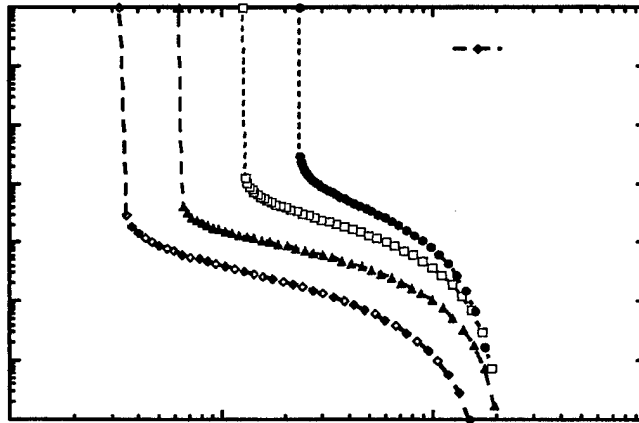


Fig. 6. Remaining crack propagation lifetime,  $N_p$ , plotted versus initial crack size,  $a_i$ , for a maximum stress of 500 MPa and a range of stress ratios for Ti-6246. The critical crack sizes for threshold crack growth at  $R = 0.1, 0.5, 0.7$ , and  $0.8$  were 0.033, 0.062, 0.125, and 0.230 mm, respectively.

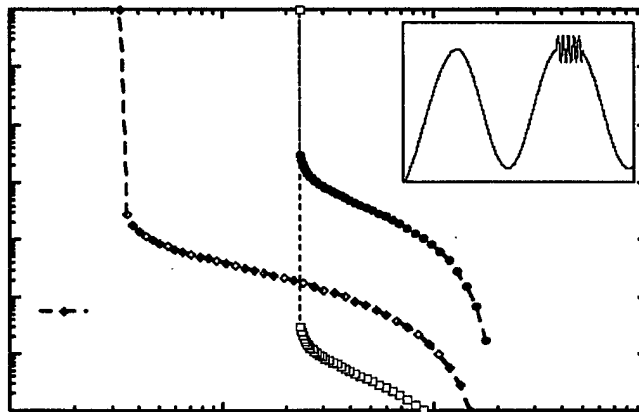


Fig. 7. Remaining crack propagation lifetime curves showing a possible combination of high and low cycle fatigue (HCF/LCF). The open squares illustrate the effective HCF prediction for a cycle ratio of 1000 HCF cycles per LCF cycle.



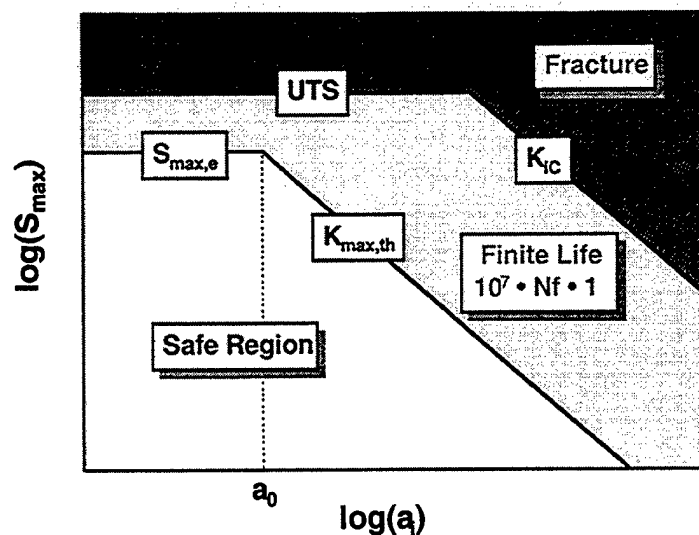


Fig. 8. Schematic fatigue-life diagram showing regions of infinite, finite, and zero remaining life. This diagram, which is based on the early work of Kitagawa and Takahashi, presents remaining life for combinations of initial crack size ( $a_i$ ) and maximum stress for a given stress ratio.

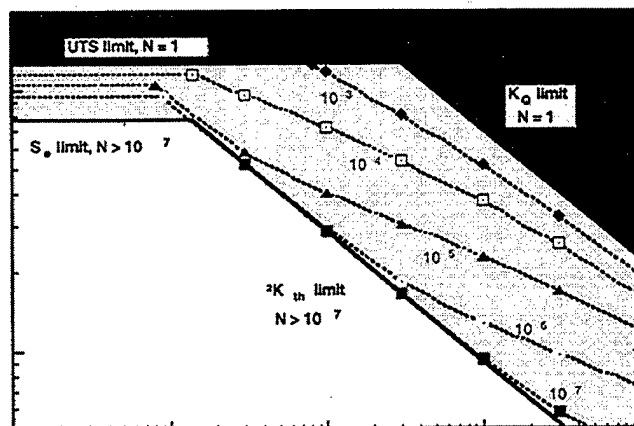


Fig. 9. Fatigue-life map for Ti-6246 plotted in terms of maximum stress versus initial crack size for a surface flaw in an infinite body under constant amplitude fatigue and a stress ratio of 0.1.

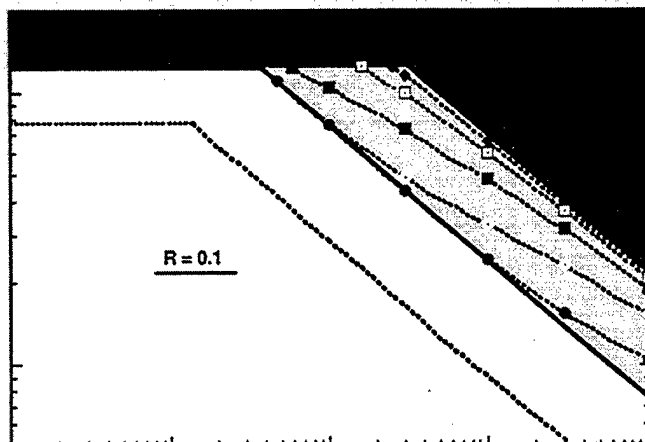


Fig. 10. Fatigue-life map for Ti-6246 plotted in terms of maximum stress versus initial crack size for a surface flaw in an infinite body under constant amplitude fatigue and a stress ratio of 0.8.

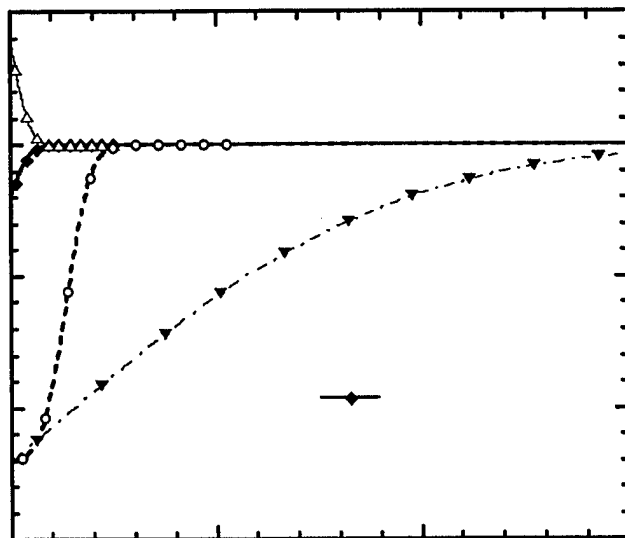


Fig. 11. Representative residual stress profiles produced by various surface-finishing and surface-treatment methods.

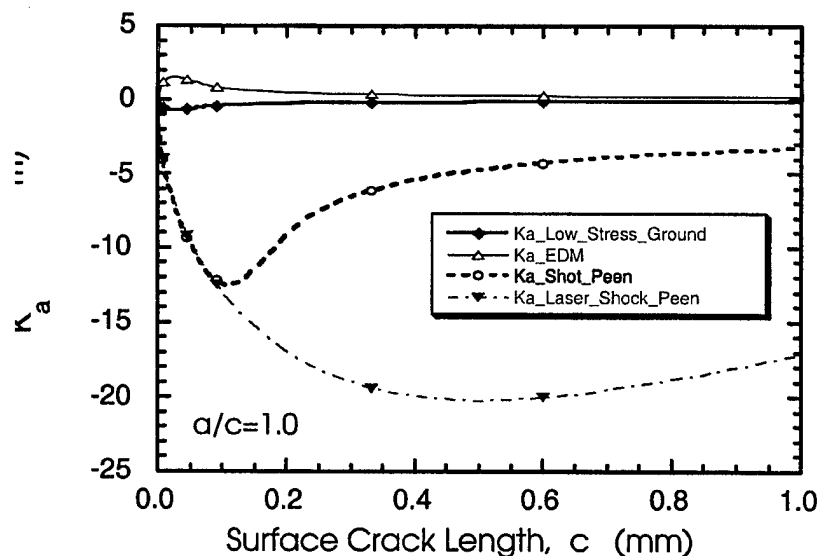


Fig. 12. Stress intensity factors at the depth of a semicircular surface crack,  $K_a$ , in a body subjected to the residual stress fields shown in Fig. 11.

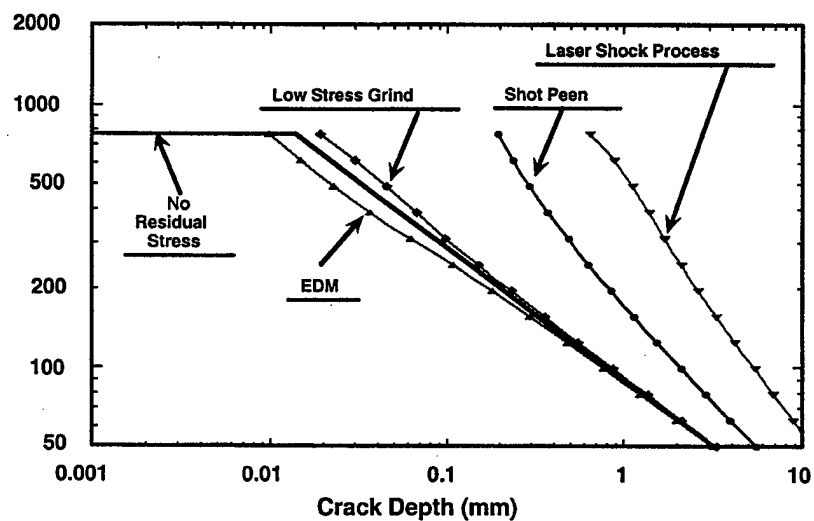


Fig. 13. Fatigue-life map for Ti-6246 showing the effect of the residual stress fields shown in Fig. 11 on  $\Delta K_{th}$  of a semicircular surface crack loaded under  $R = 0.1$  fatigue. The calculations show a dramatic effect of some of the residual stress fields on the allowable crack size below which crack growth should not occur.

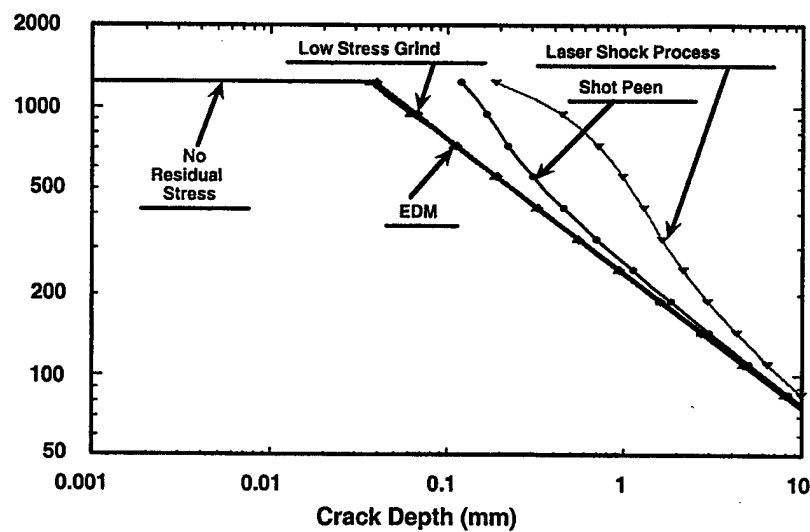


Fig. 14. Fatigue-life map for Ti-6246 showing the effect of the residual stress fields shown in Fig. 11 on  $\Delta K_{th}$  of a semicircular surface crack loaded under  $R = 0.8$  fatigue. The effect of the residual stresses on allowable crack size is much less significant under this high-stress-ratio fatigue condition than under  $R = 0.1$  loading.

Reference: Ashbaugh, N.E., Porter, W.J., Prakash, R.V., and Sunder, R., "A Fractographic Study of Load-Sequence Induced Mixed-Mode Fatigue Crack Growth in an Al-Cu Alloy," accepted for publication in ASTM STP-1359, Mixed-Mode Crack Behavior, 1999.

## **A Fractographic Study of Load-Sequence Induced Mixed-Mode Fatigue Crack Growth in an Al-Cu Alloy**

Ashbaugh, N.E.<sup>1</sup>, Porter, W.J.<sup>1</sup>, Prakash, R.V.<sup>2</sup> and Sunder, R.<sup>2</sup>  
<sup>1</sup>University of Dayton Research Institute,

1031 Irving Ave., Dayton, OH, U.S.A, 45419-0128

2BiSS Research, 41A, 1stA Cross, AECS 2nd Stage, Bangalore 560 094, India.

### **Abstract**

Fatigue crack growth behavior was studied on C(T) and SE(T) specimens from Al-Cu alloy 2014 using specially-designed load sequences. The experiments were organized to induce microscopic mixed-mode fatigue crack growth while at the same time reducing or eliminating fatigue crack closure. This was achieved by switching between high-amplitude, low-stress ratio and low-amplitude, high-stress ratio cycles. Retardation effects observed under these conditions are attributed to local crack branching and mixed-mode conditions induced by variable amplitude loading.

**Key words:** Fatigue crack growth, mixed mode, fractography, programmed loading.

### **Introduction**

Most load sequences of practical interest are random in nature. However, most laboratory research on metal fatigue is performed under constant amplitude loading. Early research on fatigue under variable amplitude loading [1,2] revealed the non-linear nature of cumulative fatigue damage. History effects in the crack formation stage were attributed to strain hardening and residual stresses at the notch root left behind by prior overloads [3, 4].

Schijve listed a variety of factors that may be responsible for load-interaction effects observed in fatigue crack growth [5, 6]. One of them was 'crack front incompatibility'. Consider the schematic in Fig. 1 showing Stage I and Stage II behavior [7,8]. Stage I involves Mode II crack extension that occurs with the assistance of Mode I (Mode I+II) that opens up the crack and thereby eliminates obstacles to reversed sliding caused by planar discontinuities. Stage I is characterized by a slanted crack along the slip plane. Stage II is normally associated with Mode I cracking. At the microscopic level, it is again Mode I+II. But the microscopic plane appears flat rather than slanted due to the smoothening of local slip plane reversal that is absent in Stage I. As the crack length increases, the associated applied stress intensity range causes increasing reversed plastic deformation along the specimen surface. As the surface area is in plane stress, such reversed deformation will promote Mode III reversed slip and associated Mode I+III growth.

Each of the three mode combinations described above is associated with well-defined crack growth rate intervals [5,8]. If crack growth rate changes abruptly, as would be the case under variable amplitude loading, any transition in mode will happen over some crack extension. In the interim, 'incompatible' crack plane conditions are likely. This situation essentially distorts crack tip similarity criteria assumed in fracture mechanics design.

The Paris equation assumes that similarity in  $\Delta K$  is an adequate criterion for similar fatigue crack growth rate,  $da/dN$ , given by  $da/dN = C(\Delta K)^m$  [9, 10]. This is essentially the basis for the application of fracture mechanics in engineering design for endurance and damage tolerance. The constants, 'C' and 'm' in the Paris equation are determined from testing under constant amplitude loading. It was later found that the stress ratio (ratio between the minimum and maximum load, represented by, R), can influence 'C'. Further, a threshold

stress intensity,  $\Delta K_{th}$ , was introduced, below which the fatigue crack may not propagate. Finally, a critical stress intensity,  $K_{c}$ , was associated with catastrophic failure.

$\Delta K$  alone is not an adequate similarity criterion for  $da/dN$ , even under constant amplitude loading. An ideal life prediction model should account for all the variables that are likely to affect  $da/dN$  under an arbitrary load sequence. At least seven load interaction mechanisms can cause distortion of similarity criteria [6]. These include crack closure, crack tip blunting/re-sharpening, residual stress, strain hardening/softening, micro-structural change, crack branching, crack front incompatibility and roughness [5,6]. Interestingly, most prediction models currently in practice are based on the crack closure phenomenon, while a few account for retardation due to plastic zone effects [11, 12].

Currently available models for crack growth do not appear to simulate the effect of more than one mechanism, indicating that success in predictions may be either due to a cross-influence of mechanisms, or, due to the predominance of a single mechanism. The former may be responsible for misinterpretation of test results or why the same result can be explained by the action of more than one mechanism. Mixed-mode experiments are conventionally organized either by varying crack orientation or by including more than one loading action, or, both. In this study, mixed-mode conditions are induced at the microscopic level by exploiting the sensitivity of mode combinations to instantaneous crack growth rate, i.e. instantaneous cyclic load magnitude. The next section describes the experimental procedure and is followed by a discussion of observations and conclusions.

## Experimental Procedure

Compact tension [C(T)] and single edge notch tension [SE(T)] specimens of thicknesses 5 mm and 3.5 mm respectively, oriented along the longitudinal (LT) direction were cut from an extruded bar stock of Al-Cu alloy 2014 and used in the experiments. This material is known to be conducive to striation formation [13] - a feature that is essential in a fractography-oriented experiment. Fig. 2 describes the programmed load sequences used in the experiments. Table 1 provides details on test coupons including a cross-reference to loading conditions.

The load sequences were designed to:

- Induce a preferential crack extension mode and plane at a given  $\Delta K$  and then enforce a change in the crack mode and plane through a change in  $\Delta K$ . Such changes are not typical of constant amplitude load conditions.
- Avoid the superposed effect of fatigue crack closure by performing tests under constant or marginally varying maximum stress. The periodic high amplitude, low stress ratio cycles will keep crack opening stress ( $S_{op}$ ) levels low and reduce or eliminate closure-induced effects under the low amplitude cycles. This reasoning is supported by  $S_{op}$  measurements appearing below.
- Vary the relative contribution of large and small cycles to induce domination of a particular crack extension mode and plane.
- Introduce sufficient cycles of small amplitude to enable measurement of  $da/dN$  due to small cycles from striation/marker bandwidth. Individual striations at very low crack growth rate may not be discernible. However, crack growth rate is estimated as the ratio of the width of striation band to the number of cycles that caused it. This technique is effective in handling near threshold crack growth rates.
- Introduce variation in stress ratio for small amplitude cycles. In sequences 'c' and 'd' of Fig. 2, as many as five steps (A-E) at different stress ratio ( $R = 0.73, 0.69, 0.63, 0.55, 0.42$ ) but with the same amplitude were introduced. All five steps were applied for an equal duration to enable ready assessment of the stress ratio effect from the width of the striation band. Crack growth rate at higher stress ratios corresponds to 'closure free' conditions, while  $da/dN$  at lower stress ratios corresponds to partly closed fatigue crack. Besides, in view of steep change in  $\Delta K$ , the lower stress ratio steps would be now sensitive to both mixed mode, as well as plasticity (closure) induced interaction effects. The cycle duration was carefully selected to ensure that all five steps (A to E) would be discernible on the

fracture surface, and at the same time, all the five steps could be seen on a single fractograph for purpose of comparison. This was not always possible, resulting in fewer data points from the long block sequences 'b' and 'd' of Fig. 2.

A question likely to arise in dealing with complex programmed load sequences concerns the mutual interaction of different steps in the sequence. Let us consider this question with reference to Fig. 2c and 2d, which are fairly complex sequences. The large amplitude steps are applied with sufficient periodicity to ensure conditions of stable crack tip plasticity. It was assumed that the crack extension in any single step is always only a small fraction of the current monotonic plastic zone size, and is unlikely to see the effect of transients. This assumption was confirmed by the results of fractography, which did not reveal any significant transients in small cycle growth. Further, the fractographic results did not appear to indicate noticeable differences between sequences 'c' and 'd' (duration effect). Any interaction between cycles A-E would be overshadowed by the influence of the large amplitude cycles.

Table 1. Summary of tests

TestNo.	Load sequence (See Fig.2)		Specimen		Maximum Load level
			Geometry	Size (mm)	
1	(a)		SE(T)	W45/B3	100 MPa
2	(b)		SE(T)	W45/B3	100 MPa
3	(c)		C(T)	W40/B5	2 kN
4	(c)		SE(T)	W25/B5	100 MPa
5	(d)		C(T)	W40/B5	2 kN
6	(d)		SE(T)	W25/B5	100 MPa
7	Constant Amplitude	R=0.1	SE(T)	W25/B5	80 MPa
8	Constant Amplitude	R=0.73	SE(T)	W25/B5	80 MPa

**Baseline crack growth rates.** Tests 7 and 8 were conducted under constant amplitude loading at  $R=0.1$  and  $R=0.73$  respectively. These data provided a reference for comparing growth rates estimated under programmed loading. Crack growth at  $R=0.73$  is assumed to represent conditions without crack closure, and at  $R=0.1$  is assumed to be similar to the low- $R$  conditions under programmed loading. These two tests were performed under computer control with a maximum stress ( $S_{max}$ ) of 80 MPa similar to the load level used in programmed loading. Crack length was estimated by the unloading compliance method. This estimate of crack length was periodically compared with optical surface measurements.

The tests were conducted on servo-hydraulic, computer controlled testing machines under ambient conditions at a constant loading rate between 40 to 80 kN/s, depending on the machine performance. The SE(T) specimens were held in hydraulic wedge grips that inhibit bending by enforcing uniform displacement. Stress intensity calculations were corrected for un-gripped height ( $H$ )/width ( $W$ ) ratio of 2.0 [14].

Crack growth rate under programmed load sequence was estimated from fractographs obtained from a scanning electron microscope (SEM). The SEM incorporates stage tracking for an accurate estimation of crack size and location across specimen thickness. Thus, it was possible to accurately determine local crack growth rates, as well as the associated  $\Delta K$  levels, which could be, if required, corrected to  $\Delta K_{eff}$ , the effective stress intensity factor. Crack growth rate was always measured as the ratio of striation bandwidth to the number of load cycles that caused it. It was not essential to identify individual striations as long as the beginning and the end of a band could be identified. Apart from making a comparison of measured crack growth rates, a detailed

examination of the fracture surface was made in an attempt to interpret underlying crack extension mechanisms and their interaction.

## Results

**Crack Closure Estimate from Fractography.** Crack closure was evaluated using three independent techniques. Specially designed 'closure' blocks were introduced in load sequences 'c' and 'd' of Fig. 2 to obtain a measure of crack closure stress,  $S_{op}$  [15]. These are cycles with constant maximum stress ( $S_{max}$ ) and tapering minimum stress ( $S_{min}$ ). Assuming  $S_{op}$  to be constant in the sequence, its magnitude can be readily estimated from the number of equally spaced striations. Fig. 3 shows a typical striation pattern caused by these cycles in Test No. 4. We see 10 equally spaced striations, suggesting an  $S_{op}$  level of 35%.

**Near and far field displacement based assessment of the effective stress intensity.** Load versus crack mouth opening displacement (CMOD) and load versus crack tip deformation were recorded during Test No. 8 by cycling at a low frequency between 100% and 10% of  $S_{max}$  at a single crack size of 12 mm. From the load versus CMOD data presented in the form of load versus offset displacement in Fig. 3b, one could infer that the  $S_{op}$  level is about 0.33. Assuming a constant  $S_{op}$ , it would follow that the crack will be fully open under steps A, B and C for load sequences 'c' and 'd' (of Fig. 2). The crack may or may not be fully open in step D and will certainly be part closed in step E. One may infer that any anomalies in crack growth rate in steps A, B and C may not be attributed to crack closure.

The load versus CMOD response is sensitive to wake behavior. The crack tip deformation measurements presented as load versus offset displacement are shown in Fig. 3c. These measurements were made using laser interferometry (IDG)[16, 17]. They represent the relative displacement of a pair of square indents 10 microns in size, located 30 microns apart, which are aligned along the loading direction and located about 15 microns *ahead* of the crack tip. Thus, the entire gauge length of measurement is well within the plastic zone, estimated to be about 100 microns in diameter. As the gauge length is extremely small, we see sinusoidal oscillations in displacement output associated with the nature of the algorithm that tracks fringe movement. If one assumes that the crack driving force will be proportional to cyclic displacement ahead of the crack tip, an effective stress intensity range,  $\Delta K_{eff}$  can be estimated as a function of relative crack tip displacement. This displacement will be sensitive to the instantaneous crack tip compliance, which varies as a function of load as shown in Fig. 3c. It may be noted that both Figs. 3b and 3c show differential displacements from a secant corresponding to the compliance at the onset of unloading. While both figures appear to be similar in trends, Fig. 3c is different both from a qualitative and quantitative sense. The values of  $\Delta K_{eff}$  and  $\Delta K$  are assumed to be the same at the highest R of 0.73. At lower R, value of  $\Delta K_{eff}$  is corrected for the change in crack tip compliance as seen in Fig. 3c. The  $\Delta K_{eff}$  data computed in this manner is used in the forthcoming presentation of results. This procedure for the determination of  $\Delta K_{eff}$  is similar to the one proposed by Keith Donald using CMOD data [18].

## Fractographic Observations

The load sequences used in the study may be broadly classified into short (Fig. 2a and 2c) and long duration sequences (Fig. 2b and 2d). Fractographs from the simplest short duration sequence ('a' in Fig. 2) provide an idea of the contrasting morphology one observes under the type of load sequences used in this study. Typical fractographs from test specimen 1 appear in Fig. 4. Figure 4a shows a typical fractograph from the mid-thickness region at a moderate  $\Delta K$ . The arrow indicates the general direction of crack growth. The white bar indicates crack extension during 100 cycles of high stress ratio, low amplitude loading. These bands are followed by two striations, one due to the single large cycle, the second (smaller one) due to loading half-cycle that leads to the following first high stress ratio, small amplitude cycle. Evidence of crack branching (Mode II) is provided by 'splits' in the fracture surface along the crack front. This is particularly so at the site of an inclusion or second phase particle. Generally, there is no ambiguity in interpreting crack extension due to the small and large cycles. At higher  $\Delta K$ , crack extension per block is comparable to grain size, and a more



chaotic crack front appears across multiple grains (as in Fig. 4b). Along the specimen surface, a curved crack front is observed (Fig. 4c), with the normal direction of crack front pointing towards the specimen surface. This is characteristic of the surface ligament that tends to lag behind the mid-thickness crack front. Also, splits associated with crack branching are not visible near the surface. This is indicative of Mode I+III behavior, rather than Mode I+II. However, much of the surface region does not provide clear striation patterns due to the abrasive wear from mode III action. Most of the fractographic estimates of  $S_{op}$  and all measurements of  $da/dN$  were therefore restricted to the mid-thickness region, which represents bulk behavior.

### Effect of Specimen Geometry

Figures 5 and 6 summarize the quantitative observations of the study. Previous studies on the same material showed that fractographic estimates of crack growth rate are similar to those derived from crack size measurements during testing [19]. In tests 1-6, crack growth rates were determined exclusively through quantitative fractography.

Study of over 300 fractographs from the three different specimen types did not indicate any qualitative difference in crack growth between geometries. However, as seen from Fig. 5, we were unable to obtain similar  $da/dN$  under programmed loading at given stress intensity range in SE(T) and C(T) specimens of the same thickness. From the limited experiments in this study, it appears that the C(T) geometry causes greater quasi-static extension in the larger cycles due to mixed-mode conditions, than in the SE(T) geometry where the specimen rotation is inhibited through wedge gripping. This may explain the differences in growth rates between C(T) and SE(T) geometry (see Fig. 5). However, available evidence appears to be insufficient to draw any systematic inferences. Therefore to eliminate specimen geometry as a variable, data in Fig. 6 are restricted to SE(T) coupons.

### Effect of Load Sequence on Crack Growth Rates

Figures 6a and 6b show results from test No. 6 and 4 which were subjected to load sequences 'c' and 'd' respectively. Included in the same figure are the baseline crack growth data obtained under constant amplitude loading at stress ratios of 0.1 and 0.73. The upward trend at crack growth rates above  $10^{-3}$  mm/cycle at a stress ratio of 0.73 may be attributed to the proximity of  $K_{IC}$ . There also appears to be a transient at growth rate of  $10^{-4}$  mm/cycle for specimens tested under  $R=0.1$  which may be attributed to pre-cracking. The constant amplitude baseline data show a stress ratio-induced horizontal shift between the  $R=0.1$  and  $R=0.73$ . This shift disappears when growth rates are plotted against effective stress intensity (see Fig. 6c).

Under programmed loading, low amplitude growth rates are retarded by a factor of five. Surprisingly, even the high amplitude (low stress ratio) cycles show retarded behavior. This effect is accentuated in Fig. 6c where the growth rate is plotted against effective stress intensity. Crack growth rate data for  $R=0.1$  was corrected using the fractographically determined  $S_{op}/S_{max}$  of 35%. For the other stress ratios, the correction was made using the data from Fig. 3c. We find that all the low amplitude data at five different stress ratios from two tests fall into a narrow band. This indicates that  $\Delta K_{eff}$  corrections based on measured crack tip displacement may be a good indicator of crack driving force.

The noticeable retardation in the low amplitude cycles may be attributed to current crack plane being different (Mode I+II) (as seen in Fig. 4) from the preferred crack plane corresponding to constant amplitude loading. Similar observations of retarded crack appear in References 20 to 22.

Retardation under large cycles may be due to crack branching which tends to unload the crack [23]. The occurrence of crack branching is shown in forthcoming fractographs. Crack branching was not observed under constant amplitude loading at  $R=0.1$ , but occurs frequently when large cycles follow a block of small cycles. One may infer that this retardation is an indirect consequence of mixed-mode conditions that promote branching. The difference in cycle duration between load sequences 'c' and 'd' did not affect growth rates at any individual stress ratio.

Figure 7 shows a few interesting features associated with sequence induced mixed-mode behavior that one may not see under constant amplitude loading. Fractographs of crack growth under sequence shown in Fig. 2c appears in Figs. 7a and 7b. This is a short block, with frequent occurrence of large cycles. This is also

evident from the extent of large cycle induced crack growth. The small amplitude cycles promote faceted morphology with a straight front across multiple grains as indicated by bands A, D and E seen in the picture. Crack extension in the large cycles is retarded along grain boundaries which leave behind stretched lips protruding from the fracture surface. These are 'straightened out' by the small cycles indicating the possibility of microscopic load interaction effects due to incompatible crack front (curved versus straight crack front). From the pairs of 'closure' blocks preceding steps A and D, one can count 5 to 9 equally spaced striations, subject to interpretation, implying an  $S_{op}$  level of between 22.5 and 32.5% of  $S_{max}$ . This ambiguity is in contrast to the clarity evident in Fig. 3.

Figure 7b provides an example of a typical reaction of the fatigue crack to second phase particles in its path. The crack front would seem to be unperturbed by the particle under step B, suggesting that given the prevailing cyclic crack tip strain, the matrix and particle behaved as one while the particle was dislodged. This is not so under the following 20 cycles at high amplitude, where one more such particle is encountered. In the rising half of the fifth cycle, the crack front locally surges forward and even branches into two cracks as evident from the split along the crack front. Local crack extension appears to be accelerated when compared to that in the nine cycles preceding step 'B', which had the same  $\Delta K_{eff}$ , suggesting  $S_{op} = 32.5\%$ . Such local accelerated crack extension and single cycle 'popping' forward behavior was consistently observed under all load sequences shown in Fig. 2, but appeared to be absent under constant amplitude loading. A typical constant amplitude picture appears in Fig. 7c at a comparable  $\Delta K$ .

Figures 8 and 9 show typical fractographs obtained under long sequence loading ('b' and 'd' in Fig. 2), with the low amplitude component dominating the fracture surface. Fig. 8 shows the evolution of striation pattern with increasing crack length in Test no. 6. Each striation band was formed by over 5,000 cycles through steps A to E and the markers in between. The 100 cycle markers applied every 20 blocks of A to E are clearly visible, even though no striations from individual cycles can be seen. One could observe striation bands immediately after crack formation and within 10 microns from the edge of the fine EDM notch that served as crack initiator (Fig. 8a). Evidently, the crack growth rates are so low in this region that no local acceleration is visible at second phase particles - even along the 100 cycle band caused by the largest cycles.

Fig. 8b shows crack growth over A to E immediately following the 100 large cycles and closure block. The closure block is visible as a single band following the 100 cycle band. Crack growth rate is marginally retarded in the first block of A to E and appears to be constant over the subsequent ones indicating recovery from the initial interaction effects. Striations from individual cycles are not yet visible at this crack size. Growth rates even under the large amplitude cycles are too low to be sensitive to the appearance of secondary particles on their path. This picture changes after another 1 mm of crack growth as shown in Fig. 8c. We now find that the 3 large amplitude cycles, which serve as markers between small amplitude steps, leave behind discernible striations that occupy a noticeable part of the overall band as opposed to those in Figs. 8a and 8b. Further, the presence of a second phase particle during these cycles causes local accelerated crack extension. It would appear that large and small amplitude cycles have developed  $\Delta K$  levels that are mutually incompatible when viewed in terms of local crack extension plane and mode.

The microscopic change in crack extension mode (to mode II) and plane appears evident even at lower  $\Delta K$  levels in the C(T) geometry (Fig. 9a). Crack growth rate in the first A to E block following the 100 cycles appears retarded. In this specimen, the effect of mixed-mode conditions appears to be more dramatic as seen in Fig. 9b. We find that even at a relatively low  $\Delta K$ , the 100 large cycles cause a sudden increase in local crack extension through quasi-static rupture through second phase particles. The white outline indicates the crack front shape before and after the 100 cycles and closure block. Fig. 9c shows crack growth during the 100 cycles step in load sequence 'b' shown in Fig. 2b between the low amplitude 'A' cycle block. Initial crack growth rate is almost twice as high as the subsequent  $da/dN$  in the step. This acceleration cannot be attributed to closure related effects, because constant amplitude  $S_{op}$  in 'A' would be greater than in the high amplitude cycles. The stretch observed in the first cycle after 'A' may be associated with crack branching in the other half of the specimen, a question, whose detailed consideration is forthcoming.

### Crack Closure in Mixed Mode

More evidence of load sequence induced mixed-mode crack growth appears in Fig. 10. The striation patterns in Figs. 10a and 10b were obtained in earlier work [24] using a load sequence similar to (d) of Fig. 2. Only three steps of low amplitude cycles, A, B and C were applied, each with 2,000 cycles and spaced by 10 cycles of high amplitude which serve as markers on the fractograph. This was a SE(T) specimen of width 45 mm and thickness 5 mm from the same material as the one used in this study. The fractograph suggests identical crack growth during steps A, B and C. This may be explained by identical  $\Delta K_{eff} = \Delta K$ , assuming a fully open crack (this is in contrast to observations in this study of a marginal, but consistent difference in  $da/dN$  for A, B and C). Towards the lower left, noticeable crack extension is observed over the 10 large cycles in a plane that is steeply inclined to the plane of A, B and C. This forms a terrace profile as crack direction is switched between high and low load amplitude. At the top right, the local crack front appears to be inclined with respect to the remaining part. In this region, crack extension in 'C' is retarded by half when compared to A and B. Similar pattern is also observed at the lower right on neighboring grains on which the local crack plane is inclined. This unique picture was seldom observed at other locations and appears to suggest an interaction between crack extension mode and crack closure. One may suggest that in 'C', the crack was fully open in Mode I and only partly so in Mode II. Thereby, wherever Mode II was imposed by local crack plane orientation, some obstruction to the local sliding process may have been present. Under normal conditions, Mode I opens up the possibility of Mode II by raising the crack surface over the height of local roughness or loose particles. This capability is attenuated by a factor equal to the cosine of the angle of the local crack plane.

### Crack Branching

Fig. 10b reveals an unusual striation pattern produced by load sequence induced mixed-mode cracking in the same specimen. Once again, we find almost equal crack extension in A, B and C. However, the 10 large cycles appear to leave behind twice as many striations, which we call as an "open book" pattern. If we draw vertical lines as striations on the left hand side page of a book and close it before the ink dries, an identical mirror image pattern is formed on the opposite page. Partial opening of the book reveals striation patterns on both sides of the page similar to what we see on the fractograph in Fig. 10b. The total striation count is twice the number of applied cycles. This unusual pattern is an optical illusion caused by crack branching. What we see is one face of the branched crack placed alongside a crack face from the other branch!

A schematic suggesting how the "open book" pattern is produced appears as Fig. 10 for a case of three large cycles embedded into a sequence of low amplitude cycles. It follows the scheme of (single) crack extension proposed by Broek [25]. The ratio of small to large load cycles (2,000:10) is so high that the small cycles control mode and crack plane (Mode I at the macroscopic level) (Fig. 10a). Sudden application of the 3 large cycles causes the crack to branch simultaneously into two cracks, *both* of which grow in each subsequent large cycle (Fig. 10 b,c,d). Further application of low amplitude cycles causes crack growth in the plane corresponding to only one of the cracks. Both crack tips may continue to grow for some time. However, eventually, only one of them progresses to failure (Fig. 10e). What we observe in Fig. 10b and also in Fig. 10c from another test are the 10 striations from one branch and another 10 from the other branch. Their arrangement, combined with the excellent depth of focus of the SEM creates the illusion of an "open book" pattern – an illusion that a single crack grew into the depth of the material, then opened up, revealing striations on either side. Fig. 10c shows another example of the "open book" pattern observed in Test No. 6 with 3 large amplitude cycles between the load cycle steps of low amplitude.

The crack branching scheme suggested above and illustrated in Fig. 10 is supported by matching fractograph-pairs that appear in Figs. 11 and 12. In these figures, the bottom fractograph is from the matching location of the other fracture surface. To facilitate comparison, the bottom image is flipped over so that a surface fracture in one fractograph would appear in the same location in the second fractograph. These pairs reveal how crack branching in one half is matched by a stretch mark on the other. They indicate that one can *never* see signs of a split (or crack branching) on *both* sides at the same time. If one side shows the 'open book' formation, the other will show a stretch followed by only one set of striations. It may be observed, that the

characteristic 'open book' pattern will be observed only when a limited number of high cycle markers are applied. A mere switch to the large amplitude cycling (without return to low amplitude) will eventually leave behind at most, a split on the fracture surface.

Crack branching due to induced mixed-mode conditions appears to momentarily accelerate crack extension in the large cycles. This is evident from the relatively large fraction of the fracture surface taken by the 10 marker cycles in Fig. 10b as opposed to Fig. 10a. One may expect that as a consequence of two crack branches, subsequent cracking is retarded (both at high and low amplitude), thereby compensating the effect of local acceleration. This may explain why data in Fig. 6 shows no signs of acceleration. This phenomenon can be studied further by performing tests with a controlled number of large cycles, so as to accentuate the initial acceleration effect. The load sequence 'a' of Fig. 2 is an example of such a test. However, baseline data for that specimen were not available for a comparative analysis.

### Concluding Remarks

The study suggests that load-history-induced mixed-mode conditions can cause retardation in growth rate by up to a factor of five at a given  $\Delta K_{eff}$ . There appears to be retardation both when switching from high to low amplitude as well as from low to high. The latter was unexpected and may be due to crack branching. Also in the case of the latter, though the average effect is that of retardation, the first few cycles invariably see accelerated growth. In the case of the former, the larger retardation is attributed to the cumulative effect of incompatible mode (mechanism) and crack branching (mechanics).

Crack branching in large cycles creates the same effect as overloads. An overload creates a large plastic zone that shields the crack tip. Crack branching dissipates crack driving force by directing it at two crack tips instead of one. The effects produced in this study may be termed as 'fatigue' overloads, rather than 'static' overloads. They occur in the mid-thickness region and are hardly visible at the surface. In sequences 'c' and 'd' of Fig. 2, the magnitude of  $S_{max}$  in the large cycles and in step 'A' was identical. The observed effects therefore appear to have been caused without any increase in monotonic plastic zone size and exclusively by a variation in  $\Delta K_{eff}$  alone. The fatigue crack apparently settles down to stable conditions that are associated with a given  $\Delta K_{eff}$  or growth rate. Any abrupt change in these parameters causes momentary unstable behavior until the new conditions including plane and crack extension mode stabilize. The retardation/acceleration effects associated with the transitional behavior require further study.

In conventional experiments under variable amplitude loading, mixed-mode effects may be obscured by the apparently overwhelming influence of other load interaction phenomena. However, there are practical situations which may involve history-induced mixed-mode conditions. These include load environments that contain a large cycles of low amplitude, high mean stress normally experienced by components in gas and steam turbines, transport aircraft wing and pressure vessels subject to usage-induced pressure oscillation. In the event the damage content of small amplitudes in such spectra is substantial, the effects observed in this study may become significant.

### Acknowledgements

Most of this work was performed at the Air Force Research Laboratory (AFRL), Materials Directorate, Wright-Patterson AFB, Dayton, Ohio with support from AF contract F33615-94-C-5200. The testing including measurements involving load versus displacement was meticulously performed by Andy Lackey of University of Dayton Research Institute. H.V. Sumana of BiSS Research was responsible for digitizing the fractographic imagery to determine programmed load crack growth rates and their consolidation versus load parameters. Support of Luann Piazza at the AFRL SEM facility is gratefully acknowledged. The authors deeply appreciate stimulating discussions with numerous colleagues at AFRL.

### References:

1. Gassner, E., "Effect of Variable Load and Cumulative Damage on Fatigue in Vehicle and Airplane Structures", *Proceedings of the International Conference on Fatigue of Metals*, Institute of Mechanical Engineers, London, 1956, pp. 304-309.
2. Schijve, J., "The Prediction of Fatigue Crack Propagation Under Service Load-Time Histories", National Aerospace Laboratory, NLR, The Netherlands, NLR MP 73016U, 1973.

3. Morrow, J.D., "Fatigue Properties of Metals" in *Fatigue Design Handbook*, Section 3.2, Society of Automotive Engineers, 1968.
4. Morrow, J. D., Wetzel, R. M. and Topper, T. H., "Laboratory Simulation of Structural Fatigue Behavior", *Effects of Environment and Complex Load History on Fatigue Life*, ASTM STP 462, ASTM, Philadelphia, 1970, pp. 74-91.
5. Schijve, J., "Fatigue Damage Accumulation and Incompatible Crack Front Orientation", *Engineering Fracture Mechanics*, Vol 6, 1974, pp 245-252.
6. Schijve, J., "Fatigue Crack Closure: Observations and Technical Significance", in *Mechanics of Crack Closure*, ASTM STP 982, J. C. Newman, Jr., and Elber, W., Eds., ASTM, Philadelphia, 1988, pp 5-34.
7. Forsyth, P. J. E., "A Two Stage Process of Fatigue Crack Growth", *Proceedings of the Crack Propagation Symposium*, Cranfield, 1961, Vol. 1, pp 76-94.
8. Laird, C., "The Influence of Metallurgical Structure on the Mechanism of Fatigue Crack Propagation", *Fatigue Crack Propagation*, ASTM STP 415, Philadelphia, 1967, pp 131.
9. Paris, P. C. and Erdogan, F., "A Critical Analysis of Crack Propagation Laws", *J. Basic Engineering*, Trans ASME, Series D, 85,4, ASME, 1963, pp 528-534.
10. Paris, P.C., "The Fracture Mechanics Approach to Fatigue", *Proceedings of the 10<sup>th</sup> Sagamore Army Materials Research Conference*, Syracuse University Press, 1964, pp 107-126.
11. Wheeler, O. E., *Journal of Basic Engineering*, March 1972, pp 181-186.
12. Willenborg, J., Engle, R. M., and Wood, H. A., "A Crack Growth Retardation Model Using an Effective Stress Concepts", TM-71-1-FER, Air Force Flight Dynamics Laboratory, WPAFB, OH, 1971.
13. Sunder, R., Prakash, R. V., and Mitchenko, E. I., "Fractographic Study of Notch Fatigue Crack Closure and Growth Rates", *Fractography of Modern Engineering Materials: Composites and Metals, Second Volume*, ASTM STP 1203, J. E. Masters and L. E. Gilbertson, Eds., ASTM, West Conshohocken, Pa, 1993, pp 113-131.
14. John, R. and Rigling, B., *Engineering Fracture Mechanics*, 1997, pp 257, Nov 1997.
15. Sunder, R. and Dash, P.K., *Int. J. Fatigue*, Vol. 4, 1982, pp 97-105.
16. Hartman, G. A. and Nicholas, T., "An Enhanced Laser Interferometer for Precise Displacement Measurements," *Journal of Experimental Techniques*, February 1987, pp. 106-112.
17. Sharpe, W. N., Jr., "Application of Interferometric Strain Displacement Gage", *Optical Engineering*, Vol. 21, No. 3, 1982, pp 483-488.
18. Donald, K. J., "Introducing the Compliance Ratio Concept for Determining Effective Stress Intensity", *Int. J. of Fatigue*, Vol. 19, Suppl. No. 1, pp S191-195, 1997.
19. Mitchenko, E. I., Raghu V Prakash and Sunder, R., "Fatigue Crack Growth under an Equivalent FALSTAFF Spectrum", *Fatigue and Fracture of Engineering Materials and Structures*, 1995.
20. Zuidema, J., and Blauuw, H. S., "Slant Fatigue Crack Growth in Al-2024 sheet Material", *Engineering Fracture Mechanics*, Vol 29, p 401, 1988.
21. Edwards, R. A. H., de Jonge, E. M., Zuidema, J., "The Fracture Mode Transition and its Effect on Crack Growth Rate Retardation", *Congress Proceedings, Fatigue 84*, Birmingham, U. K., 3-7, Sept 1984.
22. Veer, F., *The Effect of Shear Lips, Loading Transitions and Test Frequency on Constant  $\Delta K$  and Constant Load Amplitude Fatigue Tests*, Ph. D. Thesis, Tu Delft, 1993.
23. Suresh, S., and Ritchie, R. O., *Proceedings of International Symposium on Fatigue Crack Growth Threshold Concepts*, Eds: D. L. Davidson and S. Suresh, TMS-AIME, Warrendale, 1983, pp 227.
24. Sunder, R., Porter, J., and Ashbaugh, N. E., "The Effect of Stress Ratio on Fatigue Crack Growth Rate in the Absence of Closure", *Int. J. of Fatigue*, Vol 19, Suppl. No. 1, 1997, pp S 211-S221.
25. Broek, D., "Some Contributions of Electron Fractography to the Theory of Fracture", National Aerospace Laboratory, NLR TR 72029 U, The Netherlands, 1972.

### Figure Legends

1. Schematic of stages and modes of crack growth viewed from different planes.
2. Load Sequences used in experiments. All tests involved repetitive application of the load sequence from crack initiation till specimen failure.
3. Three techniques employed to estimate crack closure stress and effective stress intensity factor. (a) Fractograph of Test No. 4 under load sequence 'c' in Fig. 2 showing two 'closure' blocks preceding block D. The crack opening stress level controls the number of equally spaced striations. (b) Load versus CMOD record obtained under constant amplitude crack growth testing in Test 8. CMOD is expressed as offset displacement. (c) Load versus crack tip displacement from laser interferometry. Change in crack tip compliance at different load ranges was used to correct the crack driving force to obtain effective stress intensity range. Correction factor for different blocks shown in the inset.
4. Fractographs from an SE(T) specimen tested under sequence 'a' of Fig. 2. Crack grows from the left side to right side. Specimen stage of SEM locked during fractographic observations. (a) Mid-thickness. Crack length = 9 mm. Note crack branching during large cycles, indicated by a split along the crack front. This is accentuated at a second phase particle. Stretch marks are visible during large cycles on the right hand side, indicative of possible crack branching on the other half of the fracture. (b) Mid-thickness at a high stress intensity factor range. Crack length=12.3 mm (c) Near surface at a high stress intensity range. Crack length = 12.6 mm. Note crack growth along a curve and absence of signs of crack branching.
5. Crack growth rates determined from fractography can be different between C(T) and SE(T) specimens even for a fully open crack ( $R=0.73$ ).
6. Crack growth rate data for the SE(T) specimens tested under two load sequences 'c' and 'd' of Fig.2. Crack growth rates estimated from fractography. (a, b)  $da/dN$  versus  $\Delta K$  under load sequences 'c' and 'd', (c) data from Figs. a,b versus  $\Delta K_{eff}$  computed using correction factors for range listed in Fig. 3c.
7. Striation patterns under short duration load sequence 'c' of Fig.2. (a) High amplitude cycles cause a curved crack front within grains that are straightened out by low amplitude cycling. This is a possible load-interaction mechanism. (b) Crack front reacts differently to a second phase particle under low and high amplitude cycles. Crack branching (splitting) is visible under high amplitude cycles. (c) Striation pattern from constant amplitude loading (Test No. 7) at comparable  $\Delta K$  showing no signs of crack branching or splitting.
8. Striation patterns under long duration sequence 'd' of Fig.2. (a) Striation bands immediately after crack formation at the root of the EDM notch. Each band corresponds to over 5000 cycles of loading between steps A to E of Fig. 2. Individual steps are not visible at a crack length of 300 microns (b) individual steps are visible, but individual striations from large cycles are not discernible even at a crack length of 4.15 mm. Note retarded growth immediately after the 100 large-cycle step. (c) Individual striations from high amplitude cycles are visible at larger crack size.
9. Large cycle transients under long duration programmed loading. (a) Localized changes in the plane of crack growth during the 100 cycles of high-amplitude step is visible even at the low  $K_{max}$  of  $7.1 \text{ MPa}\sqrt{\text{m}}$ . (b) Localized burst in crack extension across second phase particles at marginally higher  $K_{max}$  of  $7.4 \text{ MPa}\sqrt{\text{m}}$ . (c) Crack extension is initially accelerated during the 100-cycle step, but later retarded due to crack branching.
10. Schematic illustration of "open-book" type striation formation due to crack branching and mixed-mode conditions (a) - Crack formed by low amplitude cycling. (b, c, d) Crack branching along slip planes during three cycles of high amplitude: first (b), second (c) and third (d). (e) Continued crack extension under low amplitude cycling along one of the two branches. Top fracture surface viewed from below would show up like an 'open book' with twice the number of large-cycle striations (thick lined contour).
11. Matching fractographs from both halves of a SE(T) specimen (Test No. 6). Bottom picture is flipped vertically to present direct comparison. The "open-book" type striation patterns are observed only on one half of the fracture surface.

12. Matching fractographs from SE(T) specimen tested under load sequence 'c' of Fig. 2. Crack branching (top) appears as stretch marks on other surface (bottom). Lower picture flipped vertically to assist comparison.

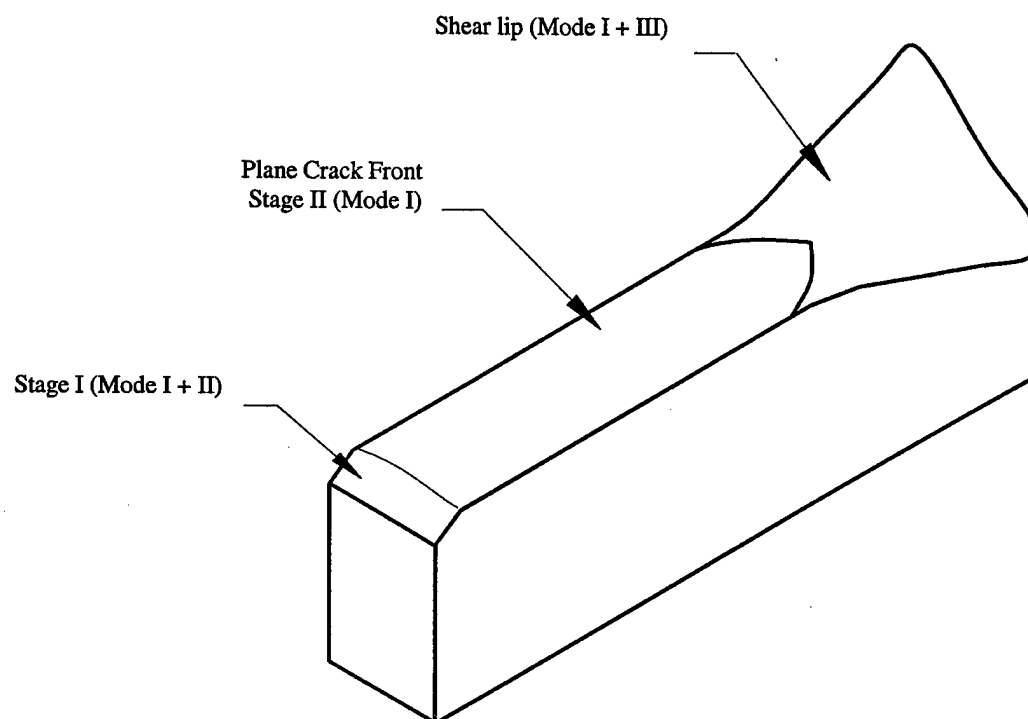


Fig.1 Schematic of stages and modes of crack growth viewed from different planes



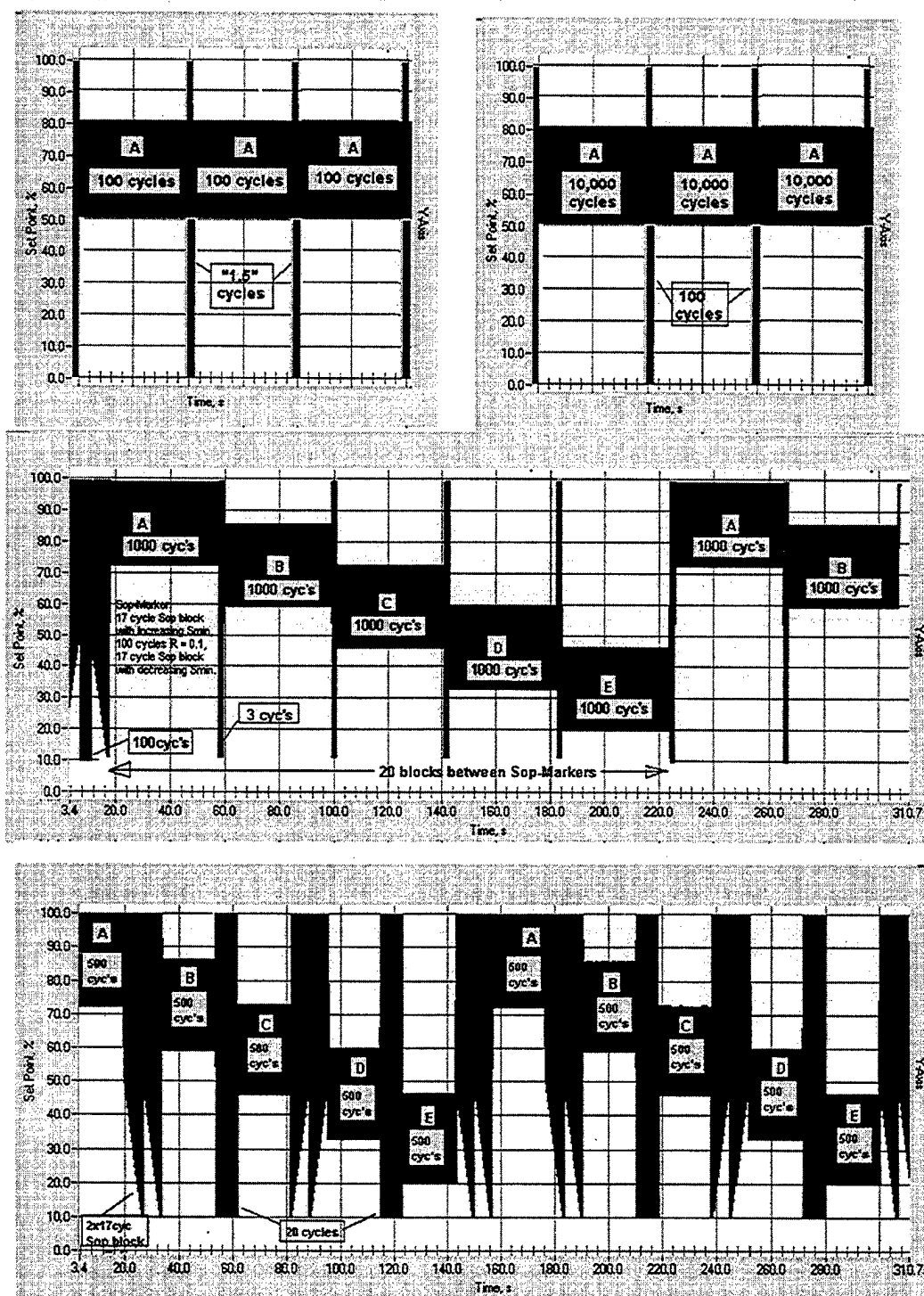


Fig. 2 Load sequences used in experiments. All tests involved repetitive application of the load sequence from crack initiation to specimen failure.

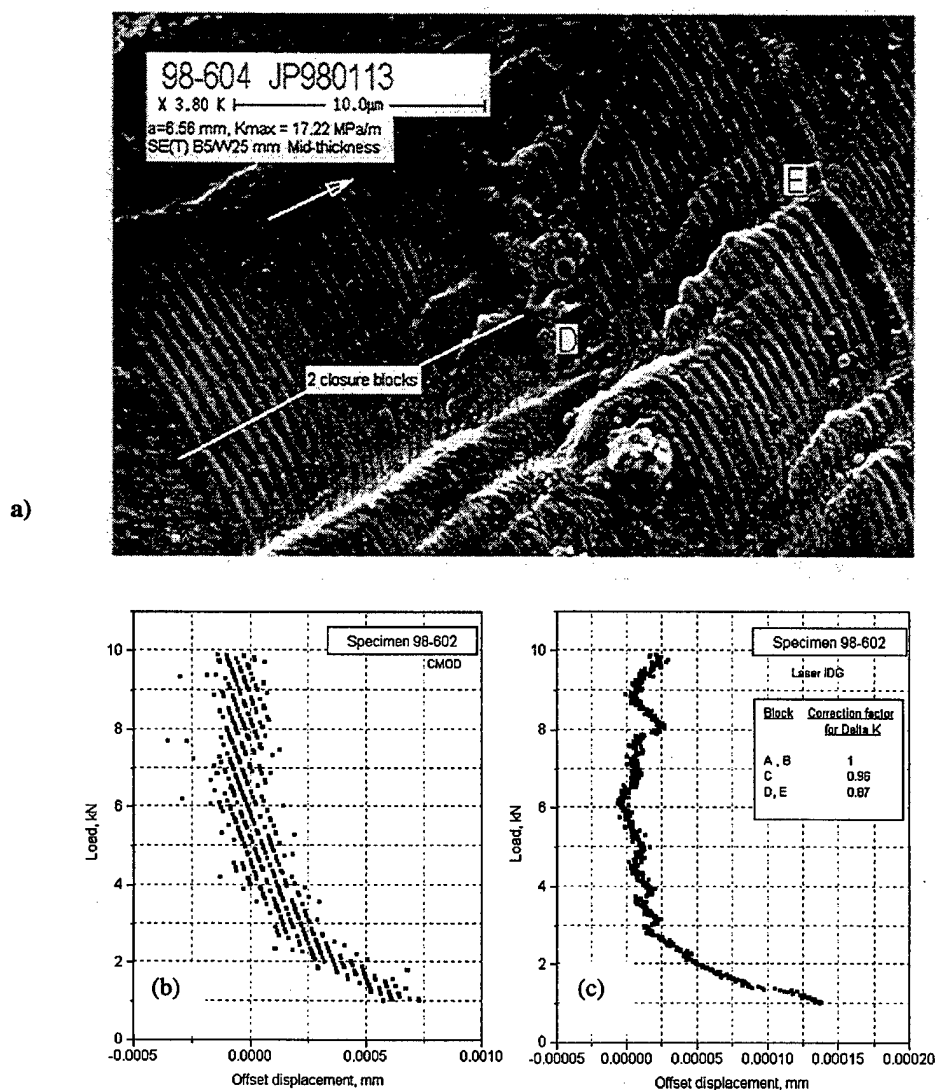


Fig. 3 Three techniques employed to estimate crack closure stress and effective stress intensity factor. (a) Fractograph of Test No. 4 under load sequence 'c' in Fig. 2 showing two 'closure' blocks preceding block D. The crack opening stress level controls the number of equally spaced striations. (b) Load versus CMOD record obtained under constant amplitude crack growth testing in Test 8. CMOD is expressed as offset displacement. (c) Load versus crack tip displacement from laser interferometry. Change in crack tip compliance at different load ranges was used to correct the crack driving force to obtain effective stress intensity range. Correction factor for different blocks shown in the inset.

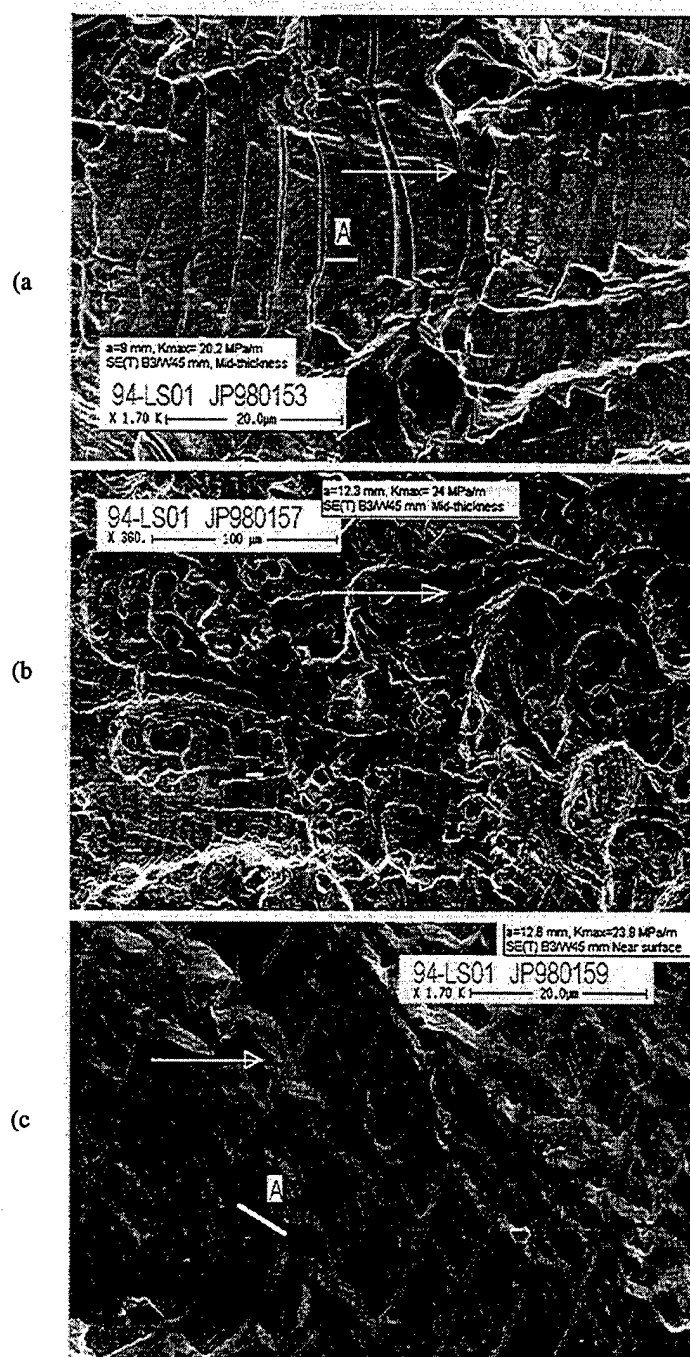


Fig. 4 - Fractographs from SE(T) specimen tested under sequence 'a'. Bar indicates crack extension in step A. (a) - Mid-thickness. Note crack branching during large cycles, indicated by split along crack front. This is accentuated at second phase particle. Stretch marks are visible during large cycles on right hand side, indicative of possible crack branching on the other half of the fracture. (b) Mid-thickness at a high stress intensity factor range. (c) Near surface at high stress intensity range. Note crack growth along a curve and absence of signs of crack branching.

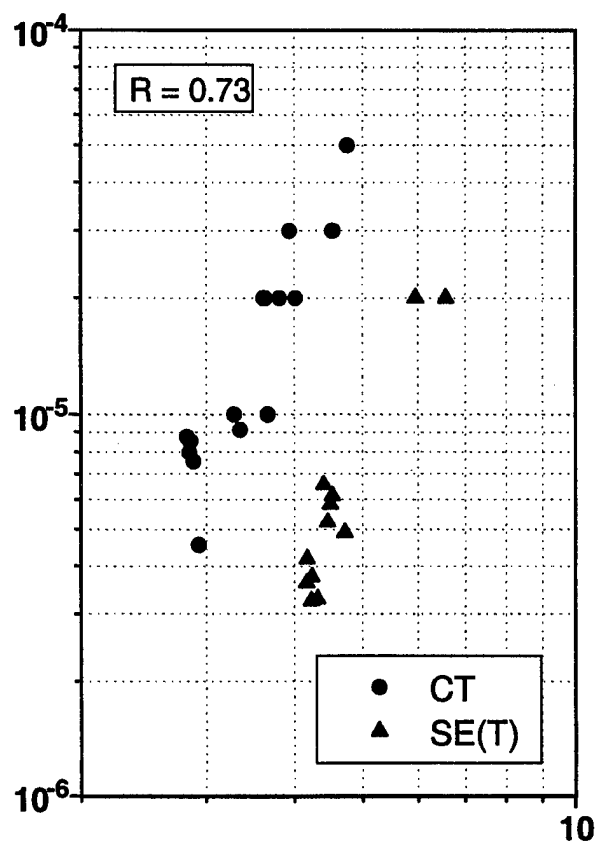


Fig. 5 Crack growth rates determined from fractography can be different between C(T) and SE(T) specimens even for a fully open crack ( $R=0.73$ ).

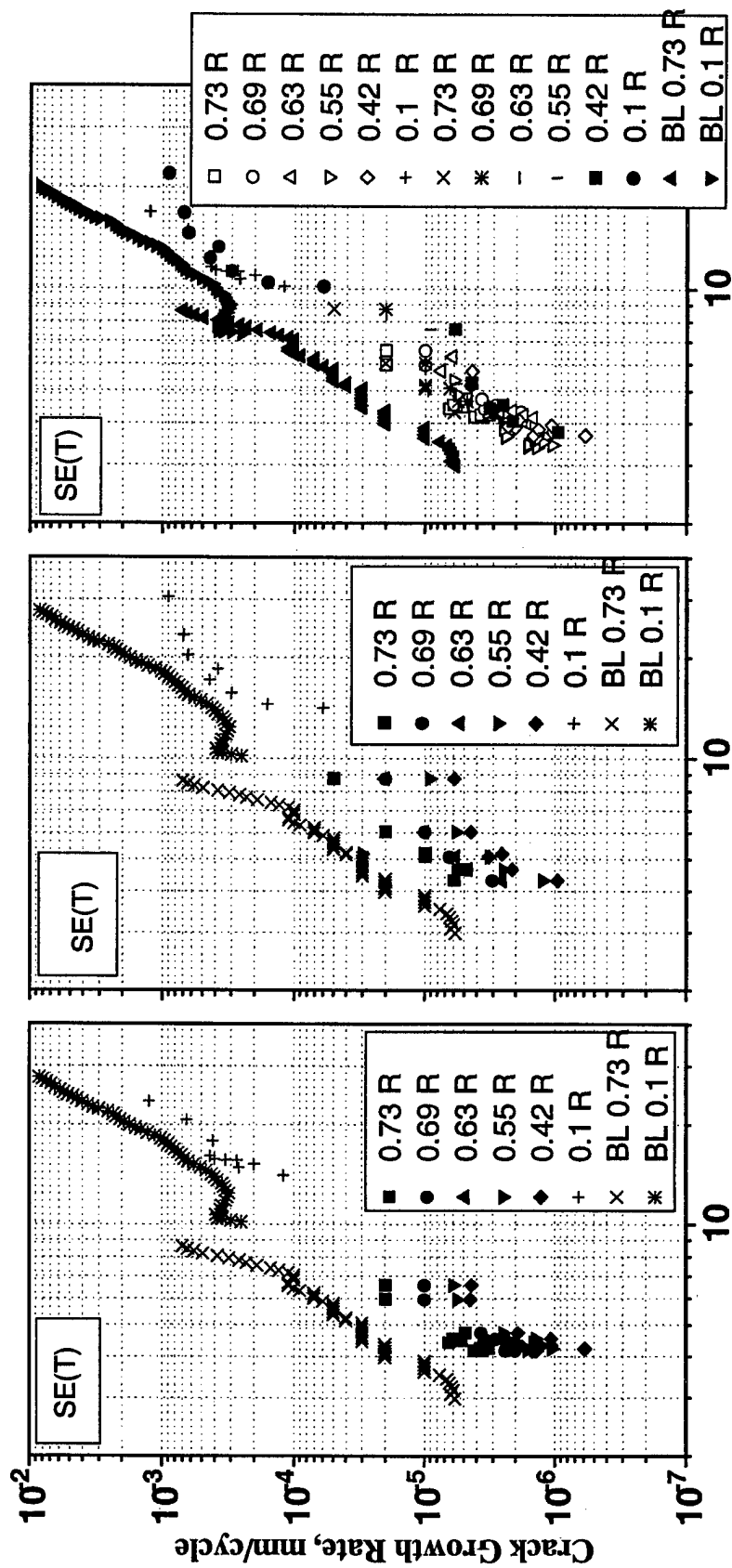


Fig 6 Crack growth rate data for the SE(T) specimens tested under two load sequences 'c' and 'd' of Fig.2. Crack growth rates estimated from fractography: (a, b)  $da/dN$  vs  $\Delta K$  under load sequences 'c' and 'd', (c) data from Figs. a,b versus  $\Delta K_{eff}$  computed using correction factors for range listed in Fig. 3c.

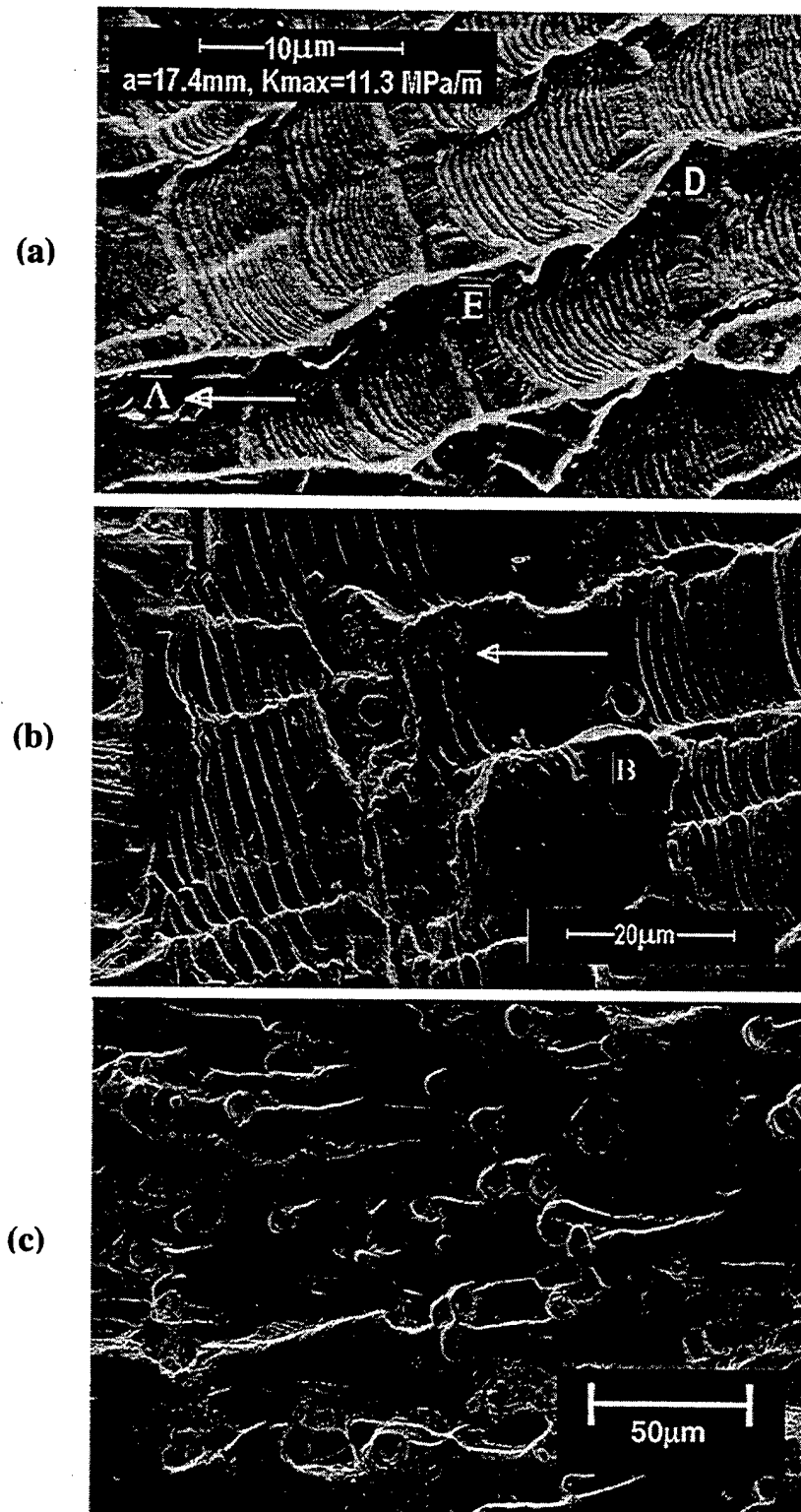


Fig. 7 Striation patterns under short duration load sequence 'c' of Fig.2. (a) High amplitude cycles cause a curved crack front within grains that are straightened out by low amplitude cycling. This is a possible load-interaction mechanism. (b) Crack front reacts differently to a second phase particle under low and high amplitude cycles. Crack branching (splitting) is visible under high amplitude cycles. (c) Striation pattern from constant amplitude loading (Test No. 7) at comparable  $\Delta K$  showing no signs of crack branching or splitting.

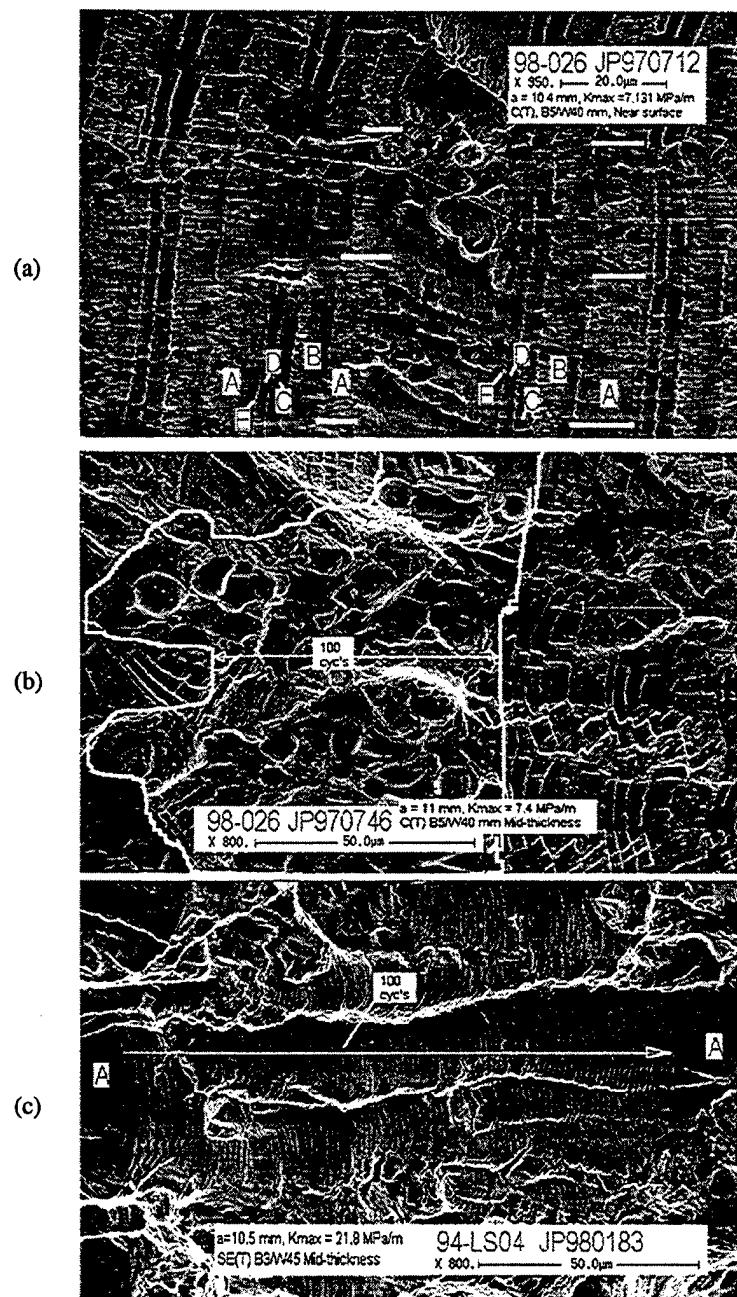


Fig. 8 Striation patterns under long duration sequence 'd' of Fig. 2. (a) Striation bands immediately after crack formation at the root of the EDM notch. Each band corresponds to over 5000 cycles of loading between steps A to E of Fig. 2. Individual steps are not visible at a crack length of 300 microns (b) Individual steps are visible, but individual striations from large cycles are not discernible even at a crack length of 4.15 mm. Note retarded growth immediately after the 100 large-cycle step. (c) Individual striations from high amplitude cycles are visible at larger crack size.

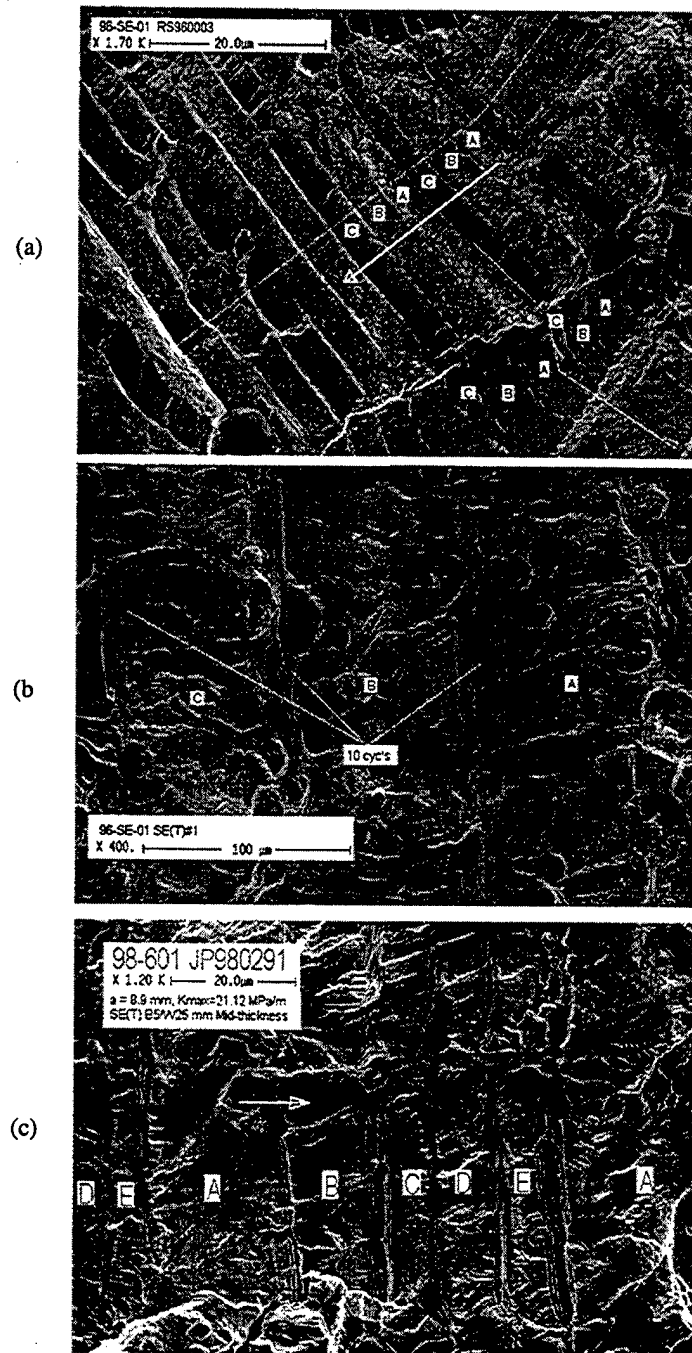


Fig. 9 Large cycle transients under long duration programmed loading. (a) Localized changes in the plane of crack growth during the 100 cycles high-amplitude step is visible even at the low  $K_{max}$  of  $7.1 \text{ MPa}\sqrt{\text{m}}$ . (b) Localized burst in crack extension across second phase particles at marginally higher  $K_{max}$  of  $7.4 \text{ MPa}\sqrt{\text{m}}$ . (c) Crack extension is initially accelerated during the 100-cycle step, but later retarded due to crack branching.



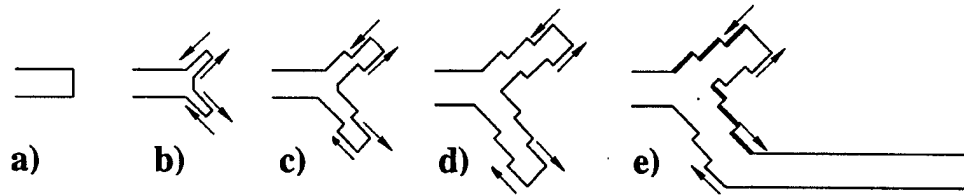


Fig.10 Schematic illustration of "open-book" type striation formation due to crack branching and mixed-mode conditions (a) - Crack formed by low amplitude cycling. (b, c, d) Crack branching along slip planes during three cycles of high amplitude: first (b), second (c) and third (d). (e) Continued crack extension under low amplitude cycling along one of the two branches. Top fracture surface viewed from below would show up like an 'open book' with twice the number of large-cycle striations (thick lined contour).

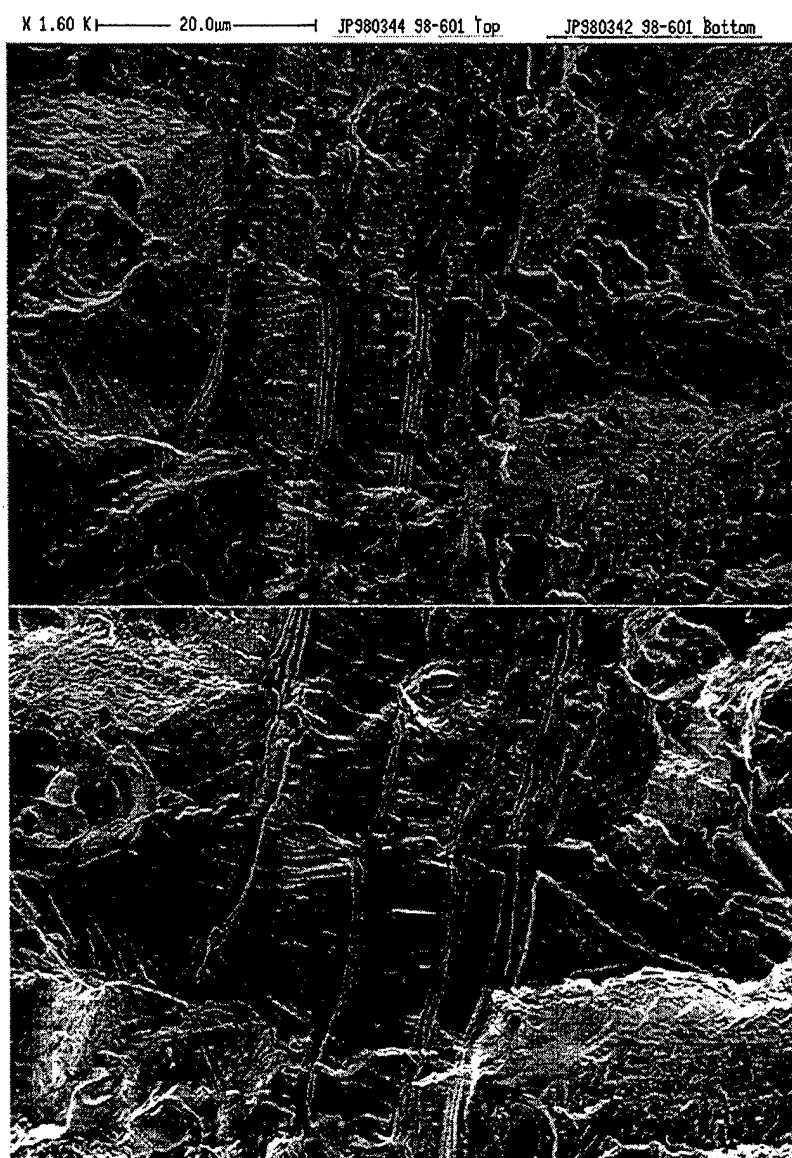


Fig. 11 Matching fractographs from both halves of a SE(T) specimen (Test No. 6). Bottom picture is flipped vertically to present direct comparison. The "open-book" type striation patterns are observed only on one half of the fracture surface.

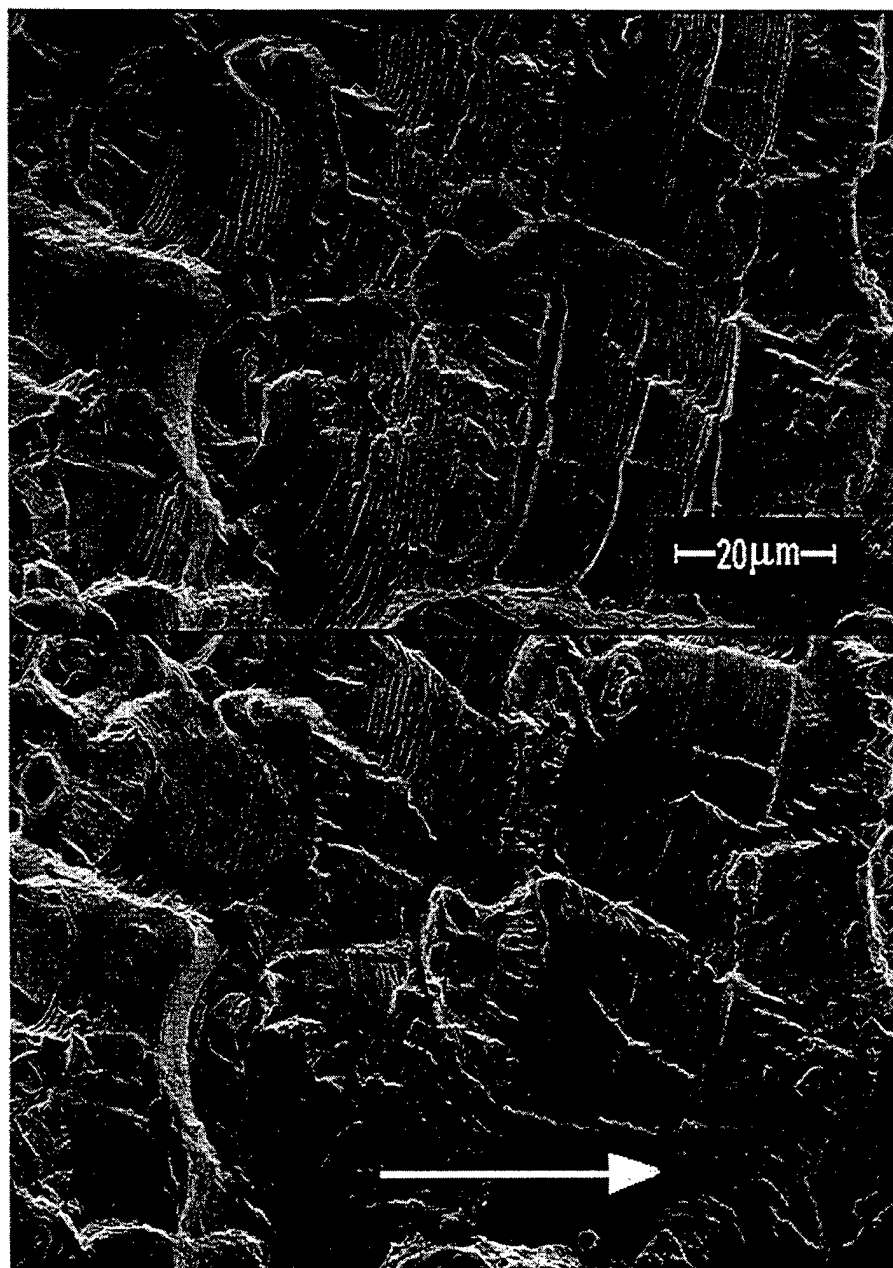


Fig. 12 Matching fractographs from SE(T) specimen tested under load sequence 'c' of Fig. 2. Crack branching (top) appears as stretch marks on other surface (bottom). Lower picture flipped vertically to assist comparison.

This page intentionally left blank.

Reference: Ruschau, J.R., John, R., Thompson, S.R., and Nicholas, T., "Fatigue Crack Growth Rate Characteristics of Laser Shock Peened Titanium," *Journal of Engineering Materials and Technology, ASME*, Vol. 121, pp. 321-329, July 1999.

### **Fatigue Crack Growth Rate Characteristics of Laser Shock Peened Ti-6Al-4V**

John J. Ruschau<sup>1</sup>, Reji John<sup>2</sup>, Steven R. Thompson<sup>3</sup>, and Theodore Nicholas<sup>4</sup>

Materials and Manufacturing Directorate, Air Force Research Laboratory,  
Wright-Patterson AFB, OH 45433, USA.

<sup>1</sup> Research Engineer, University of Dayton Research Institute, 300 College Park, Dayton, OH 45469,  
PH: 937-656-9138, FAX: 937-255-4997.

<sup>2</sup> Materials Research Engineer, AFRL/MLLN, WPAFB, OH

<sup>3</sup> Materials Engineer, AFRL/MLSC, WPAFB, OH

<sup>4</sup> Senior Scientist, AFRL/MLLN, WPAFB, OH

**ABSTRACT:** The fatigue crack growth rate (FCGR) characteristics of Laser Shock Peened (LSP) titanium 6Al-4V were examined and compared to those of unprocessed material. The FCGR resistance of LSP processed material tested at low stress ratios ( $R$ ) is shown to be significantly greater than for unprocessed, baseline material. The increased damage tolerance can be attributed to the large residual compressive stresses generated by the LSP process. Differences in the growth rate behavior due to LSP can be accounted for by using the closure corrected effective stress intensity range,  $\Delta K_{eff}$ , which takes into account only the portion of loading above the crack opening load. The rationale of using  $\Delta K_{eff}$  is also demonstrated through fractographic investigations.

## **1 Introduction**

Laser Shock Peening (LSP), originally developed in the 1970's as a fatigue enhancement surface treatment for metallic materials [1-5], is gaining renewed interest in the aerospace industry as a means of improving the damage tolerance and durability of engine fan blades. Due to the ever-present threat of foreign object damage (FOD) for aircraft turbine engines, the use of LSP has been proposed as a localized surface treatment for airfoils in the fan sections of certain military aircraft engines. The purported advantage of LSP over conventional surface treatments such as shot peening is that while current peening practices might produce high compressive surface stresses 100-200  $\mu\text{m}$  deep, the depth of the compressive stress layer produced via LSP is much larger, typically an order of magnitude greater. Compressive residual stresses at depths greater than 2 mm have been reported for steels [6] and 7xxx aluminum [2], and  $\approx 1$  mm for Ni-based superalloys [7] and 2024-T3 aluminum [4]. Since this residual stress depth, as applied to each side of an airfoil, can exceed the thickness in regions along the leading edge of several fan blades, it has been suggested that a through-thickness residual compressive stress state can be produced at the leading edge region of the blade, leading to a considerably more damage tolerant component.

With proper application of the LSP process, the tensile stresses needed to balance the compressive stresses can be located in a less critical region of the blade not

prone to FOD. The overall aim of this technology is to ensure that if FOD does occur in the LSP treated region, the blade will not fail catastrophically and damage will be detected during routine scheduled inspection of the blades. Hence, knowledge of fatigue crack growth behavior in the presence of LSP induced residual stresses is required. This paper discusses the use of a unique airfoil (leading edge) geometry to characterize the effect of the LSP process on the fatigue crack growth rate (FCGR) behavior of an engine material, Ti-6Al-4V. The influence of applied stress ratio and the correlation using the closure corrected effective stress intensity range,  $\Delta K_{eff}$ , is discussed.

## 2 LSP Process

The LSP process, depicted in Figure 1, uses a high-energy, pulsed laser to vaporize an opaque overlay (i.e., paint) applied to the surface of the sample [2,5]. The ensuing vapor created by the ablation process is trapped between the sample and the transparent overlay (water), thus generating an extremely high localized pressure pulse of short time duration ( $\sim 10$  ns) which in turn causes a shock wave to propagate into the material. Since the amplitude of this pressure pulse is much greater than the dynamic yield strength of the material, yielding occurs and the material is plastically deformed. To prevent the shock wave from exiting the back side of thin samples and causing the material to literally spall off as the shock wave exits, the process is applied to both sides of a blade or specimen, creating a symmetric "hit" on both sides of the sample, with the two waves intersecting at the center of the material. The constrained plastic deformation that occurs under a condition of nominally uniaxial strain produces deep compressive residual stresses normal to the impact direction at and below the surface. These stresses occur considerably deeper than can be achieved via conventional shot peening. The area ablated by the laser spot is approximately 5 mm in diameter, so multiple hits are required to cover a wider region (see next section).

## 3 Experimental Procedure

**3.1 Test Material and Specimens.** To examine fatigue crack growth rate (FCGR) properties of typical fan blade materials, test samples were prepared from a 44.5 mm diameter extruded bar of Ti-6Al-4V. Prior to machining, the bar was annealed at 704°C for 2 hours, followed by an argon gas quench, then stress relieved at 549°C for 2 hours, and again followed by argon gas quench. The resulting microstructure, obtained using standard optical microscopy techniques and etched with Kroll's Reagent, consists of equiaxed grains of  $\alpha$  (60% volume fraction) and transformed  $\beta$  (40%) as shown in Figure 2. The yield strength of the test material was 986 MPa, with an approximate tensile strength of 1050 MPa [8].

A unique test specimen was designed for the FCGR studies and is shown in Figure 3. In order to provide for tensile loading at the region of interest, a 3-point bend geometry was chosen. Similarly, since current interest in LSP is with leading edge regions of jet engine fan blades, the test section of the bend sample was designed to approximate a typical airfoil leading edge, with leading edge thickness of 0.75 mm. The overall size of the cross section was designed so that there was sufficient area to counterbalance the residual compressive stresses due to LSP along the leading edge. A crack starter notch was machined in the leading edge of each sample using a diamond sectioning saw, producing a stress free starter notch approximately 0.90 mm deep with a 0.2 mm root radius. The back edge of the sample (opposite the leading edge) was considerably thicker to provide constraint as well as to prevent buckling during the 3-

point bend loading. Finally, the cross section of the sample was sufficiently tapered so that fatigue crack growth information could be obtained from both regions containing through-thickness residual compressive stresses, as well as in sections where the compressive stresses were not completely through the thickness. This is of particular concern since, for the case of non-through-thickness compressive stresses, a tensile residual stress or reduced compressive stress region may be present near the centerline, possibly compromising any benefits created by LSP.

The actual shock peening was conducted by LSP Technologies, Inc., and consisted of approximately 13 hits or strikes as described in the previous section. A sketch of the laser spot pattern is shown in Figure 4 and illustrates a region 7 spots wide by 1-1/2 deep with a spot overlap of 30%. The laser spot size was approximately 5.6 mm in diameter, which resulted in a processed area that was approximately 29 mm long by 6.5 mm wide. To ensure adequate depth of the ensuing residual stress layer, each spot location was hit 3 times under identical conditions.

A mapping of the *surface* residual stress field in the LSP region was obtained via X-ray diffraction techniques [9]. Those results are shown in Figure 5 as a function of distance from the leading edge in the direction of crack growth ( $y$ ). The average compressive stress in the  $x$  direction, perpendicular to the crack plane ( $\sigma_x$ ), at the specimen surface is approximately 850 MPa and is reasonably constant throughout the LSP processed region over an area beginning  $\approx 1$ -2 mm back from the leading edge. Near the leading edge, the residual surface stresses are significantly lower and believed to be a result of a lack of constraint at the free edge of the sample. Likewise at the back edge of the LSP region ( $y \approx 7$  mm), the compressive *surface* stresses drop rapidly to zero, and become tensile just outside of the LSP processed region. The compressive surface stresses measured well outside the LSP region (i.e., 8-14 mm from edge) are believed to be attributable to low stress grinding operations used in specimen fabrication.

Residual stresses measured at the surface in the direction perpendicular to the direction of loading ( $\sigma_y$ ) were minimal. This may be due in part to the narrow LSP processed region (i.e., 1-1/2 rows of spots), in addition to the lower constraint at the leading edge where the free surface requires  $\sigma_y \approx 0$ .

The depth of the residual stress region was examined at several locations in the LSP processed area of a single sample [9]. Material was removed via electro-polishing to allow for subsurface stress measurements. Corrections for stress redistribution resulting from material removal were determined through finite element analysis. A residual stress field of the same sign and magnitude as the stress distribution measured was introduced into the model through the use of thermal loads. Layers of elements were removed to simulate the electro-polishing operation. The stress redistribution that occurred in the elements below the removed layers was used to correct the subsurface x-ray diffraction results. Errors in the measured stresses were typically within  $\pm 8$  MPa.

The resulting stress profiles are shown in Figure 6 for several locations as measured from the leading edge ( $y$ ), both within and outside of the LSP processed region. The data shown in Figure 6 represent the residual stresses measured as a function of thickness up to the centerline of the specimen. Since the LSP process was applied symmetrically to both sides of the specimen, it is reasonable to assume the stress field likewise is symmetric about the specimen centerline. Within the LSP region a compressive stress field exists throughout the sample thickness at the two locations examined ( $y=0.5$  and 5 mm), dropping from a peak compression at the surface of 600 to 800 MPa to a minimum compressive stress of approximately 200 MPa at the interior. It can also be seen that at both locations within the LSP region, the decay in peak

compression occurs over a depth of approximately 0.2-0.3 mm. At the  $y=5$  mm location where the sample thickness is approximately 2 mm the magnitude of the compressive stress field increases slightly at the center of the sample, presumably resulting from the stress waves from each surface constructively interacting at the mid-plane. For the 0.5 mm location, the stresses were not measured at the center of the sample's cross section; the dashed trend line reflects the assumption that the magnitude of the residual stress field in the middle is reasonably constant.

For two locations measured outside the LSP region ( $y=7.6$  and 10 mm) a tensile stress field occurs just below the surface, the maximum of which occurs approximately 0.05mm deep (Note the increase in sample thickness as a function of distance from the leading edge,  $y$ ). The maximum tensile stress measured was at  $y=7.6$  mm, immediately outside the LSP region, and is approximately 315 MPa. Near the interior of the sample, the stress field becomes compressive, reflecting the proximity of the LSP region. Further away from the LSP region ( $y=10$  mm) the stress field is tensile throughout most of the sample thickness.

### 3.2 Test Procedure

Fatigue testing of the simulated airfoil samples was carried out under 3-point bend, constant amplitude (CA) loading in servo-hydraulic fatigue test machines. The support span used in all tests was approximately 77 mm, with the support rollers free to rotate and move apart slightly as the specimen is loaded. An example of this fixture is available in the ASTM Standard Test Method for *Plane Strain Fracture Toughness of Metallic Materials (E399)* [10]. The test frequency for all CA tests was 50-60 Hz in a laboratory air environment. To examine mean stress effects, two stress ratios ( $R$ ) were examined:  $R = 0.1$  and 0.8. Also, to study possible load interaction effects that one would have expected during actual service, a simplified high-cycle/low-cycle fatigue (HCF-LCF) load spectrum was examined, consisting of a block of 99 cycles at  $R=0.8$  (HCF) and 1 cycle at  $R=0.1$  (LCF) with the maximum load constant throughout the block. Loading frequency for this simplified spectrum was 40 Hz. This block was repeated until failure occurred, with crack length measurements taken both as a function of total cycles and total spectrum blocks.

Crack initiation and growth was monitored on all samples using an electric potential difference (EPD) technique, whereby a constant DC current of 5 amps was passed through the specimen and the voltage difference across the notch monitored. Titanium wires for monitoring voltage changes were spot-welded immediately across the machined notch in a stress free region of the sample to prevent cracking at the welded attachment points, as well to offer the highest measurement sensitivity. With this technique, crack length changes of typically 2-3  $\mu\text{m}$  were readily detected. Since this technique requires electrical isolation of the specimen from the test machine and fixtures, ceramic load pins approximately 8 mm in diameter were used in the flex support fixture.

In addition to the EPD technique, visual monitoring of the crack length was performed periodically using a 20X traveling microscope with digital readout. These readings were used to correlate the EPD measurements to actual measured crack length for each test. Likewise a 12.7 mm gage length extensometer, electrically isolated from the sample, was affixed to the sample across the notch to obtain compliance measurements for the purpose of evaluating crack closure levels.

The FCGR data was derived from the  $a$  vs.  $N$  data following procedures described in the ASTM Standard Test Method for the *Measurement of Fatigue Crack Growth Rates (E647)* [11]. Due to the high resolution of the crack length measurements and the subsequent small intervals of crack growth between readings (i.e., 15-20  $\mu\text{m}$ ),



an incremental linear fit through 7 sequential data points was used to obtain growth rates, similar to the incremental 7-point polynomial described in the ASTM E647 Standard. The corresponding  $\Delta K$  for the 7-point interval was based on the average crack length over the interval and the following equation:

$$K = \sigma(\pi \cdot a)^{1/2} \cdot f(a/W) \quad \text{where:} \quad (1)$$

$\sigma$  = bending stress at the outermost fiber (i.e., leading edge),  
 $a$  = crack length measured from leading edge, and

$$f(a/W) = \left[ 1.1215 - 5.0402(a/W) + 14.4979(a/W)^2 - 22.0211(a/W)^3 + 12.9270(a/W)^4 \right] / \left[ 1 - a/W \right]^{3/2} \quad (2)$$

Equation 2 was developed using the results from a 3-dimensional elastic finite element analysis of the geometry shown in Figure 3 and loading conditions described. The equation is valid for all  $a/W \leq 0.6$ . The bending stress listed in Equation 1 can be computed from:

$$\sigma = Mc/I \quad \text{where:} \quad (3)$$

$M$  = the bending moment (applied load x one-half the support span),  
 $c$  = distance from the centroid of the cross section to the leading edge, and  
 $I$  = the moment of inertia of the specimen cross section.

## 4 Results and Discussion

**4.1 FCGR:** The crack growth response of a baseline, non-processed sample (under constant amplitude loading) is shown in Figure 7a along with results obtained from an LSP sample. The behavior of the baseline sample is typical of most conventional metallic samples, where cracking initiates at the machined notch tip and grows to failure under continuous fatigue cycling. The data also show that the growth rate is a monotonically increasing function which implies that the applied stress intensity factor,  $K_{\text{appl}}$ , is an increasing function of crack length for a given applied load, even though the specimen thickness increases with crack length. In contrast to this the crack growth behavior of the LSP sample indicates that cracking initiated under similar loading conditions, grew a short distance, then arrested. This crack arrest behavior for LSP samples required the maximum cyclic stress to be increased (5-10 %) in order to re-initiate cracking. Again this re-initiated crack often arrested after minimal growth, forcing the continual process of increasing the peak cyclic stress to re-propagate the crack until steady state crack growth eventually took place and propagated to failure. Such behavior is illustrated in the composite  $a$  versus  $N$  plot shown in Figure 7b. The composite records of  $a$  vs.  $N$  for the single sample shown in Figure 7b reflect cracking all within the LSP processed region.

The crack arrest behavior shown in Figure 7 for the LSP sample, contrasted with that of the baseline sample, can be attributed to the large compressive residual stresses in the LSP region which displayed a steep gradient near the leading edge, increasing in intensity a short distance from the leading edge as previously illustrated in Figure 5. For a propagating crack, this non-uniform stress field results in a residual compressive stress field at the crack tip and hence a *pseudo* compressive stress intensity,  $K_{\text{res}}$ , which increases in magnitude with increasing crack length, consistent with the crack arrest

behavior depicted in Figure 7. Thus for crack growth to occur, the applied maximum stress intensity,  $K_{max}$ , at the crack tip must exceed  $K_{res}$  as well as the inherent threshold stress intensity range,  $\Delta K_{th}$ , of the material.

The FCGR data for baseline, 3-point-bend samples under  $R=0.1$  and  $0.8$  constant amplitude loading is presented in Figure 8 as a function of the applied stress intensity range,  $\Delta K$ . Results for the 3-point bend geometry represent three samples tested per stress ratio. Individual specimen results fall directly on top of each other for each value of  $R$  examined, displaying a high degree of consistency and repeatability for this unique sample geometry. Also shown in Figure 8 are limited data obtained from standard compact tension, C(T), specimens ( $W=20$  mm,  $B=5$  mm); these data were obtained from two samples each per stress ratio. Data obtained from the C(T) samples are in reasonable agreement with the bend specimen results, but fall slightly to left of the bend test data for each of the stress ratios examined. Such differences might be attributable to the  $K$  solution developed for the unique tapered bend specimen. The  $K$ -expression developed for this sample (Eqns. 1 & 2) assumes the ideal geometry in Figure 3. Slight dimensional differences between the ideal geometry and the actual machined samples and/or test fixture may contribute to a bias in the calculated value of  $K$ ; because of the limited C(T) results, detailed comparisons between the two geometries are not possible (Note: since the purpose of this investigation was to examine the relative influence of LSP on crack growth behavior, any such bias is expected to be consistent and therefore have no influence on the FCGR trends, provided the resulting FCGR data discussed are all based on the same sample geometry.)

For comparative purposes, the 3-point-bend, baseline results for  $R=0.1$  were fitted with a power law expression (i.e.,  $da/dN=C\Delta K^n$ ), with the resulting curve extrapolated down to the value of  $\Delta K_{th}$  developed from the C(T) data at  $R=0.1$  in order to cover the range of growth rates developed on LSP samples (shown later). The curve for the  $R=0.8$  baseline data was similarly fitted with a power law expression over the range of growth rates developed for the baseline and LSP samples at this higher  $R$ .

The FCGR results for the LSP samples at  $R=0.1$  are presented in Figure 9 (solid symbols), along with the curve representing the baseline data. Closure corrected data (open symbols) are also shown and are discussed later. Data obtained from the LSP samples clearly demonstrate a significant advantage in FCGR resistance over baseline material when plotted as a function of applied  $\Delta K$ . Growth rates for the LSP samples in the range of  $\Delta K$  of 30-40 MPa $\sqrt{m}$  are nearly 3 orders of magnitude slower than for the unprocessed material, however, as the applied maximum stress intensity factor approaches the fracture toughness of the material the two data sets appear to converge.

To aid in the understanding of the differences in growth rate between baseline and LSP samples, compliance measurements were made to evaluate crack closure levels and thus compute the effective crack driving force. It should be noted here that the measurement of crack closure from compliance techniques is location sensitive [12, 13]. Such measurements, if taken right at the crack tip, can differ from those taken at a more remote location such as was done in the described effort. Since the only available means in this study to measure COD was with a commercial extensometer affixed at a relatively large distance from the specimen's crack plane, subtle nonlinearities in the compliance traces attributable to crack closure may not be clearly observable. The methods employed herein to measure crack closure are only capable of distinguishing pronounced closure behavior, thus closure levels reported are assumed to be approximate values.

Examples of such compliance measurements obtained on the 3-pt bend geometry are shown in Figure 10 for both baseline (unprocessed) and LSP samples. For the baseline sample (#2-29), the compliance traces appear linear throughout a wide range of crack lengths, indicating no apparent evidence of crack closure. The slope of the compliance curves shown for the baseline sample decreases systematically with increasing crack length and can readily be used to predict crack length. The compliance traces for an LSP sample (#2-3) shown in Figure 10b, on the other hand, display clear evidence of crack closure. Though the approximate level of crack closure varies slightly with crack length, the opening load value,  $P_{open}$ , corresponding to the fully opened crack tip was approximately 4 kN, or roughly 80-85% of the maximum applied load throughout the LSP region. Below the  $P_{open}$  level, the slopes of the compliance curves presented for a wide range of crack lengths are identical and represent the compliance of the machined starter notch only. Above  $P_{open}$  the measured compliance of the various curves in Fig 10b are consistent with what was measured for the baseline sample for similar crack sizes. Hence, below  $P_{open}$  the entire fatigue crack behaves as if it is fully closed, with compliance equal to that of only the machined starter notch. Above  $P_{open}$ , the crack becomes fully open and compliance measurements accurately predict the actual fatigue crack length.

Outside the LSP region (corresponding to crack lengths in excess of 7 mm) the closure levels begin to drop off drastically. For the LSP case shown in Figure 10b, the maximum bending stress corresponding to  $P_{open}$  is similar to the average residual compressive stress measured via diffraction techniques, reported earlier. It is the magnitude of this residual compressive stress field that appears to be directly responsible for the degree of crack closure observed.

Researchers in the field of fracture mechanics have long shown that crack growth can only take place when the crack tip is fully open. In the early 1970's Elber [14] showed that the load range above this opening load could be used to define an effective stress intensity range,  $\Delta K_{eff}$ , which can further collapse  $da/dN$  data for different stress ratios into a single curve. This value of  $\Delta K_{eff}$  is defined simply as:

$$\Delta K_{eff} = K_{max, applied} - K_{open} \quad \text{where:} \quad (4)$$

$K_{max, applied}$  = value of K based on maximum applied load, and

$K_{open}$  = value of K based on  $P_{open}$ .

Note that in the absence of closure  $K_{open}$  equals the minimum applied K, and hence the applied  $\Delta K$  is equal to  $\Delta K_{eff}$ .

Taking the LSP crack growth data in Figure 9 and correcting for crack closure by using the portion of the loading cycle above  $P_{open}$  (see Fig. 10b) to compute  $\Delta K_{eff}$ , the data for the LSP samples shift to the left and fall reasonably along the same curve extrapolated for the baseline material at  $R=0.1$  which displayed little or no closure. Again slight differences between the data sets probably result from errors in the estimation of crack closure. Nonetheless, the  $\Delta K_{eff}$  data shown in Figure 9 fall reasonably along a single trend curve, demonstrating that the enhanced FCGR resistance for LSP processed material is due to a superimposed residual stress field shielding the crack tip.

The results of LSP samples tested at  $R=0.8$  are presented in Figure 11 along with the baseline curve for the same stress ratio. Advantages in the FCGR resistance of LSP at the higher R clearly diminish at the higher stress ratio, and in fact fall along the

trend line for the baseline material. Compliance traces at this higher stress ratio (not shown) appeared linear throughout the entire loading range, suggesting that no pronounced closure is evident. The crack tip appears to remain open throughout the entire load cycle, thus  $\Delta K_{eff}$  is equal to the applied  $\Delta K$ . Again slight differences in FCGR behavior may be attributable to the inability to accurately account for subtle closure effects which, in the LSP case, would diminish the  $\Delta K$  at the crack tip and thus move the LSP data slightly to the left, more in line with the baseline curve. Regardless of whether or not a small degree of closure may be occurring on the  $R=0.8$  case, it is clear that the advantages of LSP diminish at the higher stress ratio. In fact, for any stress ratio, it seems reasonable to assume that once the minimum stress in the loading cycle equals or exceeds the residual stress field created in the LSP process, crack growth rates are unaffected. When any portion of the cyclic stress range falls below this residual stress field, growth rates are reduced accordingly.

It must be noted that in correcting crack growth rate data for closure, it is inherently assumed that stress ratio has no measurable effect on the growth rate, that is,  $\Delta K$  is the sole correlating parameter. Thus, for the case of an applied  $\Delta K$  at  $R=0.1$  in an LSP sample, closure at 80% of maximum load would correspond to an effective  $R=0.8$ . Figure 8 shows that  $R=0.1$  and  $R=0.8$  baseline data, neither of which demonstrate any significant degree of closure, produce comparable growth rates, thereby validating the use of a closure correction for the LSP data.

If residual stresses are present which produce a residual stress intensity factor,  $K_{res}$ , at the crack tip, and in the absence of other closure related mechanisms, the effective values of  $K$  at maximum and minimum loads are given by:

$$K_{max,eff} = K_{max,applied} + K_{res} \quad (5)$$

$$K_{min,eff} = K_{min,applied} + K_{res}$$

and an effective stress ratio can then be defined as:

$$R_{eff} = K_{min,eff} / K_{max,eff} \quad (6)$$

Note that in this case,  $\Delta K$  does not change due to residual stresses, but  $R_{eff}$  decreases if  $K_{res}$  is a negative number. Since the residual stresses are compressive, the computed  $K_{res}$  is negative. While the authors recognize that  $K_{res}$  being negative has no formal meaning, a negative  $K_{res}$  is used to represent the relative magnitude of the compressive loading across the crack surfaces. As discussed earlier in Figure 10b, for a crack length of 6.1 mm (as one example), the initial compliance (i.e., below  $P_{open}$ ) corresponds to the initial machined notch length of approximately 0.9 mm. The measured compliance above  $P_{open}$  corresponds to a fully open crack length of 6.1 mm, consistent with that of a non-LSP specimen (Fig. 10a). Hence,  $P_{open}$  corresponds to the point where  $K_{applied}$  overcomes  $K_{res}$ .

At the higher stress ratio test condition,

$$R_{applied} = 0.8 = \frac{K_{min}}{K_{max}} \quad \text{and} \quad (7)$$

$$K_{min} = 0.8 K_{max} \quad (8)$$

Since closure is absent in the load-displacement traces at  $R=0.8$ , with or without LSP, then,

$$K_{min} + K_{res} \geq 0 \quad (9)$$

and therefore, combining Eqns. (8) and (9) yields:

$$K_{res} \geq -0.8 K_{max} \quad (10)$$

Equation (10) implies that the magnitude of  $K_{res}$  is less than or equal to 80%  $K_{max}$  during the  $R=0.8$  test. For the case of  $R=0.1$  testing where  $K_{max}$  is the same as the  $R=0.8$  test, it follows from equations (5) that:

$$R_{eff} = \frac{0.1K_{max} + K_{res}}{K_{max} + K_{res}} \quad \text{and} \quad (11)$$

$$= \frac{0.1K_{max} - 0.8K_{max}}{K_{max} - 0.8K_{max}} = \frac{-0.7}{0.2} \quad \text{or} \quad (12)$$

$$R_{eff} \approx -3.5 \quad (13)$$

Note that  $R_{eff}$  equal to -3.5 is a limiting value or *upper bound* (in magnitude) because it is based on the assumption of  $K_{res} = -0.8K_{max}$  (Eq. 10). The above calculations imply an apparent closure level of  $\approx 80\%$  during crack growth with  $R_{eff} \approx -3.5$  at the crack tip. This high closure level during  $R < 0$  is consistent with the finite element analysis results of Sehitoglu et al.[18].

The data for crack growth under HCF-LCF loading conditions in a single LSP sample are presented in Figure 12. The loading block consists of 1 LCF cycle at  $R=0.1$  and 99 HCF cycles at  $R=0.8$  with all cycles having the same maximum load. The data are presented as two separate curves. In Figure 12a the crack growth data are presented as the crack extension per minor cycle against  $\Delta K$  of the minor cycle ( $R=0.8$ ). The same data are presented in Figure 12b which shows the growth rate data as extension per major cycle (or block) as a function of  $\Delta K$  of the major cycle, where  $R=0.1$  is defined as the major loading cycle. Note that the major cycle growth rate is exactly 100 times the minor cycle rate since there are 100 times as many minor cycles as major cycles in the load spectrum. Similarly, the ratio of  $\Delta K$  of the major cycle to  $\Delta K$  of the minor cycle is  $(1-0.1)/(1-0.8)$  or 4.5. Plotted also in Figure 12 are the constant amplitude (CA) data for  $R=0.1$  and  $R=0.8$ , each plotted as growth rate per cycle against the  $\Delta K$  of that cycle. By comparing the HCF-LCF data against the baseline CA data in the respective coordinate systems, it can be readily seen that the spectrum growth rate is dominated by the minor cycles ( $R=0.8$ ). In fact, one can conclude that the major cycle has no substantial influence on the growth rate of the spectrum. One would have to decrease the number of minor cycles per block of loading to be able to eventually correlate the growth rates on a major cycle basis, a procedure that is planned for future work.

**4.2 Microscopy:** As previously described the microstructure of the material consists of primary  $\alpha$  grains in a matrix of transformed  $\beta$  (Widmānstatten  $\alpha$ ). Microscopic examinations along the cross-sections of the specimen inside and outside of the LSP region were made in order to determine whether any microstructural changes occurred due to the LSP processing. None could be found using standard optical microscopy methods. Further examination using a scanning electron microscope (SEM) at higher magnifications also revealed no microstructural differences. There was some evidence of distorted grains at the specimens' surface, as shown in Figure 13, however, this was attributed to the low-stress grinding procedures that were used in the specimen

fabrication since the deformation substructures were also observed at locations remote from the LSP region.

A final investigation of the possible microstructural changes was performed using transmission electron microscopy (TEM). TEM foils were taken from an untested specimen that had undergone the LSP process. An example of the LSP processed region, shown in Figure 14a shows a very high dislocation density within the grains. This was evident throughout the LSP region. In contrast, Figure 14b shows a photo taken well outside of the LSP region and exhibits an extremely low dislocation density. Although these results were not totally unexpected [1, 16], they do indicate that the LSP process only causes microstructural changes at the sub-grain level. This is in contrast to other mechanical processes such as conventional shot peening, where it would be expected that a very small layer at the surface of the material would contain deformed grain structures.

To further examine the influence of LSP on FCGR behavior, limited fractographic studies were performed. For the case of a baseline sample tested at  $R=0.1$  where little or no closure was observed, fractographic features consisting of cleavage facets which were sharp and well defined as shown in Figure 15, owing to the fact that the crack tip remains predominately open throughout the entire loading cycle. In contrast to that is the fracture appearance of an LSP sample similarly tested at  $R=0.1$  in which the facets were smeared or obliterated due to the high compressive residual stresses acting to close the crack tip throughout the majority of the loading cycle. Since all the fractography was performed in low  $\Delta K$  regions there was no evidence of fatigue striations present on any of the fracture faces, since they would have only been expected at higher growth rates [17, 18].

As discussed earlier (see Eqns. 7-13), a sample undergoing test at  $R=-3.5$  should have a fracture face surface similar to that for an LSP sample tested at an applied  $R=0.1$ . To demonstrate this an M(T) sample of the same baseline Ti-6-4 material was fatigue tested at  $R \approx -3$  for the sole purpose of generating fracture topography under heavy compressive loading. Results are shown in Figure 16 and likewise demonstrate the smeared, rounded features similar to that of the LSP sample at  $R=0.1$ .

Similar SEM examinations were performed on a single LSP sample tested under  $R=0.8$  loading for a similar crack size. Fracture appearance of this sample is furnished in Figure 17. Though the overall topography appears less tortuous than the baseline material at  $R=0.1$ , the cleavage facets were still sharp and well defined, again due to the fact that the fatigue crack tip remained predominantly open throughout the entire loading cycle. Some secondary cracking is also evident; this may have also occurred in the  $R=0.1$  cases but not readily observable due to either the overall roughness or the smearing (LSP).

## 5 Summary

Laser Shock Peening is effective at introducing deep residual compressive stresses that have a marked influence on fatigue crack growth properties. Provided the cyclic stress is below the residual stress field created by the LSP process, enhanced FCGR resistance is realized due to superposition of the residual compressive stresses. For applied stresses below the residual stress magnitude, the fatigue crack remains entirely closed and hence crack propagation cannot occur. At high  $R$  values, when cycling stresses are above the residual stresses and the intrinsic threshold,  $\Delta K_{th}$ , of the material, little or no improvement in FCGR is realized. These results imply that under some high cycle fatigue (HCF) conditions (with high  $R$ ), the beneficial effects of the

residual stresses could be significantly less than that under low cycle fatigue (LCF) conditions which typically involve low or negative values of  $R$ .

The LSP process does not appear to produce any detrimental microstructure changes. However, a higher dislocation density is observed due to the LSP process. Fractographic studies performed likewise confirm that residual compressive stresses have a strong influence on FCGR properties.

#### **Acknowledgments**

This work was conducted at Air Force Research Laboratory (AFRL/MLSC & MLLN), Materials and Manufacturing Directorate, Wright-Patterson AFB, OH, USA. Mr. J. J. Ruschau was supported under an on-site contract number F33615-94-C-5061. The authors wish to recognize the contributions Mssrs. Donald Woleslagle and Joseph Kroupa of UDRI who provided testing and FEA support, respectively. Recognition is also given to Mssrs. Paul Ret and Christopher Lykins, both of the Air Force Research Laboratory (AFRL), and Dr. Robert Wheeler of Universal Energy Systems for their contributions to this effort.

## References

1. Fairand, B. P., and Clauer, A. H., "Laser Generated Stress Waves: Their Characteristics and Their Effects to Materials," Conference Proceedings #50: *Laser-Solid Interactions and Laser Processing-1978*, S. D. Ferris, N. J. Leamy, and J. M. Poate, Eds., pp. 27-42, Copyright 1979, American Institute of Physics.
2. Bates, W. F. Jr., "Laser Shock Processing of Aluminum Alloys," Conference Proceedings from the American Society for Metals *Applications of Lasers in Materials Processing*, April 1979, pp. 317-330.
3. Ford, S. C., Fairand, B. P., Clauer, A. H., and Galliher, R. D., "Investigation of Laser Shock Processing - Executive Summary," AFWAL-TR-80-3001, Volume I, August 1980.
4. Clauer, A. H., Walters, C. T., and Ford, S. C., "The Effects of Laser Shock Processing on the Fatigue Properties of 2024-T3 Aluminum," from *1983 ASM Conference on Applications of Lasers in Materials Processing*, American Society of Metals Report #8301-002, January, 1983.
5. Clauer, A. H., and Holbrook, J. H., "Effects of Laser Induced Shock Waves of Metals," from *Shock Waves and High-Strain-Rate Phenomena In Metals (1981)*, Marc A. Meyers and Lawrence E. Murr, Eds, pp. 675-702.
6. Fournier, J., Ballard, P., Merrien, P., Barralis, J., Castex, L., and Fabbro, R., "Mechanical Effects Induced by Shock Waves Generated by High Energy Laser Pulses," *Journal of Physics III*, September 1991, pp.1467-1480.
7. Forget, P., Jeandin, M., and Lyoret, A., "Determination of Laser Shock Treatment Conditions for Fatigue Testing of Ni-Based Superalloys," *Journal of Physics IV, Colloque C7*, Supplement to Journal to Physics III, Vol. 3, November 1993, pp. 921-926.
8. Maxwell, D. C. and Nicholas, T., "A Rapid Method for Generation of a Haigh Diagram for High Cycle Fatigue," *Fatigue and Fracture Mechanics: 29<sup>th</sup> Volume*, ASTM STP 1321, T. L. Panontin and S. D. Sheppard, Eds., American Society for Testing and Materials, 1998 (submitted for publication).
9. Mason, P. W., Lachtrupp, T. P., and Prevey, C. S., "X-Ray Diffraction Determination of the Residual Stress Distributions in One Ti-6Al-4V Tapered Three Point Bend (T3PB) Specimen," Lambda Research Inc., Cincinnati, OH, Report #674-6903, May 20, 1997.
10. "Standard Test Method for Plane-Strain Fracture Toughness of Metallic Materials," E 399-90 (Reapproved 1997), 1998 Annual Book of ASTM Standards, Vol. 03.01, *Metals-Mechanical Testing; Elevated and Low-Temperature Tests; Metallography*, pp. 413-443.
11. "Standard Test Method for Measurement of Fatigue Crack Growth Rates," E 647-95a, 1998 Annual Book of ASTM Standards, Vol. 03.01, *Metals-Mechanical Testing; Elevated and Low-Temperature Tests; Metallography*, pp. 562-598.



12. Donald, J. K., Bray, G. H., and Bush, R. W., "An Evaluation of the Adjusted Compliance Ratio Technique for Determining the Effective Stress Intensity Factor," *National Symposium on Fatigue and Fracture Mechanics: 29<sup>th</sup> Volume, ASTM STP 1332*, T. L. Panontin and S. D. Sheppard, Eds., American Society for Testing and Materials, 1998 (in press).
13. Ashbaugh, N. E., "Effects of Load History and Specimen Geometry on Fatigue Crack Closure Measurements," *Mechanics of Crack Closure, ASTM STP 982*, J. C. Newman, Jr., and W. Elber, Eds., American Society for Testing and Materials, Philadelphia, 1988, pp. 186-196.
14. Elber, Wolf, "The Significance of Fatigue Crack Closure," *Damage Tolerance in Aircraft Structures, ASTM STP 486*, American Society for Testing and Materials, 1971, pp. 230-242.
15. Sehitoglu, H., Gall, K., and Garcia, A. M., "Recent Advances in Fatigue Crack Growth Modeling," *International Journal of Fracture*, **80**, 1996, pp. 165-192.
16. Fairand, B. P., and Clauer, A. H., "Use of Laser Generated Shocks to Improve the Properties of Metals and Alloys," *Industrial Applications of High Power Laser Technology*, **86**, 1976, pp. 112-119.
17. Wanhill, R. J. H., Galatolo, R., and Looije, C. E. W., "Fractographic and Microstructural Analysis of Fatigue Crack Growth in a Ti-6Al-4V Fan Disc Forging," *International Journal of Fatigue*, **11**, No. 6, 1989, pp. 407-416.
18. Irving, P. E., and Beevers, C. J., "Microstructural Influences on Fatigue Crack Growth in Ti-6Al-4V," *Materials Science and Engineering*, **14**, 1974, pp. 229-238.

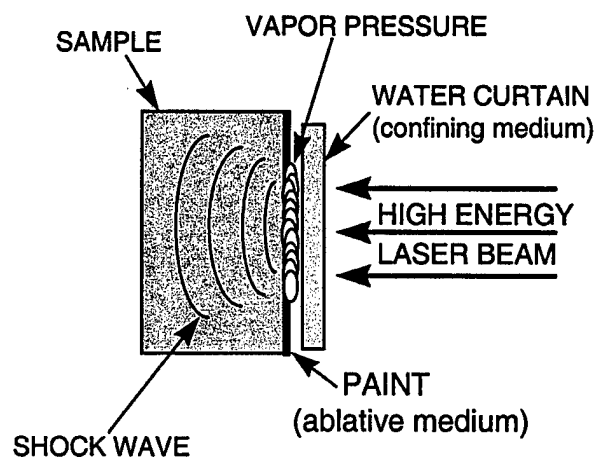


Figure 1. Schematic of LSP Process

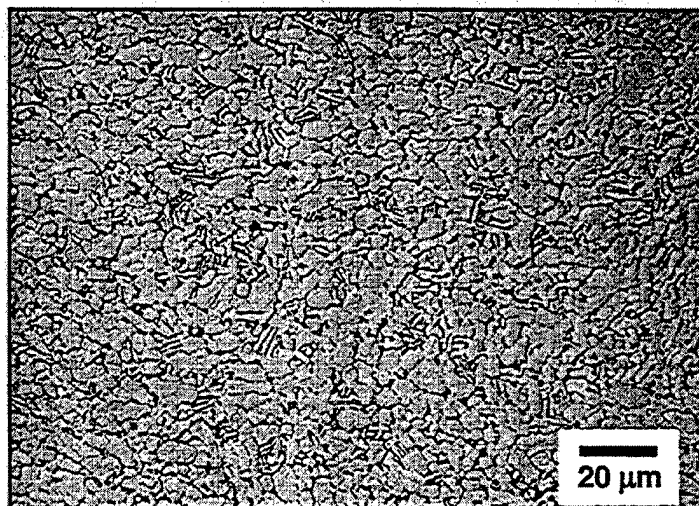


Figure 2. Microstructure of Ti-6Al-4V Test Material (as received).

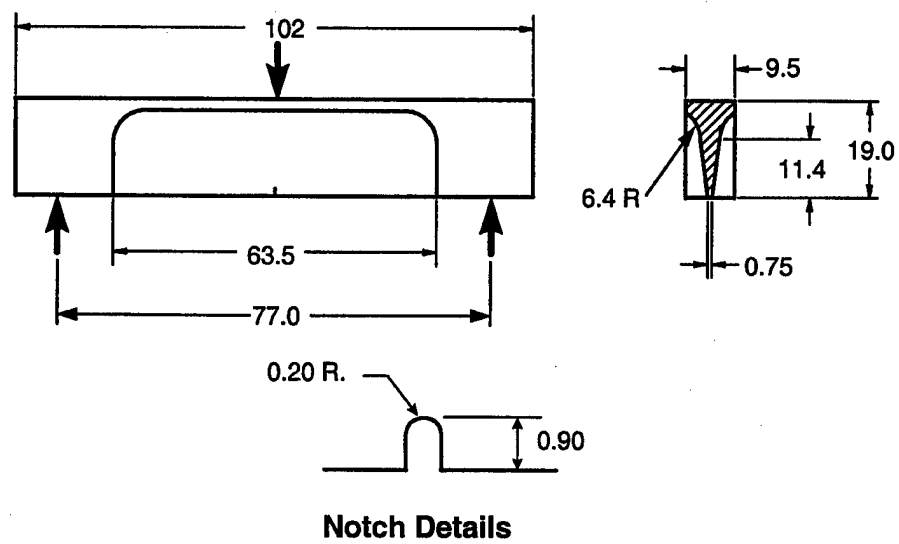


Figure 3. Geometry of 3-Point Bend Airfoil Specimen (dimensions in mm).

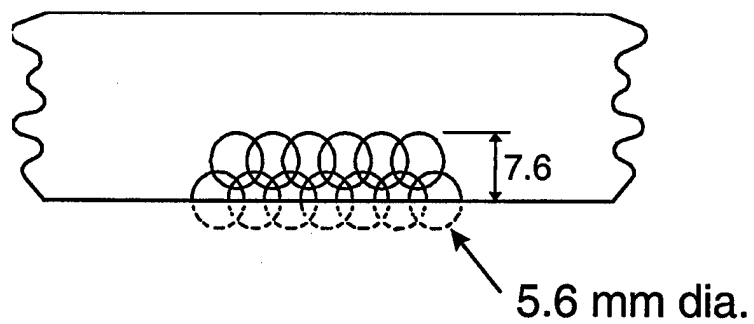


Figure 4. Laser Spot Pattern.

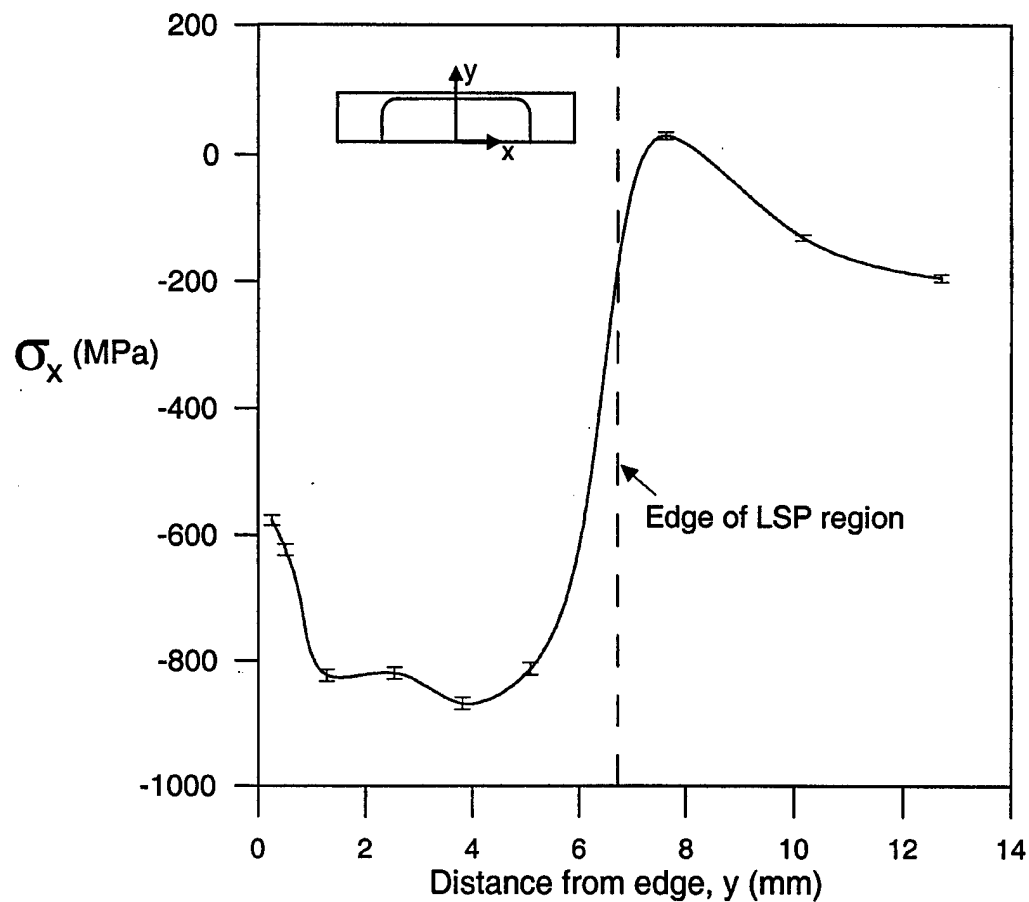


Figure 5. Surface Residual Stresses for an LSP Sample Along the Direction of Crack Growth (at  $x=0$ ).

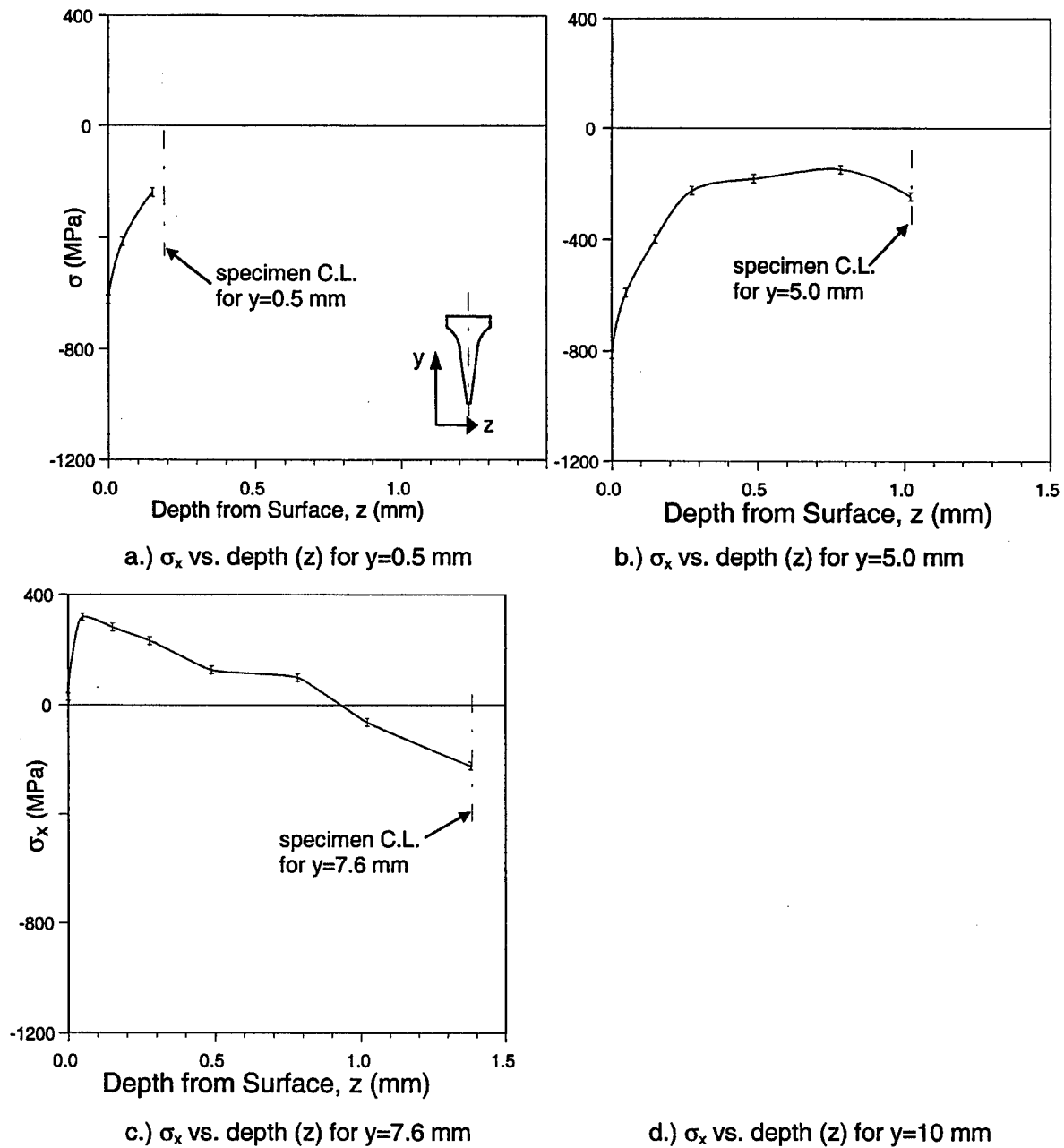
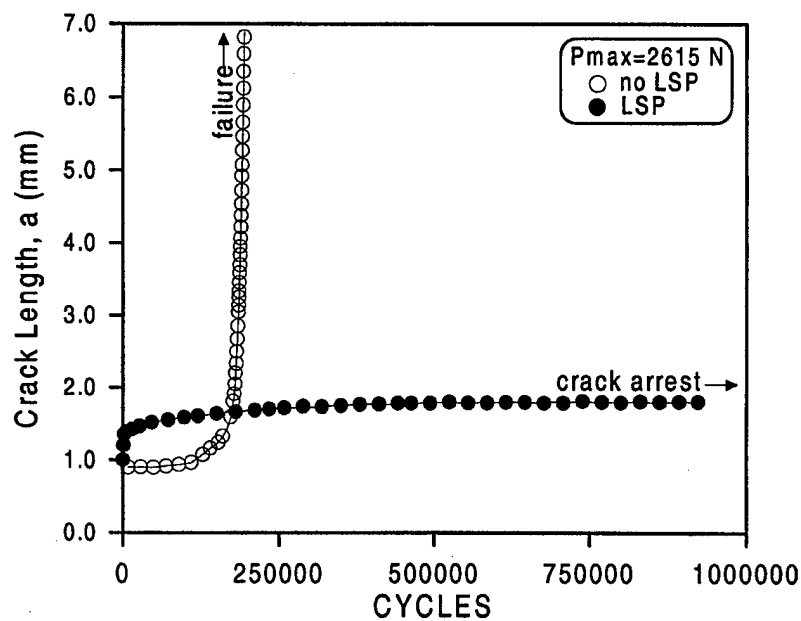
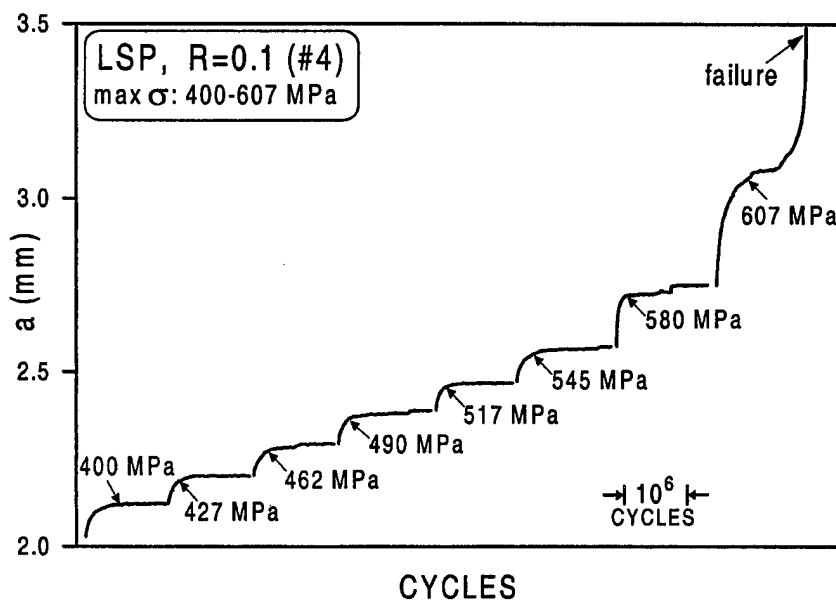


Figure 6. Through-Thickness Residual Stress Profile for an LSP Sample as a Function of Depth ( $y=0$  corresponds to leading edge).



a). Comparison of baseline and LSP  $a$  vs.  $N$  behavior.



b).  $a$  vs.  $N$  behavior for single LSP sample.

Figure 7. Crack Length vs. Cycles ( $a$  vs  $N$ ) Data for Baseline and LSP Samples.

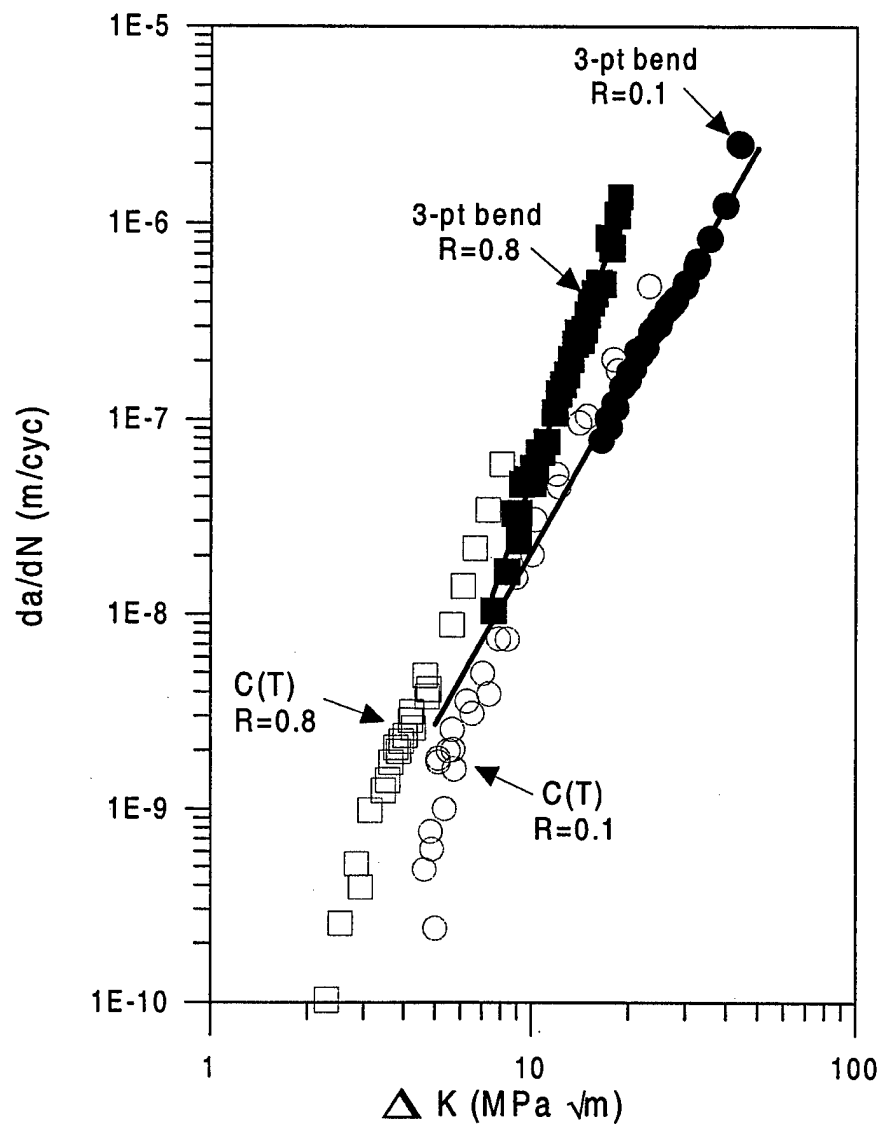


Figure 8. Baseline FCGR Data as a Function of Applied  $\Delta K$ .

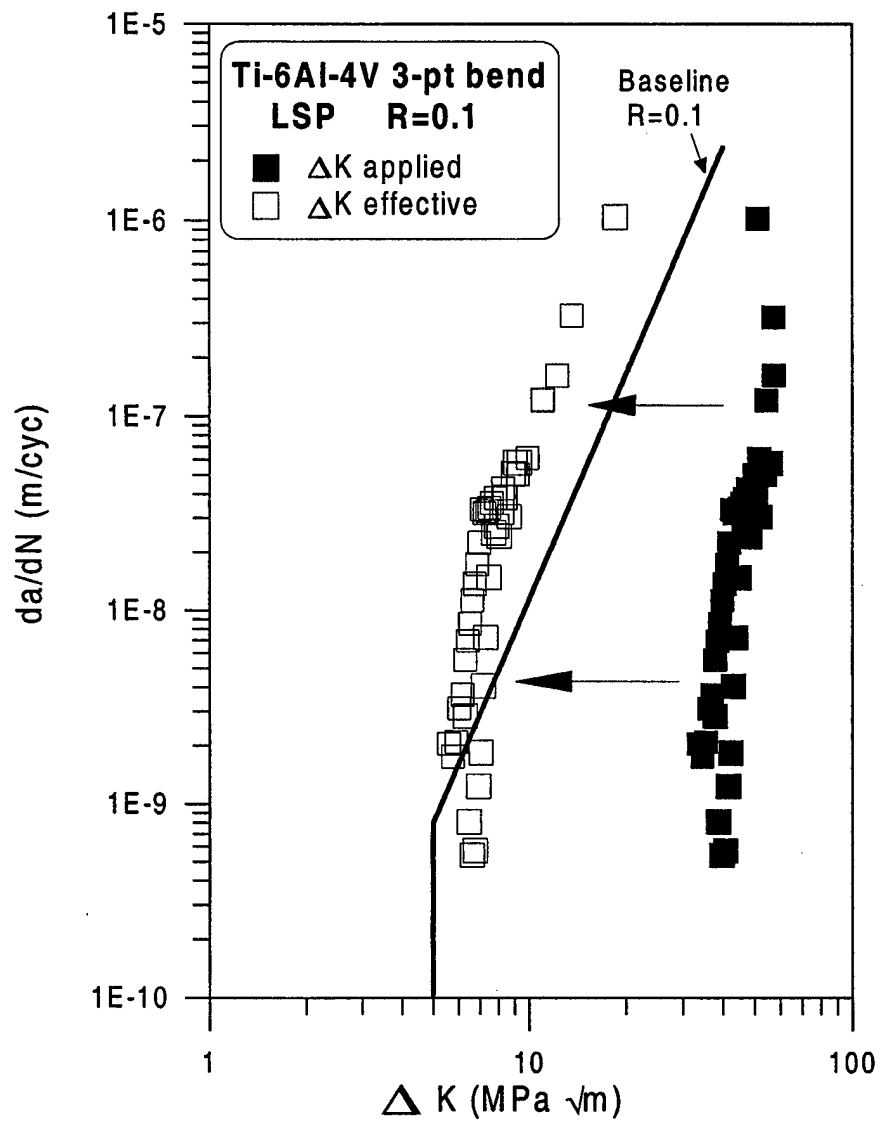
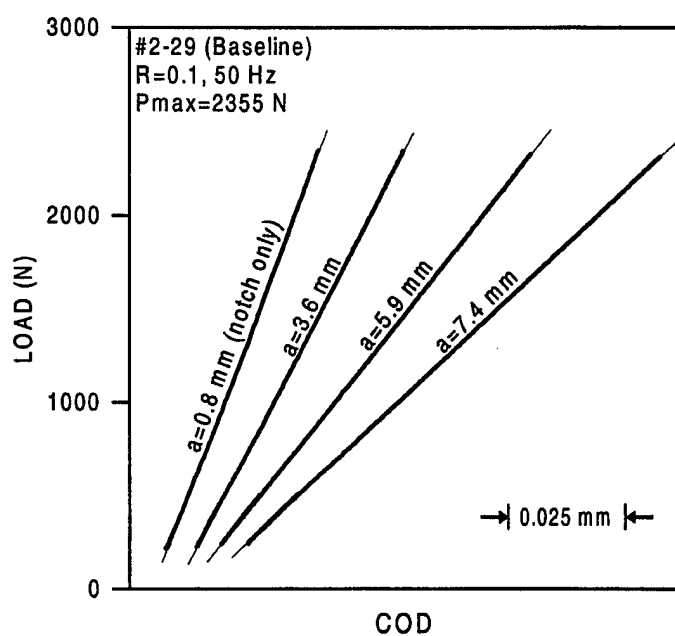
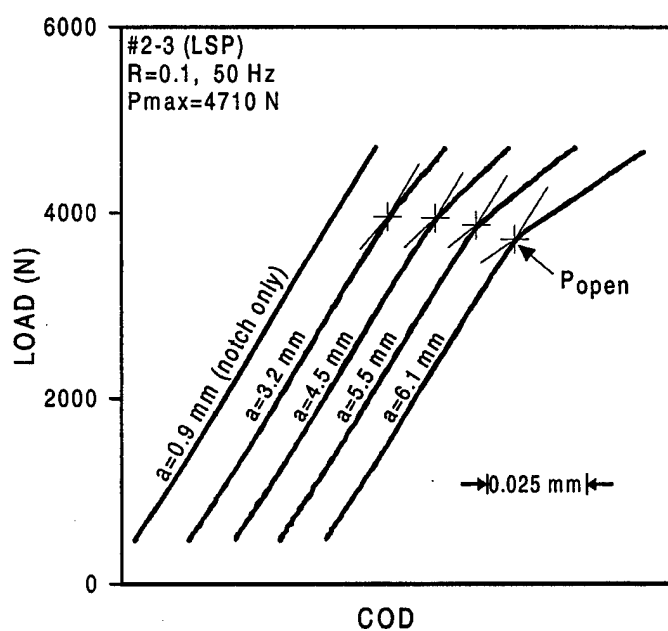


Figure 9. FCGR Data for LSP Samples at R=0.1 Corrected for Closure.





a.) Baseline



b.) LSP

Figure 10. Compliance Traces for (a) a Baseline Sample and (b) an LSP Sample Under  $R=0.1$  Loading.

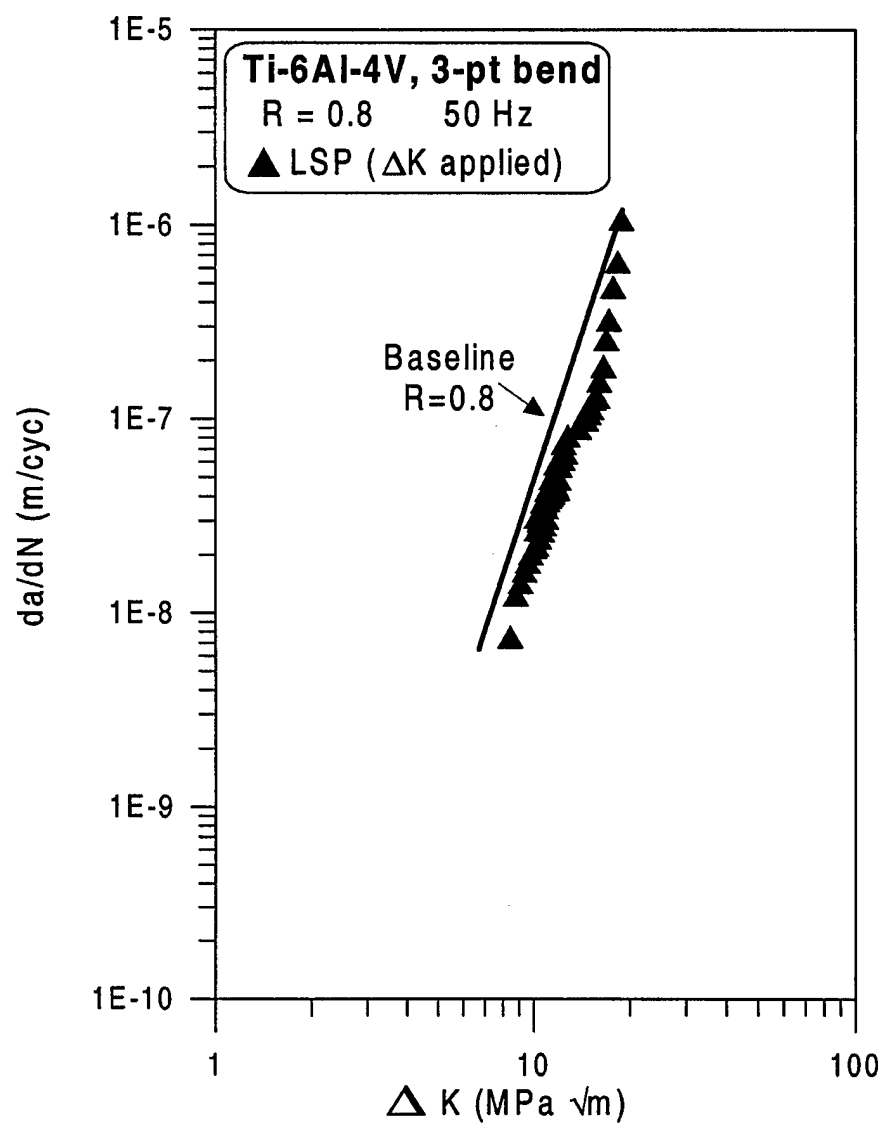
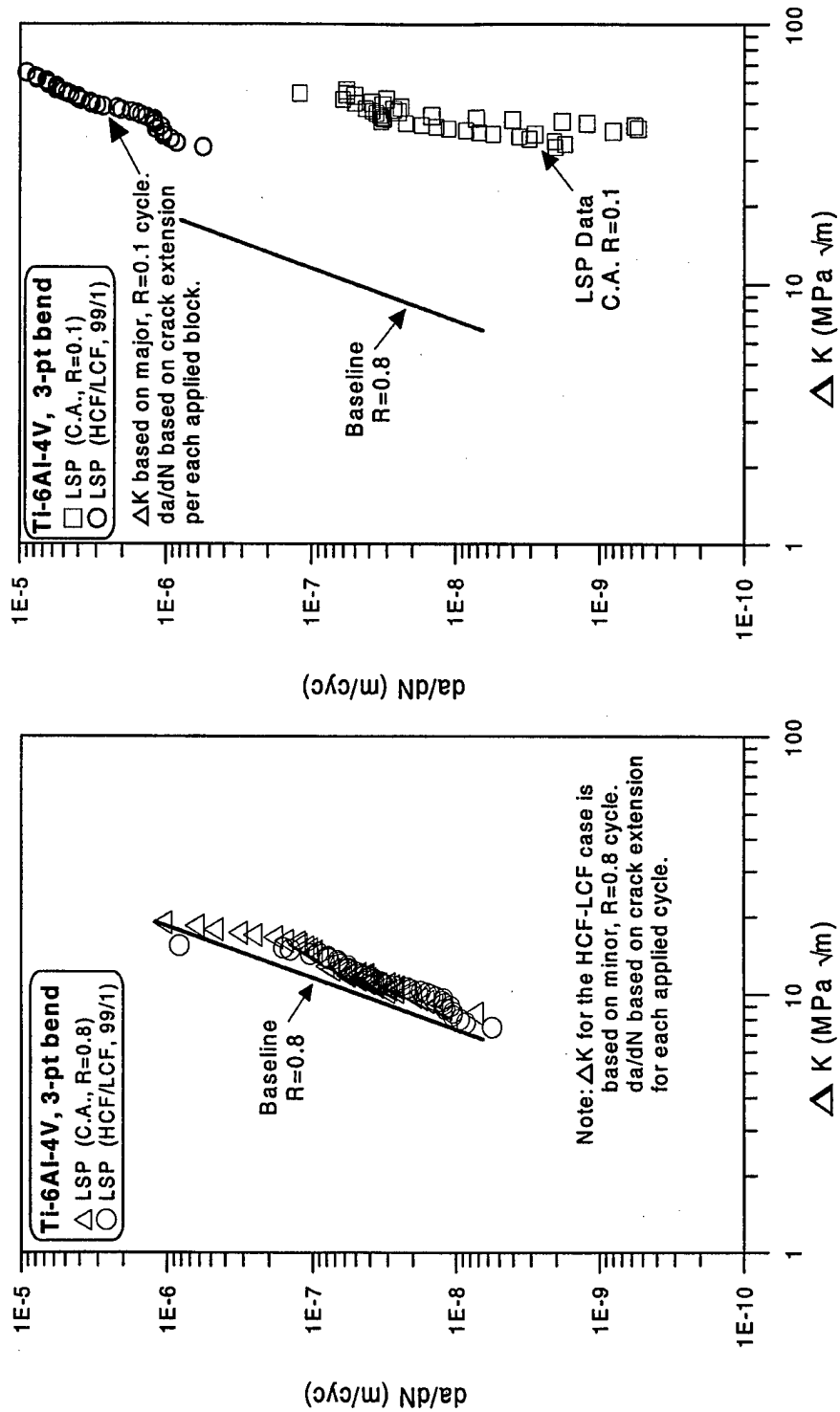


Figure 11. FCGR Data for LSP Samples at  $R=0.8$ .



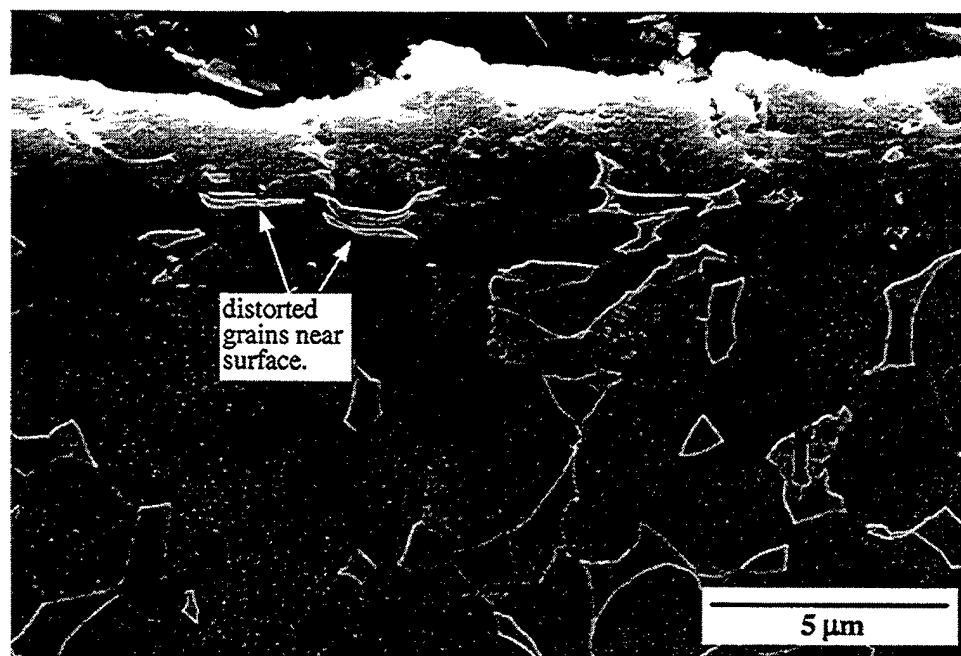


Figure 13: SEM Image of LSP Sample (Cross Section).

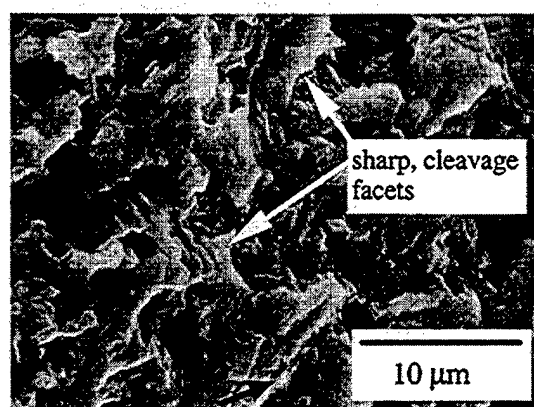


(a). LSP Region



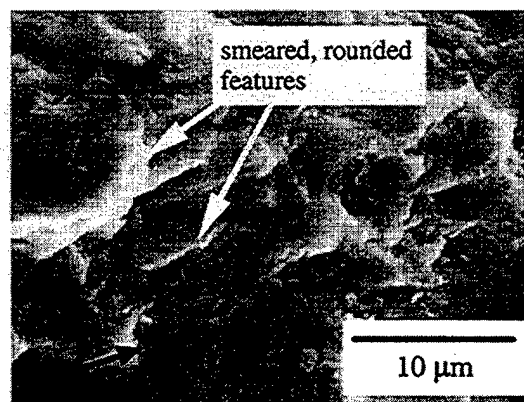
(b). Baseline Region

Figure 14. Transmission Electron Microscopy of LSP Specimen.



-dark arrow indicates crack growth direction.

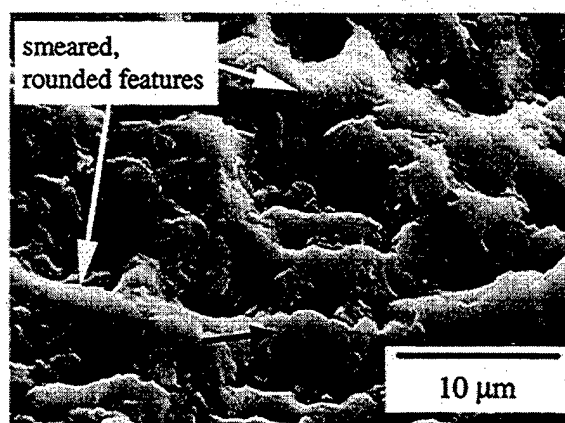
(a) Baseline



-dark arrow indicates crack growth direction.

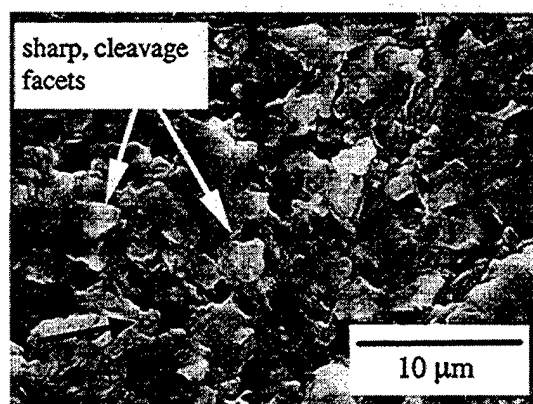
(b). LSP

Figure 15. Fracture Appearance for Airfoil Samples Tested at  $R=0.1$ .



dark arrow indicates crack growth direction.

Figure 16. Fracture Appearance of a Baseline M(T) Sample at R=-3.0.



dark arrow indicates crack growth direction

Figure 17. Fracture Appearance for a LSP Sample Tested at R=0.8.

Reference: Erdahl, D.S., Stubbs, D.A., and Rosenberger, A.H., "Nondestructive Evaluation Techniques for Detecting Surface Defects in Gamma-Titanium Aluminides," submitted for publication in Materials Evaluation, Aug 1997.

### **Nondestructive Evaluation Techniques for Detecting Surface-Connected, Crack-Like Defects in Titanium Aluminide Alloys**

Dathan S. Erdahl<sup>(1)</sup>, David A. Stubbs, and Andrew H. Rosenberger<sup>(2)</sup>  
University of Dayton Research Institute, Dayton, OH

#### **Abstract**

The goal of this project was to evaluate the capability of three existing nondestructive evaluation (NDE) imaging methodologies and equipment for small crack detection in newly developed gamma-titanium aluminide (-TiAl) alloys. Recent studies have shown that -TiAl alloys exhibit very short crack growth lives (compared to crack initiation time) during mechanical fatigue. For -TiAl alloys to be used in jet engine components, the material must be amenable to Air Force damage tolerance design philosophies. One of the key damage tolerance requirements is that NDE techniques be able to reliably detect defects before they cause component failure. Because of the short crack growth life that appears to be characteristic of -TiAl alloys, detection of cracks just after they have initiated in -TiAl alloys is important.

Three NDE imaging techniques were evaluated using -TiAl alloys containing electro-discharge machined (EDM) notches to represent surface-connected defects. The three NDE techniques selected were: eddy current imaging, ultrasonic surface wave imaging, and fluid dye penetrant inspection. These techniques were selected because each is an established NDE technique and each uses a different physical process for detecting defects. Eddy current imaging is sensitive to changes in the electric and magnetic properties of the material. Ultrasonic surface wave imaging uses propagating sound waves, and detects changes in the mechanical properties of the materials. Fluid penetrant inspection uses fluorescent dyes that fill the cracks, allowing optical inspection and detection of the cracks. Since each method interacts with defects in a different way, it was anticipated that one of the methods would have superior signal-to-noise ratios allowing detection of very small cracks in -TiAl alloys.

The results showed that the microstructure in some of the -TiAl alloys creates significant noise in the inspection process, making detection of small defects difficult. However, inspection of specimens with EDM notches on the surface showed that notches as small as 0.20 x 0.10 mm (0.008 x 0.004 inches) were detectable with ultrasonic surface wave imaging, eddy current imaging, and fluorescent dye penetrant imaging.

#### **Introduction**

The application of nondestructive evaluation (NDE) techniques for quality control and detection of defects in system components is common practice in the aerospace industry. Often, NDE techniques are developed late in the design and testing of aerospace components, sometimes even after components are put into service. When NDE is not part of the component design process, implementation of NDE methods can be costly and produce less than optimal inspection results. In fact, components are

occasionally put into service that are impossible to adequately inspect using existing NDE techniques.

The U.S. Air Force's Research Lab (AFRL) has recognized the value of including NDE early in the material design and characterization process. As part of an advanced materials development program, AFRL is encouraging the characterization of new titanium-aluminum (TiAl) alloys with both mechanical testing and NDE methods. Part of the motivation for including NDE characterization of new TiAl alloys during the material development stage results from damage tolerant design philosophies incorporated in the Air Force's Engine Structural Integrity Program (ENSIP) [1]. The Air Force ENSIP damage tolerant design philosophy currently requires engineers to calculate fatigue life based on a maximum permissible flaw size in the component. Knowing the inspection capabilities of NDE techniques for a specific material type allows designers to choose initial flaw sizes that are detectable. By knowing realistic defect detection limits, the engineers can optimize designs to meet performance requirements (loads, stresses, stiffness) while still providing safe service lifetimes.

One of the TiAl alloys currently being characterized has a microstructure containing significant percentages of a "gamma" phase and is designated a "gamma titanium-aluminide" alloy (-TiAl.) Recent studies [2,3,4] have revealed important characteristics of -TiAl alloys two of which are:

- crack propagation in -TiAl alloys is predictable once the crack size is comparable to the microstructural grain size (designated a "long-crack"),
- the long-crack growth rate is very high resulting in a crack propagation life (when NDE techniques would be useful) that is only a small fraction of total component life.

Thus, if damage tolerant design is to be used for -TiAl alloys, NDE techniques must be able to detect, and detect with a high reliability, cracks that are very small.

The microstructure of -TiAl alloys is very dependent on metallurgical processing and grain sizes vary from less than 0.10 mm to greater than 1.0 mm. Detecting cracks on the order of the size of grains requires NDE techniques with high defect detection sensitivity to ensure damage tolerance design. However, this detection requirement approaches the limits of most NDE techniques. In general, NDE techniques depend on sending energy into a material and recording the changes in the energy reflected from or passed through the material. Thus, the interaction of the energy with the microstructure of the material becomes very important. Large grains or colonies may cause distortions of the NDE signals even though no damage actually exists in the material. For some NDE techniques such as eddy current and ultrasonic testing, small changes in material properties can produce defect-like indications that obscure real defects or cause false defect detection decisions.

Many of the new -TiAl alloys have a duplex microstructure containing both lamellar colonies and equiaxed gamma grains (see Figure 1.) The variation in grain shape, size, composition, and orientation pose special problems for most NDE techniques, decreasing the probability of detecting small cracks and limiting defect detection resolutions. This paper presents results of the evaluation of three NDE techniques, eddy current imaging, ultrasonic surface wave imaging, and fluorescent penetrants, thought to be useful for the detection of small defects in new -TiAl alloys.



### Material Description

A wrought gamma titanium developed by Kim [5], was used in this study. Designated "K-5", the alloy's composition was Ti-46.5Al-3Nb-2Cr-0.2W (at%), and the material was forged and heat treated to produce three microstructures designated: duplex, refined fully lamellar (RFL), and coarse lamellar. Photomicrographs of the three microstructures appear in Figure 1.

The duplex microstructure (Figure 1A), consisting of a mixture of equiaxed gamma grains and fine colonies of lamellar gamma plus alpha-2 phase, had an average grain size from 0.01 - 0.03 mm (0.0004 - 0.0012 inches). The RFL microstructure (Figure 1B) consisted of intermediate lamellar colonies, approximately 280  $\mu\text{m}$  in diameter, with thinner lamellae than the fully lamellar microstructure and more equiaxed gamma grains on the colony boundaries. The coarse lamellar microstructure consisted of very large lamellar colonies, approximately 0.70 mm (~0.028 inches) long, with interlocking boundaries and few equiaxed gamma grains on the boundaries. More details of the material, processing, and mechanical properties of this alloy can be found in reference [2].

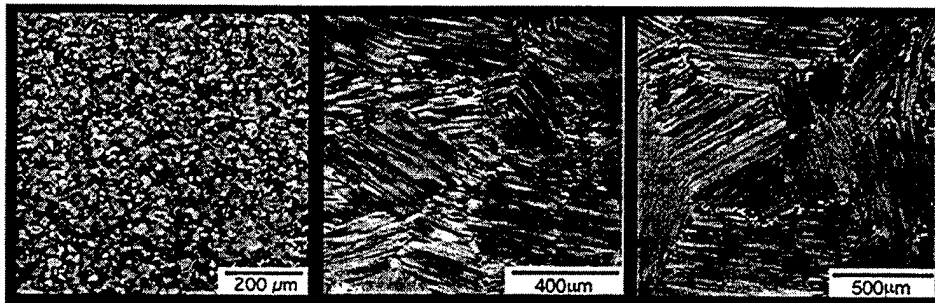


**Figure 1: Microstructure of  $\gamma$  - Titanium Aluminides a.) Duplex, b.) Refined Fully Lamellar, c.) Coarse Lamellar**

To examine the effects of material-induced noise on each NDE technique, defect-free specimens of each microstructure were machined. Each specimen was 79 mm long and 9.5 mm in diameter (3.11 x 0.37 inches). The specimens were machined to have a rectangular cross-section approximately 25 mm (~ 1 inch) long centered along the specimen length (see Figure 2). The rectangular middle section was metallographically polished and each NDE technique was applied to the defect-free, polished surface.

To examine the sensitivity of each NDE technique to small cracks, artificial defects were created in three specimens having the RFL microstructure by electrical discharge machining (EDM). Six equal-sized notches were machined into each specimen in the pattern shown in Figure 2. The machined EDM defects were: 0.20, 0.40, or 0.80 mm (0.008, 0.016, or 0.032 inches) in length. The notches, all 0.12 - 0.13 mm (~0.005 inches) wide, had a length-to-depth ratio of 2:1, which produced notch depths of 0.10, 0.20, or 0.40 mm (0.004, 0.008, or 0.016 inches).

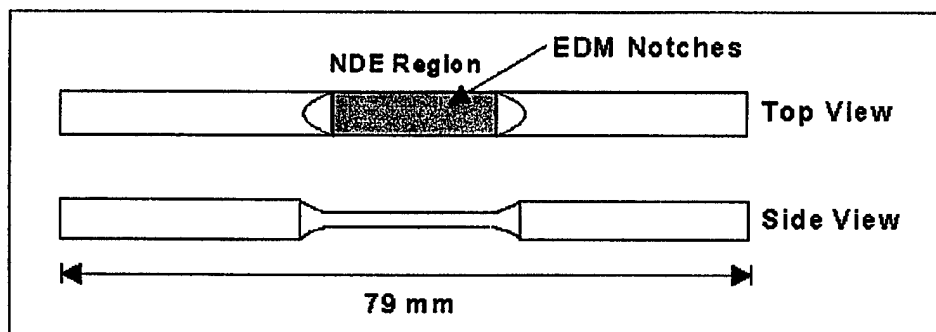


Figure 2- The specimens were machined from 9.5 mm diameter cylinders. The EDM notches were placed in the polished, rectangular, cross-section created in the middle of the specimen.

### NDE Techniques

The following sections contain a brief description of each NDE technique used in this study. Each NDE technique used a different form of energy so that the effects of the alloy microstructure on the NDE signal could be compared. Also, the three NDE techniques were chosen because:

- The equipment existed at AFRL and/or the University of Dayton,
- It was thought that each technique had defect detection sensitivities sufficient to detect 0.10 - 0.20 mm (0.004 - 0.008 inch) long cracks, and
- Each technique had the potential to be used as *in situ* NDE methods during mechanical testing of the -TiAl alloys.

The reader is encouraged to review the literature cited in the references for additional information on each of the NDE techniques.

### Eddy Current Imaging

Eddy current NDE methods utilize electromagnetic energy to characterize the conductivity of a material. Faraday's law states that a changing magnetic field passing through a conductor induces a current in the conductor. These currents, called "eddy currents", follow a closed path in the conductor. The eddy currents create their own "secondary" magnetic field that can be monitored with sensitive inductance probes. Often, the same probe that generates the changing magnetic field and creates the eddy currents, is designed to monitor the secondary magnetic field. The term "eddy current probe" will be used to describe a probe that both generates and monitors eddy currents in test specimens [6].

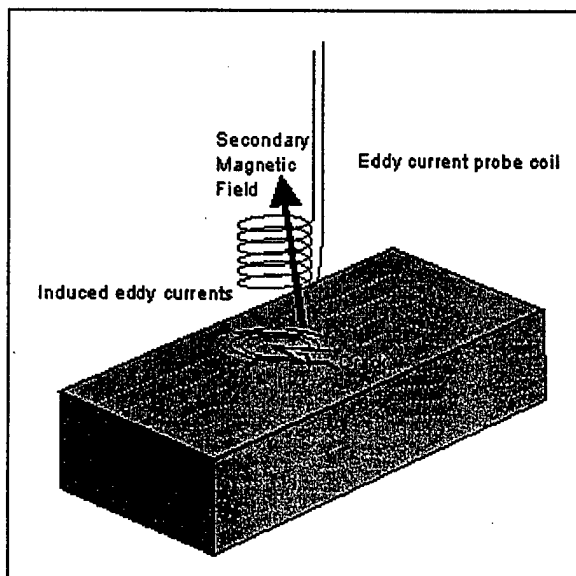


**Figure 3 - Cracks perturb the path of the eddy currents which changes the impedance of the probe.**

A crack in a material can perturb the path of the circulating eddy currents and the corresponding secondary magnetic field (see Figure 3). The eddy currents effectively penetrate below the metallic surface to a frequency-dependent "skin depth", so in order for the crack to perturb the current flow, the profile of the crack must impede a significant percentage of the current flow path. In general, this means the crack must be approximately at least as deep as the eddy current skin depth to be detected. The resulting perturbation of the secondary magnetic field is monitored by the eddy current probe and is detected as a change in the overall electrical impedance of the probe. Present eddy current technology allows the probe's changing impedance to be observed by the operator on a cathode ray tube

"impedance plane display." The impedance plane display presents a real time trace of the probe's inductive reactance versus probe resistance. Calibration of the eddy current probe's response to cracks of different sizes allows the interpretation of the impedance plane signals for crack detection and sizing [7].

For this study the eddy current probes consisted of a 1.5 mm diameter transmit coil surrounding two D-shaped receiver coils. The receiver coils were wound in opposition to cancel effects of probe lift-off from the specimen, creating a differential receiver probe. The coils were encapsulated in a polymer shoe that was attached to the probe body by a copper leaf spring. The spring coupling kept the shoe in contact with the specimen, compensating for slight variations of the specimen's flatness. This probe design was created for the U.S. Air Force's automated engine component inspection systems and has proved to be very effective for minimizing lift-off signals and maximizing small crack detection [8].

The probes were connected to a commercially available eddy current instrument, UniWest model 450R<sup>(3)</sup>. This instrument is microprocessor based, containing digital high and low pass filters, automated nulling circuitry, 80 dB of gain range, and sinusoid or square wave drive signals. The motion control hardware and software were integrated with the eddy current instrument by Structural Diagnostics Incorporated<sup>(4)</sup>.

Eddy current probes optimized for two different frequencies were selected for this study to examine the effects of the alloy microstructure on the eddy current signals. The 2 MHz and 6 MHz frequencies produced skin depths of approximately 0.42 mm and 0.27 mm respectively.

The eddy current imaging system was adjusted to produce detectable signals when the probe was moved over the EDM notches in the specimens. The eddy current probe

remained in contact with the specimen, and the lift-off signal was rotated to produce horizontal signals on the impedance plane display. Adjustments to gain, filters, and signal rotation allowed detection of the notch signals primarily on the vertical axis of the display. The EDM notches produced a figure-eight signal on the impedance plane because of the differential receiver coils. The magnitude of the signal on the vertical axis of the impedance plane was recorded and the series of amplitude data from the raster

scan was translated into an image by assigning a color to the vertical axis value. An example of the images produced appears in Figure 4A. The specimen is a RFL specimen with six EDM notches visible on the scan. All of the notches were approximately 0.40 mm long and all were clearly imaged by the eddy current system.

The color bar in Figure 4A was designed to produce the greatest possible contrast between the material-generated signals and the notch signals based on the typical response from the differential coils. The color bar is symmetric about the midpoint to compensate for the differential probe that produced both positive and negative signals for a single defect. As the absolute value of the signal amplitude increased the amplitudes were assigned values on a grayscale, changing from white to black. In addition, a transition to a color scale provided a threshold that highlights the defects while subduing natural variations in the material. In the eddy current images in this paper notches often appear as a pair of semi-circles because of the shape of the receive coils. The maximum response occurs when the notch cuts across the circular eddy current path, producing a maximum response at two locations for each D-shaped receiver coil. The size of the defect image is usually enlarged by approximately the diameter of the eddy current probe coils.

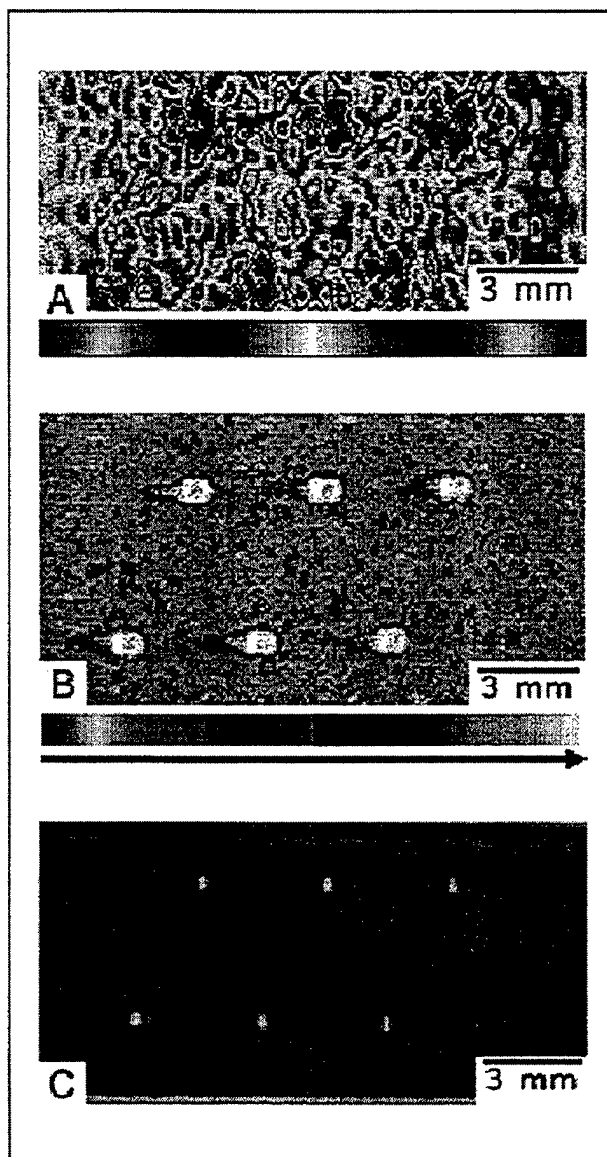


**Figure 4 - NDE images of refined fully lamellar (RFL) specimen with 0.40 mm long EDM notches: A) Eddy current, B) Ultrasonic surface wave, C) Fluorescent Penetrant.**

### Ultrasonic Surface Wave Imaging

Previous work at the Air Force Research Laboratories showed that immersion ultrasonic surface wave imaging was an effective NDE technique for detecting and characterizing defects in metal matrix composites and various alloys [9,10]. The surface waves are formed by insonifying the surface of the specimen with ultrasound at an angle sufficient to cause mode conversion from a longitudinal wave to a

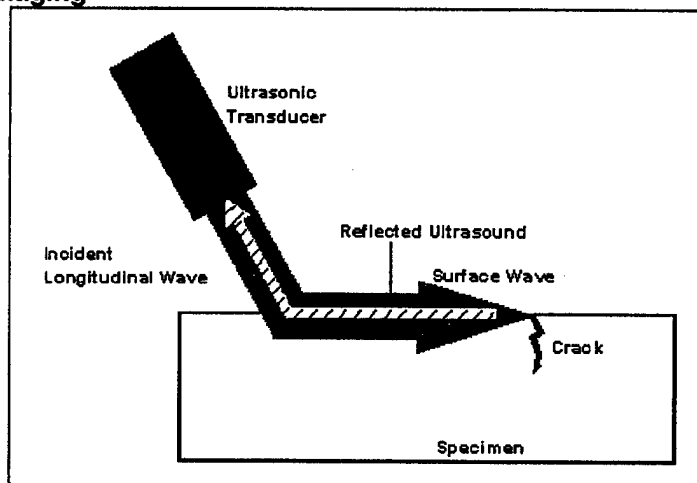


**Figure 5 - Surface wave energy is reflected by a defect and returns to the transducer.**

surface wave (Figure 5). Because the specimen is submersed in water the surface wave immediately begins to convert back to a longitudinal wave and so its propagation on the specimen occurs for only a few millimeters. If the surface wave encounters a defect on the specimen some of the surface wave energy is reflected backwards and the subsequent mode conversion to longitudinal energy is directed back towards the transducer. The mode conversion and surface wave propagation, coupled with scanning of the transducer across the specimen, produces a "surface wave image" of the specimen. Work in the AFRL laboratories has shown that the 10 to 25 MHz surface wave imaging technique is useful for detecting cracks as small as approximately 0.30 to 0.50 mm (0.012 to 0.020 inches) in length; higher frequencies and shorter focal lengths decrease the minimum detectable crack size. The technique is limited to detection of near-surface damage because the ultrasonic energy has an effective penetration depth of approximately one ultrasonic wavelength beneath the specimens's surface. At 25 MHz the wavelength of the ultrasonic energy was calculated to be 0.16 mm (~0.006 inches).

Surface wave scans acquired in this study utilized a 6.3 mm (0.25 inch) diameter 25 MHz transducer with a 13 mm (~0.5 inch) focal length. The ultrasound insonified the specimen at an incident angle of 33 degrees and was propagated along the long axis of the specimen. The reflected surface wave signals were digitized by a LeCroy<sup>(5)</sup> digitizer at 500 MHz with eight bits of amplitude resolution. The -6dB beam-width of the focal spot on the surface of the specimen was calculated to be 0.12 mm (0.005 inches).

Images were produced using a raster scanning pattern similar to that described for the eddy current technique. However, at each X-Y coordinate sixteen ultrasonic waveforms were averaged to reduce electronic noise, and the maximum peak-to-peak amplitude within a time-gated portion of the signal was recorded. An example of an ultrasonic surface wave image is shown in Figure 4B. The image is from the same specimen as shown in Figure 4A. The background in the images shows relatively small signals that usually appear as green or blue on the image, but the notches appear white, indicating a full scale signal. Using the distance scale on the image, the notches appear larger than 0.40 mm (0.016 inches), due to the ultrasound beam width. Subtracting the beam width from the defect image dimensions corrects for the distortion.

## Fluid Penetrant Imaging

Fluid penetrant imaging was also used to detect the EDM notches in the -TiAl alloy specimens. The technique depends on the ability of a liquid to penetrate into a surface-connected defect through capillary action. The surface of the specimen to be inspected was coated with a non-toxic, non-reactive fluorescent fluid. After washing excess penetrant from the surface, only the penetrant in the defect remained. To make the penetrant in the defect visible, a developing powder containing  $\text{CaCO}_3$  and talc was applied to the specimen. The developer wicked the dye out of the defect exposing a greater amount of the penetrant for observation (see Figure 6). If a fluorescent penetrant is used, the fluid in the developer glows when exposed to ultraviolet light, enhancing the outline of the defect.

A P2F6 fluorescent penetrant was chosen for this study and worked well in making the EDM notches visible. The larger EDM notches were visible without applying developer, but the use of developer enhanced the detection of all of the notches. Photographs taken using Polaroid Type 55 film, a camera aperture set at  $f/8$ , and a 45 second exposure using an ultraviolet light source captured clear images of all the notches. Momentary back lighting of the specimen with a white light source allowed the outline of the specimen to appear in the photographs. An example of the fluorescent penetrant imaging (FPI) results is shown in Figure 4c. The size of the notches measured from the image is very close to the actual notch dimensions.

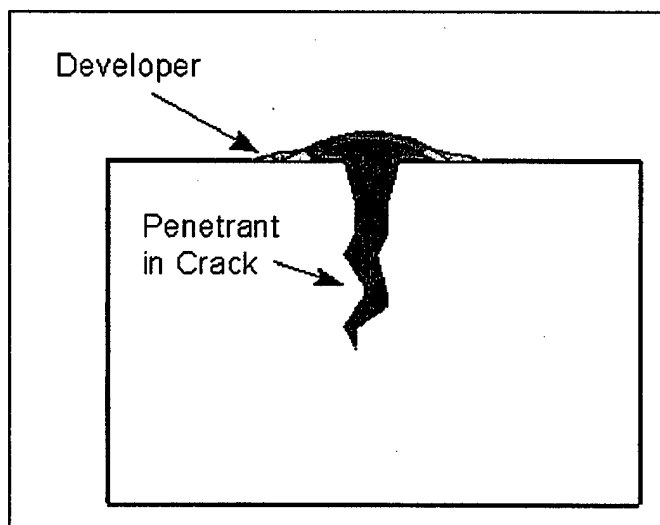


**Figure 6 - Fluorescent penetrant wicks out of a crack and is absorbed by the developer powder making the crack visible.**

## Results and Discussion

### Effects of -TiAl alloy Microstructure on NDE Images

To determine the effects of the -TiAl alloy microstructure on the NDE imaging techniques one defect-free specimen of each microstructure was scanned using the ultrasonic surface wave and eddy current imaging techniques. Since the fluorescent penetrant technique doesn't directly interact with the alloy microstructure, it wasn't applied to the different microstructures. The images are shown in Figure 7.

The ultrasonic NDE images in Figure 7 reveal different responses for each microstructure. As expected the images indicate a trend from less noise to more noise with increasing microstructural size. The duplex microstructure produces the most

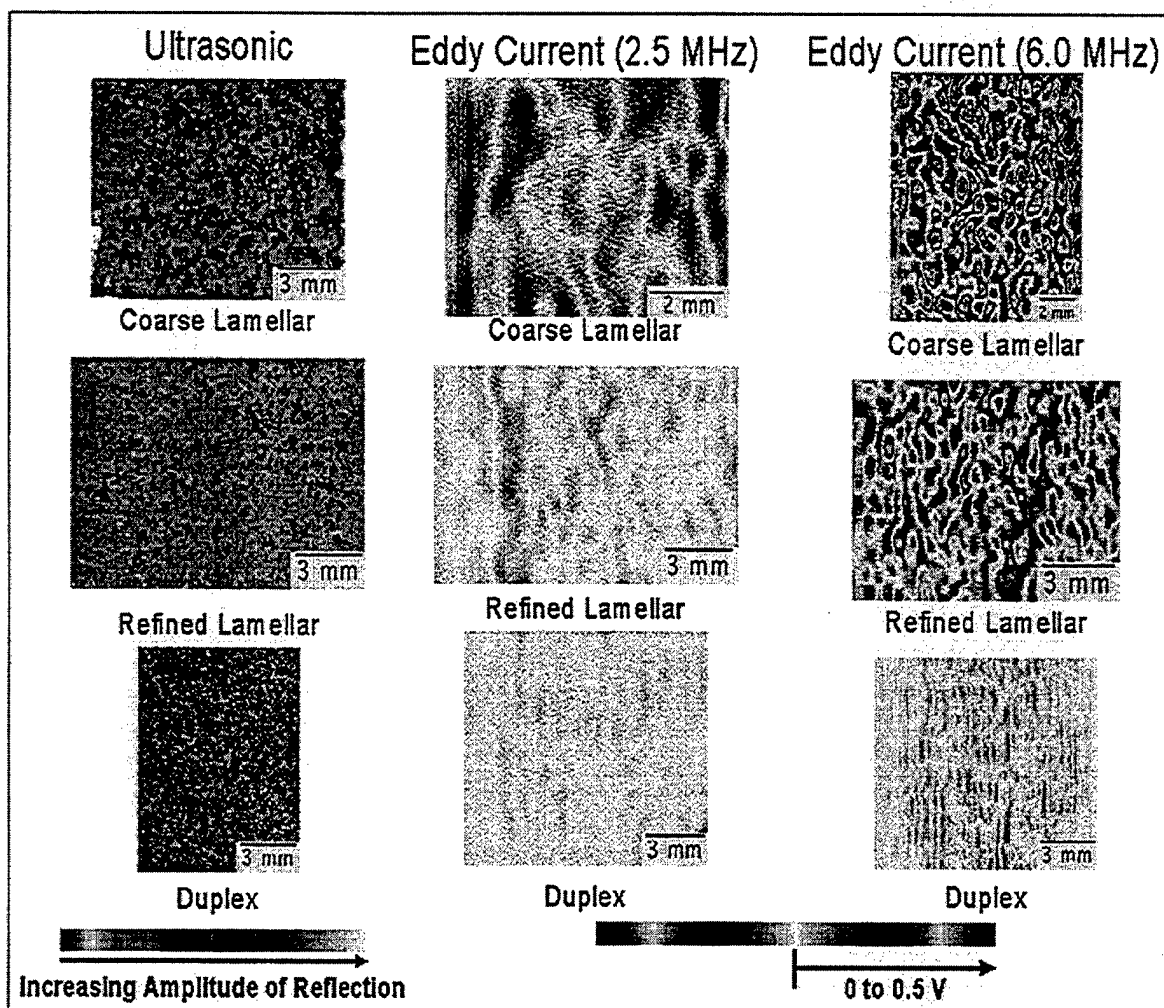


Figure 7 - The effects of the different  $\gamma$ -TiAl alloy microstructures on the baseline material noise for each NDE technique are shown in these images.

uniform C-scan image. A uniform color distribution indicates little variation in the amplitude of the reflected ultrasonic signal; the microstructure has very little effect on the signal. The C-scans of the specimens with the RFL and coarse lamellar microstructure show more variation with localized areas of higher amplitudes presumably because the wavelength of the ultrasonic signal was small enough to be reflected from the large lamellar grains. For those colonies oriented appropriately, the ultrasonic energy was reflected back to the transducer. The areas of highest amplitude appear to indicate individual grain colonies that likely were oriented perpendicular to the transducer.

The same three specimens were scanned with the eddy current system, using 2 MHz and 6 MHz probes. As stated earlier estimates of the skin depths were 0.42 mm (2 MHz probe) and 0.27 mm (6 MHz probe). The images resulting from using the two different eddy current frequencies are shown in Figure 7. The images resulting from each frequency showed an increase in the eddy current response with increasing microstructure size, but the 6 MHz probe responses were larger. The 6 MHz probe's greater sensitivity to material microstructure resulting from the shallower skin depth penetration was probably caused by the lamellar colonies impeding a greater portion of

the eddy currents. Similar to the ultrasonic images, the eddy current images contain regions of large magnitude signals that may indicate individual colonies. Although the 2 MHz probe also seemed to detect microstructures variations, the effects of the microstructure are more generalized. Instead of showing individual colonies, the images show large areas of slight changes in signal response.

### **Defect Detection Sensitivity**

Several RFL specimens, each containing six EDM notches, were imaged using each of the three NDE techniques. Two of the specimens were obtained after undergoing mechanical fatigue testing and were fractured. The notches were machined in three lengths: 0.20, 0.40, and 0.80 mm (0.008, 0.016, and 0.032 inches). NDE images of the 0.2 and 0.8 mm notches (placed in fractured specimens) are shown in Figure 8. The 0.40 mm notches are those shown in Figure 4. To avoid the effects of the fracture surface on the eddy current images, only half of the specimen was scanned in Figures 8a and 8d.

The NDE images of the 0.20 mm notches appear in Figures 8a-c (specimen #96956). The ultrasonic surface wave technique (Figure 8b) detected all five notches on the surface and also shows the fracture surface. The notches appear slightly larger than actual size due to the width of the ultrasonic beam. Fluorescent penetrant imaging (Figure 8c) also provided strong indications of the five notches. Developer was not used to produce this image so the indications are very accurate in size. The 6 MHz eddy current image (Figure 8a) only shows four of the five notches. Although the scan was repeated several times, no indication of the fifth notch was ever seen. The fifth notch was measured to be 0.184 mm long and 0.125 mm wide, making the notch slightly smaller than the other notches that averaged 0.198 mm long and 0.129 mm wide. The proximity of the fracture surface to the fifth notch also may have affected the eddy currents in the specimen. The other notches did not appear as strong signals, so it is assumed that the minimum detection limit is close to the 0.20 x 0.10 mm notches.

The specimen shown in Figures 8d-f (# 96960) containing 0.80 mm (0.032 inch) notches produced very strong indications using the ultrasonic and FPI techniques. Clearly both NDE techniques can easily detect 0.80 mm long notches. The image in Figure 8d was acquired using a 2 MHz eddy current probe because 0.80 mm long notches perturbed the eddy current so much that the 6 MHz eddy current signal was saturated for a large portion of the image. All four notches were imaged using the 2 MHz probe, but the indication for the notch closest to the fracture surface is partially obscured by the saturated signal from the fracture surface. The eddy current scan was made with the gain setting 6 dB lower than all other eddy current scans made during this study to minimize the effects of the fracture surface.

The images in Figures 4a-c (specimen #96740) contained 0.40 mm notches and all of the NDE techniques produced excellent images clearly showing the notches. The specimen was not fractured, so no fracture surface perturbed the signals. Although the ultrasonic and FPI techniques produced images of the notches that are approximately accurate in size, the 6 MHz eddy current technique greatly exaggerated the size of the notches. The notch images produced by the 6 MHz eddy current scans resulted in two halves and four lobes, typical of images of cracks smaller than the coil diameter. The four-lobed eddy current images were due to the notch "cutting" across the D-shaped



eddy current paths at two locations for each receive coil. Thus, the image of the notch is enlarged by approximately the coil diameter.

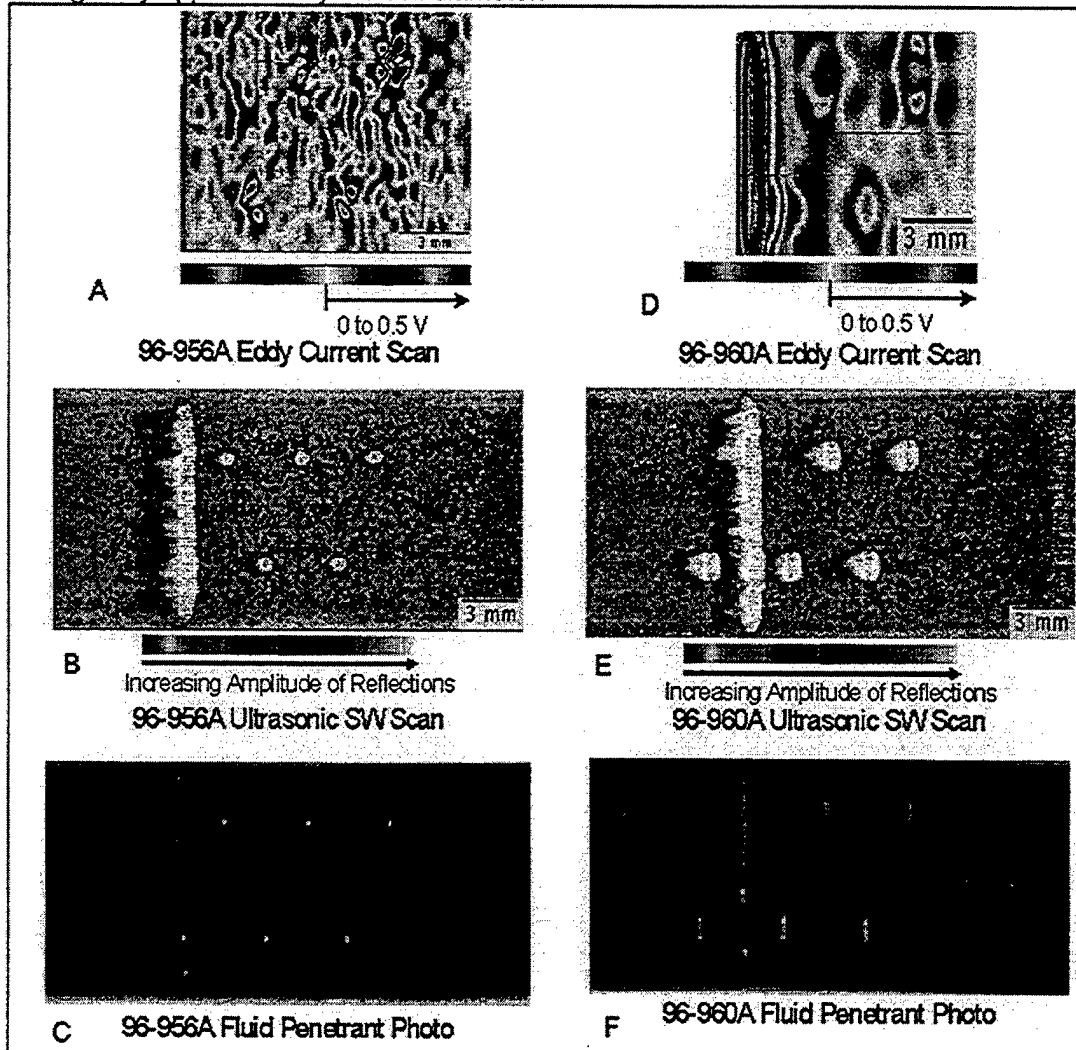


Figure 8 - Results of the three NDE imaging techniques applied to refined fully lamellar,  $\gamma$ -TiAl alloy specimens with 0.20 x 0.10 mm EDM notches (Figures A,B,C) and 0.80 x 0.40 mm EDM notches (Figures D,E,F). Eddy current images are shown in Figures A and D. Ultrasonic images are shown in Figures B and E. Fluorescent penetrant images are shown in Figure C and F.

## Discussion

The NDE images presented in this paper indicate that all three of the NDE techniques had sensitivities sufficient for detecting the smallest notches (0.20 x 0.10 mm) used in the study. Each NDE technique also had signal-to-noise ratios sufficient to discriminate the responses from the 0.20 x 0.10 mm notches from the material and electronic noise. However, it appears that the probability of detection will decrease substantially for notches smaller than 0.20 x 0.10 mm.

The ultrasonic surface wave imaging techniques arguably produced the images that provided the best defect detection. Previous experience with this technique, and consideration of the wavelength of the surface wave energy and beam width suggests that notches as small as 0.150 x 0.075 mm should be detectable. The fluorescent penetrant imaging technique also allowed easy detection of the 0.20 x 0.10 notches. Use of developer should allow even smaller notches to be detected. The eddy current imaging technique was the least able of the three techniques to produce clear indications of the 0.20 x 0.10 mm notches. However, signal processing techniques that utilize the impedance plane phase information along with the magnitude of the signal could improve defect detection. Also, optimization of the eddy current frequency and coil sizes might result in clearer defect images.

Although a thorough discussion comparing the detection of notches versus fatigue cracks is well beyond the scope of this paper, a brief comment is in order for each technique. The interaction of eddy currents with a defect is primarily affected by the length and depth of the defect. Thus, the eddy current responses from notches presented in this paper should be representative of the responses that would be obtained from cracks. Ultrasonic surface waves also should reflect from cracks with approximately the same amount of energy as from notches, as long as the cracks present similar cross-sectional areas. However, the FPI technique is likely aided by the larger volume contained in an EDM notch versus a crack. Each EDM notch was 0.12 - 0.13 mm (~0.005 inches) wide. Assuming that most cracks that would occur in -TiAl alloys would be tapered and at most only a few microns wide, the volume of the EDM notches are an order of magnitude larger than the volume of a crack. The amount of penetrant that is held in an EDM notch, and is available for wicking out to the surface, is much greater than in a crack. Thus, it is expected that FPI detection of cracks will be more difficult than notches. Another difference between notches and cracks is important if the fatigue cracks are tightly closed. The responses from all three NDE techniques may be substantially smaller for tightly closed cracks.

The ease of use of each NDE technique is also an important factor to consider. Two implementation situations were considered during the evaluation of the techniques described in this paper:

- Laboratory NDE - Specimens could be taken to an NDE facility for testing,
- *In situ* NDE - The specimen was held in a mechanical fatigue system and all NDE testing was required to take place during a brief period when fatigue loading was suspended. The specimen had to remain in the mechanical test system's grips.

The second situation wasn't encountered during this work but is expected to be applied in the near future in our laboratories.

*In situ* use of the ultrasonic surface wave technique would require substantial engineering to create a water bath around the specimen. The water bath would have to be created and removed each time an NDE inspection was performed. The FPI technique, while being a little "messy" could easily be applied *in situ*. A possible drawback could be the presence of penetrant in cracks as the effects of temperature on trapped penetrant and possible adverse effects due to penetrant/alloy interactions would have to be taken into consideration during elevated temperature mechanical testing. The eddy current technique seemed to be the most adaptable to *in situ* application. The X-Y scanning system easily could be moved into place over the specimen for NDE

inspections. No contact with the specimen would be required and thus the specimen and mechanical testing apparatus would remain unperturbed.

## Conclusions

The results of this study are summarized in Table 1 shown below. Each evaluation category has been discussed in the paper except for the final one, "Potential for development for detecting 0.05 mm cracks." It is clear from Table 1 that each NDE method has categories of strength relative to the other techniques. This table will help determine the NDE method that will be used for *in situ* laboratory work in the future.

Additional research directed towards examining the capability of each NDE technique for detecting actual fatigue cracks, rather than EDM notches, is necessary. Present understanding of -TiAl alloy fatigue life points towards the need to detect very small (0.05 - 0.075 mm long) fatigue cracks due to the relatively short crack growth life (compared to crack initiation life). As discussed earlier in this paper, the detection of EDM notches helps reveal the capability of detecting fatigue cracks but is not conclusive. Thus, further development is expected for one or more of the NDE techniques to see if 0.05 mm long (0.002 inches) cracks can be detected. The answer to that problem may influence whether or not -TiAl alloys with a given microstructure should be considered for use in components that must fall under Air Force ENSIP damage tolerance guidelines.

**Table 1 - Ranking of the NDE Techniques**

<b>NDE Technique Evaluation Category</b>	<b>Eddy Current</b>	<b>UT Surface Wave</b>	<b>FPI</b>
Ability to reject material (microstructure) noise	low - moderate	moderate	high
Sensitivity to EDM notches	moderate	high	high
Expected sensitivity to cracks	moderate	high	moderate
Typical inspection time for specimens	15 - 20 min.	60 min.	30 min.
Potential <i>in situ</i> use in mechanical test system	high	low	marginal
Cost to implement technique	\$25k-\$50k	\$25k-\$50k	< \$1k
Potential for detecting 0.05 mm long cracks	moderate	high	moderate

## Acknowledgments

Most of this work was conducted at the Air Force Research Laboratory (AFRL) Metals, Ceramics, and Nondestructive Evaluation Division, under Air Force Contract No. F33615-94-C-5200. The authors also wish to acknowledge the support of the following people and organizations during this project:

- Air Force Contract No. F33615-95-C-5241 for use of the eddy current imaging system
- AFRL/MLLP (Nondestructive Evaluation) for use of the ultrasonic imaging system

- AFRL/MLS (Systems Support) and Mr. Ed Porter with Universal Technology Corporation for assistance in the FPI technique
- AFRL/MLLN (Metals Development & Materials Processing) and Ms. Cheryl Heidenreich with Universal Energy Systems for assistance with photographing the specimens

## References

- [1] U.S. Air Force, Engine Structural Integrity Program (ENSIP), Military Standard 1783, Aeronautical Systems Division, Wright-Patterson Air Force Base, OH, (1984).
  - [2] B.D. Worth, J.M. Larsen, and A.H. Rosenberger, "Threshold Crack Growth Behavior of the Gamma Titanium Aluminide Alloy Ti-46.5Al-3Nb-2Cr-0.2W Under High Cycle Fatigue Conditions," Proceedings of the 2nd International Symposium on Structural Intermetallics, TMS, 420 Commonwealth Dr., Warrendale, PA 15086, September 21-25, 1997, pp 563-569.
  - [3] Y. Mutoh, S. Kurai, T. Hansson, T. Moriya, S.J. Zhu, "Fatigue Crack Growth in TiAl Intermetallics with Equiaxed, Duplex and Lamellar Microstructures at Elevated Temperatures," Proceedings of the 2nd International Symposium on Structural Intermetallics, TMS, 420 Commonwealth Dr., Warrendale, PA 15086, September 21-25, 1997, pp 495-503.
  - [4] V. Recina and B. Karlsson, "Tensile and Low Cycle Fatigue Properties of Ti-48Al-2W-0.5Si Gamma Titanium Aluminide," Proceedings of the 2nd International Symposium on Structural Intermetallics, TMS, 420 Commonwealth Dr., Warrendale, PA 15086, September 21-25, 1997, pp 479-487.
  - [5] Y-W. Kim, "Ordered Intermetallic Alloys, Part III: Gamma Titanium Aluminides," JOM, Vol. 46, No. 7, (1994) pp. 30-40.
  - [6] ASM Handbook Volume 17: Nondestructive Evaluation and Quality Control, American Society for Metals, Metals Park, OH, 1995.
  - [7] Hagemeyer, Donald J., Fundamentals of Eddy Current Testing. The American Society for Nondestructive Testing, Inc., Columbus, OH, 1990.
  - [8] Hoppe, W.C., and Stubbs, D.A., "RFC Eddy Current Probe Tests," Review of Progress in Quantitative Nondestructive Evaluation, Vol. 5a, Edited by D.O. Thompson and D.E. Chimenti, Plenum Press, 1986.
  - [9] MacLellan, P.T., "Damage Characterization of a Metal Matrix Composite Using Standard Ultrasonic Techniques," Materials Evaluation, (50) 10, October 1992, pp. 1148-1154.
  - [10] MacLellan, P.T., "In-Situ Ultrasonic Surface Acoustic Wave Characterization of Damage in a SCS-6/Beta 21S Metal Matrix Composite," Masters Thesis, University of Dayton, Dayton, OH, December 1993.
  - [11] Dimiduk, D.M., "Gamma Titanium Aluminides - an Emerging Materials Technology," in Gamma Titanium Aluminides, edited by Y-W. Kim, R. Wagner, and M. Yamaguchi, The Materials, Minerals, and Metals Society, Warrendale, PA, 1995, pp. 3-20.
1. Present address: Georgia Technology Institute, 332268 Georgia Tech Station, Atlanta, GA
  2. USAF, AFRL, Bldg655, 2230 Tenth St Ste 1, Wright-Patterson AFB, OH 45433-7817
  3. UniWest, 330 West Clark Street, Pasco, WA 99301
  4. Structural Diagnostics, Inc., 25 W. Easy St., Unit 303, Simi Valley, CA 93065
  5. LeCroy Corporate Headquarters, 700 Chestnut Ridge Road, Chestnut Ridge, NY 10977

**Appendix B**  
**List of Symbols, Abbreviations and Acronyms**

### ***List of Symbols, Abbreviations and Acronyms***

---

$\delta$	Relative displacement
$\tau$	Fiber/Matrix Frictional Shear Stress
AE	Acoustic Emission
ASIP	Aircraft Structural Integrity Program
B-P	Bodner-Partom
C(T)	Compact Geometry
CMC	Ceramic Matrix Composite
CMOD	Crack Mouth Opening Displacement
COD	Crack Opening Displacement
CTE	Coefficient of Thermal Expansion
EDM	Electrical Discharge Machining
EDS	Energy Dispersive Spectroscopy
ENSIP	Engine Structural Integrity Program
FCG	Fatigue Crack Growth
FCGR	Fatigue Crack Growth Rate
FOD	Foreign Object Damage
HCF	High Cycle Fatigue
IDG	Interferometric Displacement Gage
IHPTET	Integrated High Performance Turbine Engine Technology
K	Stress Intensity Factor
LCF	Low Cycle Fatigue
LSP	Laser Shock Peening
LVDT	Linear Variable Differential Transformer
MLLN	Ceramics Development & Material Behavior Branch
MMC	Metal Matrix Composite
MSE(T)	Modified Single Edge Geometry
NDE	NonDestructive Evaluation
OPTMF	Out-of-Phase Thermomechanical Fatigue
OTMC	Orthorhombic Titanium Matrix Composite
P/M	Powder Metallurgy
PRDA-IV	Program Research and Development Announcement – IV
R	Stress Ratio
RT	Room Temperature
SE(T)	Single Edge Geometry
SEM	Scanning Electron Microscope
S-N	Stress-Cycle Life
TMC	Titanium Matrix Composite
TMCTECC	TMC Turbine Engine Component Consortium
TMF	Thermomechanical Fatigue
UDRI	University of Dayton Research Institute
WUD	Work Unit Directive

## BIBLIOGRAPHY

---

### Journal/Refereed Articles

Buchanan, D.J., John, R., and Goecke, K.E., "Influence of Temperature and Stress Ratio on the Low-Cycle Fatigue Behavior of Trimarc-1/Ti-6Al-2Sn-4Zr-2Mo," Composite Materials: Fatigue and Fracture, Seventh Volume, ASTM STP 1330, Ronald B. Bucinell, Ed., American Society for Testing and Materials, 1998, pp. 199-216.

Buchanan, D.J., John, R., and Johnson, D.A., "Determination of Crack Bridging Stresses from Crack Opening Displacement Profiles," International Journal of Fracture, vol. 87, no. 2, 1998, pp. 101-117.

Buchanan, D.J., John, R., Stubbs, D.A., Benson, D.M., and Karpur, P., "Ultrasonic Longitudinal and Surface Wave Methods for *In Situ* Monitoring of Damage in Metal Matrix and Ceramic Matrix Composites," Nontraditional Methods of Sensing Stress, Strain, and Damage in Materials and Structures, ASTM STP 1318, George F. Lucas, and David A. Stubbs, Eds., American Society for Testing and Materials, 1997, pp. 173-186.

John, R., "Stress Intensity Factor and Compliance Solutions for an Eccentrically Loaded Single Edge Cracked Geometry," Engineering Fracture Mechanics, vol. 58, no. 1/2, 1997, pp. 87-96.

John, R., and Rigling, B., "Effect of Height to Width Ratio on K and CMOD Solutions for a Single Edge Cracked Geometry With Clamped Ends," Engineering Fracture Mechanics, vol. 60, no. 2, 1998, pp. 147-156.

John, R., Buchanan, D.J., Stubbs, and Herzog, J.A., "Characterization of Damage Progression in Ceramic Matrix Composites Using an Integrated NDE/Mechanical Testing System," Thermal and Mechanical Test Methods and Behavior of Continuous-Fiber Ceramic Composites, ASTM STP 1309, M.G. Jenkins, S.T. Gonczy, E. Lara-Curzio, N.E. Ashbaugh, and L.P. Zawada, Eds., American Society for Testing and Materials, 1997, pp. 193-208.

John, R., Jira, J.R., and Larsen, J.M., "Effect of Stress and Geometry on FCG Perpendicular to Fibers in Ti-6Al-4V Reinforced with SiC Fibers," Composite Materials: Fatigue and Fracture, Seventh Volume, ASTM STP 1330, Ronald B. Bucinell, Ed., American Society for Testing and Materials, 1998, pp. 122-144.

John, R., Kaldon, S.G., Johnson, D.A. and Coker, D., "Weight Function For A Single Edge Cracked Geometry With Clamped Ends," International Journal of Fracture, vol. 72, no. 2, 1995, pp. 145-158.

John, R., Khobaib, M., and Smith, P.R., "Prediction of Creep-Rupture Life of Unidirectional Titanium Matrix Composites Subjected to Transverse Loading," Metallurgical and Materials Transactions, vol. 27A, 1996, pp. 3074-3080.

John, R., Khobaib, M., and Smith, P.R., "Rupture Life of Unidirectionally Reinforced Titanium Matrix Composites Subjected to Sustained Transverse Loading," Scripta Metallurgica et Materialia, vol. 33, no. 3, pp. 473-478, 1995.

John, R., Lackey, A.F., and Ashbaugh, N.E., "Fatigue Crack Propagation Parallel to Fibers in Unidirectionally Reinforced SCS-6/Timetal21S," Scripta Metallurgica et Materialia, vol. 35, no. 6, 1996, pp. 711-716.

John, R., Zawada, L.P., and Kroupa, J.L., "Stresses Due to Temperature Gradients in CMC Aerospace Components," J. American Ceramic Society, vol. 82, no. 1, 1999, pp. 161-168.

Kramb, V.A. and John, R., "Fatigue Crack Growth Behavior of a Woven Silicon Carbide/Silicon Carbide Ceramic Matrix Composite," Thermal and Mechanical Test Methods and Behavior of Continuous-Fiber Ceramic Composites, ASTM STP 1309, Michael G. Jenkins, Stephen T. Gonczy, Edgar Lara-Curzio, Noel E. Ashbaugh, and Larry P. Zawada, Eds., American Society for Testing and Materials, 1997, pp. 142-157.

Larsen, J.M., Worth, B.D., Annis, C.G., and Haake, F.K., "An Assessment of the Role of Near-Threshold Crack Growth in High-Cycle Fatigue Life Prediction of Aerospace Titanium Alloys Under Turbine Engine Spectra", International Journal of Fracture, vol. 80, no. 2/3, pp. 237-255, 1996.

Nicholas, T. and Johnson, D.A., "Time- and Cycle-Dependent Aspects of Thermal and Mechanical Fatigue in a Titanium Matrix Composite," Thermo-Mechanical Fatigue Behavior of Materials, ASTM STP 1263, M.J. Verrilli and M.G. Castelli, Eds., American Society for Testing and Materials, 1996, pp. 331-351.

Nicholas, T. and Kroupa, J.L., "Micromechanics Analysis and Life Prediction of Titanium Matrix Composites," Journal of Composites Technology & Research, vol. 20, no. 2, pp. 79-88, 1998.

Smith, P.R., and Porter, W.J., "The Effect of Heat Treatment on the Tensile and Creep Behavior of 'Neat' Matrix Ti-22Al-23Nb," Journal of Materials Science, vol.32, 1997, pp. 6215-6220.

Smith, P.R., Gambone, M.L., Williams, D., and Garner, D.I., "Heat Treatment Effects on SiC Fiber," Journal of Materials Science, 33, 1998, pp. 5855-5872.

Sunder, R., Porter, W.J., and Ashbaugh, N.E., "The Effect of Stress Ratio on Fatigue Crack Growth Rate in the Absence of Closure," Int. J. Fatigue, vol. 19, Supp. no. 1, pp. S211-S221, 1997.

Worth, B.D., Larsen, J.M., Balsone, S.J., and Jones, J.W., "Mechanisms of Ambient Temperature Fatigue Crack Growth in Ti-46.5Al-3Nb-2Cr-0.2W," Metallurgical and Materials Transactions A, March 1997, pp. 825-835.

### **Technical Reports**

Ashbaugh, N.E., Mechanical Behavior of Advanced Aerospace Materials, Interim Annual Report for Period 25 May 1994-24 May 1995, Materials Directorate, Wright Laboratory, Air Force Materiel Command, Wright-Patterson AFB, OH 45433-7734, 1996.

Ashbaugh, N.E., John, R., Porter, W.J., and Worth, B.D., Mechanical Behavior of Advanced Aerospace Materials, Interim Annual Report for Period 25 May 1995-24 May 1996, WL-TR-96-4087, Materials Directorate, Wright Laboratory, Air Force Materiel Command, Wright-Patterson AFB, OH 45433-7734, 1997.

Ashbaugh, N.E., John, R., Porter, W.J., Worth, B.D., Mechanical Behavior of Advanced Aerospace Materials Interim Technical Report for period 25 May 1996-24 May 1997, AFRL-ML-WP-TR-1999-4049, Wright Laboratories, Wright-Patterson Air Force Base, Ohio, 1999.



Coker, D., Frank Boller, Joseph Kroupa, and Noel Ashbaugh, FIDEP2 User Manual to Micromechanical Models for Thermoviscoplastic Behavior of Metal Matrix Composites, AFRL-ML-WP-TR-1999-XXXX, Wright Laboratories, Wright-Patterson Air Force Base, Ohio, 1998.

Metzcar, J. and Ashbaugh, N.E., Modeling the Deformation and Failure of a Unidirectional Metal Matrix Composite Under Sustained Load, The University of Dayton Honors Program, October 1996.

#### **Conference Proceedings**

Dolley, Jr., E.J., Ashbaugh, N.E., and Worth, B.D., "Isothermal High-Cycle-Fatigue of a Ti-46.5Al-3.0Nb-2.1Cr-0.2W (at%) Gamma Titanium Aluminide," Fatigue '96, Proceedings of Sixth International Fatigue Congress, Berlin, FRG, G. Lütjering and H. Nowack, Eds., Elsevier Science Ltd., Oxford, UK, 1996, pp. 1755-1760.

John, R., Nicholas, T., Lackey, A.F., and Porter, W.J., "Mixed Mode Crack Growth in a Single Crystal Ni-Base Superalloy," Fatigue '96, Proceedings of Sixth International Fatigue Congress, Berlin, FRG, Elsevier Science Ltd., Oxford, UK, 1996.

Larsen, J.M., Worth, B.D., Balsone, S.J., and Rosenberger, A.H., "Reliability Issues Affecting the Implementation of Gamma Titanium Aluminides in Turbine Engine Applications," Proceedings from the Eighth World Conference on Titanium, Birmingham, U.K., 23-26 October 1995.

Larsen, J.M., Worth, B.D., Balsone, S.J., Rosenberger, A.H., and Jones, J.W., "Mechanisms and Mechanics of Fatigue Crack Initiation and Growth in TiAl Intermetallic Alloys," Fatigue '96, Proceedings of the Sixth International Fatigue Congress, G. Lütjering and H. Nowack, Eds., Elsevier Science Ltd., Oxford, U.K., 1996, pp. 1719-1730.

Lykins, C. and John, R., "Prediction Of Crack Growth In A Laser Shock Peened Zone," Proceedings of International Symposium on Inelastic Deformation, Damage and Life Analysis, Ed. V.K. Arya, Springer-Verlag Publishers, 4-9 May 1997.

Rosenberger, A.H., Sankaran, S., Smith, P.R., Glass, D., and Rice, D., "Multilayer Coating for the Oxidation Protection of Orthorhombic Titanium Aluminides During Fatigue," Orthorhombic Titanium Matrix Composites II, WL-TR-97-4082, P.R. Smith, Ed., Materials Directorate, Wright Laboratory, Air Force Materiel Command, Wright-Patterson AFB, OH 45433-7734, 1997, pp. 368-378.

Rosenberger, A.H., Worth, B.D., and Balsone, S.J., "Environmental Effects on the Fatigue Crack Growth of Titanium Aluminides," Fatigue '96, Proceedings of Sixth International Fatigue Congress, Berlin, FRG, G. Lütjering and H. Nowack, Eds., Elsevier Science Ltd., Oxford, UK, 1996, pp. 1785-1790.

Rosenberger, A.H., Worth, B.D., and Larsen, J.M., "Effects of Microstructure, Temperature, and Environmental on Fatigue Crack Growth in Ti-46.5Al-3Nb-2Cr-0.2W  $\gamma$  Titanium Aluminide," Structural Intermetallics, Eds. M.V. Nathal, et al, TMS Warrendale, PA, 1997, pp. 555-561.

Russ, S.M., Rosenberger, A.H., and Stubbs, D.A., "Isothermal Fatigue of a SCS-6/Ti-22Al-23Nb Composite in Air and Vacuum," Recent Advances in Composite Materials, S.R. White, H.T. Hahn, and W.F. Jones, Eds., American Society of Mechanical Engineers, New York, 1995, pp. 13-22.

Smith, P.R., Porter, W.J., Kralik, W.J., and Graves, J.A., "The Effect of Post-Consolidation Heat Treatment on the Tensile and Creep Behavior of Neat Ti-22Al-23Nb," Metal Matrix Composites, Proceedings of the Tenth International Conference on Composite Materials, A. Pousartip and K.N. Street, Eds., vol. 2, 1995, pp. 731-738.

Worth, B.D., Larsen, J.M., and Rosenberger, A.H., "Threshold Fatigue Crack Growth Behavior of the Gamma Titanium Aluminide Alloy Ti-46.5Al-3Nb-2Cr-0.2W Under High Cycle Fatigue Conditions," Structural Intermetallics, M.V. Nathal, *et al.*, Eds., TMS Warrendale, PA, 1997, pp. 563-569.

Worth, B.D., Larsen, J.M., Balsone, S.J., and Jones, J.W., "Mechanisms of Ambient & Elevated Temperature Fatigue Crack Growth in Ti-46.5Al-3Nb-2Cr-0.2W," Proceedings from the Eighth World Conference on Titanium, Birmingham, U.K., 23-26 October 1995.